UQAC
Université du Québec
à Chicoutimi

Development of Self-cleaning Polymeric Surfaces Using Polymer Processing Systems for Application to High-voltage Insulators

by

Khosrow Maghsoudi

Manuscript-Based Thesis Presented to Université du Québec à Chicoutimi in Partial Fulfillment of the Requirements for the Degree of Doctor of Philosophy Ph.D.

Summer 2020

Québec, Canada

BOARD OF EXAMINERS

This thesis has been evaluated by the following board of examiners

Professor Gelareh Momen, Thesis Supervisor
Department of Applied Sciences at Université du Québec à Chicoutimi

Professor Reza Jafari, Thesis Co-supervisor
Department of Applied Sciences at Université du Québec à Chicoutimi

Professor Yasar Kocaefe, Internal Member of Jury and President of the Board of Examiners
Department of Applied Sciences at Université du Québec à Chicoutimi

Professor Mohamed Bournane, Internal Member of Jury
Department of Applied Sciences at Université du Québec à Chicoutimi

Professor Éric David, External Member of Jury
Department of Mechanical Engineering at École de Technologie Supérieure

This thesis was presented and defended in the presence of a board of examiners and public on June 4th, 2020 at Université du Québec à Chicoutimi.

Développement de surfaces polymériques autonettoyantes par systèmes de mise en forme des polymères pour applications aux isolateurs à haute tension

Résumé

Dans cette thèse, les systèmes de transformation des polymères sont utilisés pour fabriquer des surfaces superhydrophobes de caoutchouc de silicone vulcanisé à haute température (HTV) à partir d'une réplication directe. Le HTV est l'un des principaux matériaux polymères utilisés dans la fabrication des isolateurs à haute tension. Les systèmes considérés sont des procédés de moulage par compression et de moulage par injection.

L'approche de réplication directe nécessite un modèle ou un insert ayant les structures de surface souhaitée à répliquer sur la surface du polymère. Les micronanostructures appropriées pour obtenir la non-mouillabilité de la surface ont été créées sur les matériaux d'insert (alliage d'aluminium) en utilisant un procédé de gravure chimique. Comme un démoulage sans défaut est essentiel pour obtenir la qualité de réplication souhaitable, un revêtement antiadhésif est appliqué sur les surfaces de l'insert avant le processus de moulage afin d'assurer l'élimination complète du caoutchouc de silicone lors du démoulage. Les surfaces de caoutchouc de silicone développées possédaient des micronanostructures produisant un angle de contact eau (WCA) de > 160 ° et une hystérésis angle de contact (CAH) de < 3 °. La rugosité optimale de surface des inserts en aluminium est obtenue à une concentration massique de HCl de 15%.

Les propriétés autonettoyantes des surfaces produites ont été rigoureusement étudiées pour assurer que ces propriétés autonettoyantes demeuraient efficaces dans des conditions extérieures réelles. La présence de poches d'air entre les aspérités de surface est responsable de la formation du régime de Cassie-Baxter. La consistance de ces poches d'air est cruciale pour obtenir des propriétés autonettoyantes. Par conséquent, une série d'essais ont été effectués pour confirmer la stabilité du régime Cassie-Baxter.

Ensuite, une série complète d'expériences de propriétés autonettoyantes a été réalisée en impliquant des contaminants en suspension et non suspendus (non dispersés) utilisant divers matériaux (par exemple, le kaolin, le noir de carbone, la silice, etc.) et des méthodes d'application de contaminants (par exemple, goutte à goutte, pulvérisation, contaminants humides ou secs) ont été effectuées. Les tests d'autonettoyage ont été organisés, du test le moins sévère, c'est-à-dire de la contamination non suspendue (non dispersée), au test plus sévère, c'est-à-dire de la contamination en suspension humide, et se terminant par le test le plus sévère, à savoir la contamination en suspension sèche. En raison du CAH ultra-bas, les surfaces produites ont montré des propriétés autonettoyantes favorables contre les différents types de contaminants et de différents moyens d'application de contaminants. Les surfaces produites ont conservé leurs propriétés répulsives après l'application des contaminants et après le nettoyage des surfaces, permettant ainsi de vérifier les performances d'autonettoyage et la résistance des surfaces en silicone superhydrophobe fabriquées.

Les propriétés anti-givrantes (la formation retardée de la glace) et les propriétés glaciophobes (la force d'adhérence réduite de la glace) des surfaces produites ont été évaluées. Les surfaces produites sont exposées à la formation de deux types de givrage. Les techniques bien connues de mesure de l'adhésion sur la glace, à savoir le test d'adhérence par centrifugation et le test de poussée, ont été utilisées pour obtenir une comparaison précise des résultats. Les surfaces superhydrophobes produites ont considérablement retardé la formation de glace et réduit la force d'adhérence de la glace. Afin d'évaluer de manière rigoureuse les propriétés de durabilité, une série complète d'expériences a été réalisée sur les surfaces. Les expériences de durabilité ont été menées pour couvrir un large éventail d'applications réelles. En ce qui concerne la capacité attractive du caoutchouc de silicone dans la récupération des propriétés anti-mouillantes, la perte de la propriété de répulsion de l'eau a été régénérée jusqu'à un niveau satisfaisant dans certains cas.

Compte tenu de l'importance de la qualité de la réplication dans la réplication directe des micronanostructures d'une part, et d'autre part du rôle des micronanostructures dans la formation de surfaces superhydrophobes et glaciophobes, les effets des paramètres de moulage par compression des surfaces en caoutchouc de silicone sur la superhydrophobicité, la glaciophobicité et la qualité de la réplication ont été évaluées. Le temps de durcissement, la température de moulage, la pression de moulage et l'épaisseur de la pièce ont été choisis comme paramètres de traitement à évaluer. La méthodologie de surface de réponse a été utilisée pour déterminer les paramètres de traitement optimaux. Bénéficiant des résultats, la pression et l'épaisseur ont été révélées comme les deux paramètres

d'influence principaux des propriétés superhydrophobes. La densité de réticulation des échantillons de caoutchouc de silicone fabriqués s'est toutefois révélée être significativement affectée par le temps et la température. Les valeurs de qualité de réplication ont été déterminées en fonction de diverses pressions et épaisseurs. Il y avait une valeur de pression optimale à chaque niveau d'épaisseur pour obtenir la meilleure qualité de réplication. Il a également été observé que les surfaces présentant la meilleure qualité de réplication affichaient le plus long retard de gel de la gouttelette d'eau, ce qui représentait leur potentiel élevé d'utilisation en tant que surfaces antigivrantes. Bien que toutes les surfaces superhydrophobes aient présenté des propriétés potentiellement glaciophobes, il a été constaté que le scénario d'adhérence sur la glace était plus compliqué en termes de paramètres influents.

Ce projet de doctorat fait partie d'une collaboration industrielle-académique. Les résultats obtenus en laboratoire ont été utilisés pour la mise en œuvre dans l'industrie (K-Line Insulators Limited). À cette étape, des inserts en aluminium et en acier inoxydable ont été utilisés. En utilisant le système de moulage par injection disponible chez K-Line Insulators Ltd., des isolateurs en caoutchouc de silicone ayant des propriétés superhydrophobes ont été produits avec succès. Par conséquent, le partenaire industriel fournit des installations pour modifier son moule afin de produire des isolateurs superhydrophobes à l'échelle industrielle.

Mots-clés: Superhydrophobicité; Caoutchouc de silicone; Micronanostructures; Réplication directe; Moulage par compression; Moulage par injection; Autonettoyant; Glaciophobicité; Paramètres de moulage

Development of Self-cleaning Polymeric Surfaces Using Polymer Processing Systems for Application to High-voltage Insulators

ABSTRACT

Herein, polymer processing systems are used to fabricate superhydrophobic high-temperature vulcanized (HTV) silicone rubber surfaces by direct replication. HTV silicone rubber is one of the main polymeric housing materials used in high-voltage insulators. The selected polymer processing techniques are compression molding and injection molding.

The direct replication approach requires that a template or insert having the desired surface patterns be replicated onto a target polymer surface via a polymer processing. The appropriate micro-nanostructures, required for achieving ultra-water-repellency, were created on the insert materials (an aluminum alloy) using a wet-chemical etching method. As a flawless demolding is essential to acquire desirable replication quality, an antistiction coating was applied to the insert surfaces prior to the molding process to ensure the thorough removal of the silicone rubber during the demolding. The resulting silicone rubber surfaces possessed micro-nanostructures producing a water contact angle (WCA) of >160° and a contact angle hysteresis (CAH) of <3°. The surface roughness of the aluminum inserts was optimized at HCl concentrations of 15 wt.%.

The self-cleaning properties of the produced ultra-water-repellent silicone rubber surfaces were rigorously investigated to ensure a self-cleaning surface at real outdoor imitated conditions. The presence of air pockets in between the surface asperities produced the Cassie-Baxter regime. The consistency of these air pockets is crucial for attaining the self-cleaning properties. A series of tests, including droplet impact, water-jet impact, trapped air layer, and severe droplet contact tests were conducted to confirm the stability of the Cassie-Baxter regime. A comprehensive series of self-cleaning experiments involving both suspended and non-suspended contaminants, e.g., kaolin, carbon black, and silica as well as contaminant-applying methods, e.g., dropwise, spraying, wet or dry contamination were performed. Self-cleaning tests were organized from less severe, i.e., non-suspended contamination tests, to severe, i.e., the wet suspended contamination test, to most severe, i.e., the dry suspended contamination test. Due to their ultra-low CAH, the produced surfaces demonstrated favorable self-cleaning properties against the various types of contaminants and the different means of contaminant application. The produced surfaces retained their water repellency following the application of the contaminants and successful cleaning of the surfaces, thereby verifying the self-cleaning performance and resistance of the fabricated superhydrophobic silicone rubber surfaces.

The anti-icing properties (delayed ice formation) and de-icing properties (reduced ice adhesion strength) of the produced surfaces were evaluated. Two types of icing (atmospheric glaze and bulk ice) were considered to accumulate ice on the surfaces. The well-known ice adhesion measurement techniques, i.e., the centrifuge adhesion and push-off tests were employed to provide quantitative comparisons of the ice adhesion strength of the produced surfaces. The produced surfaces significantly delayed ice formation and reduced the ice adhesion strength. To rigorously assess the durability of the produced surfaces, a comprehensive series of experiments that covered a wide range of real-life conditions were carried out. In some cases, where the water repellency was lost, the silicone rubber surfaces demonstrated a satisfactory recovery of their anti-wetting properties.

Given the importance of replication quality in the direct replication of micro-nanostructures and the role of micro-nanostructures in the formation of superhydrophobic and icephobic surfaces, the effect of processing parameters on the superhydrophobicity, icephobicity, and replication quality in the compression molding of silicone rubber surfaces were evaluated. Curing time, mold temperature, molding pressure, and part thickness were assessed via response surface methodology to determine the optimal processing parameters. Molding pressure and part thickness were revealed as two main influencing parameters in the superhydrophobic properties. The crosslink density of the fabricated silicone rubber samples, however, was found to be significantly affected by curing time and mold temperature. Replication quality was determined for various molding pressures and part thicknesses. There was an optimal molding pressure value at each part thickness level to obtain the best replication quality. Surfaces having the highest replication quality showed the longest freezing delay reflecting their potential use as anti-icing surfaces. Although all superhydrophobic surfaces offered potential icephobic properties, identifying the influential parameters controlling ice adhesion was more complicated.

As this PhD project is part of an industrial-academic collaboration, the results obtained in the laboratory experiments were used for implementation in the industry (K-Line Insulators Limited). This step includes the use of aluminum and stainless-steel inserts. Using the injection molding system available at K-Line Insulators Ltd., silicone rubber insulators having superhydrophobic properties were produced successfully. The industrial partner provided facilities to modify its mold to produce superhydrophobic insulators in an industrial scale.

Keywords: Superhydrophobicity; Silicone rubber; Micro-nanostructures; Direct replication; Compression molding; Injection molding; Self-cleaning; Icephobicity; Processing parameters

TABLE OF CONTENTS

LIST OF TABLES

LIST OF FIGURES

LIST OF ABBREVIATIONS

Al	Aluminum
AAO	Anodized aluminum oxide
CA	Contact angle
CAH	Contact angle hysteresis
CAT	Centrifuge adhesion test
CL	Contact line
CNT	Carbon nanotube
COC	Cyclo-olefin-copolymer
Cu	Copper
DoE	Design of experiment
DRIE	Deep reaction ion etching
ECM	Electrochemical machining
EPDM	Ethylene-propylene-diene-monomer
ETFE	Ethylene-tetra-fluoro-ethylene
FDTS	Perfluorodecyltrichlorosilane
FEP	Fluorinated ethylene propylene
HDPE	High-density polyethylene
HTV	High-temperature vulcanized

LDPE	Low-density polyethylene
LIGA	German acronym for Lithographie, Galvanoformung und Abformung
LIPSS	Laser-induced periodic surface structure
LSR	Liquid silicone rubber
µCM	Micro compression molding
µEDM	Micro-electrical discharge machining
MWCNT	Multi-wall carbon nanotube
Ni	Nickel
OLED	Organic light-emitting diode
PC	Polycarbonate
PDMS	Polydimethylsiloxane
PE	Polyethylene
PLA	Polylactic acid
PMMA	Poly(methyl methacrylate)
PP	Polypropylene
PS	Polystyrene
PSR	Pristine silicone rubber
PTFE	Polytetrafluoroethylene
PU	Polyurethane

PVC	Polyvinyl chloride
RTV	Room-temperature vulcanized
SA	Sliding angle
SAM	Self-assembled monolayer
SEM	Scanning electron microscopy
SHSR	Superhydrophobic silicone rubber
Si	Silicon
SR	Silicone rubber
SS	Stainless steel
Ti	Titanium
TPE	Thermoplastic elastomer
UHMWPE	Ultra-high-molecular-weight polyethylene
UV	Ultraviolet
WCA	Water contact angle

LIST OF SYMBOLS

χ	Flory-Hoggins polymer-solvent interaction coefficient
E	Young's modulus
f_{sl}	Area fraction of solid-liquid interface
γ_{la}	Interfacial energy per unit area of the liquid-air interface
γ_{sa}	Interfacial energy per unit area of the solid-air interface
γ_{sl}	Interfacial energy per unit area of the solid-liquid interface
k	Boltzmann's constant
M_c	Average molecular mass of the crosslink points
v	Number of chains per unit volume
φ	Volume fraction of silicone rubber in swollen sample
φ_s	Area fraction of solid-liquid interface
R	Gas constant
r	Roughness ratio
ρ	Density
T	Absolute temperature
T_{emboss}	Embossing temperature
T_g	Glass transition temperature
T_m	Melting temperature

θ_c	Cassie apparent contact angle
θ_w	Wenzel apparent contact angle
θ_y	Intrinsic contact angle

DEDICATION

To my parents, *Shokouh Akbarzadeh* and *Mostafa Maghsoudi*, who taught me humanity and love,

to my nephew, *Adrian*, with huge love from his uncle,

and

to my beloved wife, *Elham Vazirirnasab*, my endless source of tranquility and delight, without whom this work would not have been possible.

ACKNOWLEDGEMENT

I would like to thank my supervisor Prof. Gelareh Momen, for her continuous guidance, support, and trust during my PhD. She provided excellent opportunities for me to become a better researcher and to learn many valuable skills.

I would like to thank my co-supervisor Prof. Reza Jafari, for working with me at every step of this long journey. His constructive criticism improved the quality of my research. Interactions with him has helped me to learn creativity.

I would like to thank my co-supervisor Prof. Masoud Farzaneh, whose scientific prestige has always been inspiring for me. I also thank him for his valuable comments and worthwhile experience.

I would like to thank my committee members Prof. Kocaefe, Prof. Bournane, and Prof. David for their time, comments, guidance, and support.

I address my special thanks to Mr. Tony Carreira, the president of K-Line Insulators Ltd., for his outstanding role in this academic-industry collaboration and for his support and belief in research work. I also thank Mr. Stephen Bell, Mr. David Blyth and every team member of K-Line for their help and hospitality during our visits and trials.

I would like to thank Mr. Pierre Camirand, not only for his countless technical helps but also for his warm supports at every moment of my PhD life.

I would like to thank Mr. Murray Hay, for his continuous contribution throughout my PhD project as English editor of my works.

I would like to thank Mr. John Coleman for conducting the profilometry analyses at Filmetrics (A KLA Company) and Prof. Zhan Zhang for carrying out the Scanning Electron Microscopy (SEM) tests at University Research Centre on Aluminum (CURAL).

I would like to acknowledge the financial support from the Natural Sciences and Engineering Research Council of Canada (NSERC) and K-Line Insulators Ltd., Toronto, Canada.

Finally, I owe my family, especially my brother Hamid Maghsoudi, and friends many thanks for their support throughout this period in my life.

INTRODUCTION

Definition of the problem

Numerous electrical and mechanical issues have been reported due to the accumulation of pollution and ice on the surface of high-voltage outdoor insulators. Although accumulation of pollution is more severe in coastal areas, desert areas, industrial regions, and highly-polluted cities, the surfaces of outdoor insulators become contaminated inevitably after being operated for several years [1]. The accumulation of ice on high-voltage outdoor insulators has caused many serious issues for power transmission systems in cold climate regions. The presence of pollutants and ice can create a conductive electrolyte layer. This conductive layer followed by dry-band formation allows passing current that will facilitate conditions favoring short circuit. This has a remarkable effect on the insulator flashover [2]. The loss of billions of dollars has been reported in many countries due to the insulators flashover resulted in power outage. Hence, the performance of the insulation materials in the polluted areas and cold climate countries should be addressed carefully and the problem of flashover on the contaminated or iced insulators' surfaces needs to be solved by power and material engineers. Figure 1 shows some examples of the accumulation of pollution and ice on the outdoor insulators with the associated flashover problem.

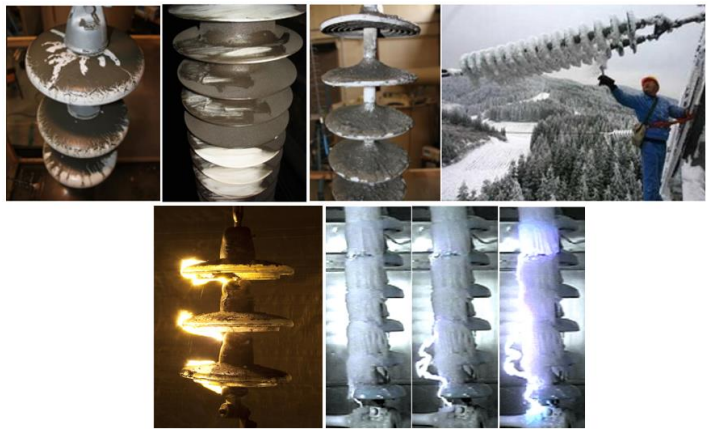

Figure 1. Pollution and ice accumulation on various insulators' surfaces and the resulted flashover [3-5].

Polymeric insulators are widely used as outdoor high-voltage insulator materials. In comparison to the porcelain and glass insulators, polymeric insulators possess superior service properties when exposed to heavy pollution and wet conditions. They also benefit highly from great electrical parameters, i.e., low dielectric permittivity, high breakdown voltage, and high surface and volume resistance. Moreover, polymeric insulators

are resistant to vandalism, they are prone to almost no damage during transportation, and they weigh much less than porcelain and glass insulators [6]. In the 1980s, ethylene-propylene-diene monomer (EPDM) and high-temperature vulcanized (HTV) silicone rubber were presented and accepted as two main polymeric materials for housing high-voltage outdoor insulators (Figure 2) [6]. HTV silicone rubber materials due to their hydrocarbon methyl groups show excellent hydrophobic and water repellent properties [7]. Consequently, the HTV silicone rubber insulators demonstrated favorable electrical performance under contaminated and wet conditions.

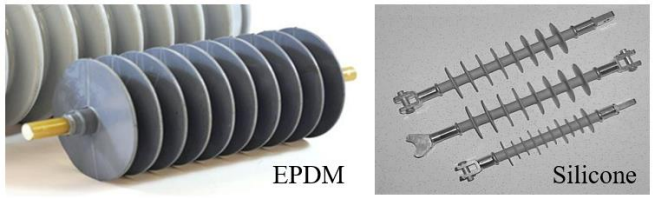

Figure 2. Ethylene-propylene-diene monomer (EPDM) and high-temperature vulcanized (HTV) silicone rubber insulators [8, 9].

However, the HTV silicone-based insulators cannot fully prevent the accumulation of pollution and ice on their surface. Many investigations have reported the flashover problems associated with the contaminated and/or iced silicone rubber insulators [10-14]. Therefore, many attempts have been made to prevent or reduce the accumulation of pollution and ice on the surface of high-voltage insulators most of which were focused on the preparation of a superhydrophobic coating mainly using room-temperature vulcanized (RTV) silicone rubber [15-19]. Although an ability of removing contaminant and a reduction of ice adhesion strength have been shown, there are yet several issues attributed to the use of coatings: i) a considerable amount of chemical solvents is required; ii) additional approvals and testing are required to use new products having coating; and iii) coatings deal with durability issue as they are less mechanically stable and wear out more easily than the bulk materials.

Fabrication of superhydrophobic silicone rubber surfaces having self-cleaning and icephobic properties out of bulk material can significantly reduce the drawbacks of coatings. In this approach, no preceding or subsequent process step is needed on the produced insulator. Therefore, the risk and frequency of problems associated with the accumulation of pollution and ice e.g. power outage and financial loss can be eliminated.

The main purpose of this project is development of self-cleaning and icephobic HTV silicone rubber as polymeric outdoor insulator housing materials by direct replication method out of bulk material.

Overview

By definition, superhydrophobic surfaces having a static water contact angle (WCA) of more than 150° and a dynamic contact angle (contact angle hysteresis (CAH) and sliding angle (SA)) of less than 10° can be achieved by a combination of low surface energy materials and micro-nanostructured surface [20]. Numerous applications have been counted for superhydrophobic surfaces including water repellency, self-cleaning surfaces, viscous drag reduction, icephobicity, anti-bio-fouling, anti-corrosion, desalination, anti-reflective, water-oil separation, and anti-fogging surfaces [21]. Two main properties considered as the objectives of this project are self-cleaning and icephobicity.

Self-cleaning

The self-cleaning properties have influenced considerably industrial applications including self-cleaning window glasses, paints, textile industry, solar panels, electronic devices, bioengineering, and drug delivery [22]. Water droplets, with an almost spherical shape on superhydrophobic surfaces, carry away hydrophilic contaminants adhered to the surface when the droplets roll off the surface. This results from the stronger adhesion of the contaminant particle to the water droplet than the adhesion of the particle to the superhydrophobic surface.

Icephobicity

Superhydrophobic surfaces could also effectively be applied for the icephobic application. Icephobicity can be defined as the ability of a surface to decrease, delay, or prevent icing of water on the surface, and if ice is formed, by weakening the adhesion, the ice removal demands less energy and effort [21]. In the literature, icephobic surfaces are achieved with the goal of: (i) decreasing heterogenous nucleation temperature, (ii) increasing the freezing delay, and/or (iii) reducing ice adhesion strength to the surface.

The study of the delay in freezing onset is a good representative of the icephobic behavior of the superhydrophobic surfaces. The freezing onset is defined as the initiation of water droplet freezing on the surface. A superhydrophobic surface with longer freezing delay time can be potentially considered as an anti-

icing surface because less ice will be accumulated on its surface by the time [23]. Mainly the ice adhesion shear strength is measured via spinning the ice-covered sample in centrifuge (Centrifuge Adhesion Test (CAT)), tensile strength test, and push-off test [24]. It has been always under question if superhydrophobicity enhances the icephobicity or decreases it. Some investigators showed that the superhydrophobic surfaces reduced ice adhesion strength [25, 26], while others observed that superhydrophobicity led to an increase in ice adhesion strength [27].

There are many methods by which superhydrophobic surfaces can be fabricated including lithography, electrospinning, electrochemical processes, sol-gel, chemical vapor deposition, insert (template) making, spray coating, layer-by-layer, and laser ablation [21]. The insert making or direct replication method is a simple yet efficient, non-expensive method capable to be industrialized. In this method, firstly the appropriate micro-nanostructures are created on the surface of a negative replica using various methods. Then, positive replica is produced via the polymer processing methods such as compression molding and injection molding as direct replication methods.

Objectives

The main objective of this project is to develop self-cleaning polymeric surfaces using polymer processing systems namely compression and injection molding through the concept of direct replication for application to high-voltage insulators.

To achieve the main goal of this project, the following objectives are sought after:

- Determining the suitable insert materials and techniques for micro-nanostructured insert making
- Understanding and solving the processing challenges during compression molding of micro-nanostructured surfaces
- Determining the best processing conditions to fabricate ultra-water-repellent superhydrophobic silicone rubber surfaces
- Development of a comprehensive assessment of the self-cleaning/icephobic/durability properties of the produced superhydrophobic silicone rubber surface
- Development of superhydrophobic HTV silicone rubber surfaces using the specific mold geometry of injection molding system at K-Line Insulators Ltd.

Industrial implementation

This project is an industrial-academic collaboration between *University of Quebec in Chicoutimi (UQAC)* and *K-Line Insulators Ltd*. The fabrication of superhydrophobic silicone rubber surfaces having self-cleaning and icephobic properties can significantly reduce the risk and frequency of problems associated with the accumulation of pollution and ice e.g. power outage and financial loss. To this end, polymer processing systems e.g. compression molding and injection molding were considered. This project demanded an extensive work at both lab and industrial scales. The results obtained in the lab (samples produced via a compression molding system with simple insert geometry) needed to be verified at the industrial scale to produce samples via an injection molding system with a complex mold geometry. Moreover, two insert materials, i.e., aluminum alloy and stainless-steel alloy were considered. The injection molding system of K-Line Insulators Ltd. was used for the experiments carried out in the industry. Therefore, the results of this project were used to develop superhydrophobic HTV silicone rubber by the direct replication method at the industrial scale.

Originality statement

Over the last decade, several types of self-cleaning and icephobic coatings have been developed using RTV silicone rubber which led to improvement of the hydrophobicity and performance under pollution. However, there are some issues attributed to this use of coating technology such as (i) coatings easily wear out and are less durable compared to bulk materials, (ii) chemical solvents used in coating preparation raise environmental concerns, and (iii) applying coatings needs much time and labor which is unpleasant for industry. Moreover, in many cases, an unfavorable shutdown in the system is needed to apply coating. To overcome these issues a process that produces self-cleaning and icephobic insulators without any preceding or subsequent process steps such as applying coating is favorable. To meet the objective of developing superhydrophobic insulators from an initially hydrophobic silicone rubber material, the presence of micro-nanostructure roughness is needed. On the other hand, as the main polymer processes to produce HTV silicone rubber are compression molding and injection molding, these appropriate micro-nanostructures should be achieved through compression/injection molding of silicone rubber in micro-nanostructured mold cavities. The originality of the present project can be concluded in the main items as follows:

• Some studies have investigated the micro injection molding of polymeric materials used in micro-fluidic platforms or to produce parts having a weight of milligrams or less. As such, the application of micro compression/injection molding in high-voltage insulation industry is completely a new field of technology.

• Most of the studies on development of superhydrophobic and icephobic surfaces having micro-nanostructures have been accomplished on the metal surfaces such as aluminum and steel. Although there are some studies on the fabrication of polymeric superhydrophobic surfaces via creating micro-nanostructures on their surface, to the best of our knowledge, none of them have explored the fabrication of icephobic surfaces with self-cleaning properties using rubber materials.

• As most injection molding processes are related to production of thermoplastic polymers and as it is more straightforward than the injection molding of rubber materials, this field of study has been out of the ordinary for researchers. To the best of our knowledge, there is no investigation on the compression/injection molding of HTV silicone rubber materials to fabricate superhydrophobic surfaces having icephobic and self-cleaning properties by direct replication concept.

• For the first time, to our knowledge, a comprehensive study was accomplished on the different pollution scenarios imitating the real outdoor condition. This study can be a cornerstone for the future self-cleaning investigations. Moreover, different aspects of icephobicity including delaying ice formation and decreasing ice adhesion reduction were investigated via different icing conditions as well as different ice adhesion measurement techniques.

• The objectives of this PhD project were not limited to the laboratory experiments and article publishing. Using the obtained results, many trials were carried out in the industrial partner trying to fabricate superhydrophobic silicone rubber insulators using an industrial injection molding system.

Methodology

The main objective of this project is to develop self-cleaning HTV silicone rubber surfaces via direct replication method using polymer processing methods such as compression and injection molding systems. The insert making method was selected for direct replication of desired micro-nanostructures. A proper material should be chosen among metals or polymers as insert. Then, a series of inserts having different micro-

nanostructured surface were fabricated using wet-chemical etching. The concentration of acid solution and the etching time were optimized. The morphology of the created inserts was studied using scanning electron microscopy (SEM) and Profilometry analyses. At this step, the inserts production conditions were optimized to acquire the best results in the direct replication using compression molding system which was available in our laboratory. The produced silicone rubber surfaces were characterized using the physicochemical analyses. Moreover, at this step to ensure a flawless demolding, the effect of antistiction coatings on the insert surfaces were examined (Chapter 2).

Then, the self-cleaning properties of the produced superhydrophobic surfaces were assessed via a comprehensive series of experiments from lab-scale tests to real outdoor imitated conditions. A new methodology to investigate self-cleaning properties of superhydrophobic surfaces was introduced. These experiments involved both suspended and non-suspended contaminants using various materials (e.g., kaolin, carbon black, silica, etc.) and contaminant-applying methods (e.g., dropwise, spraying, wet or dry contaminants) (Chapter 3). Moreover, the icephobic properties of the produced surfaces were evaluated regarding the anti-icing and de-icing approaches. The ice adhesion strength measurements were conducted via two well-known techniques, i.e., the centrifuge adhesion and push-off tests providing quantitative comparisons of the ice adhesion strength of the produced surfaces. Furthermore, since the durability and stability of the superhydrophobic surfaces under harsh environmental conditions is an important factor for their application, the stability of the produced superhydrophobic surfaces was assessed under accelerated aging tests that covered a wide range of real-life conditions. The mechanical robustness and chemical stability of the produced surfaces were rigorously examined through various surface durability tests. In addition, the degree of superhydrophobic recovery was also studied where water repellency of a surface was lost (Chapter 4).

Given the role of micro-nanostructures in producing superhydrophobic and icephobic surfaces and the importance of high-quality replication of these micro-nanostructures in direct replication processes, the effect of processing parameters on the superhydrophobicity, icephobicity, and replication quality of silicone rubber surfaces produced via compression molding were evaluated. Curing time, mold temperature, molding pressure, and part thickness were selected as the processing parameters to be assessed. The contribution of surface

roughness and replication quality were determined in the icephobic properties. Response surface methodology was employed to determine the optimal processing parameters. (Chapter 5).

Benefitting from the obtained results and given the specific mold geometry of the injection molding system for production of high-voltage insulators, the appropriate mold inserts having micro-nanostructured surface were produced to run the tests using the injection molding system at K-Line Insulators Ltd. The aluminum inserts were produced using the same conditions by which the inserts were produced for compression molding. For a flawless insertion, the main challenge was to create the desirable micro-nanostructured inserts without any dimensional change during the wet-chemical etching process. A silicone rubber coating protected the inserts from undesired etching. Then, a series of whole silicone rubber insulators having superhydrophobic properties on the sheath area were produced using injection molding system at K-Line Insulators Ltd. Moreover, regarding the interest of K-Line Insulators Ltd., the special alloy of their mold (stainless-steel alloy) was also considered as the material for production of inserts. A special wet-chemical etching was accomplished to create micro-nanostructures on the new inserts' surfaces. The optimal conditions for making micro-nanostructured stainless-steel inserts were determined, and silicone rubber surfaces were produced using compression molding. Then, using the obtained results, inserts compatible with the injection mold geometry were produced. Finally, a series of whole silicone rubber insulators having superhydrophobic properties on the sheath area were produced via injection molding using the inserts with the same material as the injection mold material (Chapter 6).

Thesis outline

The present Ph.D. thesis contains 6 chapters. Following the introduction, a brief literature review regarding the fabrication of superhydrophobic polymeric surfaces by polymer molding processes is presented in chapter 1. In the literature review chapter, the wettability theories, the replication-based fabrications' steps, the challenges of micro-nanostructures production to achieve superhydrophobicity using polymer processing systems such as injection molding, compression molding, hot embossing, etc. are provided. Moreover, a brief literature review regarding the self-cleaning and icephobic properties and the durability of the superhydrophobic surfaces are presented. To prepare this chapter, two of our review papers entitled "Micro-nanostructured polymer surfaces using injection molding: A review" published in *Materials Today*

Communications journal and "Advances in the fabrication of superhydrophobic polymeric surfaces by polymer molding processes" published in *Journal of I&EC Research* were partially used. In each one of the next four chapters, an article corresponding to each part of the above-mentioned project's sub-categories is presented.

In chapter 2, the paper "Direct replication of micro-nanostructures in the fabrication of superhydrophobic silicone rubber surfaces by compression molding" published in *Applied Surface Science* journal is presented. This paper is drawn from the results of the first part of this project on the fabrication of different micro-nanostructured insert surfaces to fabricate silicone rubber surfaces via direct replication technique in a compression molding system. It also addresses the demolding issues of the micro-nanostructured surfaces as well as the suggested solution to enhance the demolding quality. The preliminary study on the anti-icing and self-cleaning properties of the produced surfaces are also presented in this paper.

In chapter 3, the paper "Rigorous testing to assess the self-cleaning properties of an ultra-water-repellent silicone rubber surface" published in the journal of *Surface and Coatings Technology* is presented. In this article, first the consistency of micro-nano air pockets that are present in between the surface asperities responsible for the formation of the Cassie-Baxter regime was investigated. Then, a comprehensive systematic is provided to assess the self-cleaning properties of a superhydrophobic surface regarding different types of contaminants and the contaminant-applying methods. The self-cleaning ability of the produced superhydrophobic surfaces was quantified in this paper.

In chapter 4, the paper intitled "Icephobicity and durability assessment of superhydrophobic surfaces: the role of surface roughness and the ice adhesion measurement technique" which is under review at the journal of *Materials Processing Technology* is presented. In this paper, the icephobic properties were assessed through the measurement of freezing delay time and ice adhesion strength. The ice adhesion strength was evaluated via two common techniques namely the centrifuge adhesion and push-off tests. This aims at providing a comprehensive comparison between two well-known ice adhesion measurement techniques. In addition to repetitive icing/de-icing cycles to study the durability of the produced surfaces, the durability of the surfaces under mechanical forces and chemical media was studied. The recovery of anti-wetting properties of the produced silicone surfaces was rigorously examined in this paper.

In chapter 5, the paper "Evaluating the effect of processing parameters on the replication quality in the micro compression molding of silicone rubber" published in the journal of *Materials and Manufacturing Processes* is presented. The main objective of this paper is to evaluate the processing parameters effect on the superhydrophobic and icephobic properties and the replication quality in the micro-compression molding of silicone rubber materials. The mold temperature, molding pressure, curing time and part thickness were selected among the processing parameters to scrutiny the optimal parameters combination. Then, a design of experiment (DoE) was carried out to identify the influence of four parameters on the superhydrophobic properties and crosslink density. The replication quality and its influence on the icephobic capability of the surface were assessed according to the results obtained from the surface profilometry studies. Thanks to the output response surface maps, the results of this paper can be considered as a key in decision-making for fabrication of superhydrophobic/icephobic silicone rubber surfaces.

Chapter 6 is allocated to the efforts that have been made toward the implementation of the results of this PhD project in industry. Using the results obtained from the laboratory experiments (compression molding), a series of appropriate aluminum inserts were produced to run the tests in the injection molding system available at K-Line Insulators Ltd. Silicone rubber insulators were produced having superhydrophobic properties in their sheath area.

Finally, partial conclusions, general conclusions, and recommendations for future work are presented. In addition to these main body chapters, 3 appendices are also included at the end of this thesis providing supplementary information for articles 2, 3, and 4.

CHAPTER 1

LITERATURE REVIEW

1.1 Introduction

It is a well-established fact that for a material to possess superhydrophobic properties i.e. water contact angle (WCA) >150° and contact angle hysteresis (CAH) and sliding angle (SA) <10°, it must satisfy both physical (surface roughness) and chemical (non-polar groups on its surface) prerequisites [29]; therefore, appropriate materials and surface roughness micro/nanomorphology must be selected [30]. Various methods have been developed to create superhydrophobic surfaces. In general, these approaches can be divided into three groups: (i) top-down, (ii) bottom-up, and (iii) combined approaches [21]. Bottom-up approaches, including chemical vapor deposition (CVD), electrochemical deposition, layer-by-layer (LbL) deposition, and sol-gel methods, create surface roughness by depositing materials onto a surface. These methods produce micro-nanoscale superhydrophobic surfaces even from hydrophilic materials that have a very low air fraction; however, they are limited in their use in industrial applications due to the elaborated procedures and high costs of fabrication [21]. Top-down approaches, which include electron beam lithography, LIGA (German acronym for Lithographie, Galvanoformung und Abformung), templating, micromachining, plasma treatment, and etching, are based on removing materials from the surface to create an appropriate surface roughness [21, 31]. The produced roughened surface becomes a template in a polymer processing method to replicate directly the created roughness on the polymer surface.

Polymer materials have significantly lower surface free energy than metallic materials. Moreover, they demonstrate excellent workability and a high modulus of elasticity. Consequently, fabricating polymeric superhydrophobic surfaces has drawn the attention of many researchers [31]. Superhydrophobic polymeric surfaces can be used for a wide range of potential applications, including gene delivery, self-cleaning surfaces, fluidic drag reduction, non-wetting liquid transfer, micro-fluidic channels, lab-on-a-chip devices, anti-icing and anti-bio-adhesion purposes, transparent surfaces for solar cells and building windows, as well as plastic containers that can be washed without using detergent or can be completely drained of liquid [31-37].

Regarding the great importance of the mass production of superhydrophobic surfaces, polymer molding processes to fabricate superhydrophobic surfaces are highly sought after. There are, however, methods to create

superhydrophobic surfaces other than templating or replication-based routes such as spray coating [38-42], spin coating [43-45], plasma surface treatment [46-53], self-assembled monolayer (SAM) coating [31, 54], dip coating [55, 56], electrospinning [57], or specific case study techniques [58-60]. Many of these methods are not yet practical in an industrial context as they are only achievable when starting them during the initial steps of production [61]. Moreover, most of these techniques suffer from process complexity, a low-level of automation, a limitation of available materials, and high specialization of the required equipment [62]. However, replication-based techniques can be applied to already-produced polymer surfaces, sheets, films etc. The replication-based fabrication processes can be applied to surfaces having complex shapes and sizes, and these methods are usually relatively simple and require less expensive equipment [63]. Moreover, the range of available polymer materials provides a wide selection and variety for fabricating patterned surfaces that meet specific properties [62].

In a word, templating or replication-based techniques are simple yet mass producible for the fabrication of final polymer materials having superhydrophobic property. Not only the replication-based methods are effective in the fabrication of regular surface structures, but also relatively complex patterns can be created by this means. The key element is the use of a high-quality template for the manufacturing of multiple samples. However, micro-nanostructures are prone to mechanical damage, and this requires a careful use of both the produced samples and templates.

Conventionally, microstructures are created to produce the required surface roughness for superhydrophobic surfaces. To achieve a desirable superhydrophobicity by creating surface microstructures, a high aspect ratio is required. Increasing the aspect ratio increases WCA [64]. However, the production of high aspect ratio structures is limited due to processing constraints [65]. Moreover, high aspect ratio structures are prone to faster wear and bending by mechanical forces [61]. The introduction of nanostructures to create hierarchical micro-nanostructures can improve the performance of the produced surfaces in terms of wettability [31]. A dual-scale roughness, i.e. both micro- and nanostructures, not only establishes a more stable superhydrophobic condition, but also requires a lower aspect ratio than a single scale roughness [66]. This occurs due to the formation of a more stable Cassie-Baxter regime where the microstructures are covered by nanostructures [67]. A lower aspect ratio is highly sought after, particularly in terms of the production process

and demolding issues. Nonetheless, surfaces having hierarchical structures display a lower mechanical durability than single-scale microstructures [68]. Furthermore, hierarchical micro-nanostructures create significant challenges for molding technologies [31]. Although the processing challenges in fabricating micro-nanostructured surfaces have been thoroughly studied [28, 69, 70], there remains a knowledge gap for understanding the challenges for producing hierarchical structures specifically for superhydrophobic surfaces.

It is worth mentioning that in some studies, although a replication process was used—the applied methods included injection molding [71-77], hot embossing [78-82], and polymer casting processes [83, 84], the resulting surface possessed only hydrophobic properties (WCA <150°). These unsuccessful attempts to achieve superhydrophobicity via replication can be explained by an inappropriate selection of structure size, a low aspect ratio of the structures, and demolding issues that resulted in a poor replication quality. In some cases, however, the replicated hydrophobic surfaces were used to fabricate superhydrophobic surfaces in a subsequent step, such as applying a nanocomposite coating [83], using plasma treatment [85], or depositing a self-assembled monolayer [35, 86].

In the present chapter, firstly we present a short background of the superhydrophobic theories with a focus on the relationship between structure and wettability. A summary of existing template- or replication-based techniques will be presented including the insert fabrication, the role of processing parameters and demolding in the acquiring the superhydrophobic surfaces. Then, the fabrication of superhydrophobic surfaces using specific polymer molding processes will be studied through four main categories i.e. injection molding, compression molding, hot embossing, and polymer casting. Within each section, the contents are organized based on the used polymer material and its application. Moreover, the pros and cons of microstructures, nanostructures, hierarchical micro-nanostructures, hierarchical micro-microstructures, and three-level hierarchical micro-micro-nanostructures were thoroughly scrutinized in terms of challenges related to processing and their effects on the surface wettability. A short literature review of three main objectives of the current project namely self-cleaning properties, icephobic properties, and durability of superhydrophobic surfaces will be presented afterwards.

1.2 Superhydrophobicity

1.2.1 Theoretical background

The equilibrium contact angle of a water droplet on an ideal smooth and chemically homogeneous solid surface can be calculated by the Young's equation [87]:

$$cos\theta_Y = \frac{\gamma_{sa}-\gamma_{sl}}{\gamma_{la}} \qquad \textit{Eq. 1.1}$$

where θ_Y is the intrinsic contact angle, γ_{sa}, γ_{sl}, and γ_{la} are the interfacial energies per unit area of the solid-air, solid-liquid, and liquid-air interfaces, respectively [88]. The maximum achievable contact angle on such a flat surface is 120° [32] which is due to the surface being chemically homogeneous.

Wenzel and Cassie-Baxter equations were introduced to describe the wetting of rough surfaces. The Wenzel equation, which addresses a non-composite wetting state where the water droplet fills the asperities and wets the pillars, is defined as [89]:

$$cos\theta_W = rcos\theta_Y \qquad \textit{Eq. 1.2}$$

where θ_W is the Wenzel apparent contact angle, r is the roughness ratio, defined as the ratio of the actual wetted area to the projected wetted area. However, for a composite wetting state where air becomes trapped between the asperities due to a standing water droplet that sits on top of the asperities rather than penetrating them, the Cassie-Baxter equation applies [90]:

$$cos\theta_C = \varphi_s(1 + cos\theta_Y) - 1 \qquad \textit{Eq. 1.3}$$

where θ_C is the Cassie apparent contact angle, φ_S is the area fraction of solid-liquid interface [88].

Another marked difference between Wenzel and Cassie-Baxter theories occurs when θ_Y is about 90°. Wenzel's equation produces little difference in the contact angle of a smooth and a rough surface, whereas the Cassie-Baxter equation produces a much larger difference [32]. For the transition from a Cassie-Baxter regime (higher Gibbs free energy) to a Wenzel regime (lower Gibbs free energy), a critical contact angle can be defined as a criterion:

$$cos\theta_{crit} = \frac{\varphi_S-1}{r-\varphi_S} \qquad \textit{Eq. 1.4}$$

Therefore, when $\theta_Y < \theta_{crit}$ the Wenzel state or the metastable Cassie-Baxter state is energetically more favorable, and when $\theta_Y > \theta_{crit}$, only the stable Cassie-Baxter state is possible. This can therefore be useful for designing surface structures [91, 92]. To use *Eq. 1.4*, it is necessary to calculate the φ_s and *r* precisely. These two respective terms can be calculated for square, barrel, and rectangular microchannel structures [61, 91, 93-96] via the following equations:

$$r_{square} = \frac{[(a+b)^2+4aH]}{(a+b)^2} \quad \textit{Eq. 1.5}$$

$$(\varphi_S)_{square} = \frac{a^2}{(a+b)^2} \quad \textit{Eq. 1.6}$$

$$r_{barrel} = \frac{[(a+b)^2+\pi aH]}{(a+b)^2} \quad \textit{Eq. 1.7}$$

$$(\varphi_S)_{barrel} = \frac{\pi a^2}{4(a+b)^2} \quad \textit{Eq. 1.8}$$

$$r_{rectangular} = 1 + \frac{2h}{w+d} \quad \textit{Eq. 1.9}$$

$$(\varphi_S)_{rectangular} = \frac{w}{w+d} \quad \textit{Eq. 1.10}$$

where *a* is the width or diameter of the micropillars, *b* is the distance between the micropillars, and *H* is the height of the micropillars. *h* is the depth, *w* is the width, and *d* is the distance between the rectangular structures.

The presence of air pockets and their stability is essential for maintaining a Cassie-Baxter regime; therefore, the height of the microstructures plays a key role in the determining the transition from a Cassie-Baxter to Wenzel state [92]. For micro-nanostructured surfaces having structure heights ranging from 1 µm to 35.8 µm, the critical structure height for the transition to occur is 4.2 µm, based on the fitted curves in Figure 1.1(a) [61]. However, only texture heights >30 µm lead to a WCA >150° and a SA <10°. In terms of structure diameter, the optimal diameter for achieving a maximum WCA is 40 µm when the spacing and height are fixed at 10 µm and 15 µm, respectively (Figure 1.1(b1)) [61]. As can be seen in Figure 1.1(b2), the WCA increases as diameter increases to 40 µm. Greater than 40 µm, i.e. $\varphi_S > 0.5$, $b/a < 0.25$; see *Eq. 1.7* and *Eq. 1.8*, the WCA is reduced as the flat surfaces of the wider pillars favor an easier contact between the water droplet and pillar tops [61]. In summary, the highest WCA occurred when φ_S was at its lowest value and *r* was at its highest

value (i.e. a = 40 µm). However, their results could have included the CAH or SA values to provide a more comprehensive assessment of the Wenzel and Cassie states. Among the various structures, including pyramid, sawtooth, rectangular, and conical forms, the spherically topped cylindrical and pyramidal structures produced a better superhydrophobicity, i.e. higher WCA and lower CAH [62].

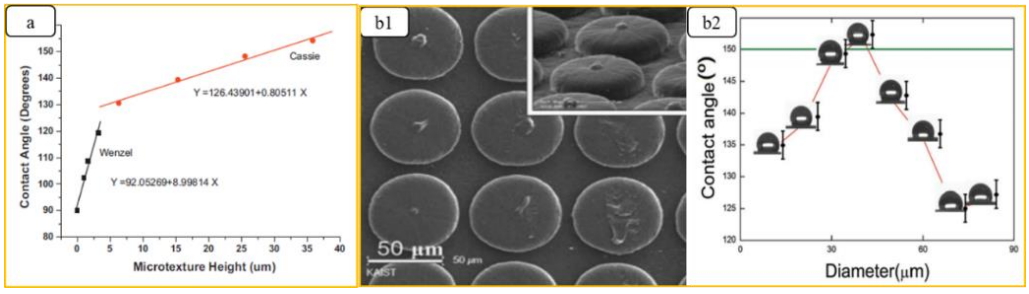

Figure 1.1. (a) The critical structure height for the transition from a Cassie-Baxter to Wenzel regime [92]; (b1) SEM image of PP pillars, 40 µm in diameter; and (b2) the variation of WCA with PP pillar diameters, the peak WCA occurs at a 40-µm diameter [61].

To design a structured surface having the desired superhydrophobic properties, these general requirements must be met: (i) the well-established requirement of a hydrophobic substrate having an initial WCA >90°; (ii) high aspect ratio of the surface asperities to provide a large surface area for the structures; (iii) pillars lacking sharp edges to limit pinning of the water droplet; (IV) tight packing of the structures to avoid destabilization of the solid/liquid/air composite; and (V) small-sized asperities relative to droplet size [97].

1.2.2 Templating or replication-based fabrication

A replication-based method generally involves three steps: template making (insert, stamper, or inlay) where a template having suitable structures is fabricated; a molding step where polymer materials are replicated on the template surface based on the specific processing techniques; and a demolding step where the structured polymer surface is very carefully detached from the template surface in a manner to avoid damaging the micro-nanostructures.

An insert is an exchangeable cavity that can extend the longevity of the main mold, provide the possibility of changing and testing various microstructural designs, and reduce the cost of tool making [28, 98]. A heatproof epoxy adhesive can be used to glue the insert onto the mold plate. This fixing is critical, especially for horizontal injection molding processes [91, 99-101]. A wide range of materials can be used for making inserts through various methods that include LIGA-based technologies, micro-electrical discharge machining

(μEDM), micro-mechanical milling, electrochemical machining (ECM), deep reaction ion etching (DRIE), plasma treatment, wet-chemical etching, and laser ablation [28, 69, 102-105].

One of the most prevalent techniques for fabricating templates is laser ablation. Ultrashort lasers—lasers with a pulse duration of several femtoseconds or picoseconds—can create microstructured surfaces having minimal debris contamination, a good reproducibility, and a very limited heat-affected zone [77]. Nanosecond lasers produce heat-affected zones that are considerably larger than those of ultrashort lasers. Comparing femtosecond and picosecond ultrashort lasers, the femtosecond laser reduces the size of the heat-affected zone due to its shorter pulse duration; however, the femtosecond laser is disadvantaged by a low average power, low repetition rate, a higher probability of breakdown, and higher cost. As such, the use of femtosecond lasers in industrial applications is more difficult [32]. The picosecond laser is therefore more widely used in the production of microstructured surfaces [32, 106]. Compared to picosecond- or femtosecond-pulsed lasers used for micropatterning, the nanosecond laser has a lower quality of ablation due to the creation of rough edges or burrs. Moreover, nanosecond lasers cannot create laser-induced periodic surface structure (LIPSS) or ripples, which are necessary for fabricating hierarchical micro-nanostructures [32, 77]. Ripple structures can be controlled by altering the laser parameters. Nevertheless, the nanosecond-pulsed laser is often used in industry for material processing [107]. Laser ablation parameters, such as the number of pulses, pulse width, wavelength, fluence, and laser Gaussian intensity distribution at the laser focus, markedly influence the resulting surface roughness [106]; for example, the greater the laser irradiation fluence, the higher the resulting WCA upon the replication of a polymer surface on a titanium (Ti) template due to the creation of more nanostructures on single spikes [106].

The molding process begins with the flow of polymer into the cavity, driven by the applied pressure. There is low flow resistance until the molten polymer reaches the microfeatures. At the edge of the microfeatures, resistance increases significantly, and the polymer hesitates to fill the microstructures. Higher pressure is required to overcome this resistance and force the polymer down into the microfeatures [108]. During the filling stage, due to the very fast heat loss of the molten polymer once in contact with the cavity wall, a solidified premature layer can quickly form. As soon as this solid layer is formed, there is not enough back pressure to push this layer into the structures and, consequently, the polymer is prevented from easily

filling the micro-nanostructures. To avoid this problem, a number of solutions have been proposed including manipulating the mold temperature as well as increasing the molding pressure [109]. In addition to the high molding pressure and desirable mold temperature, an even distribution of cavity pressure is also required to achieve the highest level of uniformity and uniform height for microfeatures [110].

A means of ensuring the efficient filling and more economic process design, it is suggested that the micro injection could be first accomplished by using the conventional processing parameters, and then by using elevated temperature and pressure to ensure a high filling ratio [111]. However, this technique is highly questionable in the case of rubber injection molding. The mold temperature in the latter process is much lower than that for plastic injection molding. As such, in the rubber injection molding process, increasing the temperature after the filling stage leads to an increase in crosslink density and crosslinking reaction rate. This is highly undesirable especially in terms of micro-nanostructure filling.

Consequently, to achieve a complete and preferable replication, a combination of different processing parameters is necessary. A DoE method has been used in a number of studies [108, 110, 112-114]. Through a DoE method, experimental data is acquired in a controlled way; the significant and non-significant factors affecting a process are determined, and, finally, the behavior of molding of micro-nanostructures can be carefully monitored. To better understanding the effect of various processing parameters on the replication quality and to help finding the optimum conditions, a process window could be provided [115].

Both processing parameters and demolding conditions affect the final heights of the replicated micro-nanopatterns. In addition to a complete mold filling, high quality replication requires a flawless demolding where all micro-nanostructures withstand demolding forces. Inappropriate design of demolding forces used to remove the manufactured piece from the cavity can lead to irreparable structural deformation or even failure of the molded features on the polymer surface, and also can affect the lifetime of the mold [116-118].

Accurate design is needed considering many factors from polymer selection and mold conditions to processing parameters and part design [119]. Applied forces to the polymer surface, difference in the thermal conduction coefficient between the polymer material and mold metal, generated forces due the shrinkage of the polymer during the solidification stage, process parameters, cavity shape and material, molding material and geometry, features shape and aspect ratio-to be name but a few [117].

There are two different main demolding methods. Either one or both methods can be used to release the final product from the mold. The first uses demolding chemical surface agents named antistiction coatings. The second is a mechanical ejector such as pins, blades, rings, sleeves, and stripper blades [112, 117, 120]. Both methods have advantages and disadvantages. Use of chemical demolding agents is restricted in the medical or some microfluidic applications due to probable harmful effects on human health [121]. Mechanical ejectors can lead to permanent deformation especially when the part geometry is complicated or the distribution of the ejector pins is not appropriate [114, 117]. Therefore, a proper design of produced tool and the location of ejector pins is necessary to avoid damage and failure to the polymeric parts [112]. To circumvent the disadvantages of both chemical and mechanical demolding approaches, novel methods such as ultrasonic vibration [121] and reduction the surface roughness to decrease the coefficient of friction of the mold surface [122] require further investigation. In general, demolding is comprised of two different forces (Figure 1.2): adhesion and friction. Adhesion is the force at the intersection of the microfeature bottom and the top surface of polymer material. Friction is the force produced by the movement of the molded polymer inside the feature along the walls of the microfeature. The force acts in the opposite direction to the ejection movement [117].

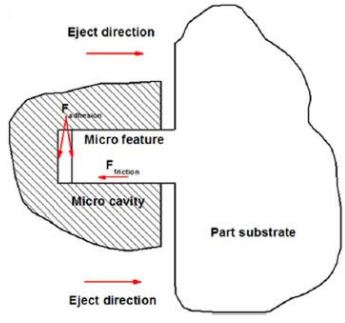

Figure 1.2. Illustration of the demolding forces [117].

Using antistiction coating, which is also known as hydrophobization of the template surface, to improve the demolding process was approved in many investigations [28, 65, 85, 123-125]. The low surface energy coatings are commonly used as the antistiction coating using self-assembled monolayer method. Fluorocarbon or hydrocarbon-based coatings such as fluorocarbonsilanes are the most common antistiction coating [123, 124]. However, utilization of siloxane-based coatings and aqueous ethanol solution of stearic acid were also reported [96, 126, 127]. Figure 1.3 shows the positive effect of perfluorodecyltrichlorosilane (FDTS) coating on demolding [116].

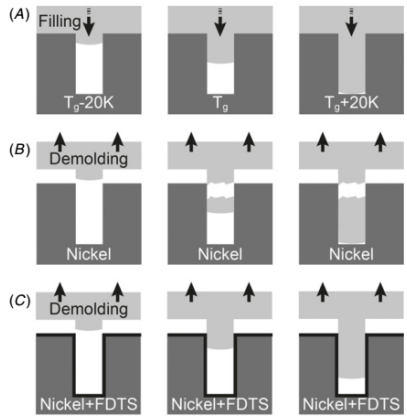

Figure 1.3. Schematic of the filling and demolding processes: (A) Filling of mold nanostructures with different temperatures (below Tg, at Tg, and above Tg) by polymer melt. (B) Demolding at a mold temperature far below Tg leading to fracture of structures. (C) FDTS coated nickel molds at a mold temperature far below Tg leading to a proper demolding [116].

1.2.3 Superhydrophobic surfaces produced by injection molding

Among the different polymer processing techniques, injection molding is preferred for the mass production of materials having a specifically desired size and shape. Injection molding benefits from a low-cost fabrication of polymer parts in large quantities, the possibility of producing versatile shapes, short cycle times, and simple automation. Injection molding generally consists of filling, packing, holding, cooling, and demolding steps [28]. In the injection molding of micro-nanostructured surfaces, the greatest challenge is the proper filling of polymer into the micro-nanostructures. This difficulty stems from the arduous filling of polymer melt into the micro-nanostructures due to the microscopic dimensions and the relatively fast cooling rate of polymer material—due to the increased surface to volume ratio [28, 115]. The fabrication of micro-nanostructured surfaces via the injection molding process has been studied for various applications [28, 69, 128]. Here, we report on recent advances in using injection molding for fabricating superhydrophobic surfaces having micro-nanostructures.

1.2.3.1 Thermoplastics

Zhou et. al. [31] used two grades of polycarbonate (PC) and polypropylene (PP), both having excellent toughness. To enhance the replication quality, an anodized aluminum oxide (AAO) template was coated with an antistiction coating (self-assembled FAS-17). The geometrical morphologies and replication qualities of the injection-molded PC and PP were altered by changing the mold temperature. For both polymers, the increased mold temperature increased the WCA of the surfaces replicated on dual micro-nanostructured templates. This

enhanced WCA was due to the creation of hair-like nanostructures on the micropillar arrays at high mold temperatures. At lower mold temperatures, the WCA was lower than when microstructured templates were used; thus, the use of dual structures is irrelevant when the mold temperature is low. Finally, although the WCA of the produced surfaces was >150°, the SA of ~18.8° demonstrated that the surface had a non-favorable water repellency.

Weng et al. [88] fabricated superhydrophobic hierarchical PP surfaces by having the surface acquire two types of microstructures via a punching plate and ultraviolet (UV) lithography. Due to the high cost of nanoarray fabrication via electron beam lithography, nanostructures were produced using the electrochemical method. The WCA of the hierarchical micro-nanostructured surface reached 163° with a SA of 5°; the observed superhydrophobicity of the micro-nanostructured surface was greater than for the various microstructured surfaces.

Given that many applications could benefit from having curved superhydrophobic surfaces, injection molding has been used to create hierarchically micro-microstructured and curved PP surfaces [129]. A microworking robot created microstructures on a 0.2-mm thick aluminum (Al) foil template. This approach can be applied to both convex and concave surfaces as well as both spherical and cylindrical curved surfaces (Figure 1.4(a1-a6)). The produced micro-microstructured PP surfaces showed a WCA >160° and a SA <10°. From this, two main advantages of micro-microstructures over micro-nanostructures became apparent: 1) the simple one-step fabrication process via the microrobot technique, and 2) the greater durability and mechanical robustness of the micro-microstructured surfaces relative to the micro-nanostructured surfaces [91, 129]. As such, the use of micro-micro hierarchical structures was proposed as a solution for avoiding use of the more vulnerable micro-nano hierarchical structures that would be subjected to mechanical forces [130]. However, a comparative study that would evaluate micro-microstructured surfaces against micro-nanostructured surfaces composed of the same materials under specific mechanical loads is required to truly test this possibility.

Recently, three-level hierarchical structures (i.e. micro-micro-nanostructures) were shown to significantly enhance superhydrophobicity (Figure 1.4(b1, b2)) relative to the more common two-level hierarchical structures [99]. WCA attained 170°, and a CAH as low as 5° was obtained for micro-micro-nanostructured PP surfaces; a two-level micro-microstructured PP surface produced a WCA and CAH of 153°

and 8°, respectively. Moreover, these produced three-level surfaces may be less susceptible to losing their water-repellency properties as the nanostructures are protected by microstructures [99]. This idea also needs to be confirmed by a mechanical abrasion test to determine whether the presence of microstructures actually offers a protective role for the nanostructures.

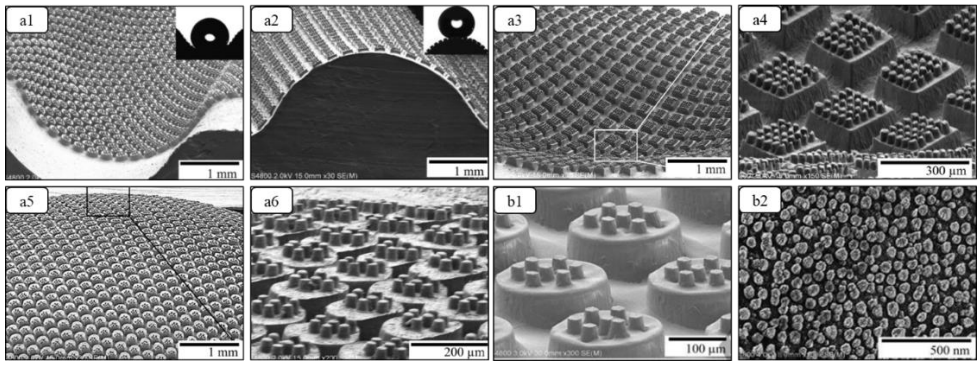

Figure 1.4. SEM images of a curved PP surface having (a1) concave cylindrical, (a2) convex cylindrical, (a3) concave spherical, (a4) close-up from the top of the concave spherical, (a5) convex spherical, (a6) close-up from the top of the convex spherical structures [129]and SEM images of micro-micro-nanostructured PP surface; (b1) micro-microstructures and (b2) nanobumps on top of upper micropillars [99].

The possibility of achieving superhydrophobicity using only nanostructures has also been studied [131]. Polyethylene (PE) nanowire arrays were fabricated using a nano-molding technique via an injection molding. A piezoelectric transducer produced a frequency of ~10 kHz. The induced oscillatory shear rate helped orient the polymer chains to better fill the 100-nm and 200-nm template pores [131]. However, to produce a 50-µm thick PE nanowire, about 1 hr was required. Having the created nanowires on the surface, the fabricated PE showed superhydrophobic properties with a WCA >150°.

In summary:

- Polyolefins are the main materials for fabricating superhydrophobic surfaces by injection molding;
- Injection molding provides an opportunity to fabricate various complex surface geometries;
- Hierarchical structures show better superhydrophobicity if the processing parameters are manipulated precisely;
- Micro-microstructures and micro-micro-nanostructures present a favorable superhydrophobicity and an enhanced mechanical durability compared to conventional micro-nanostructures;
- This enhanced durability remains to be properly evaluated.

1.2.3.2 Elastomers

When fabricating superhydrophobic liquid silicone rubber (LSR) surfaces having micro-cones [33], lower base diameters of the individual cones and lower peak-to-peak distances between the cones increase the WCA. However, arbitrarily reducing the peak-to-peak distance can lead to a more compact surface that facilitates droplet spreading. Moreover, larger aspect ratios result in a higher WCA. In a study by Berendsen et al. [132], aspect ratios >0.41 produced an advancing WCA of >150°, whereas aspect ratios >1 led to both an advancing WCA >150° and a CAH <10°. To successfully achieve larger aspect ratios, the rubber curing should be delayed as much as possible. The best results are obtained by using higher injection rates and lower mold and melt temperatures [33].

Benefitting from the elastic property of thermoplastic elastomers (TPEs), Saarikoski et al. [101] succeeded in producing nanograss-covered, nail-shaped micropillar surfaces having overhang angles up to 101°. Although the injection molding of high aspect ratio or overhanging structures (or re-entrant structures) has always faced challenges in their processing [65], structures having a high overhang angle produce the best WCA values [34, 133]. Nail-shape structures are not observed in the case of micropillars, while the presence of nanostructures stretches the elastic micropillars during the demolding step. Consequently, the height of the hierarchically structured micropillars was about 1.5× higher than that of the sole micropillars (Figure 1.5(a, b)). Among the different surfaces having microstructures, nanostructures, and hierarchical structures, only the hierarchical structured surfaces achieved a WCA >150°. The calculated surface fraction of liquid in contact with the structures (φ_S in *Eq. 1.3*) revealed that the hierarchical surface had the lowest φ_S value between all the surfaces (i.e. 0.08). It indicates the presence of a large fraction of trapped air between the micropillars (i.e. 0.92), which has a key role in forming a water-repellent polymer surface [101].

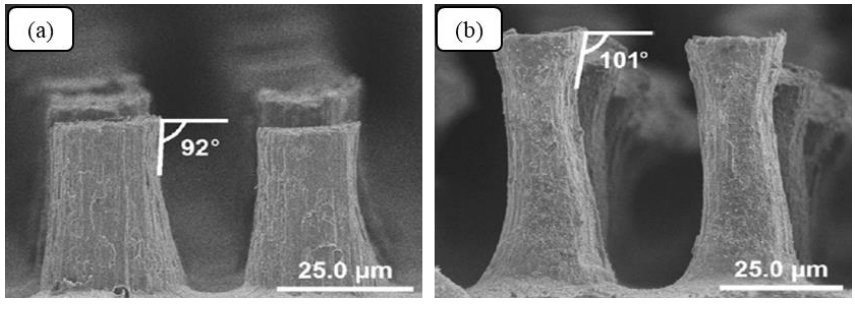

Figure 1.5. Overhang angle for (a) micropillars and (b) hierarchical micronails [101].

In summary:

- This is a less-studied domain despite the multiple applications of elastomers for fabricating superhydrophobic surfaces;
- By benefitting from the elastic properties of elastomers, larger aspect ratios and overhang structures can be produced during demolding.

1.2.4 Superhydrophobic surfaces produced by compression molding

Compression molding is a well-known closed-molding technique for producing polymer parts under high pressure and adjustable temperatures. In compression molding, usually one plate is stationary, and the other plate is moveable. Various closed-mold geometries are used in compression molding systems. The materials flow due to the application of pressure and heat to form the mold cavity shape. To achieve the desired molding quality, three factors should be highly controlled during the compression molding process: pressure, temperature, and time. Compression molding is rarely used to fabricate micro-nanostructured surfaces due to the relatively high pressure applied to the materials. The high pressure may damage fragile insert materials, such as silicon (Si) wafers. However, it is an appealing technique to produce industrial-scale superhydrophobic micro-nanostructured polymer surfaces.

1.2.4.1 Thermoplastics

To achieve anisotropic wetting surfaces, polymer surfaces having microscale directional groove patterns having a triangular cross-sectional shape have been fabricated using the compression molding of PP plates [35]. Inspired from rice leaves, bamboo leaves, and butterfly wings, anisotropic wetting surfaces are sought after for their applications in liquid shape control and transportation. Such surfaces demonstrate two different wettability behaviors in directions that are parallel and perpendicular to the pattern direction. To avoid forming wrinkles, side wall slope, and uncontrollable surface roughness when laser machining a surface, Lee et al. [35] created three different groove patterns on a Cu plate using an ultra-precision machining system (Figure 1.6(a1-a3)). WCA decreased as the groove depth increased. Only the surface having a 10-μm groove depth showed a WCA >150° in the direction parallel to the grooves. Other surfaces produced a WCA <150°. However, regardless of groove size, the water droplet remained pinned to the surface when the surface was tilted, even at a large tilt angle. This indicates that these designs are not appropriate for achieving superhydrophobicity

using PP materials and that strong pinning occurs on the microscale structures [35]. These observations also demonstrate the importance of the presence of nanostructures for the superhydrophobicity of surfaces. Nanostructures can be created by wrinkle formation during laser ablation [32, 77] or by applying a nano-scaled low surface energy coating [35].

A femtosecond laser has also been used to create hierarchical micro-nanostructured grooves on Ti templates (Figure 1.6(b1)). The compression-molded PP surface produced by these means showed a favorable superhydrophobicity (Figure 1.6(b2)) [127]. An optimal temperature and pressure of 115 °C and 15 MPa, respectively, achieve a replication fidelity as high as 90% and a WCA of 154°. Higher temperatures and pressures, however, damage both the Ti template and the PP surface; lower temperatures and pressures lead to unfavorable filling. To guarantee a high-quality replication, therefore, the use of xylene liquid is recommended to remove PP residue from Ti templates after repetitive cycles [127].

In another study, three different patterns, i.e. paraboloidal, tripled, and cauliflower micro-nanostructures, which originated from various laser ablation conditions, were replicated on three different polymer materials, i.e. high-density polyethylene (HDPE), polylactic acid (PLA) and medical polyvinyl chloride (PVC). The cauliflower patterns produced the highest R_a (arithmetic average of the surface roughness) due to the presence of submicron structures, and the highest WCA and the lowest CAH values were obtained from both the HDPE and PLA surfaces [134]. The results improved when T_{emboss} was greater than T_m, rather than when $T_g < T_{emboss} < T_m$ because the polymer flows more easily into the micro-nanostructures due to the lower viscosity of thermoplastic materials at elevated temperatures. The medical PVC, however, did not show favorable superhydrophobic properties (WCA <150°) due to the presence of the Tris (2-ethylhexyl) trimellitate plasticizer. The abundance of C=O groups creates a strong adhesion between the water droplet and the PVC surface resulting in a CAH >90°.

In terms of effect of thermoplastic demolding at elevated and cooled temperatures on the final surface roughness, HDPE surfaces were demolded from the mold insert without allowing the surface to completely cool down (85–100 °C). By doing so, re-entrant micro-fibril structures can form on the surface due to the strong adhesion between the polymer chains and the high surface energy of the stainless-steel mold insert [134] (Figure 1.6(c1, c2)). Such hook-like structures on the surface of HDPE produce a superoleophobic behavior.

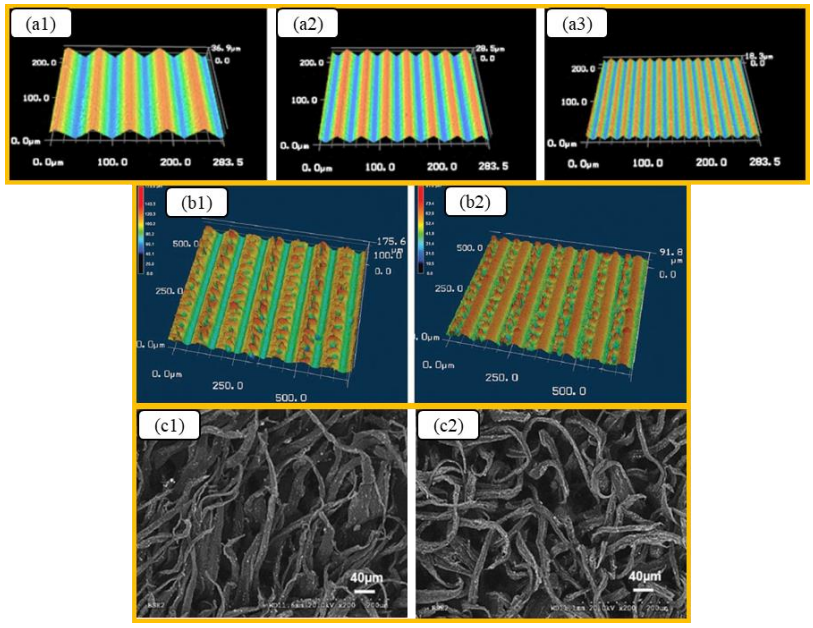

Figure 1.6. Confocal microscopy images of the replicated groove patterns on the PP surface with (a1) 30 μm, (a2) 20 μm, and (a3) 10 μm depth [35]. Laser microscope profiles of (b1) Ti template and (b2) a replicated PP sheet [127]; SEM images of superoleophobic fibrous rough structures of HDPE formed by demolding from a hot mold surface (85–100 °C), where (c1) tripled and (c2) cauliflower roughness structures were used as a template [134].

Studies addressing the effect of pressure and processing time on the achievable height of protrusions, the WCA, and the SA of micro-nanostructured polytetrafluoroethylene (PTFE) films have demonstrated that increasing pressure beyond a certain level has no significant effect on the height of the protrusions, the WCA, or the SA [135]. However, by increasing the processing time, the attained height of the protrusions and the WCA both increase, and the SA decreases (Figure 1.7(a1-a3)). At longer processing times, the micro-scale protrusions and the nanoscale fiber structures became well developed to produce a WCA >150° and a SA <10° (Figure 1.7(a3)). This formation of a nanoscale filamentous structure is attributed to the filamentation of the long polymer chain molecular structure of PTFE under certain pressures and temperatures [135].

Lim et al. [136] successfully produced micro-nanostructured hierarchical superhydrophobic surfaces using a cyclo-olefin-copolymer (COC) film. Micro-sized dimples were created on aluminum (Al) sheets using laser ablation (Figure 1.7(b1)). Then, the rough recast layers produced by the laser ablation were removed through wet-chemical etching in a NaOH solution and electropolishing in a mixed solution of $HClO_4$ and C_2H_5OH (Figure 1.7(b2)). The nanostructures, however, were created on the Al 1050 sheets via a one-step anodization process and on high-purity Al via a two-step anodization process (Figure 1.7(b3, b4)). Therefore,

the hierarchical micro-nanostructured templates resulted from the sequential utilization of both techniques. The replicated COC surface fabricated at 120 °C at 8.3 MPa had a WCA of 162.3°, testifying to the high-quality replication of the micro- and nanostructures (Figure 1.7(b5-b7)). However, the microstructured template, the nanostructured template at two temperatures (100 °C and 120 °C), and the micro-nanostructured template at 100 °C did not produce a WCA >150 °C upon replication due to a poorer replication quality [136].

A stretching effect was also observed when nanostructures were replicated on the COC surface with the anodized high-purity Al produced by the two-step anodization process. This effect was not observed in the case of the anodized Al 1050 produced by one-step anodization (Figure 1.7(b7, b8)). This stretching effect was related to the more regular nanopores created on the high-purity Al; the higher the temperature, the greater the stretching of the structures. Consequently, the highest WCA (~162.3°) was attained with hierarchical micro-nanostructures processed at a higher temperature [136].

Transparent superhydrophobic surfaces have potential applications in self-cleaning solar cells, protective optics, and building windows. Transparent superhydrophobic PS surfaces have been produced using compression molding [107]. Among six step sizes tested (50 μm to 300 μm), only the 50, 100, and 150 μm step sizes led to a WCA >150°; there is an easier transition from the Cassie-Baxter regime to Wenzel as step size increases. However at each step size, the pillar height determines the possible wetting area, although this effect of different pillar heights has not been studied. For transparency, the larger the step size, the more transparent the surface; the increase in the area fraction of the flat surface and decrease in the area fraction of the patterned surface causes scattered reflection. Therefore, the optimum step size of 150 μm was introduced to acquire both superhydrophobicity and acceptable transparency.

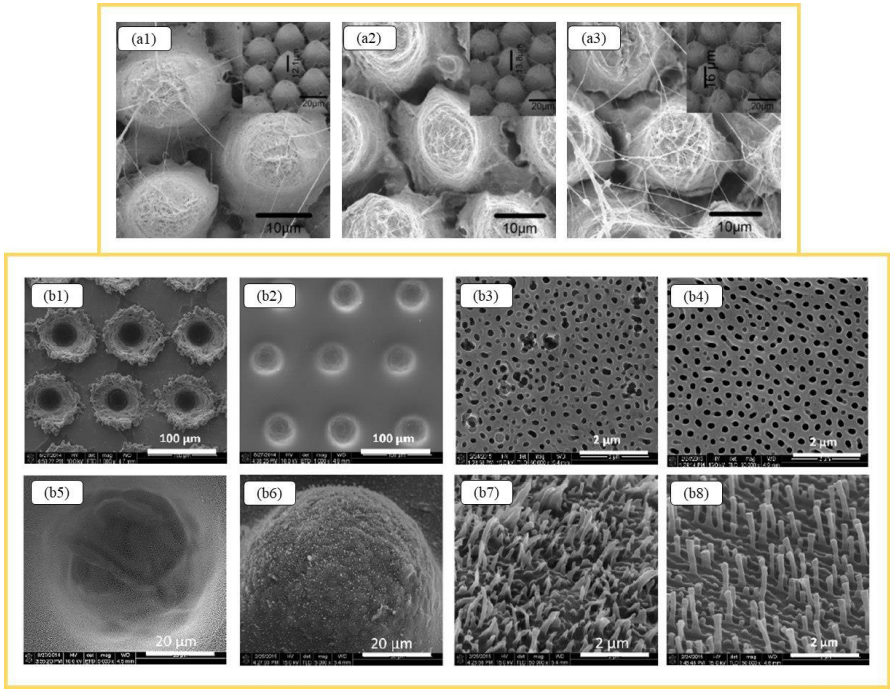

Figure 1.7. SEM images for the processing times of (a1) 5 min, (a2) 10 min, and (a3) 15 min on a PTFE surface (pressure is 70 MPa and temperature is 130 °C) [135]. (b1) Dimples by laser ablation; (b2) removing of recast layers by wet-chemical etching and electropolishing; (b3) porous AAO created by a one-step anodization process; (b4) regular nanopores on anodized high-purity Al; (b5) microstructured dimples on the Al 1050 template containing nanopore structures; (b6) replicated COC representing microstructures; (b7) magnified view of the center of (b6) representing nanostructures; (b8) stretched structures on the replicated COC surface on the anodized high-purity Al at 120 °C [136].

In summary:

- The presence of hierarchical micro-nanostructures can ensure the emergence of superhydrophobicity;
- Temperature, time, and pressure should be carefully controlled in compression molding systems to obtain favorable water repellency.

1.2.4.2 Elastomers

Corona aging can transform the superhydrophobic behavior of silicone rubber into a superhydrophilic behavior by altering the surface energy of silicone rubber. However through self-healing, the superhydrophobic properties can be recovered in full [137]. This restoration occurs due to the rotation and movement of the low molecular weight chains that are thermodynamically driven to the surface to minimize the surface free energy. Such a self-healing property was not observed, however, in a case of aging after water immersion [137]. Thus for the self-healing process to occur, the Cassie-Baxter regime must be achieved; however, it is hindered by

the energy barrier of the Cassie–Wenzel transition. Strengthening the stability of the surface chemical composition and improving the surface roughness can facilitate self-healing [137].

1.2.5 Superhydrophobic surfaces produced by hot embossing

Hot embossing or the thermal nanoimprint technique is one of the most highly used processes for fabricating micro-nanostructured surfaces. Amorphous and semicrystalline thermoplastic polymers and thermoplastic elastomer polymers can be replicated via hot embossing [138]. In general, a thin polymer film is heated up to attain a temperature that lies between its softening and melting points. Then, the desired pattern is replicated on the surface by a pressure that is significantly less than the compression molding pressure: pressures of several kPa and less for hot embossing compared to several MPa pressures for compression molding. The polymer part is demolded after the polymer surface cools down and the structures are sufficiently fixed. However, some studies have shown how to benefit from the stretching effect of the thermoplastic polymers during demolding at elevated temperatures to create high aspect ratio structures. This will be thoroughly discussed in the following section.

1.2.5.1 Thermoplastics

The effect of replication temperature on the WCA of PC surfaces (T_g = 147 °C) replicated on microtextured Si wafer masters has been investigated. By increasing the temperature from 155 °C to 175 °C, the average height of the micropillars on the PC surface increases from 1.34 µm to 6.68 µm. This change in the micropillar height increases the WCA from 82° to 155° [29]. To avoid transferring ablated debris from the Si wafer surface to the PC surface during replication, the Si surface is etched by hydrofluoric acid for two minutes prior to the replication process.

To obtain nanostructures on dome-like PC microstructures, Ho et al. [139] used two different fabrication methods. The first approach was the anodizing of an Al-coated dome-like Si mold fabricated by photolithography. The second was via the assembly of a porous membrane on top of a micromachined dome-like mold. Then, upon molding the polymer substrate, the porous membrane was etched. The first approach produced surfaces having 10 µm as a first hierarchical level and 200 nm as a second hierarchical level. The second approach created surfaces having 400 µm for the micro-domes (the first hierarchical level) and 0.8–3.0

μm for the second level. The obtained WCAs showed an improved superhydrophobicity for the first approach due to the more appropriate hierarchical structures [139].

A novel approach involves fabricating hierarchically structured surfaces via direct replication [140]. This technique is a combination of a two-level hot embossing, the first creates microstructures, the second creates an additional level of sub-micro or nanostructures (Figure 1.8(a1, a2)). This technique is only applicable for thermoplastic materials as two heating-cooling cycles are needed. To detect the first hierarchical level of structures when the second level is about to imprinted, electromechanical sensing is implemented as detailed in [140].

In contrast to hot embossing, where the mold should become cold before demolding, the hot pulling process occurs when the mold is hot during demolding. Therefore, softened polymer chains are elongated due to adhesion and normal forces during demolding [138]. Benefitting from this phenomenon, high aspect ratio nanostructures are produced on a PC surface possessing superhydrophobic and superoleophilic properties at the same time (Figure 1.8(b1-d2)) [138, 140]. The density of the created nanohairs, which is defined by the crater width, affects the adhesion of water droplets to the surface. The transition from the Cassie-Baxter regime to a Wenzel regime, observed by water droplet evaporation measurements, occurs faster in the case of less dense nanohairs (typical crater width of 125 μm) than the denser nanohairs (typical crater width of 30 μm). This observations confirms that greater the amount of underlying air film between the nanohairs, the easier it is for evaporation to occur and thus an earlier regime transition [138].

A threefold hierarchy of micro-nanostructures can be fabricated on a PC surface. This process involves a hot embossing step to create micropillars, a second hot embossing step to create quadrangular pillars, and a hot pulling step to create nanohairs having an aspect ratio as high as 10 (Figure 1.8(e1-g2)) [140]. It remains, however, uncertain if this combination of techniques can lead to superhydrophobic surfaces.

Vullers et al. [141] enhanced the current density of a multicrystalline Si solar cell by optically coupling a thin micro-nanohair film having superhydrophobic and self-cleaning properties. It was also observed that the produced surfaces attaching to a monochromatic OLED (organic light-emitting diode) significantly increased the out-coupling efficiency. The high-aspect-ratio micro-nanohairs were created on the surface during the hot pulling of the PC film from the sandblasted steel template (Figure 1.8(h1)). The height of the micro-nanohairs

was up to 150 µm with tips diameters of <200 nm (Figure 1.8(h2)). COC was used as a sacrificial polymer layer to maintain the backside of the PC film flat. This was advantageous in terms of reflection losses. This method is potentially applicable for upscaling into a standard roll-to-roll polymer process, discussed below.

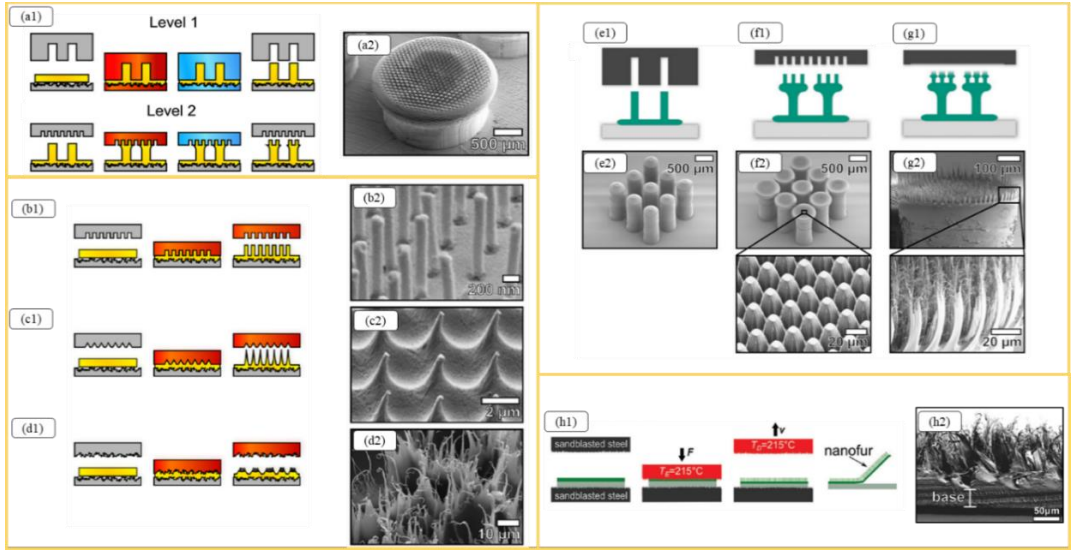

Figure 1.8. Schematic of (a1) the creation of the first level of hierarchy via a conventional hot embossing process at level 1 and adding an additional hierarchical level at level 2. For level 2, only the insert is heated, and the substrate plate remains at an ambient temperature. (a2) SEM image of the hierarchical structure produced by the combination of level 1 and level 2 [140]. Different insert geometries are used for the hot pulling technique to create high-aspect-ratio structures on a PC surface: (b1) 1 µm-depth insert led to structures 1.4 µm in height and 140 nm in width, (c1) 3.2-µm high and 270-nm wide structures, and (d1) nanohairs of less than 200 nm diameter and up to several micrometer long. The associated SEM images are presented in (b2), (c2), and (d2), respectively [140]. The fabrication steps of a threefold hierarchy of micro- and nanostructures via combining (e1) classical hot embossing, (f1) hierarchical hot embossing, and (g1) hot pulling. The associated SEM images are presented in (e2), (f2), and (g2), respectively [140]. (h1) Schematic of the fabrication process of the thin nanofur films and (h2) a cross-sectional SEM image of the produced nanofur film having an average hair length of 110 µm and a base thickness of 35 µm [141].

In summary:

- Processing parameters have a critical effect on the fabrication of superhydrophobic polymeric surfaces via hot embossing;
- Benefitting from the capacity of thermoplastics to undergo repetitive softening/cooling, threefold hierarchical micro-micro-nanostructures have been fabricated by a combination of hot embossing and hot pulling;
- The nanostructures can be produced either by the stretching effect of thermoplastics during hot demolding or by the introduction of a nanostructured template.

1.2.5.2 Elastomers

The breath figure (BF) method, which is a self-assembly alternative templating method [142], can be used to fabricate a micropatterned porous PS film as the template (Figure 1.9(a1)). The polydimethylsiloxane (PDMS) elastomer is poured onto the template to replicate microstructures by dissolving the polystyrene (PS) template in chloroform after curing the elastomer (Figure 1.9(a2)) [143]. The produced microstructured surfaces obtained a WCA of 130.0°–133.5°. Superhydrophobicity, however, was achieved by introducing nanostructures via hot embossing. The close-packed monodispersed monolayer of silica particles on a glass substrate served as the nanopatterned template and had sizes of 200, 400, and 600 nm (Figure 1.9(a3)). The composite-structured PDMS films with the microsized protrusions covered by nanoscale silica particles achieved a WCA as high as 150.0° (Figure 1.9(a4)). The size of intervals of the microprotrusions and the size of nanoparticles affected the surface roughness and surface wettability [143]. The best result was obtained for a diameter of 2.44 μm, a pitch of 3.53 μm, and a silica particle size of 400 nm.

To improve the surface quality when demolding PDMS from microtextured template, Mulroney et al. proposed the use of an intermediary [144]. First, the microtexture was transferred from the Al template to the PC surface and then from the PC to the PDMS (Figure 1.9(b1, b2, and b4)). The PDMS was demolded more easily and at a higher quality from the PC than from the Al. The as-produced PDMS surface is, however, a positive replica of the Al template, not a negative replica; this produced a marked effect on the performance of the fabricated PDMS surface. Therefore, this represents a direct replication of the Al templates (Figure 1.9(b3)). Due to the large spacing between the microstructures (~53.78% of the surface was not microtextured), sticking was insignificant. The PDMS surfaces could be successfully replicated using both the Al and PC templates [144].

In the Mulroney et al. study, the SA for the PDMS surfaces replicated directly on Al templates was <2° for textures spaced between 60 μm to 160 μm. However, the PDMS surfaces replicated from PC barely produced a SA <6°, while in half of the samples the SA was >10° reflecting the pinning of the water droplet. The height of the microstructures replicated directly from Al (with an average microstructure height of 12.24 μm) was 10.20 μm, while those replicated on the PC had an average height of 6 μm. This difference between the PDMS surface structure heights explained the differing obtained wettability [144].

Hot embossing suffers from some drawbacks, including multiple cycles to produce high-volume products, several processing steps, and limitation of the fabricable area. As such, there have been attempts to industrialize the techniques used for the manufacturing of micro-nanostructured surfaces [145]. Park et al. [145] used a relatively inexpensive roll-to-roll process to fabricate a mechanically robust superhydrophobic PDMS film consisting of 10 wt.% multiwalled carbon nanotubes (MWCNTs) (Figure 1.9(c1)). This method requires no patterned template or stamp. The created morphology and the subsequent WCA of the produced surfaces was only affected by the effective shear rate ($\eta = \Delta V/h$), where ΔV is the difference between rolls' rotating velocities ($V_1 - V_2$), and h is the thickness of the film (Figure 1.9(c2)). When $\eta > 0\ s^{-1}$, no considerable patterning was observed. For $\eta < 0\ s^{-1}$, irregular surface morphologies were created. The highest WCA (161.3°) was achieved at $\eta = -82\ s^{-1}$ (meaning $V_2 > V_1$). In terms of durability, the created shark skin–like patterns on the surface (Figure 1.9(c3)) remained intact and resistant after being abraded for 2000 cycles under an applied load of 1.5 N [145].

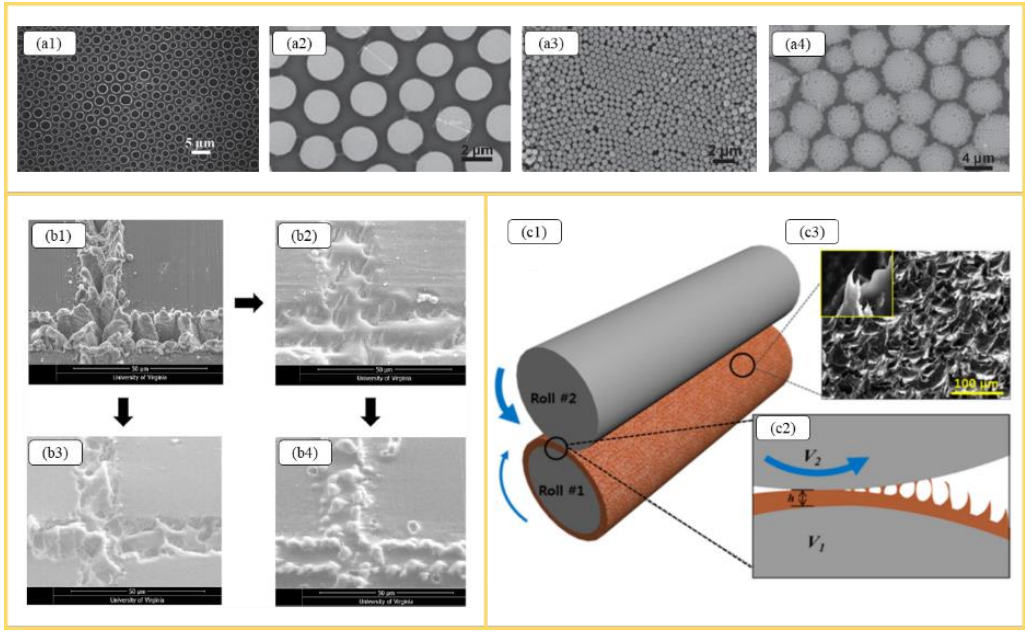

Figure 1.9. SEM images of (a1) the PS breath figure (BF) film with a pore size of 2.0 μm used to fabricate a micropatterned PS template film; (a2) micropatterned PDMS films replicated on the PS honeycombed template with a pore size of 2.5 μm; (a3) closely packed layers of monodispersed silica particles having a size of 400 nm; and (a4) composite-structured PDMS films with the microsized protrusions covered by nanoscaled silica particles with a size of 400 nm [143]; (b1) microtextured Al as an insert; (b2) PC replicated on the Al insert; (b3) PDMS replicated on the Al insert; and (b4) PDMS replicated on the PC surface [144]; (c1) schematic diagram of a double-roll film-making machine, (c2) pattern forms on the film surface when their rotation speeds are inverted; and (c3) SEM images of the shark skin–like pattern created on the surface [145].

In summary:

- The height of the microstructures plays an important role in creating superhydrophobic surfaces having a low SA;
- A high-quality demolding replicating the template's pattern is recommended.

1.2.6 Superhydrophobic surfaces produced by polymer casting or pouring

In a polymer casting technique, the polymer material having a suitable flowability is poured onto the template surface. The material can fill the micro-nanostructures without any pressure needing to be applied due to the low viscosity of the polymer. Nonetheless, the filling is occasionally quite difficult—especially for nanostructures—due to the presence of trapped air. Therefore, filling can also be accomplished under vacuum; for example, a vacuum pressure of ~1×10^{-4} torr was successfully used to cast PDMS [96]. Given the specific properties that a polymer should possess for use in the polymer casting method, i.e. low viscosity and favorable flowability, PDMS is the main material used in this subcategory.

The surface structures of taro (*Colocasia esculenta*) and lotus (*Nelumbo spp.*) leaves have been biomimetically replicated on the PDMS surfaces [146-148]. Negative molds have been produced via casting PDMS on the leaves; these casts are then used to produce the positive PDMS molds [146, 147]. Although both taro and lotus leaves have a WCA >150°, only the replicated PDMS surface on the lotus leaf showed a WCA >150°. This observation may be due to the degradation of taro leaves during the replication of the negative replica [147]. This approach, i.e. using natural leaves as an insert, has little practical interest for industrial manufacturing.

Noh et al. [32] fabricated a superhydrophobic PDMS surface (having a WCA of 157°) by casting the polymer on micro-nano-patterns shaped like those of lotus leaves, the patterns being fabricated by a laser ablation process. The microstructures were produced by a picosecond laser ablation process, while the nanostructures were produced by LIPSS or ripple formation (See Section 1.1.2). Noh et al. demonstrated that when the depth of the ablation is small, there is a detrimental effect on the WCA. The depth of ablation can be controlled by the laser scan numbers. Therefore, superhydrophobic surfaces were produced with quadrangular pyramid shapes where only 8.1% of the triangular area (each side of the pyramid) was wetted by the water droplets, and 91.9% remained non-wetted. This confirmed that the Cassie-Baxter regime was dominant.

1.2.7 Superhydrophobic surfaces produced by other processing systems

Some superhydrophobic polymer surfaces have also been produced using less common processing techniques, such as rotomolding [149], micro-injection compression molding (μICM) [62], and ultrasonic imprinting [95]. These studies are quickly summarized in this section. Different topographies of hierarchical micro-microstructures have been introduced to PP surfaces by μICM for use in open microfluidic devices (Figure 1.10(a1-a4)) [62, 150]. The two-level structures, i.e. micro-pyramids and sub-micro blades on the top of micropillars, had a higher WCA due to the reduced liquid–solid contact area fraction. However, compared to single-level structures, i.e. micro-pyramids and sub-micro blades, two-level structures had an undesirable roll-off angle due to the pinning effect stemming from the less rough surface on top of the micropillars as well as the low roughness of the sidewalls of the micropillars (Figure 1.10(b1-b4)) [62]. Although both compression force and mold temperature markedly affect replication quality, mold temperature was the major contributing factor of pillar height and the fidelity of replicated pillar top shape [150].

Ultrasonic imprinting has been used to fabricate poly(methyl methacrylate) (PMMA) surfaces having four types of microchannels that differed only in terms of channel distance (Figure 1.10(c)) [95]. Ultrasonic vibration energy softened the surface of thermoplastic material for replication of the microchannels. The microchannels were engraved on the tip of ultrasonic horn using a polycrystalline diamond fabricated by μEDM. For the four different imprinting loads, the greater the load, the higher the replication ratio achieved for each geometry. The best results in terms of superhydrophobicity occurred with a channel distance of 418.7 μm, where the water droplet was in contact with only two channels. Nonetheless, there was no discussion regarding the consistency of the water droplet standing over the microchannels in a such case [95].

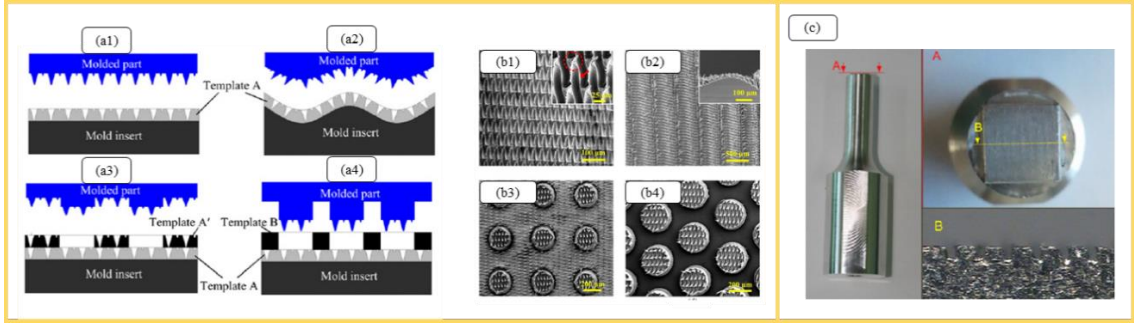

Figure 1.10. (a1, a2, a3, and a4) Schematic of different hierarchical structures and (b1, b2, b3, and b4) corresponding SEM images of the replicated PP surfaces [62]. (c) Photograph of the ultrasonic horn and the profile with microchannels as a template [95].

In summary:

- Various geometries have been produced via micro-injection compression molding (μICM);
- Mold temperature has the most significant effect on replication fidelity;
- Ultrasonic imprinting was introduced as a means to fabricate channel-like microstructures; however, the feasibility of this technique must be assessed for fabrication at the scale of tens of μm or nm.

1.3 Self-cleaning properties of superhydrophobic surfaces

This property has been demonstrated for plant surfaces by Barthlott and Neinhuis [151]. Over 200 plant species benefit from using rolling droplets to self-clean their surfaces [152]. The most well-known of these, the lotus plant, has an intrinsic hierarchical structure on the surface of its leaves that produces a very low water CAH leading to their self-cleaning ability [153, 154]. Thus, self-cleaning properties, known as the "lotus effect", have influenced considerably industrial applications including self-cleaning window glasses, paints, textiles, solar panels, etc. [154]. Water droplets, with an almost spherical shape on superhydrophobic surfaces, carry away hydrophilic contaminants adhered to the surface when the droplets roll off the surface. This results from the stronger adhesion of the contaminant particle to the water droplet than the adhesion of the particle to the superhydrophobic surface [153]. The tilted angle of a surface on which a water droplet begins to move is defined as the sliding angle (SA), tilt angle (TA) or roll-off angle; this is in direct relation with the CAH [155]. Figure 1.11 shows the self-cleaning ability of a lotus leaf contaminated with clay owing its micro-nanostructured surface [22].

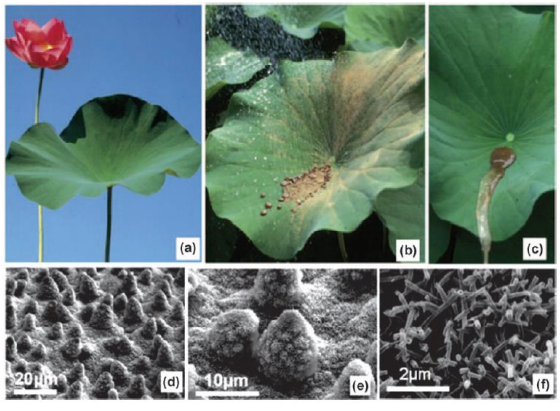

Figure 1.11. (a) An image of a lotus leaf and its flower, (b) a lotus leaf contaminated with clay, (c) movement of the adhered contaminant particles due to the self-cleaning ability of the lotus leaf. The SEM images of the lotus leaf in different magnifications representing the (d) randomly distributed cell papillae, (e) a single cell papilla, and (f) the epicuticular wax tubules on the cells [22].

A series of parameters, including surface roughness, the degree of particle adhesion and water repellency, are dominant in the self-cleaning ability of these surfaces [155]. Bhushan and co-workers [155] introduced a systematic study of the self-cleaning property of different nanostructured, microstructured, and hierarchically structured superhydrophobic surfaces. They observed that a droplet having nearly zero kinetic energy was unable to clean nanostructured and microstructured surfaces. However, the hierarchical surface was almost entirely cleaned. Many explanations have been suggested for functionality of the hierarchical structures [156-158]. They showed that only a hierarchical surface roughness can repel both macroscopic and microscopic droplets. Bagheri and co-workers [159] measured the minimum surface tilt angle needed for the appearance of the self-cleaning property of the different surfaces.

The self-cleaning glasses are also highly demanded [160, 161]. An important requirement for self-cleaning glasses is transparency. So, the produced superhydrophobic/self-cleaning surface must be transparent. To create a transparent superhydrophobic surface, the surface roughness should be smaller than 400-700 nm which is the wavelength of visible light [156]. Carbon nanotubes (CNTs) has attracted numerous attentions in the fabrication of self-cleaning coatings due to their ability to be aligned [162, 163]. The production of stimuli-responsive self-cleaning surfaces is a new approach in this field. In such surfaces, the wettability can switch by a stimulus including temperature, electric field, pH, and light [162, 164]. The self-cleaning characteristics of superhydrophobic coatings used for high-voltage outdoor insulators are of great importance [165]. The wet pollution layer followed by dry-band formation on the insulator surface has a significant effect on the insulator pollution flashover [36, 49, 166]. The IEC 60507 standard has been widely used to study the flashover performance in the artificial pollution testing of high-voltage outdoor insulators [167]. There are three polluting methods used in the solid layer method of artificial pollution testing: spraying, dipping, and brushing [168]. Kaolin [169, 170], active carbon [165, 171], and NaCl solutions [168] are some of the most common artificial pollutions applied to evaluate the self-cleaning property of the insulators.

A detailed assessment of outdoor settings reveals that there are different pollution scenarios: dry dust may be deposited onto surfaces in desert areas by the wind, or air-suspended pollution can be fall onto exposed surfaces by raindrops. The liquid component of this latter suspension may then be evaporated by solar radiation or elevated temperatures, leaving the polluted surface exposed to the next rainfall cycle. Moreover, whenever

rainfall is involved, the diameter of rain droplets varies from 400 μm to ~2 mm as a function of rain rate ($mm \cdot h^{-1}$), and this variability must also be considered [172].

1.4 Icephobic properties of superhydrophobic surfaces

Icing phenomena on outdoor equipment such as transmission cables, aircraft, wind turbines, and telecommunication towers can lead to their mechanical failure and their becoming safety hazards. Surfaces facing ice buildup can encounter severe damage or interrupted operation as witnessed by the ice-related electrical blackout in 2008 in the northeastern US that left over 1 million people without power at an estimated cost above US$1 billion. The December 2013 North America storm complex resulted in 27 deaths, loss of power to over a million residents and over $200 million in damages. According to Catastrophe Indices and Quantification Inc., the severe weather across Canada cost $1.9 billion in 2018. Hydro-Quebec reported that ice storms only in April 2019 during which 316,000 residential lost power cost $14 million due to various damages. As such, there is a heightened interest in the application of icephobic materials to protect exposed outdoor structures and ensure their safe operation. Therefore, attempts have been made to create anti-icing/icephobic surfaces [45, 173-179].

Two main strategies exist to preserve the surfaces from ice. The first is composed of active methods where thermal or mechanical energy is used to de-ice the surface. The second represents passive methods where no external energy is applied [180]. The first approach as the conventional de-icing approach including electro-impulse, thermal treatment, and mechanical removal could not successfully remedy the problem due to inefficiency, being costly, or being environmentally unfriendly [181]. The second approach, known as anti-icing surfaces, attempt to reduce the accretion of ice or to decrease the adhesion of accreted ice. To this end, the icephobicity is defined as the capability of the surface to delay heterogenous ice nucleation, delay freezing time, reduce ice adhesion strength, and rebound supercooled water droplets [182]. Different icephobic strategies are shown in Figure 1.12.

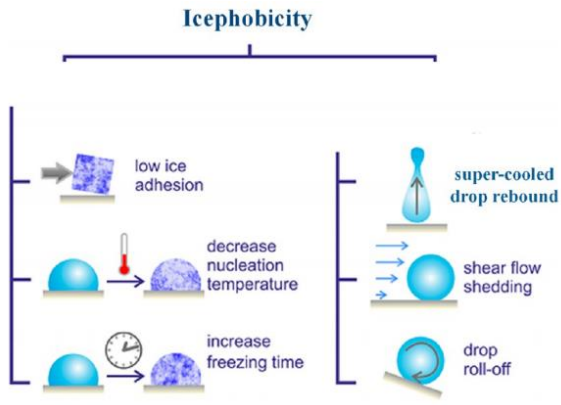

Figure 1.12. Different icephobic strategies [182].

Superhydrophobic surfaces are among the best candidates for delaying ice formation and reducing the energy needed for de-icing. Superhydrophobic surfaces having various surface roughness—microstructures, nanostructures, hierarchical structures—demonstrate different icing behaviors during both ice formation and de-icing [183-191]. The ice formation on a superhydrophobic surface having micro-nanostructures is affected by (1) the reduced contact area between the surface and water droplets due to the high WCA [45], (2) the reduced heat transfer through the air trapped in between the surface asperities [185], (3) the effect of surface roughness on the heterogeneous nucleation rate of ice at water-solid interface [189], and (4) the shorter rebounding or shedding time of water droplets compared to the nucleation time [192]. However, the reduced ice adhesion strength is due to the formation of microcracks caused by surface roughness acting as interfacial stress concentrations [193] and the reduced contact area between the formed ice and the surface due to the small solid-liquid contact area [173]. However, the latter may cause negative impact on the icephobicity due to the mechanical interlocking of the ice into the surface asperities [193]. This mechanical interlocking can be governed by the consistency of Cassie-Baxter regime. Considering that there is a fully Cassie-Baxter state on one hand and a Wenzel state on the other hand, there is also an intermediate state where the water droplet partially penetrates into the surface structures [194]. Therefore, the degree of this penetration can directly affect the mechanical interlocking of ice prior to conducting the ice adhesion strength measurement resulting in so-called “Cassie ice” or “Wenzel ice” [181]. Consequently, the surface geometry has a decisive effect on the icephobic behavior of the produced surfaces. It has been shown that among different surface geometries including microstructures, nanostructures, and hierarchical micro-nanostructures, the latter demonstrates lower ice adhesion strength [191].

1.5 Durability of superhydrophobic surfaces

Although multiple applications benefit from superhydrophobic surfaces, the durability of these surfaces against mechanical forces and chemical media remains questionable, a field that has drawn many attentions recently [195-199]. Superhydrophobic surfaces prone to mechanical or chemical damage either lose their surface roughness or the low surface energy chemical bonds [197]. This fragility can lead to a transition from the Cassie-Baxter state to the Wenzel state which is energetically more favorable for the water droplet. The transition to the Wenzel state induces a strong pinning that increases the adhesion between the water droplet and the surface. The result is a loss of water-repellency or anti-wetting performance of the surface [200]. The lack of a defined standard procedure for evaluating the durability of different types of superhydrophobic surfaces has led to a myriad of home-made set-ups and procedures to measure surface durability. These investigations are categorized under these main groups: Abrasion resistance under a specific force, wear resistance by rubbing the surface, the tape-peel tests, water pressure stability, water jet impact, immersion in aqueous solutions with various pH values, ultrasonic treatment of surface in water, durability under UV-light exposure, scratch tests, plasma treatment, fatigue testing, and the durability of the superhydrophobic/icephobic surfaces after repetitive icing/de-icing cycles [28, 195-199, 201-203]. Due to the lack of a single and standardized method for determining the durability of the superhydrophobic surfaces through abrasion by sandpaper, there are different test parameters for characterizing abrasion effects. It was observed that several factors including surface roughness of the abrading surface, its chemical composition, its Young's modulus, the applied pressure on the surface during abrasion, the amount of contact between the two surfaces, type of applied motion, and the relative speed between the two surfaces in contact [200]. For example, Su et al [204] studied the abrasion resistance properties of a superhydrophobic coating made of a polyurethane elastomer on a porous aluminum template. They used an abrasive load of ~2.9 kPa and showed that the surface contact angle remained greater than 150° even after 10,000 abarasions. Li et al. [205] investigated the mechanical durabilty of resin based superhydrophobic coatings using a 2,000 mesh sandpaper with 200-g loading (corresponding to a stress of 3.3 kPa). Although the WCA remained >150° after 300 abraison cycles, the SA of the coating was >10° after 50 abraison cycles. In some cases, lower sandpaper grit (280–400#) led to superhydrophobicity due to the creation of new surface roughness, while the higher grit deteriorated the superhydrophobic properties of the surface [206].

As many superhydrophobic surfaces cannot withstand being touched by a finger, the finger-press test can be considered to evaluate the robustness of superhydrophobic coatings and surfaces [207, 208]. The mechanical stability of the superhydrophobic surfaces were quantified by pressing a tape with approximately 10 kPa and then peeling the tape from the surface. Deng et al. [209] observed that when only Van der Waals interaction retain the particles to a surface, they can be removed easily by tape-peeling. However, tape-peeling has no cinsiderable effect on particles if they were chemically binded to the surface by silica bridges. A switch in wettability state has also been observed after a tape-peeling test [210], i.e., the surface showed a sticky superhydrophobic property (WCA ~156° and no water droplet sliding). It was due to the decreased surface roughness after peeling the adhesive tape from the surface. The ultrasonication had a diverse influence on superhydrophobic durability. The result was highly dependent on the adhesive strength between the superhydrophobic coating and the substrate [211]. While in some cases ten min of ultrasonication can considerably decrease the WCA and increase the CAH [212], in other cases the superhydrophobic fabric remained intact even after almost 100 hours of ultrasonication [213]. The examination of the surface chemical stability under both acidic and alkaline conditions is one of the most prevalent tests which can be performed in a pH ranging from 1 to 14 [173, 202, 214, 215]. The durability of the surfaces also can be assessed with dynamic impact durability test. The surface undergoes a collision with a solid, e.g., siliocn dioxide or silicon carbide particles, liquid (in the form of sprayed micro-droplets, regular size drops, or jet), or gas (strong wind) phases [200].

Given the vulnerability of the superhydrophobic surfaces when exposed to mechanical forces, durable superhydrophobic hierarchical structures have been manufactured on PP using protective sacrificial micropillars (Figure 1.13(a1)) [199]. Various area fractions of the protective pillars (ca. 5%, 15%, and 25%) were examined to assess whether the Cassie-Baxter regime could be maintained and to determine the optimal surface density. To study the wettability of the surfaces, the sliding angle was measured instead of CAH due to the anisotropic arrangement of protective pillars in some surface patterns, such as for the 5% and 25% area fractions. At an area fraction of 25%, the protective micropillars led to a deterioration of superhydrophobicity due to the stiction of water droplets to the side walls of the protective pillars. The optimal density of the protective pillars was 15%. In this study, the heights of the protective micropillars were 15–30 μm above those of the hierarchical structures to improve mechanical durability (Figure 1.13(a2)). The mechanical durability of

the protected surfaces was double that of the unprotected surfaces. The unprotected surfaces lost their superhydrophobicity after applying a compressing pressure of 10 MPa, while the protected surfaces maintained their superhydrophobicity despite being compressed with a pressure up to 20 MPa [199]. The positive effect of protective pillars in wear tests was confirmed (120 kPa), as only the protective pillars wore out after the abrasive wear tests, i.e. the patterns remained unaffected.

The production of high aspect ratio structures is limited due to processing constraints. On the other hand, low aspect ratio structures normally lead to an easy transition from a Cassie-Baxter regime to a Wenzel regime. Andersen et al. [65] figured how introduce random multiple heights (7 different height levels) to overcome the latter problem (Figure 1.13(b1)). The surface coverage by microstructures was a determining factor of the CAH. The reduction in surface coverage led to a higher CAH, due to the increased number of pinning sites. This was confirmed by the stick-slip behavior of water droplets rolling on the surface. Nevertheless, the receding WCA depended on the surface coverage, as the advancing WCA showed the independent behavior of the structures. To reduce the roll-off angle, the authors proposed rounding off the corners of microstructures [65].

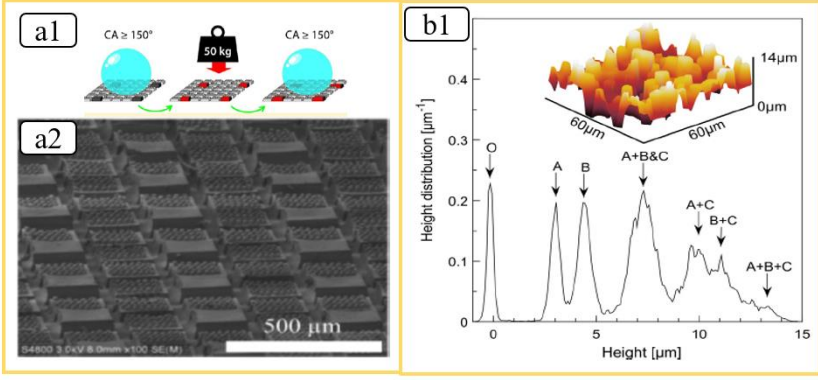

Figure 1.13. (a1) Schematic of protective micropillars to enhance the mechanical durability of the superhydrophobic surfaces, (a2) SEM image of the fabricated structures on the PP surface [199], and (b1) Height distribution of multi-scale features for a surface coverage of 33%. A, B, and C are attributed to different etching steps which are seen as peaks with different heights [65].

To overcome the durability issue associated with superhydrophobic surfaces, Lv et al. [124] fabricated a superhydrophobic micro-nanostructured surface from an epoxy-based shape memory polymer. Lv et al. applied an external pressure on the surface by a glass slide at a temperature above that of the glass transition temperature of the epoxy-based polymer, i.e. 120 °C. The pillars on the surface collapsed uniformly after

pressing. After further heating at 120 °C for 45 s, the surface micro-nanostructures were recovered and the superhydrophobicity was regenerated [124]. This cycle was repeated for 50 times, and the same behavior was observed after each cycle. Regarding the spacing between pillars, the micro-nanostructures showed more favorable results than the microstructures. A 20-μm spacing appeared to be the threshold below which the SA >10° for both microstructures and micro-nanostructures. However, the microstructured surface showed a SA >10° for spacing of 20 μm, while micro-nanostructured surfaces showed a SA <10° [124].

CHAPTER 2

ARTICLE 1: DIRECT REPLICATION OF MICRO-NANOSTRUCTURES IN THE FABRICATION OF SUPERHYDROPHOBIC SILICONE RUBBER SURFACES BY COMPRESSION MOLDING

K. Maghsoudi, G. Momen, R. Jafari, M. Farzaneh

Department of Applied Sciences, University of Quebec in Chicoutimi (UQAC)

555, boul. de l'Université, Chicoutimi, Québec, G7H 2B1, Canada

This article has been published in:

Applied Surface Science, Volume 458, 15 November 2018, Pages 619-628

https://doi.org/10.1016/j.apsusc.2018.07.099

2.1 Abstract

We describe a simple method for fabricating superhydrophobic high-temperature vulcanized (HTV) silicone rubber surfaces by direct replication using a compression molding system. The resulting rubber samples possessed micro-nanostructures on the surface. This micro- and nano-scale roughness produced a water contact angle of >160º and a contact angle hysteresis of <3º. The roughness patterns on chemically etched aluminum surfaces, which served as templates, were successfully replicated on the rubber surfaces. An antistiction coating applied to the template surface ensured that the rubber was completely removed during demolding and that the replicated micro-nanostructures on the silicone surface were preserved. Surface roughness of the aluminum templates was optimized at HCl concentrations of 15 wt. %, with a lower roughness value observed at acid concentrations above and below this value. The developed HTV silicone rubber surfaces also demonstrated a freezing delay and a self-cleaning capacity.

Keywords: Superhydrophobicity; Silicone rubber; Micro-nanostructures; Direct replication; Self-cleaning properties; Compression molding

2.2 Introduction

Due to its hydrophobic properties, silicone rubber has attracted much attention for application as high-voltage outdoor insulation [7]. Silicone rubber used in high-voltage outdoor insulation can be divided into three

main subcategories: high-temperature vulcanized (HTV) silicon rubber, room-temperature vulcanized (RTV) silicone rubber and liquid silicone rubber (LSR). HTV rubber cured at high-temperature and pressure and catalyzed with peroxide or a noble metal, such as platinum, possesses an inherent hydrophobicity as well as superior electrical and mechanical properties [216, 217]. Given that the accumulation of ice and pollution is responsible for numerous electrical and mechanical issues involving insulators exposed to these harsh environmental conditions, outdoor insulators should ideally have superhydrophobic and self-cleaning properties [216, 218].

Silicone rubber, due to its hydrophobic nature, causes water droplets to form on its surface rather than allowing water to immediately flow over the surface or to form a continuous water film [219]. The water contact angle (WCA) of its smooth surface is <120º [220-222]. However, adding surface roughness can increase the WCA without altering surface chemistry. Superhydrophobic surfaces having a WCA >150º and a contact angle hysteresis (CAH) <10º can be created through a combination of low surface energy materials and a micro- and nanostructured surface topography [30, 223]. When water droplets roll off a superhydrophobic surface, they also carry away hydrophilic contaminants adhered to the surface [224]. Due to surface tension, the adhesion of a contaminant particle to a water droplet is stronger than the particles' adhesion to the solid surface. Thus, superhydrophobic surfaces can be considered as self-cleaning surfaces [218].

Surfaces with micro-nanostructures have been used for a range of applications including antireflection coatings, bioinspired non-reflective coatings, antipollution and self-cleaning surfaces, cell culturing and differentiation, microlenses, dry adhesion surfaces and superhydrophobic surfaces [28]. Many methods have been used to create such surfaces including self-assembly, layer-by-layer methods, plasma treatments, chemical vapor deposition, sol-gel methods, lithography, spray coating, dip coating, electrostatic spinning and electrochemical deposition [153, 223]. There are several problems and challenges associated with the use of these methods including complex engineering procedures, long fabrication times, expensive facilities, environmental concerns and less than optimal robustness when the methods are applied to real-world settings [223, 225]. Consequently, a simple approach, such as the use of templates to create replicates having surficial micro-nanostructures, is preferable for reducing fabrication time and costs, applying to a wide range of materials, being easy to use and being reproducible. Moreover, using templates as replica to create micro-

nanostructured surfaces favors mass production and is a method that is widely acceptable to industry. In addition, direct replication creates a superhydrophobic surface out of the bulk material, while the aforementioned techniques create an additional layer on the parent material.

Use of templates or direct replication has been widely used for making micro-nanostructures on the surface of polymeric materials [225, 226]. A variety of materials can be used to fabricate such templates or inserts: nickel, steel, BMG (bulk metallic glass) and aluminum [28]. Considering the ease of creating patterns through mechanical machining, chemical etching and electroforming on metals, they represent materials that offer a high potential as templates. Moreover, there are numerous ways to create an aluminum surface having micro and/or nanostructures including chemical etching [227, 228], anodization [229-232], boiling water [233, 234], plasma treatment [233, 235, 236], laser ablation [237-239] and lithography [240-242]. Various solutions have been used for chemically etching aluminum surfaces. Hydrochloric acid—at various concentrations—is one of the most common chemical etchants used for this purpose [243-245].

These structured templates can then be used in a wide range of polymer processing techniques, such as injection molding [28, 246-248], injection compression molding [249-251], compression molding [252-254] and hot embossing [255-259], to produce micro-nanostructured polymer surfaces via replication. Liu et al. [225] produced superhydrophobic polymeric surfaces using Al and Al_2O_3 replicas obtained via the anodization technique. Weng et al. [260] achieved a superhydrophobic electro-active epoxy coating by direct replication of fresh plant leaves, while Bhagat et al. [261] fabricated superhydrophobic polycarbonates (PC) using silicon wafer templates via a hot embossing process. Through femtosecond laser ablation and a hot embossing system, Toosi et al. [134] imprinted topographical stainless-steel micro-nanostructured patterns onto the surface of thermoplastic polymers that included high-density polyethylene (HDPE), polylactic acid (PLA) and medical PVC. Cao et al. [262] fabricated superhydrophobic high-density polyethylene (HDPE) surfaces via a nanoinjection molding technique using a template of porous anodic aluminum (PAA) having pore diameters of 200 nm. Injection-molded superhydrophobic polypropylene (PP) surfaces with microstructures and hierarchical anisotropic micro-nanostructures (dual structures) have also been studied [93, 263]. The fabrication of microstructured inserts, produced using a micro-working robot on aluminum foil, and micro-nanostructured inserts, obtained by anodizing aluminum foil, demonstrated that microstructures can, in some

cases, produce superhydrophobic surfaces, while dual surfaces (i.e. surfaces with micro-nanostructures) always lead to a superhydrophobic surface having a WCA of >150º.

Most studies involving the fabrication of superhydrophobic polymeric surfaces have used thermoplastics as the matrix. Some studies have also used poly(dimethylsiloxane) (PDMS) [92, 264] and LSR [33, 226] for producing structured superhydrophobic surfaces. However, few studies have employed HTV rubber materials to create textured superhydrophobic surfaces [218], and thus there is a need for further investigation using this material.

Here, we present an efficient and simple method for fabricating micro-nanostructured rubber surfaces using a compression molding system. Compression molding is one of the most common methods for producing high volume polymer parts and components. Unlike conventional means for making superhydrophobic HTV silicone surfaces that rely mainly on coating techniques [7, 265-267], we produce a micro-nanostructured template using simple chemical etching and subsequent direct replication of micro-nanostructures on the HTV silicone during its vulcanization process. Consequently, no additional coating is required to achieve a WCA of >160º. Replication quality depends greatly on having a well-structured and durable template that can be used repeatedly without considerable loss of roughness and having a technique to detach the mold without damage to the produced surface nor to the original template.

2.3 Materials and methods

All samples were made of HTV silicone rubber composites supplied by K-Line Insulators Limited (Canada) consist of two main parts, a matrix of long-chain silicone rubbers and fillers like alumina trihydrate ($Al_2O_3.3H_2O$) and silicon oxide (SiO_2). The direct replication method was used to fabricate samples marked by micro-nanostructures (Figure 2.1).

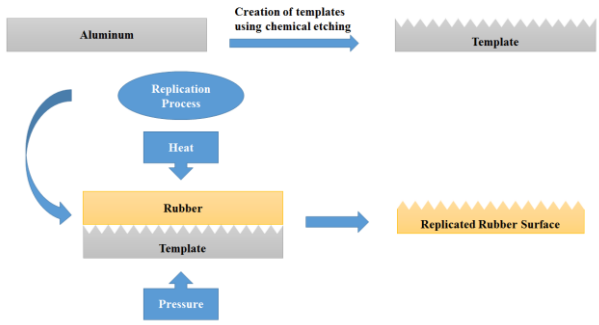

Figure 2.1. Schema of the replication of micro-nanostructures on the surface of HTV silicone rubber from chemically etched aluminum templates to illustrate the replication of patterns on the template through curing under pressure and heat.

2.3.1 Equipment

A press machine (Carver Inc., USA) was used in the compression molding process to fabricate micro-nanostructured rubber surfaces. Minimum and maximum clamp capacities of the machine are 3 kN and 194 kN. The machine has two temperature-controllable platens. Temperature range varies from ambient temperature to 350 °C. A three-piece flat mold having a cavity size of 25 × 25 × 6.5 mm cast the rubber materials.

2.3.2 Fabrication of templates

A chemical etching method created micro-nanostructures on a A6061 aluminum alloy composed of Al 97.9 wt. %, Mg 1.0 wt. %, Si 0.60 wt. %, Cu 0.28 wt. % and Cr 0.20 wt. %. The templates were cut into the desired size and ultrasonically cleaned in acetone and distilled water for 0.5 h. They were then dried in an oven at 70 ºC for 1 h. The surfaces were chemically etched using three different hydrochloric acid (CAS number: 7647-01-0, Laboratoire MAT, Canada) concentrations (10, 15 and 20 wt. %) for various etching times (1, 2, 3 and 4 h). All etched templates were then ultrasonically cleaned with acetone and distilled water for 0.5 h to remove any residual particles from the surfaces. The clean etched templates were dried in an oven at 70 °C for 1 h. The nomenclature of samples relates to the conditions under which the samples were produced. For example, sample C15H2 represents a silicone rubber sample produced using a template created using 15 wt. % HCl acid for 2 h.

Although the templates produced using the chemical etching method possessed micro-nanostructures, they did not show favorable demolding behavior. Throughout the demolding step, rubber material stuck onto the template surface, and the final product was ruined or lacked the roughness of the template. Use of a proper demolding agent could solve this problem, but this would still not guarantee a perfect demolding due to the

micro-nanostructures on the surface. Moreover, post-process cleaning is required as most release agents leave contaminants on the surface [268]. Therefore, working with micro- and nano- scale structures requires more targeted strategies. Furthermore, dislodging the rubber materials entangled in the template structures—due to the high molding pressure and the structures being cured in situ—represents a serious challenge and makes it impossible to reuse the template after the first molding cycle. Therefore, we applied an antistiction coating to make the insert surfaces intact against rubber materials.

Low surface energy coatings are commonly used as antistiction coatings via the self-assembled monolayer (SAM) method. Fluorocarbon- or hydrocarbon-based coating materials are the most common antistiction coatings [28]. We applied a 6 mM solution of diluted Trichloro(1H,1H,2H,2H-perfluorooctyl)silane in methanol (TPFS = $CF_3(CF_2)_5CH_2CH_2SiCl_3$, supplied by Sigma-Aldrich®) as an antistiction coating for the aluminum template surfaces. The solution was stirred for 15 min before dip coating. Immersion lasted 2 h at a temperature of 70 ºC. After drying at 70 ºC for 1 h, the dip-coated aluminum templates were ready to be used in the replication process. The difference between the replication qualities when using an antistiction coating is schematically illustrated in Figure 2.2. Templates having an antistiction coating were not damaged during the demolding phase and the replicated rubber surface had an adequate roughness. The main advantages of the antistiction coatings were a considerable improvement in replication quality and a reduced filling of micro-nanostructures on the template by polymer materials [116, 269].

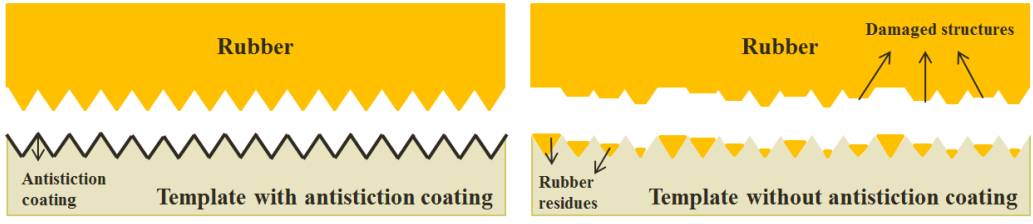

Figure 2.2. Comparison of replication quality for samples with and without an antistiction coating.

2.3.3 Replication process

The template was placed carefully into the cavity. The rubber compound was put into the cavity on the template; three pieces of the mold were fastened and placed on the lower platen of the press machine at 182 °C. According to the manufacturer guidelines, cross-linked bonds within the rubber material form at such temperature. Subsequently, the two platens were pressed closer together using a hydraulic pump until the desired pressure (4.3 MPa) was reached. The platens were kept closed to let the rubber be completely cured. When the cycle was over (20 min), the platens opened and the cured rubber was demolded.

2.3.4 Surface characterization

A Kruss™ DSA100 goniometer determined WCA and CAH at 25 ± 0.5 °C. A 4 µL water droplet deposited onto the sample surface permitted us to determine the WCA using the Young-Laplace approximation. The CAH equaled the difference of advancing and receding contact angles when the water droplet moved on the surface. To ensure accuracy and reproducibility, we conducted WCA measurements at different points on each sample; we reported the average WCA and standard deviation for each sample. In a cold chamber, where sample stage temperatures can reach -30 °C, we determined freezing delay using the same equipment as for contact angle measurements. Freezing delay time was defined as the time required for a water droplet on the sample surface to start freezing (freezing onset). Fourier transform infrared spectroscopy (FTIR) analyzed the chemical functions on the surface to evaluate surface chemical composition and its contribution to wetting behavior. These analyses ran using a Cary 630 FTIR Spectrometer (Agilent, USA) in ATR (attenuated total reflection) mode to acquire the highest quality spectra in the infrared range of 400 to 4000 cm^{-1}. A scanning electron microscope (JSM-6480 LV SEM manufactured by JEOL Japan) provided an observation of the micro-nanostructure morphology of the molded silicone rubber surfaces. Prior to analyzing, the HTV samples were coated with a thin layer of gold-palladium alloy to enhance the imaging. An optical profiler (Profil3D, Filmetrics, USA) quantified surface roughness which permitted an assessment of replication quality. We also studied the self-cleaning properties of the produced silicone surfaces using a high-quality digital camera (PowerShot SX50 HS, Canon) to record images. The samples were set on a substrate with an imposed tilt angle of 3°. Carbon black particles were selected as contaminants. We examined the self-cleaning capacity of produced samples by using a microsyringe to release droplets, having a diameter of about 3 mm, onto the contaminant-covered surface.

2.4 Results and discussion

2.4.1 Superhydrophobicity

All silicone rubber samples having micro-nanostructures, regardless of the conditions under which they were produced, showed WCA >160° (Figure 2.3).

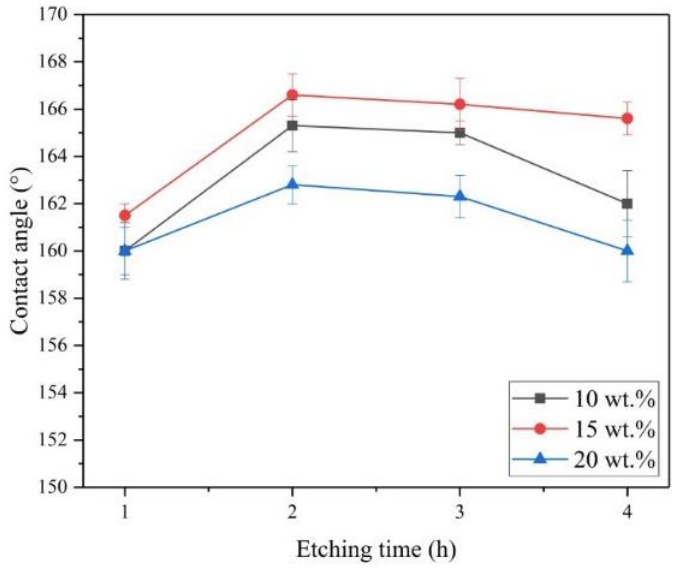

Figure 2.3. Contact angle of various replicated rubber surfaces produced from templates subjected to various acid concentrations (10, 15, 20 wt. %) as a function of etching time.

As expected, the silicone rubber surface without micro-nanostructures (hereinafter referred to as pristine silicone rubber) produced a WCA of 116.0 ± 2.0 °. The WCA of silicone rubber surfaces having micro-nanostructures were significantly greater in comparison to the pristine silicone rubber. Water droplets on the replicated rubber surface clearly demonstrated the superhydrophobic properties of the produced samples (Figure 2.4).

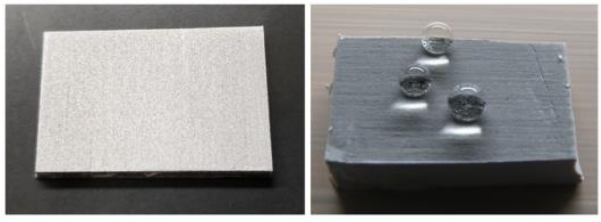

Figure 2.4. Aluminum template and the replicated superhydrophobic rubber surface.

2.4.2 Contact angle hysteresis

Relative to pristine HTV, CAH values for the replicated rubber samples obtained from the etched surfaces were very low (Table 2.1). Ultralow CAH values were obtained, however, for the C15 samples. We selected those samples having the lowest CAH and highest WCA values for further detailed study (indicated in bold in Table 2.1). Comparison of CAH of the pristine HTV silicone rubber and that of the C15H2 sample demonstrated that the replicated patterns created a sufficient surface roughness to achieve a Cassie-Baxter state

[90]. The presence of entrapped air in micro-nanostructures underneath the water droplet created a composite solid-liquid-air interface that explained this water droplet behavior [236].

Table 2.1. Water contact angle and contact angle hysteresis values for the pristine HTV silicone rubber surface and the replicated HTV surfaces. Samples in bold were selected for further detailed study.

Sample	**WCA (°)**	**CAH (°)**
Pristine HTV	116.0 ± 2	46.5 ± 2.4
C10H1	160 ± 1.2	1.8 ± 0.3
C10H2	**165.3 ± 1.1**	**1.5 ± 0.2**
C10H3	165 ± 0.5	1.6 ± 0.3
C10H4	162 ± 1.4	2 ± 0.4
C15H1	161.5 ± 0.5	0.4 ± 0.1
C15H2	**166.6 ± 0.9**	**0.6 ± 0.3**
C15H3	166.2 ± 1.1	0.3 ± 0.2
C15H4	165.6 ± 0.7	0.4 ± 0.2
C20H1	160 ± 1	1.4 ± 0.3
C20H2	**162.8 ± 0.8**	**1.3 ± 0.8**
C20H3	162.3 ± 0.9	1.0 ± 0.5
C20H4	160 ± 1.3	1.2 ± 0.4

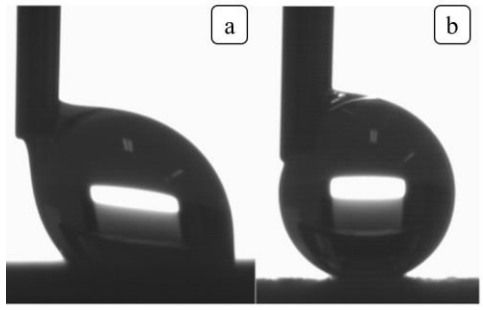

Figure 2.5. Water droplet showing contact angle hysteresis of (a) pristine silicone rubber and (b) sample C15H2 surfaces.

2.4.3 Surface characterization

SEM images testify to the creation of micro-nanostructures on the HTV silicone rubber after the replication process (Figure 2.6). These micro-nanostructures were responsible for the superhydrophobic behavior.

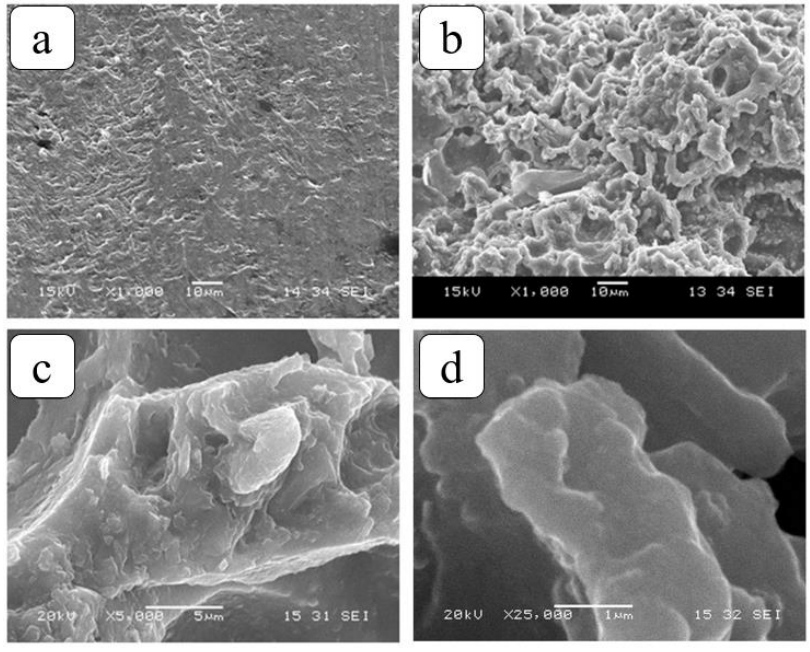

Figure 2.6. SEM images of (a) pristine silicone rubber and sample C15H2 at magnifications of (b) ×1000, (c) ×5000 and (d) ×25,000. The images were taken with a tilt angle of ~35° to improve the quality of the scan imagery.

In order to study the effects of acid concentration on the produced replicates, SEM images of three replicated silicone samples from templates produced at three different acid concentrations, each immersed for 2 h (C10H2, C15H2 and C20H2) were compared. Relative to the other samples, sample C15H2 had a more uniform roughness across the surface (Figure 2.7). These homogeneous micro-nanostructures on C15H2

improved non-wettability properties; the large-diameter depressions of sample C10H2 and the fewer nanostructures on the surface of sample C20H2 reduced their respective superhydrophobicity.

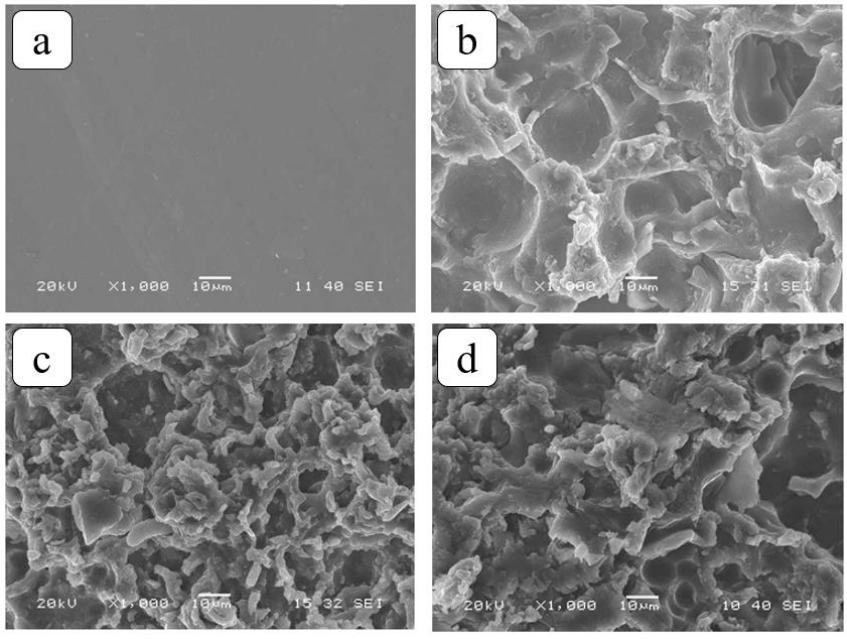

Figure 2.7. SEM images of (a) pristine HTV silicone rubber surface and samples (b) C10H2, (c) C15H2 and (d) C20H2. All images were taken vertically and represent the pitted morphology of the surfaces.

We selected sample C15H2 to study template replication quality. SEM images of the original template and the replicated silicone rubber surfaces confirm the successful replication of the patterns on the silicone surfaces (Figure 2.8). Compression molding efficiently forced materials into the roughened areas to successfully recreate the patterns on the silicone surface. These replicated patterns were almost identical to the aluminum template patterns. Obviously, protrusions on the template surface led to the creation of pitted morphology on the silicone surface, and thus depressions on the template produced protrusions on the silicone surface.

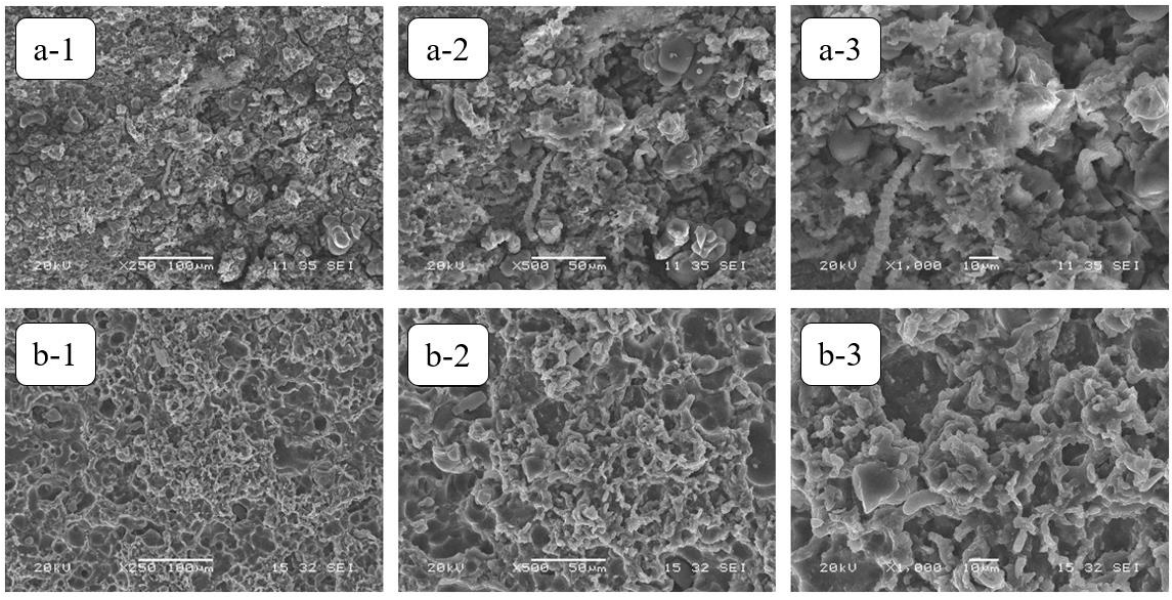

Figure 2.8. SEM images of (a) aluminum template and (b) C15H2 with various magnifications.

As the templates were covered with an antistiction coating, we needed to ensure that the coating was not removed from the aluminum template and transferred to the silicone surface. If so, the superhydrophobic property of replicated surfaces would be attributed to the presence of the fluoric bonds produced from the antistiction coating. To assess the presence of chemical bonds on the sample surfaces, we performed FTIR analyses (Figure 2.9). FTIR spectra results for pristine HTV silicone rubber (without micro-nanostructures) and sample C15H2 (with micro-nanostructures) all had absorption spectra of Si-O-Si, $Si(CH_3)_2$ and $Si(CH_3)$ at approximate positions 1000–1110 cm^{-1}, 805–855 cm^{-1}, and 1245–1275 cm^{-1}, respectively, attributed to silicone rubber chemical bonds and no fluorinated bonds being observed. Thus, the silicone surfaces were not altered chemically after the replication process. Consequently, the superhydrophobic behavior of silicone rubbers was only due to the creation of micro-nanostructures on the surface.

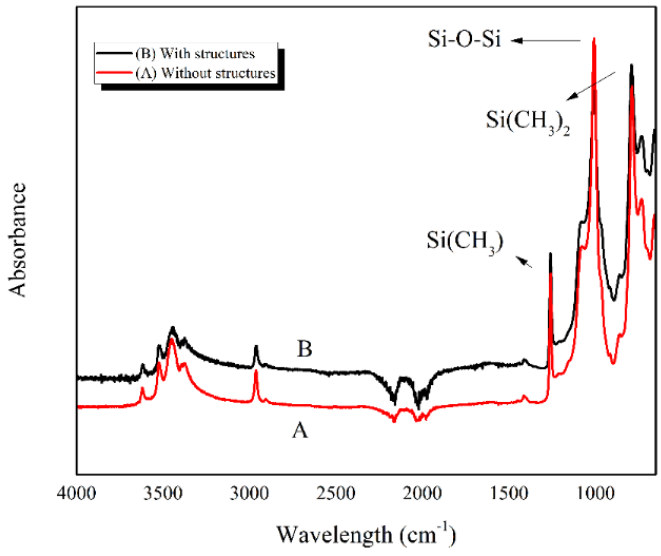

Figure 2.9. FTIR spectra for HTV silicone rubber with and without structures.

We applied a profilometry technique to evaluate sample roughness of a 300 × 400 μm surface. Roughness on the sample C15H2 was significantly greater than that of the pristine surface after replication process (Figure 2.10). The increased roughness was apparent for all three acid concentrations (Table 2.2).

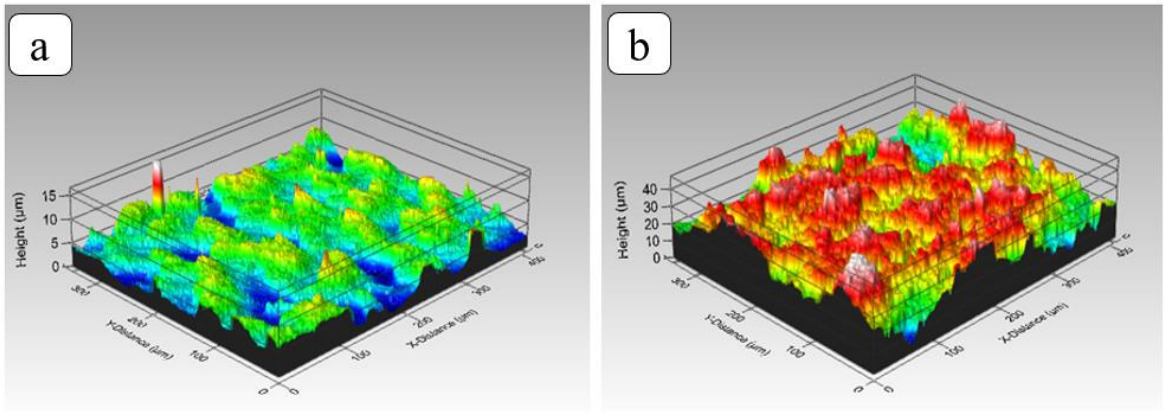

Figure 2.10. Surface profiles of (a) pristine silicone rubber and (b) sample C15H2.

Table 2.2. Roughness values obtained from profilometry analysis.

Roughness parameters	**Roughness values (µm)**			
	Pristine silicone rubber	C10H2	C15H2	C20H2
R_a (arithmetic average)	0.79	4.79	6.49	4.75
R_q (root mean squared)	0.91	5.80	7.90	5.81
R_v (maximum valley depth)	1.65	11.00	16.07	11.54
R_p (maximum peak height)	1.95	11.57	16.71	11.85
R_z (ten-point height)	3.227	22.58	32.78	23.39
R_t (maximum height of the profile)	3.60	28.61	40.03	31.25

The highest roughness values were obtained for the sample C15H2, a template produced using an acid concentration of 15 wt. % and a 2 h etching time. Relative to the pristine silicone surface, R_a and R_t roughness of sample C15H2 increased ~8 and ~11 times, respectively. This testifies to the creation of a micro-nanostructured surface and the presence of micro air pockets as well.

For samples C10H2 and C20H2, roughness values were very similar, mirroring these samples' wettability behavior. Thus, we observed optimal chemical etching conditions for the fabrication of the highest quality micro-nanostructures. Increasing the acid concentration from 10 wt. % to 15 wt. % created a rougher surface due to the higher etchant concentration and reaction rate. However, when the acid concentration was increased to 20 wt. %, a greater amount of etching actually produced a flatter surface as increased etching degraded the roughened areas and smoothed the structures.

2.4.4 Freezing delay measurements and wettability behavior at supercooled temperatures

As the behavior of produced surfaces at supercooled temperatures is important for developing icephobic and superhydrophobic surfaces that will be exposed to harsh environmental settings [26], we studied the delay in freezing onset, i.e. the initiation of water droplet freezing on the surface. For this purpose, we tested

samples C10H2, C15H2, C20H2 and a pristine sample at freezing temperatures of -15 °C, -20 °C and -25 °C. The freezing delay at -5 °C and -10 °C was too long and, thus, was not considered for this experiment. Surfaces having micro-nanostructures froze later than the rubber surface lacking these structures (Figure 2.11). Due to the micro-nanostructures, micro air pockets between the rubber surface and water droplets acted as thermal barriers to produce the freezing delay. Moreover, in the case of surfaces having a higher contact angle, the contact area between the water droplets and the rubber surface was less than that for pristine surfaces, meaning a decrease in thermal conductivity for the former. In other words, superhydrophobic surfaces dissipate less heat than pristine surfaces to produce a freezing delay [270].

The inset images in Figure 2.11 represent the droplets at the moment of complete freezing for pristine silicone rubber and sample C15H2 at -25 °C. The small protrusion on the top of the frozen droplets is formed when the droplets are in a solid state. The lag time between freezing onset and solid state is short. At the onset of freezing, the white spot at the center of the liquid state water droplet disappears and the droplet becomes cloudy due to the crystallization nucleation [271]. As crystallization propagates, the solid-water interface line migrates from the bottom to top until the protrusion is created at the top of the droplet. The entire process takes less than 50 s.

Sample C15H2 was marked by the maximum WCA and had the longest freezing delay. Compared to pristine silicone rubber, it took >3x longer for sample C15H2 to freeze at -25 °C and -20 °C. This difference relates to the more suitable surface roughness resulting in a smaller contact area between the rubber asperities and water droplets.

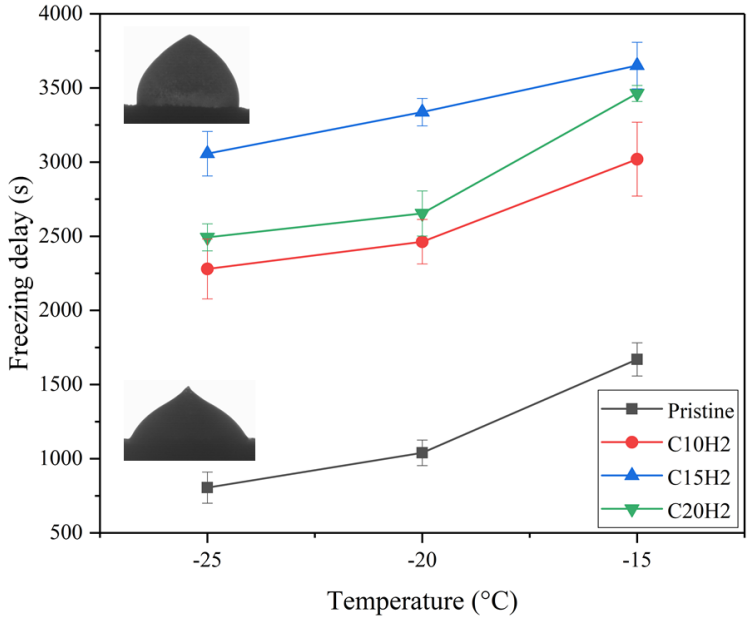

Figure 2.11. Freezing delay of the silicone surface samples at various temperatures. Inset images represent the droplets at the moment of complete freezing for the pristine silicone rubber and sample C15H2 at -25 °C.

We studied the variations of static WCA at temperatures of -25, -20, -15 and -10 °C for the different surfaces (Figure 2.12). WCA decreased with the surface temperature. This reduction is expected as it is attributed to water surface tension at low temperatures [235].

Based on the literature, the decreased WCA for superhydrophobic samples should be greater than for the hydrophobic samples [26]. However, as temperatures decreased from 25 °C to -25 °C, the WCA of the pristine sample decreased ~17% while decreasing by only ~18% for sample C15H2. Thus, although the micro-nanostructured samples showed superhydrophobic properties, these properties were altered at low temperatures as was the case for hydrophobic surfaces. However, the superhydrophobic surfaces still possessed a higher WCA than that of the pristine sample.

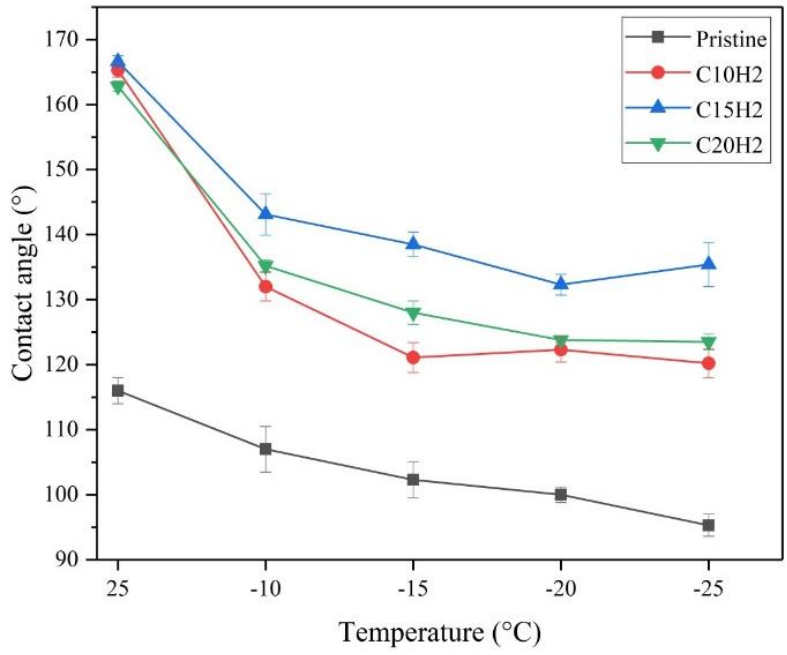

Figure 2.12. Changes in static water contact angle at various temperatures for the different experimental silicone surfaces.

2.4.5 Self-cleaning properties

Self-cleaning is the ability of a surface to repel water droplets and remove dust particles adhered to the surface. As dust and pollution particles are generally hydrophilic, they easily adhere to water droplets rolling on a superhydrophobic surface, and they are removed as the droplets roll off the surface [272]. This behavior is due to the greater adhesion between water droplets and pollution particles than between pollution particles and a micro-nanostructured superhydrophobic surface [273]. Moreover, the very small contact area between the water droplet and the surface has a crucial effect in such behavior. For a certain type of surface, however, CAH is more important than static WCA for self-cleaning [274]. Therefore, a surface having a CAH <10° is generally referred to as a self-cleaning surface [274].

The self-cleaning property of the produced silicone surfaces was clearly observed when we compared the pristine and the produced silicone samples. When an equal amount of contaminants was added to the pristine (Figure 2.13(a)) and C15H2 (Figure 2.13(b)) samples, the cleaning route of a single water droplet on the latter surface was clearly visible with the contamination removed by the water droplet (red circle in Figure 2.13(b)). A 1.5 × 2.5 cm area of the contaminated sample was self-cleaned using ~4 water droplets. Fabricated superhydrophobic silicone rubber surfaces having a CAH <3° were self-cleaning; the pristine silicone rubber

surface did not demonstrate this self-cleaning capacity as the water droplets simply accumulated on the contaminated surface (Figure 2.13(a)).

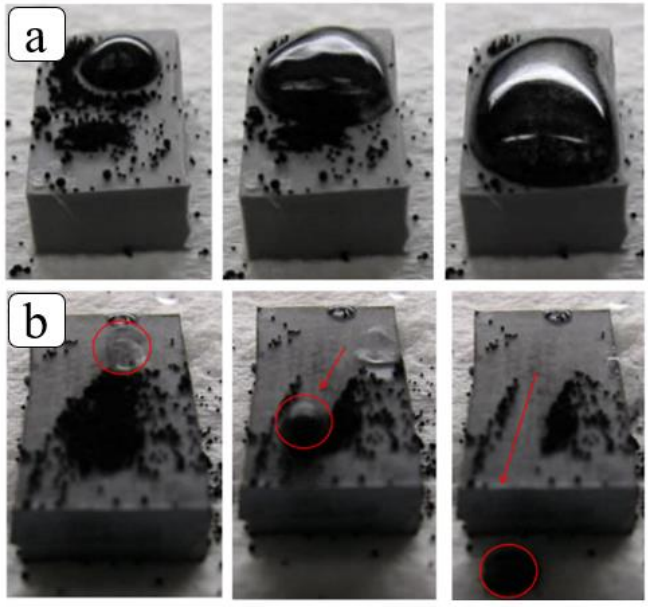

Figure 2.13. Self-cleaning properties of (a) pristine and (b) superhydrophobic silicone rubber surfaces. Equal amounts of contaminants were added to the surfaces. The pristine surface shows an accumulation of water without removal of the contaminants. The superhydrophobic silicone causes water droplets to flow across the surface and pick up contaminants along the flow route (arrows in b). The removed contaminants are observed in the red circle in the third image for the superhydrophobic surface (b).

To demonstrate the remarkable ability of the superhydrophobic silicone surface to repel water, we placed the superhydrophobic sample into a Petri dish. Using a syringe and needle, we then added three red water droplets onto the prepared surface. Water was added to the Petri dish bringing the water level equal to the height of the sample. While it was expected that by pouring more water into the Petri dish, the sample would be completely immersed in water and the red droplets dissolved into the water mass, the superhydrophobic surface acted as a barrier against water thereby keeping itself dry (Figure 2.14). Consequently, the red water droplets remained intact. To assess the longevity of this barrier, we kept the sample in the water container for more than one week. The sample remained dry during this period.

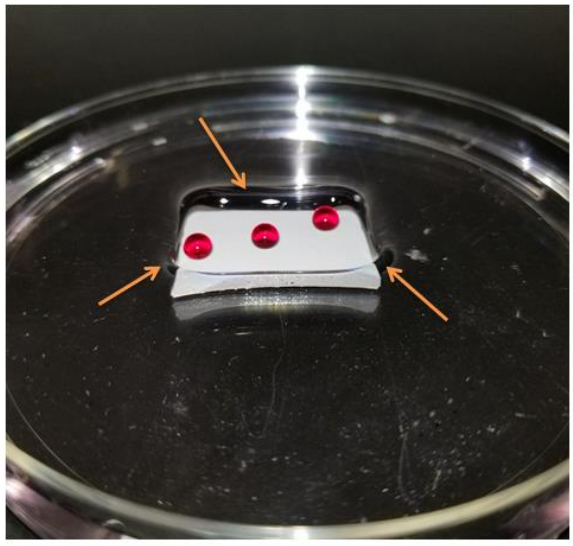

Figure 2.14. A superhydrophobic silicone surface remaining dry while immersed in water. The red water droplets illustrate the separation of the surface from the surrounding water.

2.5 Conclusions

We developed a direct replication method for the manufacturing of micro-nanostructured superhydrophobic silicone surfaces. All samples produced under the various etching conditions displayed water contact angles >160º and contact angle hysteresis <3º. Samples replicated from inserts produced with an acid concentration of 15 wt. % demonstrated a slightly higher water repellency than samples produced from lower and higher acid concentration inserts. This higher water repellency was due to the relatively higher surface roughness of the 15 wt. % acid samples. SEM images confirmed the successful replication of the templates' patterns on the rubber samples produced via compression molding. The micro air pockets entrapped between the water droplets and the silicone surface (due to the surface roughness) were responsible for the observed superhydrophobic behavior. As demolding without damaging the replicate is a crucial factor in the processing of micro-nanostructured surfaces, we applied an antistiction coating, which contained fluorinated bonds, to the template surfaces prior to molding. FTIR analysis revealed that fluorinated bonds of the template surfaces did not transfer to the silicone rubber surfaces during the replication process. Remarkably, superhydrophobic samples delayed freezing onset confirming the icephobic capacity of the produced surfaces. The fabricated surfaces were also self-cleaning and easily removed introduced contaminants on the surface.

Acknowledgments

The authors acknowledge the financial support from the Natural Sciences and Engineering Research Council of Canada (NSERC) and K-Line Insulators Limited, Toronto, Canada. We also thank Filmetrics Inc. for carrying out the profilometry analysis, the Laboratory of Icephobic Coatings and Surface Engineering (LaRGIS) at the Université du Québec à Chicoutimi (UQAC) for providing the necessary equipment and materials for the experiments, and we thank Mr. Pierre Camirand for his technical assistance and valuable help.

CHAPTER 3

ARTICLE 2: RIGOROUS TESTING TO ASSESS THE SELF-CLEANING PROPERTIES OF AN ULTRA-WATER-REPELLENT SILICONE RUBBER SURFACE

K. Maghsoudi, G. Momen, R. Jafari, M. Farzaneh

Department of Applied Sciences, University of Quebec in Chicoutimi (UQAC)

555, boul. de l'Université, Chicoutimi, Québec, G7H 2B1, Canada

This article has been published in:

Surface and Coatings Technology, Volume 374, 25 September 2019, Pages 557-568

https://doi.org/10.1016/j.surfcoat.2019.05.073

3.1 Abstract

Ultra-water-repellent silicone-based surfaces were produced to study their self-cleaning properties. First, we investigated the consistency of the micro-nano air pockets that are present between the surface asperities responsible for the formation of the Cassie-Baxter regime. We then performed a comprehensive series of self-cleaning experiments involving both suspended and non-suspended contaminants using various materials (e.g., kaolin, carbon black, silica, etc.) and contaminant-applying methods (e.g., dropwise, spraying, wet or dry contaminants). In this paper, the self-cleaning tests were arranged from the less severe, i.e., non-suspended contamination tests, to more severe, i.e., wet suspended contamination test, and ending with the most severe, i.e., dry suspended contamination test. Due to the ultra-low contact angle hysteresis, the produced surfaces showed favorable self-cleaning properties against the various types of contaminants and the different means of contaminant application. The produced surfaces retained their water repellency properties following application of the contaminants and after the cleaning of the surfaces, thus verifying the self-cleaning performance and resistance of the fabricated superhydrophobic silicone surfaces.

Keywords: Silicone rubber, Wenzel and Cassie-Baxter regimes, Ultra-water-repellent surface, Self-cleaning, Suspended contamination, Outdoor condition

3.2 Introduction

Superhydrophobic surfaces are used in a wide range of applications in both research and industrial settings, including applications requiring anti-corrosion, icephobic, anti-fogging, anti-biofouling, oil-water separation, low-adhesion, low-drag, non-wetting, buoyancy enhancement, and self-cleaning properties [21, 30, 275-281]. Superhydrophobic surfaces, specified by a water contact angle (WCA) >150º, a sliding angle (SA) or roll-off angle <10º, and contact angle hysteresis (CAH) <10º, are produced via a combination of low surface-energy material and a hierarchical micro-nanostructured surface [20, 282].

There are two main regimes for describing the wetting behavior of rough surfaces. The first is the Wenzel state [89], where a water droplet penetrates the surface features, thereby wetting the entire surface. The second is the Cassie-Baxter state [90] where the water droplet rests on top of the surficial micro-nanofeatures in contact with only the peaks of the features, and air pockets are trapped underneath the water droplet. In the Cassie-Baxter state, also known as heterogeneous wetting regime, where the surface is composed of two fractions, the contact angle is given by the following equation:

$$\cos\theta_{CB} = f\cos\theta + f - 1 \qquad \textit{Eq. 3.1}$$

where θ_{CB} is the Cassie-Baxter contact angle, f is the fractional area defined as the ratio of the solid area wetted by water to the total solid area, and θ is contact angle defined by Young's equation. In the Cassie-Baxter state, the water droplets can roll easily due to low resistance from the entrapped air pockets, whereas in the Wenzel state, the water droplets stick to the surface structures [283]. Dynamic effects of a droplet, such as impacting, bouncing, or vibrating, can lead to the transition from a solid-air-liquid interface to a solid-liquid interface [284]. Therefore, the presence of the trapped air pockets and the robustness of these air pockets to dynamic water droplet effects play an important role in the formation and maintenance of the Cassie-Baxter state allowing a droplet to roll across a surface.

In addition to WCA and CAH measurements, there are several means by which the wettability properties and the dominant regime of a superhydrophobic surface can be investigated. The first approach to evaluate the robustness of the entrapped air pockets responsible for the formation of the Cassie-Baxter regime is to study the droplet impact process on an ultra-water-repellant surface. There are three scenarios whereby a Newtonian liquid droplet impacts a superhydrophobic surface: complete rebounding, partial rebounding, or

shattering. The possibility for each scenario to occur depends on surface roughness, the surface tension of the liquid, and the initial kinetic energy of the droplet, all of which affect the dynamic pressure [285]. Li and co-workers [286] investigated the influence of WCA and the roll-off angle on the dynamic characteristics of superhydrophobic surfaces having different micro-pillar arrays. They showed that CAH and the advancing contact angle are fundamental wetting parameters affecting drop spreading and recoiling phases. The spreading coefficient of a droplet is influenced by both the WCA and the roll-off angle (roll-off angle is defined as the inclined angle at which the droplet begins to roll off the surface), whereas the rebounding coefficient of a droplet is highly defined by the roll-off angle [286]. Although in the droplet impacting process the water-repelling property of the surface cannot be measured by a specific parameter, such as WCA and CAH, it can be a reliable representative of the wetting property of a surface [287].

Moreover, the study of superhydrophobic surface behavior against water-jet impact [273, 288-290] and severe droplet contact [291], as well as the presence of the plastron layer on an ultra-water-repellant surface [292-294] are some of the existing complementary experiments for evaluating Cassie-Baxter regimes on surfaces.

The self-cleaning properties of superhydrophobic surfaces have been investigated frequently [22, 155, 210, 231, 273, 295-298]. This property has been demonstrated for plant surfaces by Barthlott and Neinhuis [151]. Over 200 plant species benefit from using rolling droplets to self-clean their surfaces [152]. The most well-known of these, the lotus plant, has an intrinsic hierarchical structure on the surface of its leaves that produces a very low water CAH leading to their self-cleaning ability [153, 154]. Thus, self-cleaning properties, known as the “lotus effect”, have influenced considerably industrial applications including self-cleaning window glasses, paints, textiles, solar panels, etc [154]. Water droplets, with an almost spherical shape on superhydrophobic surfaces, carry away hydrophilic contaminants adhered to the surface when the droplets roll off the surface. This results from the stronger adhesion of the contaminant particle to the water droplet than the adhesion of the particle to the superhydrophobic surface [153]. The tilted angle of a surface on which a water droplet begins to move is defined as the sliding angle (SA), tilt angle (TA) or roll-off angle; this is in direct relation with the CAH [155]. Figure 3.1 shows a water droplet sliding easily across a superhydrophobic surface to carry away contaminants.

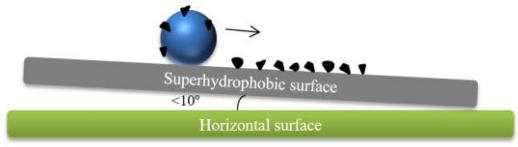

Figure 3.1. Self-cleaning property of a superhydrophobic surface.

A series of parameters, including surface roughness, the degree of particle adhesion and water repellency, are dominant in the self-cleaning ability of these surfaces [155]. Bhushan and co-workers [155] introduced a systematic study of the self-cleaning property of different nanostructured, microstructured, and hierarchically structured superhydrophobic surfaces. They observed that a droplet having nearly zero kinetic energy was unable to clean nanostructured and microstructured surfaces. However, the hierarchical surface was almost entirely cleaned. Many explanations have been suggested for functionality of the hierarchical structures [156-158]. They showed that only a hierarchical surface roughness can repel both macroscopic and microscopic droplets. Bagheri and co-workers [159] measured the minimum surface tilt angle needed for the appearance of the self-cleaning property of the different surfaces.

The self-cleaning glasses are also highly demanded [160, 161]. An important requirement for self-cleaning glasses is transparency. So, the produced superhydrophobic/self-cleaning surface must be transparent. To create a transparent superhydrophobic surface, the surface roughness should be smaller than 400-700 nm which is the wavelength of visible light [156]. Carbon nanotubes (CNTs) has attracted numerous attentions in the fabrication of self-cleaning coatings due to their ability to be aligned [162, 163]. The production of stimuli-responsive self-cleaning surfaces is a new approach in this field. In such surfaces, the wettability can switch by a stimulus including temperature, electric field, pH, and light [162, 164]. The self-cleaning characteristics of superhydrophobic coatings used for high-voltage outdoor insulators are of great importance [165]. The wet pollution layer followed by dry-band formation on the insulator surface has a significant effect on the insulator pollution flashover [36, 49, 166]. The IEC 60507 standard has been widely used to study the flashover performance in the artificial pollution testing of high-voltage outdoor insulators [167]. There are three polluting methods used in the solid layer method of artificial pollution testing: spraying, dipping, and brushing [168]. Kaolin [169, 170], active carbon [165, 171], and NaCl solutions [168] are some of the most common artificial pollutions applied to evaluate the self-cleaning property of the insulators.

A detailed assessment of outdoor settings reveals that there are different pollution scenarios: dry dust may be deposited onto surfaces in desert areas by the wind, or air-suspended pollution can be fall onto exposed surfaces by raindrops. The liquid component of this latter suspension may then be evaporated by solar radiation or elevated temperatures, leaving the polluted surface exposed to the next rainfall cycle. Moreover, whenever rainfall is involved, the diameter of rain droplets varies from 400 μm to ~2 mm as a function of rain rate ($mm \cdot h^{-1}$), and this variability must also be considered [172].

Therefore, to imitate realistic pollution scenarios that are representative of outdoor conditions, three factors must be considered: i) the condition of the contaminant as either a solid particle or a suspension; ii) the method of applying the contaminant and cleaning the polluted surface, i.e., dropwise, spraying, immersion of the sample within a contaminant suspension; iii) the condition of the contaminated surface before the cleaning process, i.e., has the original contaminant suspension dried off the surface? Therefore, a series of self-cleaning tests can be designed using the collection of these scenarios. Given that self-cleaning studies on superhydrophobic surfaces in the literature, to the best of our knowledge, are limited to only one specific set of conditions, we felt the necessity of addressing this gap in the general knowledge of self-cleaning properties.

Here, we successfully produced superhydrophobic silicone rubber (SHSR) surfaces having a high WCA and a very low CAH. As the industrialization of superhydrophobic surfaces has attracted much attention, we used an industrialized approach to produce the superhydrophobic silicone rubber surfaces, i.e., a compression molding system and molding inserts [28]. A stable interface guaranteed by the presence of micro-nano air pockets is necessary for ensuring a successful water-repellant surface. Therefore, it becomes necessary to study the robustness of these air pockets when evaluating their self-cleaning ability. We investigate the consistency of the Cassie-Baxter regime to create and maintain low CAH surfaces via various tests, including the droplet impacting process, water-jet impact, a trapped air layer, and severe droplet contact. Based on the stability of the Cassie-Baxter regime, these surfaces show promising self-cleaning properties and a resistance to the accumulation of contaminants. We used various analyses to comprehensively assess the self-cleaning properties of the produced SHSR surfaces by manipulating the three abovementioned self-cleaning factors (Figure 3.2).

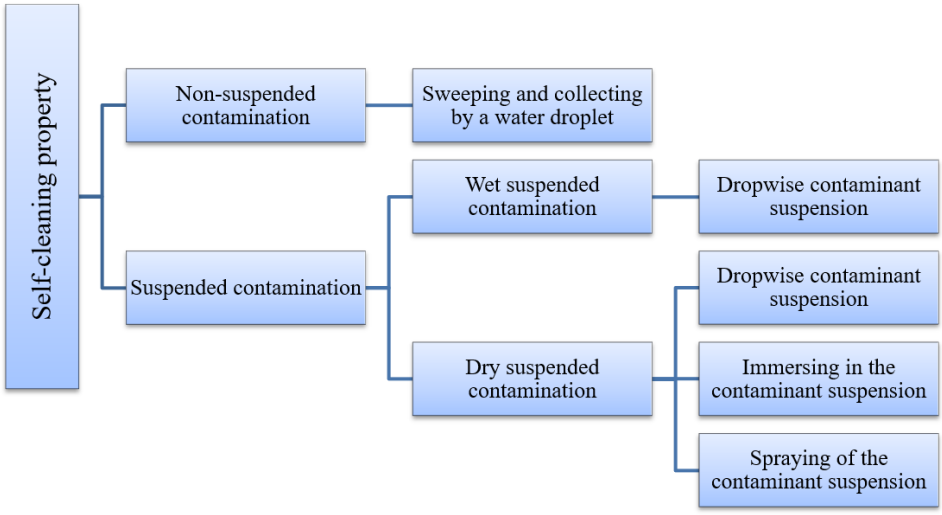

Figure 3.2. Flow diagram of the multiple various tests used to evaluate the self-cleaning properties based on the conditions of contaminant deposition.

3.3 Materials and methods

3.3.1 Fabrication of superhydrophobic silicone rubber surfaces

We applied a compression molding system (Carver Inc., USA) to fabricate silicone rubber having a micro-nanostructured surface. We used a molding insert to create the appropriate micro-nanostructured mold surface, whereas a chemical etching approach, using hydrochloric acid, created micro-nanostructures on an A6061 aluminum template. We set the etching parameters at 15 wt.% acid solution and an etching time of 2 h as to obtain optimal superhydrophobic properties for the produced silicone rubber surface [125].

3.3.2 Surface characterization

A scanning electron microscope (JSM-6480 LV SEM manufactured by JEOL Japan) provided visual confirmation of the morphology of the produced silicone rubber surfaces. An optical profiler (Profil3D, Filmetrics, USA) measured surface roughness and the area roughness quantities were calculated based on an ASME B46.1 3D standard.

3.3.3 Wettability and the Cassie-Baxter regime

A Kruss™ DSA100 goniometer determined WCA and CAH at 25 ± 0.5 °C. A 4-µL water droplet deposited onto the sample surface allowed determining the WCA using the Young-Laplace approximation. The CAH equaled the difference between the advancing and receding contact angles when the water droplet moved across the surface. To ensure accuracy and reproducibility, we conducted WCA and CAH

measurements at five different points on each sample; we reported the average WCA and CAH along with the standard deviation. A high-speed camera (FASTCAM SA1.1 by Photron) recorded the process of the droplets impacting on the SHSR surfaces. The framing rate was set to 5400 fps. All experiments were carried out in a closed chamber (60 cm × 45 cm × 45 cm) at a constant temperature of 22 °C. A 20-µL DI water droplet having a diameter of ca. 3.4 mm impacted onto the surface. The surface was placed onto a flat holding device, and the water droplets were released from a height of 6 cm. We used a syringe equipped with a needle (diameter = 0.8 mm) to create a water jet that impacted the surface under normal force. The distance and the angle between the needle tip and the surface was ca. 3 cm and 25–30°, respectively. The water jet impacted the surface at a velocity of ca. 2.5 $m.s^{-1}$.

3.3.4 Self-cleaning properties

In the self-cleaning tests, we used two different contaminant suspensions. One suspension consisted solely of 40 g kaolin particles (ranging from 1–25 µm in diameter, mean = 11 µm) as the contaminant in 1000 g deionized water, based on IEC standard 60507 [167]. The second suspension was a 40 $g \cdot L^{-1}$ dirty suspension consisting of equal amounts of SiO_2 particles, carbon black, salt, and kaolin in water as a multi-contaminant suspension. All suspensions were mixed continuously for 1 h at 600 rpm to obtain a homogenous suspension before their use in the tests. A syringe having a 0.8-mm diameter needle was used for the sweeping test. Images were captured by the Kruss™ DSA100 goniometer. An optical microscope (Nikon Eclipse E600Pol, polarizing microscope, maximum magnification = 1000×) was used to observe the contaminant-covered surfaces. For evaluating the chemical composition of the surface, we used Fourier transform infrared spectroscopy (FTIR) using a Cary 630 FTIR Spectrometer (Agilent, USA) in ATR (attenuated total reflection) mode to acquire the highest quality spectra in the infrared range of 400–4000 cm^{-1}. For the spraying contaminant test, we used an air-powered gravity-feed spray gun having a 1.0-mm diameter nozzle and applied a 15-bar pressure to spray the suspension onto the surfaces. For the self-cleaning tests, a high-quality digital camera (PowerShot SX50 HS, Canon) captured all images.

3.4 Results and discussion

3.4.1 Fabrication of superhydrophobic silicone surface

An obtained WCA of 166.2º ± 1.3º and CAH of 1.6º ± 0.4º demonstrated the superhydrophobic nature of the produced silicone rubber sample. The pristine silicone rubber (PSR) surface had a WCA of 116.0º ± 2.0º and CAH of 42.2º ± 3.1º demonstrating its hydrophobic properties. SEM images highlight micro-nanostructures on the superhydrophobic silicone rubber (SHSR) surface (Figure 3.3). These micro-nanostructures created by a replication process are responsible for the water-repellent behavior by satisfying the required conditions of low surface energy material and roughness for achieving superhydrophobicity.

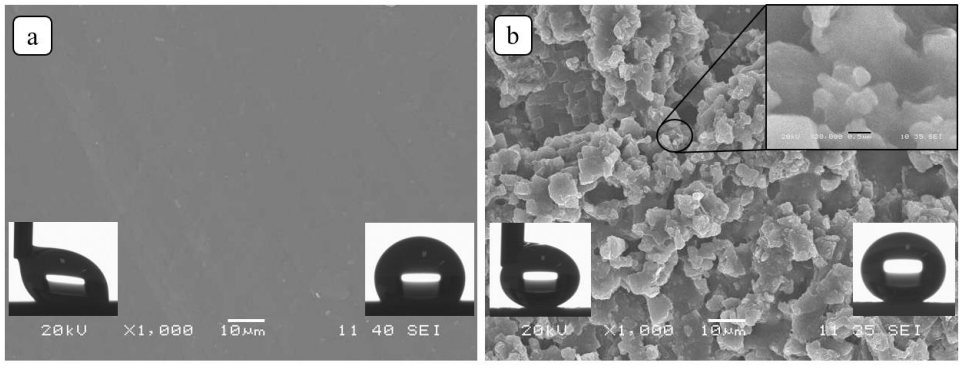

Figure 3.3. SEM images of (a) pristine silicone rubber (PSR) surface and (b) superhydrophobic silicone rubber (SHSR) surface with two different magnifications ×1,000 and ×30,000 (the scale bar in the ×30, 000 magnification is 500 nm). Inset images represent the contact angle and the contact angle hysteresis images.

We evaluated the roughness of the smooth, aluminum template, and superhydrophobic surfaces using a profilometry technique (Figure 3.4). A 350 × 300 µm^2 area of each surface was observed. The S_q (root mean square height) of the silicone surface increased from 1.748 µm to 8.124 µm after the replication process. This increase in the area roughness number reflects the creation of the micro-nanostructures being responsible for its ultra-water-repellent properties.

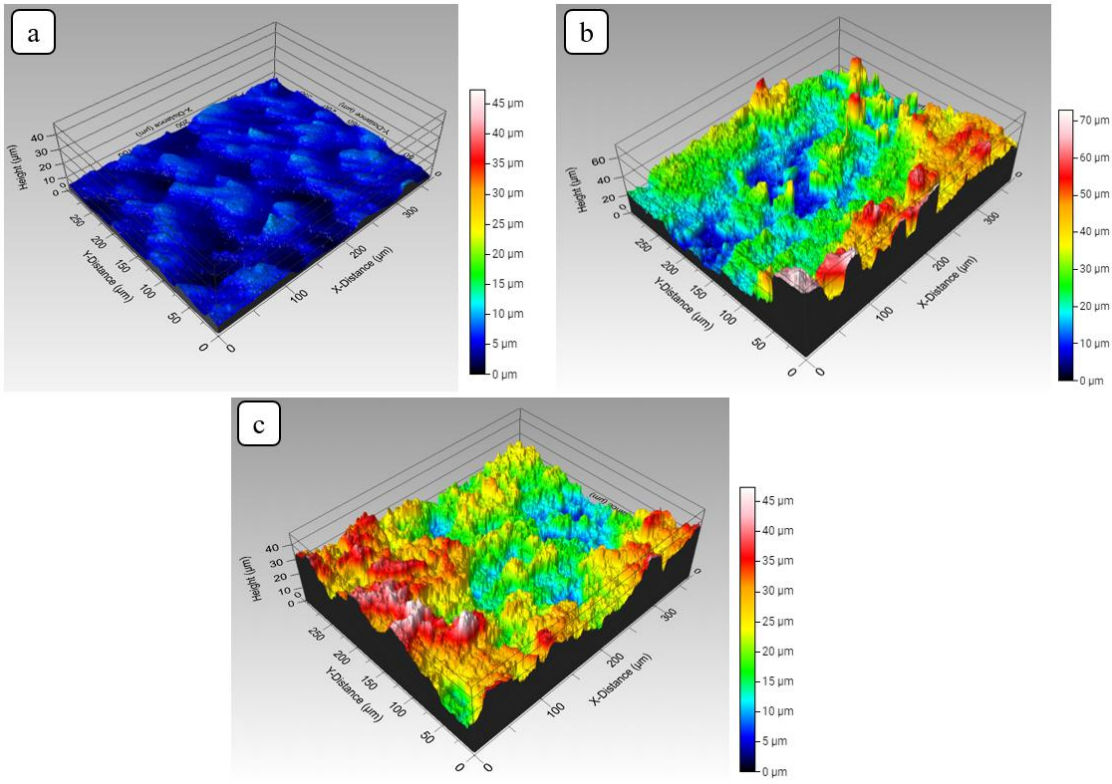

Figure 3.4. 3D profiles of the (a) pristine silicone rubber surface, (b) aluminum template, and (c) superhydrophobic silicone rubber surface.

The CAH values of the produced surfaces confirm that the created roughness led the surface to fall into the Cassie-Baxter state of ultra-water repellency. To confirm the superhydrophobic nature and the stability of being in the Cassie-Baxter regime, we carried out a series of tests including the droplet impacting process, the water-jet impact, the trapped air layer, and the severe droplet contact. The consecutive rebounding in the droplet impacting process can demonstrate the consistency of the Cassie-Baxter state. The rebounding behavior of the water in the water-jet impact also verifies whether the transition from the Cassie-Baxter regime to Wenzel regime can take place. The trapped air layer in the surface structures can be studied by immersing the samples underwater, and a severe droplet contact with the surface can demonstrate the consistency of the Cassie-Baxter regime on the surface. Each test will be detailed in the following subsections.

3.4.2 Wettability and the Cassie-Baxter regime study

3.4.2.1 Droplet impacting process

The process of a droplet moving on the surface is divided into four stages: the dripping stage, spreading stage, recoiling stage, and rebounding stage [286]. A droplet impacting on a solid surface is a function of

several factors that include impact velocity, droplet size, the properties of the liquid, surface roughness, and surface wettability [299]. On both the PSR and SHSR surfaces, a maximum spreading stage in the *x*-direction (pancake shape) was observed after 6–7 ms. On the PSR surface, the water droplet receded symmetrically. At 13 ms, a tiny jet was formed, but the droplet could not recoil or detach from the surface due to the high PSR surface energy that caused energy dissipation (Figure 3.5). However, due to the hydrophobic properties of the PSR surface, the water droplet did not spread over the surface as observed on flat bare aluminum [299]. A gentle up-down vibration of the droplet on the surface continued until the energy was fully dissipated and the droplet approached its final equilibrium shape at 95 ms.

The consistency of the Cassie-Baxter regime was observed in the images of the SHSR surface (Figure 3.6). The droplet impacted the SHSR surface and began to spread over the surface as the droplet's kinetic energy is converted into surface energy caused by frictional and adhesion forces [287]. At t = 7 ms, the droplet reached its extreme spreading in the *x*-direction (pancake shape). At the recoiling stage, driven by surface tension, the droplet contracted and began to rebound from the surface in the *y*-direction (15 ms, jet shape). This stage is highly dependent on the wettability of the surface. On a hydrophilic surface, the droplet remains in a flattened shape and wets the surface. On a hydrophobic surface, however, the droplet recedes and forms a jet shape [287]. From 48 ms to 91 ms, the droplet was in the fully rebounding stage. Various shapes for the droplet were observed at this stage, and the droplet reached its highest position at 56 ms. From this point, the droplet fell again onto the surface, and all four stages were repeated. A total of four rebounding stages were observed, through which the maximum height of the droplet steadily decreased (3.6 mm at 56 ms, 2.2 mm at 170 ms, 1.2 mm at 263 ms, 0.6 mm at 325 ms). Therefore, the presence of fully rebounding stages on the SHSR surface testifies to the Cassie-Baxter regime being dominant. Figure 3.7 shows schematically the influence of micro-nano air pockets of the SHSR surface in the forming of the Cassie-Baxter regime that leads to the full rebound of the impacting water droplet.

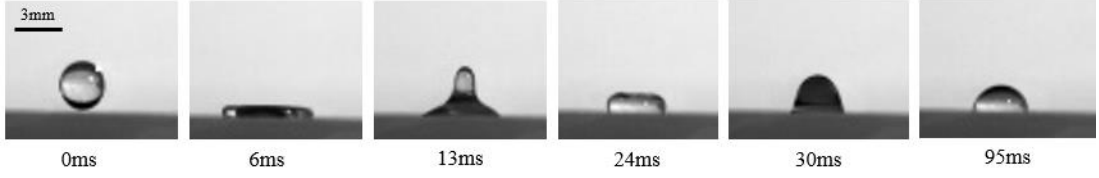

Figure 3.5. Sequential images of a droplet impacting onto the PSR surface.

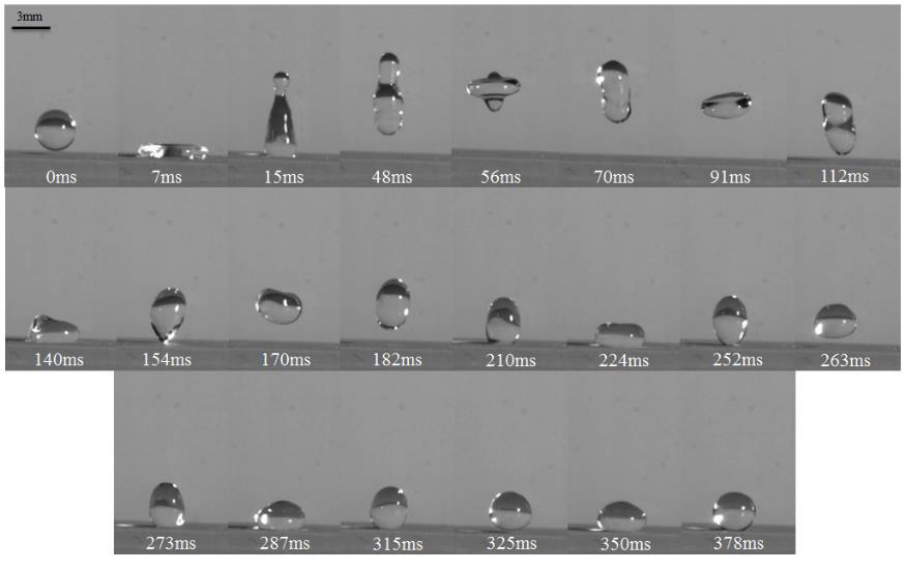

Figure 3.6. Sequential images of a droplet impacting onto the SHSR surface.

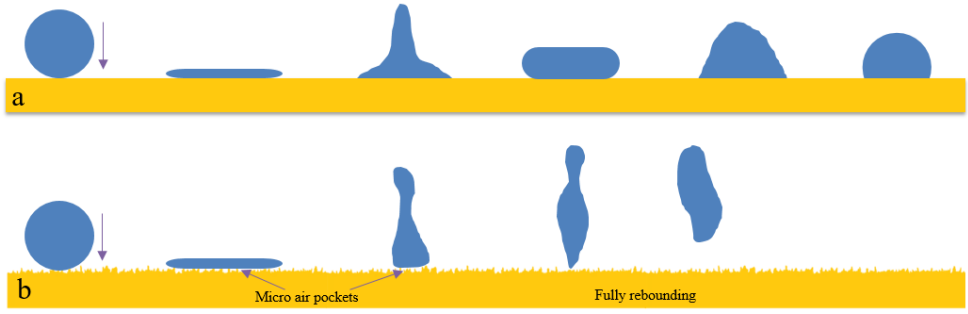

Figure 3.7. Schematic diagram of a water droplet impacting on (a) smooth surface of PSR; and (b) the effect of the presence of micro-nano air pockets in producing Cassie-Baxter regime on the SHSR surface.

3.4.2.2 Water-jet impact

We used the impact of a water jet on the fabricated surfaces to evaluate the water repelling property of the surfaces. A water jet can remove micro-nano air pockets entrapped in between the micro-nanostructures. As such, this may change the wettability character of the surface [273]. As expected, the water jet adhered to the PSR upon reaching the surface. The water accumulated on the PSR surface (Figure AI. 1(a)). The high-speed water jet was held on to the PSR surface due to the lack of air pockets in the intervening spaces. In the case of the SHSR surface, the water jet rebounded fully off the surface without leaving any residual water adhering to the target surface (Figure AI. 1(b)). The air pockets remained intact, and the cylindrical shape of the water jet was unaltered upon rebounding from the surface. The WCA of the SHSR surface did not change even after replicated tests (10 times i.e. ~50 mL of water jet), thereby confirming the resistance of these micro-nano air pockets.

3.4.2.3 Plastron air layer

Images of PSR and SHSR surfaces underwater show that the bright plastron air layer is obvious on the SHSR surface (Figure AI. 2). This is due to the total reflectance of light at the air layer that is trapped in between the SHSR surface micro-nanostructures [292]. This phenomenon did not occur on the PSR surface due to the complete contact of the water with the PSR surface interstices. This property is highly important in reducing drag or friction of a superhydrophobic surface [293].

3.4.2.4 Severe droplet contact

Using the severe water droplet contact with the surface test, we assessed the stability of the Cassie-Baxter regime (Figure AI. 3). A 4-µL water droplet adhering to a needle was brought to the surfaces. After the initial contact between the droplet and the surface (which is a representative of the surface WCA), the droplet was pushed toward the surface using the needle. The droplet was then lifted upward. Due to the ultra-water repellency property of the SHSR surface, the droplet detached easily and rapidly from the surface without leaving any traces of water. This ascertains the stability of the Cassie-Baxter regime when additional forces are applied [291].

3.4.3 Self-cleaning property

To study the self-cleaning properties of the produced SHSR surfaces, we divided the test conditions into two categories: non-suspended and suspended contamination. The latter was again divided into a *wet* subcategory where the contaminant suspension was not allowed to dry on the surface, and a *dry* subcategory where the contaminant suspension dried and sediment remaining on the surface was then cleaned off. The non-suspended contamination test includes the sweeping and collection of contaminant particles by a water droplet. The wet suspended contamination test includes a dropwise contaminated suspension. The dry suspended contamination tests include dropwise contaminant suspension, immersion, and spraying.

The *dry* suspended contamination tests that involve drying and sedimentation processes imitated outdoor conditions where suspensions of contaminants are deposited onto the surface and then dry out and adhere to the surface, thereby rendering the cleaning of the surfaces more difficult.

3.4.3.1 Non-suspended contamination tests

3.4.3.1.1 Sweeping and collection by a water droplet

In this first test, we compared the adhesion between the water droplet and pollution particles with the adhesion between pollution particles and the superhydrophobic surface. Kaolin powder was scattered homogeneously on the silicone surface using a 60 mesh. The kaolin contaminant was set onto the surface for 30 min before carrying out the next step. A water droplet, still fixed to the syringe needle, swept the contaminant off the surface. Following the passage of the droplet, no trace of contaminants remained along the droplet path on the SHSR surface. Thus, the CAH of the SHSR surface was low enough to allow the water droplet to move easily over the surface while remaining stuck to the syringe needle. Furthermore, it demonstrated the self-cleaning property of the surface as the contaminants adhered to the water droplet rather than the SHSR surface. A single water droplet cleaned almost an entire 22 × 17 mm^2 surface (Figure 3.8). When we performed the same experiment on the PSR surface, we observed that the water droplet stuck to the polluted surface as soon as it contacted the surface.

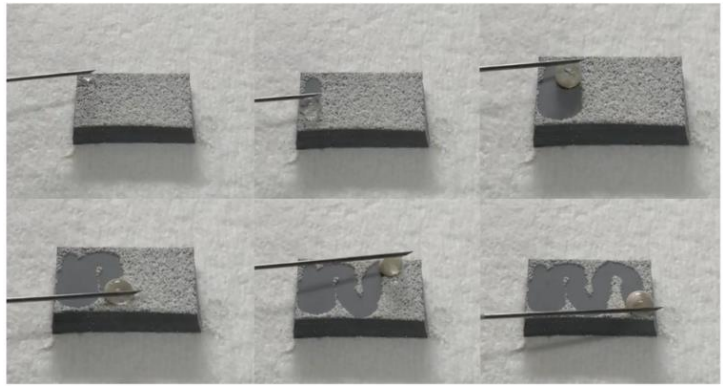

Figure 3.8. Self-cleaning of the silicone surface by water droplet sweeping.

As contaminant particles are hydrophilic and the surface is superhydrophobic, the particles adhere very strongly to the water droplet (Figure AI. 4). In contrast to being transparent at the onset of the test, the opaque appearance of the water droplet at the end of the process relates to the collected contaminants by the water droplet.

3.4.3.2 Wet suspended contamination tests

3.4.3.2.1 Dropwise contaminant suspension

Using the prepared 40 $g \cdot L^{-1}$ multi-contaminant suspension, we evaluated the self-cleaning property of the SHSR on a 3°-tilted surface—the chosen angle is similar to the inclination of an electrical insulator shed. We used a syringe needle to place the suspension onto the surfaces in a continuous manner from ca. 3 cm above the surface (Figure 3.9). The PSR surface retained many of the droplets, whereas the SHSR surface, as expected, repelled the droplets and remained thoroughly clean. Figure 3.9(a) sequentially shows the accumulated dirty suspension on the PSR surface and Figure 3.9(b) presents in sequence the self-cleaning behavior of the produced SHSR. The SHSR surface repels the dirty suspension droplets in a similar manner as with pure water droplets. The dirty droplets roll off the surface immediately upon landing on the surface. The removed dirty suspension can be clearly seen on the underlying paper towel.

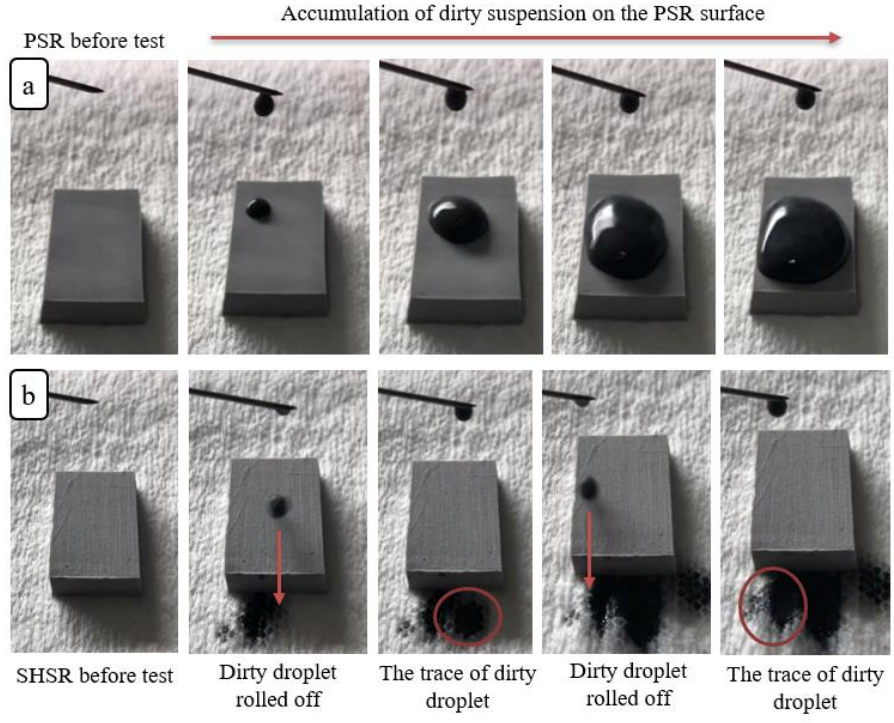

Figure 3.9. Sequential representation of (a) the accumulation of dirty suspension on the pristine silicone rubber (PSR) surface and (b) the self-cleaning behavior of the produced superhydrophobic silicone rubber (SHSR) surface after wet suspended contamination.

3.4.3.3 Dry suspended contamination tests

3.4.3.3.1 Dropwise contaminant suspension

In the first test of dry suspended contamination tests, we examined the self-cleaning ability of the surface through the cleaning of two dried droplets of a kaolin suspension on the prepared surfaces. We prepared a 40 $g \cdot L^{-1}$ kaolin suspension (regarding IEC standard 60507 [167]) and thoroughly mixed the water-kaolin suspension. Before any sedimentation could occur, we gently placed two droplets onto each surface using a syringe (Figure 3.10(a, b)). The surfaces were then dried at ambient temperature for 4 h to evaporate all water and have the kaolin sediment onto the surfaces (Figure 3.10(c, d)). It must be noted that a completely flat trace remained on the PSR surface after drying (Figure 3.10(c)); however, due to the ultra-water repellency of the SHSR surface, the shape of the dried kaolin suspension was spherical even after drying (Figure 3.10(d)), retaining its initial shape. We then assessed the self-cleaning performance of the surfaces placed on a completely flat holding plate by removing the dried kaolin stains using water droplets. All added water (~0.4 mL) to the PSR surface accumulated on the surface, and the dried kaolin stains remained fixed on the surface (Figure 3.10(e)). In contrast, two water droplets (40 µL) were sufficient to remove completely the kaolin spots from the SHSR surface. The removed kaolin spots are obvious on the base plate (Figure 3.10(f)), and no trace is detectable on the SHSR surface.

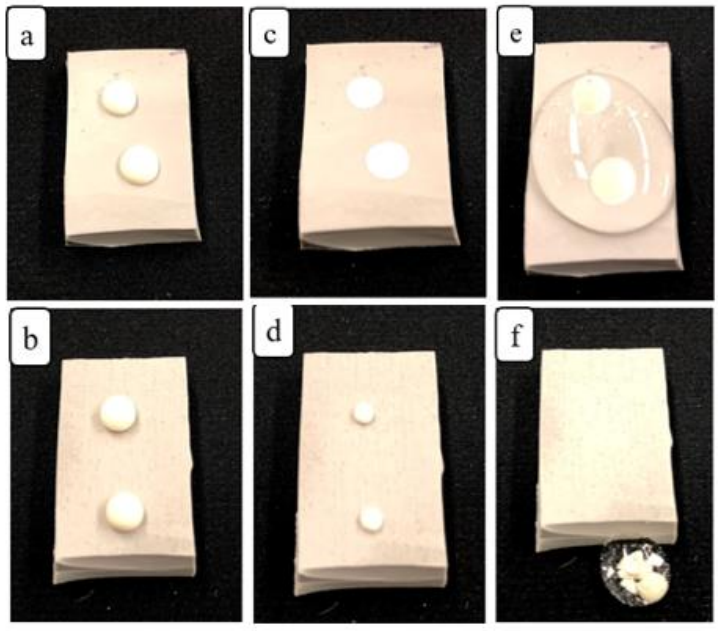

Figure 3.10. Placement of two kaolin suspension droplets on the (a) pristine silicone rubber (PSR) and (b) superhydrophobic silicone rubber (SHSR) surfaces; droplets dried at ambient temperature for 4 h to produce (c) thoroughly flat traces on the PSR and (d) marble-like droplets on the SHSR surfaces; cleaning the dried droplets of kaolin suspension off the (e) PSR and (f) SHSR surfaces.

We also repeated the same test to compare the self-cleaning ability of the surfaces on a 3°-tilted holding plate (inspired by the electrical insulators' shed inclination). This time, although some contaminant was removed from the PSR surface, the dried kaolin stain remained fixed on the surface even after rinsing with ~10 mL of water for nearly 7 s. Comparing the initial weights and after-rinsing weights of the surfaces, we calculated that ~79% of the contaminant mass remained on the PSR surface. In contrast, the SHSR surface exposed to the same conditions self-cleaned easily, and we detected no weight increase (Table 3.1).

Table 3.1. The weight of PSR and SHSR surfaces before applying the kaolin contaminant and after rinsing the surfaces.

Sample	**Initial weight (g)**	**Weight after sedimentation (g)**	**Weight after rinsing (g)**	**Accumulated contamination on the surface**
PSR	2.801 ± 0.002	2.891 ± 0.002	2.872 ± 0.003	~79%
SHSR	3.613 ± 0.001	3.703 ± 0.002	3.613 ± 0.002	~0%

When we compared the optical microscopic images of the SHSR and PSR surfaces prior to application of the kaolin suspension (Figure AI. 5(a, b)) and following the rinsing of the surfaces by water droplets (Figure

AI. 5(c, d)), no contamination residue was observed on the SHSR surface, whereas much of the PSR surface remained covered by the contaminant.

Our FTIR spectra results for SHSR and the PSR surfaces illustrated no difference between the FTIR spectra of the SHSR and PSR surfaces (Figure 3.11). In addition, the self-cleaning property of the produced superhydrophobic surface left no trace of contaminants on the surface. Changes in FTIR spectra of the PSR surface is attributed to the amount of the kaolin pollution that remained on the surface post-rinsing. Kaolin consists mainly of SiO_2, Al_2O_3, and H_2O (48.12, 36.33 and 4.77 wt.%, respectively) [300]. Due to the SiO_2 of the kaolin, we observe a peak corresponding to Si-O stretching at 1000–1030 cm^{-1} on the FTIR spectra. However, peaks around approximately 805–855 cm^{-1} and 1245–1275 cm^{-1}, which are related to $Si(CH_3)_2$ and $Si(CH_3)$, respectively, had almost vanished as the silicone rubber surface was covered by the kaolin contamination. The new peaks at 3620–3654 cm^{-1} were characteristic of OH stretching of the inner surface hydroxyl groups. Moreover, the sharp band at around 912 cm^{-1} and the weak shoulder at 940 cm^{-1} were due to the OH deformation of inner hydroxyl groups and Al(VI)-OH vibrations [301].

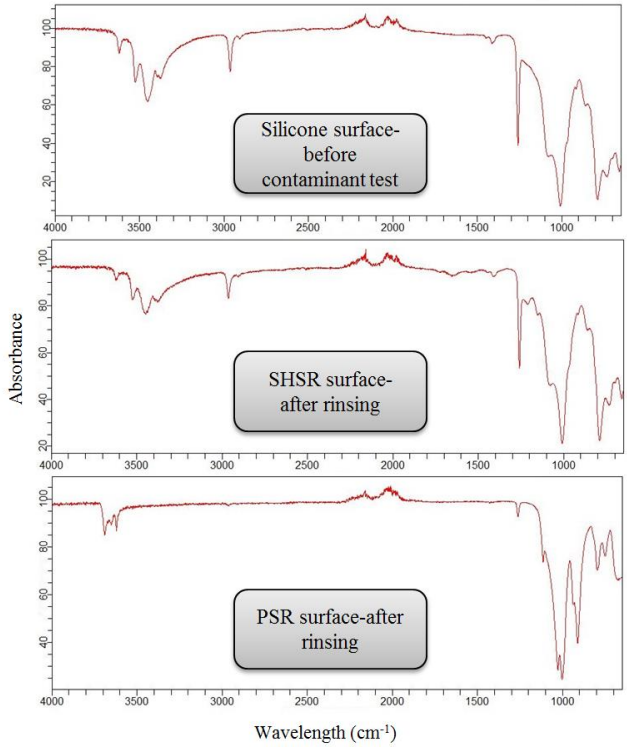

Figure 3.11. FTIR spectra of the silicone surface before the application of the kaolin contaminant and after the rinsing of the two superhydrophobic silicone rubber (SHSR) and pristine silicone rubber (PSR) surfaces.

3.4.3.3.2 Immersion in the contaminant suspension

The multi-contaminant suspension (i.e., 40 $g \cdot L^{-1}$ dirty suspension consisting of SiO_2 particles, carbon black, salt, and kaolin in water) was used for the immersing in the contaminant suspension test as the second test for the dry suspended contamination. The PSR and SHSR surfaces (Figure 3.12(a)) were completely immersed in the dirty suspension (Figure 3.12(b)) and were then placed on a hot plate at 70 °C for 2 h to evaporate the water from the dirty suspension to dry and fix the sediment onto the surfaces (Figure 3.12(c)). Following this application and the drying of the contaminant suspension, much sediment had accumulated on the PSR surface, whereas the SHSR surface remained clean (Figure 3.12(d)). Using water droplets, we then attempted to remove the accumulated contaminants from the PSR surface. We used ~10 mL water to clean the PSR surface. The surface of the paper towel surrounding the PSR surface was covered by a portion of the surface contaminants, whereas most of the contaminants adhered strongly to the PSR, and droplets also accumulated on the surface (Figure 3.12(e)). Thus, the adhered contaminants to the PSR surface converted the surface into a hydrophilic surface (WCA of ~63°), whereas the SHSR retained its superhydrophobicity under such severe contamination, i.e., no change of WCA was observed.

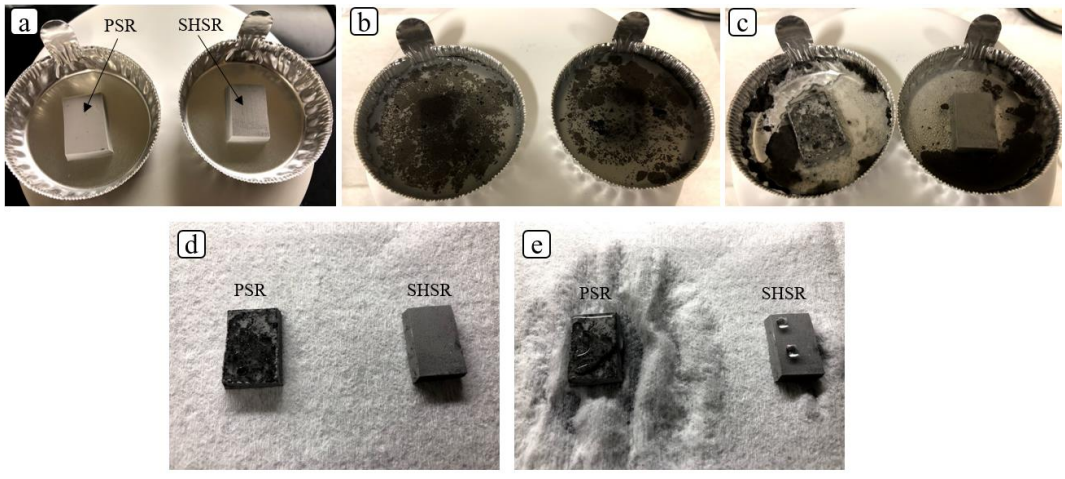

Figure 3.12. (a) Placement, (b) immersion, (c) drying, (d) removing, and (e) cleaning steps of pristine silicone rubber (PSR) and superhydrophobic silicone rubber (SHSR) surfaces.

3.4.3.3.3 Spraying of the contaminant suspension

In the third test, we imitated rainy outdoor conditions in an area marked by air pollution where rainwater mixes with the atmospheric contaminants. The contaminated rain falls on the surfaces, and after rain stops, the dirty suspension on the surfaces gradually dries. Thus, there is a chance for the dirty surfaces to be cleaned off

by the next rainfall, although not all contaminants may be removed. Due to this deposition-drying-deposition cycle and possible lack of complete removal of the contaminants by the subsequent rainfall, this scenario (or test) is considered as the most severe. This test provides a very realistic scenario to compare the functionality of the produced SHSR surface with the PSR surface.

The kaolin suspension (40 $g.L^{-1}$ based on the IEC standard [167]) was sprayed onto the surfaces, dried at ambient temperature, and then cleaned off the surfaces by spraying deionized water. We used 15 bar air pressure spray to apply 100 mL of kaolin suspension onto both SHSR and PSR surfaces (Figure 3.13(a, b)). The surfaces were attached in a vertical position onto a base. After spraying, the samples were dried at ambient temperature for 15 min to let the contaminant adhere to the surface (Figure 3.13(c, d)). We then washed the surfaces using 50 mL of deionized water using the same air pressure spray (Figure 3.13(e, f)). We repeated this cycle five times. The appearance of the surfaces after the five spraying, drying, and washing cycles is shown in Figure 3.13(g, h), (i, j), and (k, l), respectively. We then let the surfaces rest for 1 h (Figure 3.13(m, n)) and measured the surface WCA and CAH. The hydrophobic property of the PSR surface deteriorated and produced a WCA of 77º ± 3º and a CAH of 54º ± 2º after five cycles. This is due to the stiction of the hydrophilic contaminants to the PSR surface rendering the surface hydrophilic. However, the SHSR retained a WCA of 150.1º ± 1.9º and a CAH of 16º ± 2º even after the five cycles.

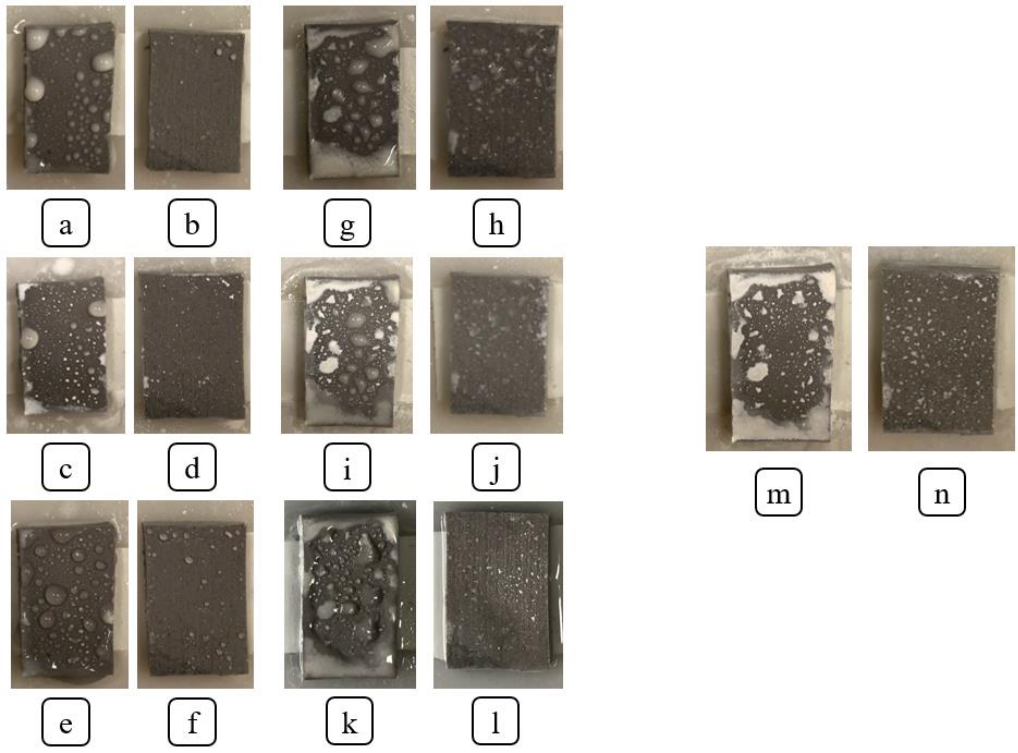

Figure 3.13. Images captured after the initial (a) spraying, (c) drying, (e) washing cycle of pristine surface and for the superhydrophobic surface (b-d-f); after the fifth (g) spraying, (i) drying, (k) washing cycle of PSR and SHSR surfaces (h-j-l); Final appearance of the (m) PSR and (n) SHSR surfaces.

Following the spraying test, we used optical microscopic images of the SHSR and PSR surfaces to compare the amount and size of adhered contaminants to each surface (Figure 3.14). The edges of the PSR surface are obvious in Figure 3.13(m) as the surface is completely covered by contaminants (Figure 3.14(a)). This severe accumulation of contaminants on the edges of PSR can lead to a functional failure after multiple contamination-drying cycles. The edges and the middle of the SHSR surface indicated an insignificant difference in contaminant accumulation (Figure 3.14(b, d)). The largest accumulations in the middle of SHSR surface were 85 µm in diameter, while spots 300–500 µm in diameter were found in the middle of PSR surface (Figure 3.14(c, d)). The covered surface area by contaminant in the edge and in the middle of pristine surface was 67% and 39% respectively, while these values for the superhydrophobic surface were only 6.2% and 2.3% respectively. Thus, even though the sprayed contaminant particles could adhere to the SHSR surface and accumulate in some spots, the surface could still preserve its WCA of >150°. This is especially important when noting that the PSR lost its hydrophobicity after a significant amount of contaminants had accumulated on its surface. Weighing the samples before and after the spraying test indicated a 1.96% increase in weight for the PSR surface and a 0.1% increase in weight for the SHSR surface. This marked difference in accumulated

contaminants on the two surfaces (i.e., SHSR surface accumulated ca. 19 times less contamination than the PSR surface) testified to the self-cleaning properties of the SHSR surface during the test, as the SHSR surface could repel the contaminant suspension and also self-clean when sprayed with water.

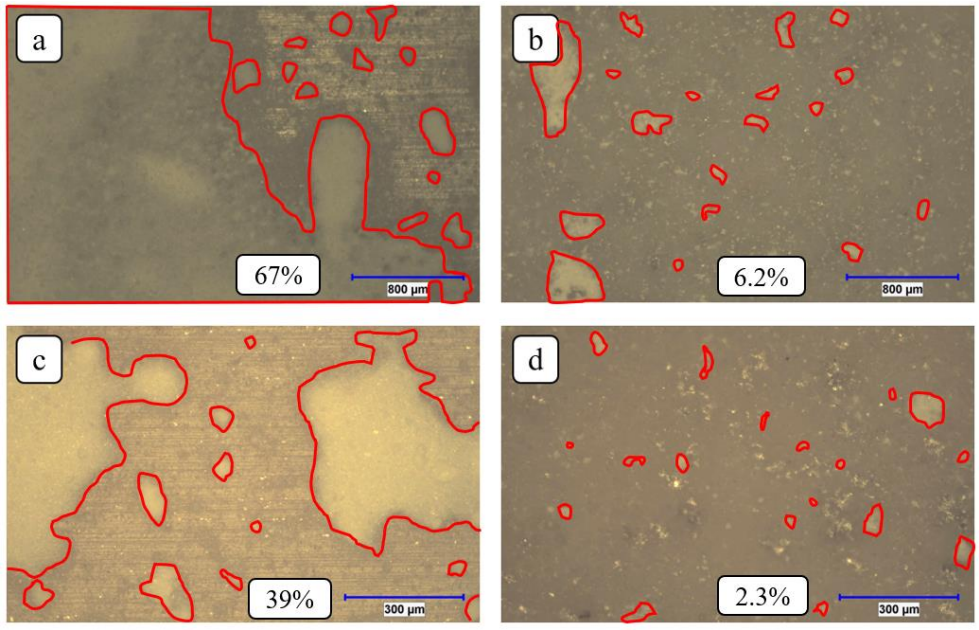

Figure 3.14. Optical microscope images of the edges of (a) pristine silicone rubber (PSR) and (b) superhydrophobic silicone rubber (SHSR) surfaces after five spraying cycles, and images of the middle of (c) PSR and (d) SHSR surfaces.

The low molecular weight silicone (LMWS) can diffuse from the bulk of the silicone rubber to the surface, reorient by conformational changes, and then cover the contamination. This leads to hydrophobicity/superhydrophobicity recovery [218, 302]. Benefitting from the hydrophobic-recovery property, and thanks to the self-cleaning property of the SHSR surface, the WCA of the SHSR surface increased to 154.1º ± 1.2º and 158.2º ± 1.6º; and the CAH decreased to 10º ± 1º and 8º ± 1º after one and two weeks, respectively. However, the PSR could not retain its hydrophobicity due to the marked accumulation of contaminants on its surface. The WCA and CAH of PSR had no considerable change after one week. After two weeks, the WCA of the PSR surface increased to 81º ± 4º, and its CAH decreased to 52º ± 2º.

3.5 Conclusions

We produced an ultra-water-repellent silicone rubber having a WCA >150° and a CAH <10° using a straightforward industry-applicable method. We used the compression molding system as an industrialized means to produce silicone rubber surfaces, and we used molding inserts to replicate the micro-nanostructures

on the silicone rubber surfaces as a means for mass production. As the transition from the Cassie-Baxter regime to the Wenzel regime is the main factor in determining the self-cleaning ability of a superhydrophobic surface, we first conducted a series of experiments to investigate the dominance and robustness of the Cassie-Baxter regime. These tests included assessment of the droplet impacting process, water-jet impact, trapped air layer, and a severe droplet contact tests. These tests confirmed the ultra-water repellency of the surfaces as well as the consistency of the created micro-nano air pockets in between the surface asperities. To address a lack of comprehensive testing of the water-repellency and the self-cleaning nature of developed superhydrophobic surfaces, we undertook a comprehensive set of experiments using various contaminants and several methods for applying the contaminants and cleaning the surface, under both wet and dry scenarios. The test conditions were inspired by actual outdoor conditions to which electrical insulators, for example, are exposed. We sprayed a kaolin suspension on PSR and SHSR surfaces and dried and redeposited contaminants via spraying. The maintained ultra-low CAH of the surfaces ensured that the self-cleaning properties remained robust for all tests.

Acknowledgments

The authors acknowledge the financial support from the Natural Sciences and Engineering Research Council of Canada (NSERC) and K-Line Insulators Limited, Toronto, Canada. We also thank Filmetrics Inc. for carrying out the profilometry analysis.

CHAPTER 4

ARTICLE 3: ICEPHOBICITY AND DURABILITY ASSESSMENT OF SUPERHYDROPHOBIC SURFACES: THE ROLE OF SURFACE ROUGHNESS AND THE ICE ADHESION MEASUREMENT TECHNIQUE

K. Maghsoudi, E. Vazirinasab, G. Momen, R. Jafari

Department of Applied Sciences, University of Quebec in Chicoutimi (UQAC)

555, boul. de l'Université, Chicoutimi, Québec, G7H 2B1, Canada

This article is under review at:

Materials Processing Technology

4.1 Abstract

The durability of anti-wetting properties is of great importance for ensuring long-lasting superhydrophobic and icephobic surfaces that require minimal maintenance and resurfacing. Herein, we fabricated superhydrophobic silicone rubber surfaces having ultra-water repellency and icephobic properties via two industrially applicable methods: micro compression molding (μCM) and atmospheric pressure plasma (APP) treatment. We produced a series of surfaces covered by micro-nanostructures of differing sizes. We evaluated the anti-icing properties (delayed ice formation) and de-icing properties (reduced ice adhesion strength) of the produced surfaces that were subjected to two forms of icing conditions. The well-known ice adhesion measurement techniques, i.e., the centrifuge adhesion and push-off tests, provided quantitative comparisons of the ice adhesion strength of the produced surfaces. Although both superhydrophobic surfaces reduced ice adhesion strength, the smaller surface micro-nanostructures produced a greater reduction in ice adhesion by favoring less ice interlocking with the surface asperities. To rigorously assess the durability of the produced surfaces, we carried out a comprehensive series of experiments that covered a wide range of real-life conditions. Under harsh environmental conditions, the surfaces maintained a water contact angle and contact angle hysteresis of >150° and <10°, respectively, thereby confirming the resistance of the superhydrophobic silicone surfaces to severe chemical and mechanical damage. In some cases where water repellency was lost, the silicone rubber surfaces demonstrated a satisfactory recovery of their anti-wetting properties.

Keywords: Superhydrophobicity; Icephobicity; Anti-icing; Ice adhesion measurement; Durability; Recovery.

4.2 Introduction

Superhydrophobic surfaces have been the focus of multiple recent studies due to their wide range of applications, which includes low-adhesion, low-drag, anti-wetting, anti-corrosion, icephobic, anti-fogging, anti-biofouling, oil-water separation, buoyancy enhancement, and self-cleaning applications [28, 201-203]. Water-repellent superhydrophobic surfaces, as determined by a water contact angle (WCA) >150° and a contact angle hysteresis (CAH) or sliding angle (SA) <10°, are fabricated via a combination of low surface energy materials and hierarchical micro-nanostructured surfaces [303]. For a material to possess superhydrophobic properties, it usually fulfills two prerequisites: 1) having the non-polar groups on the surface to provide the necessary hydrophobic characteristics and 2) the presence of micro-nanofeatures that roughen the surface [304].

Superhydrophobic surfaces are among the best candidate surfaces for exhibiting icephobic properties. Such water-repelling surfaces can delay ice formation [125, 183], the anti-icing property, and reduce ice adhesion strength [44, 191, 305], the de-icing property. Ice formation on a superhydrophobic surface having micro-nanostructures is affected by (1) the reduced contact area between the surface and water droplets due to the high WCA. This scenario leads to a reduced heat transfer via conduction [45], (2) a reduced heat transfer through the air trapped between the surface asperities, the air acting as an insulating layer [185], (3) a limited number of sites available for the heterogeneous nucleation of ice at the water-solid interface [189], and (4) a shorter rebounding time—shorter rest time—of water droplets compared to the nucleation time [192]. Moreover, the reduced ice adhesion strength is due to the formation of microcracks caused by surface roughness causing interfacial stress concentrations [193] and the reduced contact area between the formed ice and the surface due to the limited solid–liquid contact area [173]. However, surface roughness may negatively affect icephobicity due to the mechanical interlocking of the ice within the surface asperities [193]. This mechanical interlocking is governed by the consistency of the Cassie-Baxter regime. Although there is, on one hand, a fully Cassie-Baxter state and, on the other, a Wenzel state, an intermediate state can exist where a water droplet penetrates partially into the surface structures [194]. Therefore, the degree of this penetration can affect the mechanical interlocking of ice producing either a “Cassie ice” or “Wenzel ice” [181]. Consequently, the

surface geometry has a decisive effect on the icephobic behavior of the produced surfaces. Among the various surface geometries, including microstructures, nanostructures, and hierarchical micro-nanostructures, hierarchical micro-nanostructures have demonstrated the lowest ice adhesion strength [191, 306].

Although multiple applications benefit from superhydrophobic surfaces, the durability of these surfaces against mechanical forces and chemical media remains questionable, and studies have begun to access this element [195-199]. Superhydrophobic surfaces prone to mechanical or chemical damage either lose surface roughness or the low surface energy chemical bonds [197]. This fragility can lead to a transition from the Cassie-Baxter state to the Wenzel state, a state that is energetically more favorable for the water droplet. The transition to the Wenzel state induces a strong pinning that increases the adhesion between the water droplet and the surface; the result is a loss of water repellency or anti-wetting performance of the surface [200]. The lack of a defined standard procedure for evaluating the durability of different types of superhydrophobic surfaces has led to a myriad of set-ups and procedures to measure surface durability. These durability measurements are divided into tests of mechanical durability and chemical resistivity. Mechanical durability analyses include abrasion resistance under a specific force, wear resistance by rubbing the surface, the tape-peel tests, scratch tests, fatigue testing, and sandstorm simulations. The chemical durability analyses include immersion in aqueous solutions of varying pH, and exposure to UV light. Some analyses, such as water droplet impacts, the ultrasonic treatment of surfaces in water, and the durability of the superhydrophobic/icephobic surfaces after repetitive icing/de-icing cycles, involve both mechanical and chemical testing [28, 195-199, 201-203].

Due to the lack of a single and standardized method for determining the durability of the superhydrophobic surfaces through abrasion by sandpaper, there are different test parameters for characterizing abrasion effects. The abrasion test results are affected by several factors that include the surface roughness of the abrading surface, its chemical composition, its Young's modulus, the applied pressure on the surface during abrasion, the amount of contact between the two surfaces, the type of applied motion, and the relative speed between the two surfaces in contact [200]. For example, Su et al. [204] studied the abrasion resistance properties of a superhydrophobic coating made of a polyurethane elastomer on a porous aluminum template. They used an abrasive load of ~2.9 kPa and demonstrated that the surface WCA remained at >150° even after

10,000 abrasions. Li et al. [205] investigated the mechanical durability of resin-based superhydrophobic coatings using 2000-mesh sandpaper with 200-g loading (corresponding to a stress of 3.3 kPa). Although the WCA remained >150° after 300 abrasion cycles, the SA of the coating was >10° after 50 abrasion cycles. In some cases, lower sandpaper grit (280–400#) created superhydrophobicity due to the creation of new surface roughness, while the higher grit deteriorated the superhydrophobic properties of the surface [206].

As many superhydrophobic surfaces cannot withstand being touched by a finger, the finger-press test can evaluate the robustness of superhydrophobic coatings and surfaces [207, 208]. Another means of evaluating durability is through the pressing of a tape onto a surface with approximately 10 kPa and then peeling the tape from the surface. Deng et al. [209] observed that when only Van der Waals interactions retain particles to a surface, the particles can be removed easily by tape-peeling; however, tape-peeling has no considerable effect on particles if silica bridges chemically bind particles to the surface. A switch in wettability state has also been observed after a tape-peeling test [210], i.e., the surface showed a sticky superhydrophobic property (WCA ~156° and no sliding of the water droplet). This scenario occurred due to the decreased surface roughness after peeling the adhesive tape from the surface. The ultrasonication has a diverse influence on superhydrophobic durability. The outcome is highly dependent on the adhesive strength between the superhydrophobic coating and the substrate [211]. While in some cases, ten minutes of ultrasonication can decrease the WCA considerably and increase the CAH [212], in other cases the superhydrophobic fabric has remained intact even after almost 100 hours of ultrasonication [213].

In terms of chemical tests of durability, the examination of the surface chemical stability under both acidic and alkaline conditions is one of the most common tests, with liquids ranging in pH from 1 to 14 being used [173, 202, 214, 215]. Surface durability can also be assessed through the dynamic impact durability test. The surface undergoes a collision with a solid, e.g., silicon dioxide or silicon carbide particles, liquid (in the form of sprayed microdroplets, regular size drops, or a jet), or gas (strong wind) phases [200].

In addition to abovementioned conditions where a superhydrophobic surface can lose its water repellency, icing/de-icing cycles can also be very damaging to surfaces. Although many investigations have reported changes to ice adhesion strength when surfaces are subjected to various mechanical tests [24], few studies have reported changes of the WCA and CAH after multiple icing/de-icing cycles [45, 48, 305, 307]. Of

the published results, the WCA generally decreases and the CAH increases after multiple icing/de-icing cycles. The adhesive strength and the mechanical bonding between the fabricated micro-nanostructures and the substrate are critical in explaining the wettability of the superhydrophobic surfaces after icing/de-icing cycles. Icing/de-icing cycles can transform a spiky surface morphology into a bumpy surface when the nanostructured protrusions become damaged [308].

Many surfaces can also recover their superhydrophobic properties after undergoing one of the abovementioned destructive tests. Such highly promising surfaces regenerate either their surface roughness or restore the surficial chemical functions [197]. This recuperation of the superhydrophobic properties of a surface occurs through the self-healing of topographic structures and surface chemistry [202]. Silicone rubber material has exhibited hydrophobic-recovery properties where low molecular weight silicone (LMWS) chains diffused from the bulk material to the surface. This self-healing has also been demonstrated via the reorientation of methyl groups from the bulk material to the surface, the reorientation of hydroxyl groups from the surface into the bulk material by the partial segmental movement of silicone rubber chains, and as well through the condensation of silanol groups [309, 310]. While the migration of LMWS to the surface dominates the hydrophobic recovery of polluted silicone rubber surfaces, the conformational reorientation of groups is mainly responsible for the hydrophobic recovery of surfaces when silicone rubber chains become aged or oxidized [304, 311]. Thus, the ability of a surface to recover its anti-wetting properties is as important as the assessment of the durability of superhydrophobic surfaces.

In the present study, we produce superhydrophobic silicone rubber surfaces having a high WCA and very low CAH using a direct replication method via micro compression molding (μCM) and atmospheric pressure plasma (APP). The low CAH of both produced surfaces was created by micro-nanostructures that established a Cassie-Baxter regime. Due to the ultra-low CAH of the produced superhydrophobic surfaces, these produced surfaces demonstrated icephobic properties. We assessed the anti-icing and de-icing properties by measuring freezing delay times and ice adhesion strength, respectively. We applied two common methods to measure ice adhesion strength, the centrifuge adhesion (CAT) and push-off tests. This is, to our knowledge, the first study to investigate the ice adhesion strength by two methods to provide a comprehensive comparison. In addition to applying repetitive icing/de-icing cycles to study the durability of the produced surfaces, we also

studied the durability of the surfaces under mechanical and chemical forces. We also rigorously examined the recovery of surface hydrophobicity/superhydrophobicity of the silicone surfaces in cases where the superhydrophobicity of a surface was lost.

4.3 Materials and methods

4.3.1 Fabrication of superhydrophobic silicone rubber surfaces

We fabricated the superhydrophobic silicone rubber surfaces using a direct replication method (via a µCM, Carver Inc., USA) and an atmospheric pressure plasma machine (Plasmatreat GmbH, Germany) (Figure 4.1). A chemical-etching method—15 wt.% HCl acid solution for 2 h—created micro-nanostructures on an A6061 aluminum template (for more details on the fabrication procedure, see [125]). The selected optimal plasma parameters were a reference voltage of 100%, plasma jet speed of 4 $m \cdot min^{-1}$, gas flow rate of 2500 $L \cdot h^{-1}$, plasma frequency of 21 kHz, a cycle time of 100%, as well as a distance between nuzzle and substrate of 8 mm. The plasma jet passed along the surface four times (for more details on the fabrication procedure, see [312]).

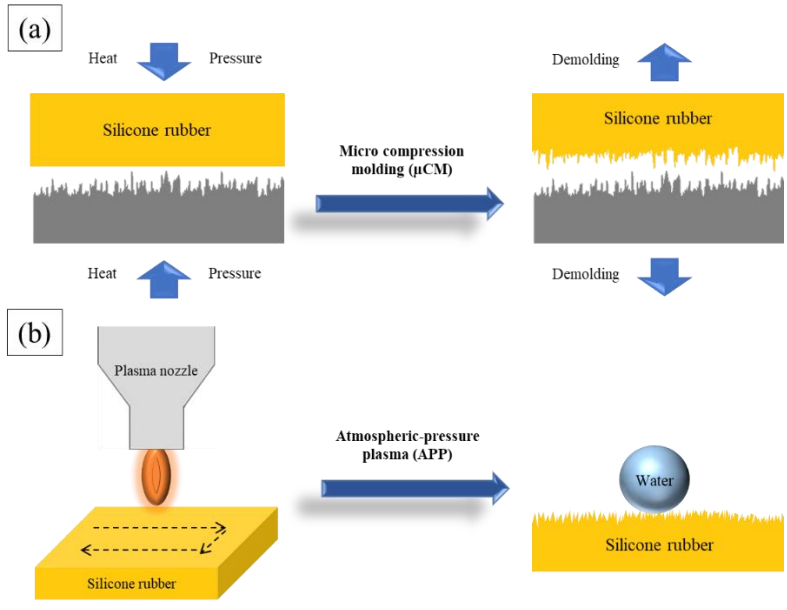

Figure 4.1. Schematic of the (a) micro compression molding (µCM) and (b) atmospheric pressure plasma (APP) techniques to create a micro-nanostructured silicone rubber surface.

4.3.2 Surface characterization

A Kruss™ DSA100 goniometer determined the WCA and CAH at 25 ± 0.5 °C. We deposited a 4-µL water droplet onto the sample surface to determine the WCA using the Young-Laplace approximation. The

CAH equaled the difference between the advancing and receding contact angles when the water droplet moved across the surface. To ensure accuracy and reproducibility, we measured the angles at five points on each sample; the average and standard deviation of the measurements are reported. We relied on scanning electron microscopy (SEM) (JSM-6480 LV SEM manufactured by JEOL Japan) to observe the produced surfaces, and we applied a thin layer of gold-palladium alloy coated on the silicone surfaces to enhance imaging quality. An optical profiler (Profil3D Filmetrics, USA) measured surface roughness. The line and area roughness values were calculated based on the ASME B46.1 2D and ASME B46.1 3D standards, respectively. To analyze the chemical functions on the surface based on an evaluation of the surface chemical composition, we ran Fourier transform infrared spectroscopy (FTIR) using a Cary 630 FTIR Spectrometer (Agilent, USA) in ATR (attenuated total reflection) mode to acquire the highest quality spectra in the infrared range of 400–4000 cm^{-1}. A 4-µL water droplet was observed during the evaporation process, and the images were captured by a digital camera placed on a Kruss goniometer machine. The camera images were set at 8× magnification. The software (DSA1 v 1.9, Drop Shape Analysis for DSA100) calculated the contact line length and the contact area with the substrate as a function of time. We therefore monitored changes in the contact line length between the droplet and the surfaces. The temperature of all experiments was identical to that used during the WCA tests.

4.3.3 Icephobic properties

The WCA of surfaces at below-zero temperatures as well as the freezing delay times were determined in the cold chamber of the Kruss™ DSA100 goniometer where sample stage temperature can reach -30 °C with a control precision of 0.1 °C. We determined the ice adhesion strength of the produced samples via two separate methods to obtain a comprehensive comparison of the icephobic properties under various conditions.

For the centrifuge test, samples were iced under freezing drizzle conditions in a climatic chamber at -8.0 ± 0.2 °C by spraying supercooled water microdroplets onto the surfaces. Such conditions resulted in the deposition of glaze ice from the water droplets, having a median volumetric diameter (MVD) of 324 µm on an 1100 ± 70 mm^2 surface and a thickness of around 7 ± 1 mm. Droplet speed corresponded to their free-fall values in the vertical airflow. The samples were iced for about 35 minutes to obtain around 5.5 ± 0.5 g of ice. All samples were iced simultaneously. The iced samples were tested individually in a centrifuge placed in a climatic chamber at -10.0 ± 0.2 °C. The centrifugal force (F) was calculated as $F = mr\omega^2$, using the detached

ice mass (m), the speed at which the detachment occurred (ω), and the beam radius (r). The ice adhesion shear stress was then calculated as $\tau = F/A$, where A is the iced area. The reduction in ice adhesion was defined as [τ (pristine silicone rubber) - τ (superhydrophobic silicone rubber)]/ τ (pristine silicone rubber).

In the push-off test, a thin 1-cm diameter cylindrical plastic mold was placed onto the substrate. We then filled the mold with deionized water and placed the mold and substrate into a cold chamber at -10.0 ± 0.2 °C for 24 h to form an ice cylinder. We placed the test sample onto the holder and fixed the sample using two screws. A remote computer-controlled interface then controlled the turning of the screws at a fixed rate of 0.05 $mm \cdot s^{-1}$ so that the sample holder was pushed gradually toward the force gage. The force gage measured the shear force ten times per second until the ice detached. The adhesion stress was therefore calculated knowing the maximum force and the icing area. We calculated the corresponding de-icing energy for each surface using the area under the developed force-displacement curves.

4.3.4 Durability properties

We used an Elcometer 3000 Clemen Unit (Elcometer, USA) with 4000-grit silicon carbide sandpaper to evaluate the durability of the superhydrophobic surfaces against abrasion. The applied pressures on the samples' surfaces during abrasion were 1.6 kPa, 3.2 kPa, and 6.4 kPa. We ran the process repeatedly over 2.5 cm of the surface. We measured the WCA and CAH after each block of 50 abrasion cycles.

We also evaluated the durability of the produced silicone rubber surfaces via a finger-press test where a vertical pressure of 80 ± 8.8 kPa was applied to the surface by a bare thumb. We also carried out a tape-peeling test by applying and removing a pressure-sensitive Scotch-600 tape at approximately 30 kPa pressure to the surface. To test surface durability when subjected to ultrasonication, the surfaces were placed into 100 mL of deionized water in a Branson 2510 ultrasonication bath. After each 60-min interval, we removed the sample, dried the sample for 15 min at 70 °C, then measured the CA. In the continuous water droplet impact durability test, water droplets produced at a rate of 1 $mL \cdot min^{-1}$ from a distance of ~10 cm above the surface fell onto the surface that was placed at a slope of ~5°. The impact point was marked for WCA measurements. Each cycle required 1000 s, during which time ~17 mL water dropped onto the surface. The test ran for 7000 s, i.e., ~120 mL of water in total.

We used buffer solutions having a pH of 2 and 12 as the acidic and alkaline media and used also deionized water (pH 7) to study the durability of the produced surfaces over 15 days. After a 3-day interval, we removed each sample from the solution, rinsed the sample ultrasonically for 15 min, dried the sample at 70 °C for 15 min, and we then measured the WCA and CAH. We used a QUV accelerated weathering tester for the accelerated UV-weathering test to evaluate the destruction of the surface anti-wetting properties when subjected to simulated outdoor conditions within a controlled laboratory setting. The tests were conducted according to ASTM G154 using UVA-340 fluorescent lamps and a test cycle of 8 h, a temperature of 60 °C, and an irradiance of 0.89 $W \cdot m^{-2}$.

Given the extensive use of high-temperature vulcanized (HTV) silicone rubber in high-voltage insulators, it is relevant to assess the durability of our produced surfaces against harsh weather conditions, e.g., sandstorms. We sandblasted our samples in a sandblasting cabinet under conditions of air blow pressure at 20 psi, an air blower velocity of 10 m/s, a sand feed of 0.07 g/s—thus 4.2 g of sand blown onto the surface after 1 min of air blowing. This amount corresponds to a single sandstorm in Borg-El-Arab, Egypt. Given that approximately 20 sandstorms occur per year at this location, a 20-min test simulates one year of exposure to sandstorm conditions [313]. The distance between the gun and the sample surface was 25 cm, and the impact angle was set at 90°. We used silicon carbide (SiC) particles to conduct the tests. During a sandstorm, the height to which sands and dust can reach depends on wind strength and the amplitude of wind velocity fluctuations. This height thus varies from 1 m above the ground to 15.24 m. However under similar conditions, dust or finer sediments (<63 µm) are lifted higher than coarse sand (>63 µm) [314]. On the other hand, a typical height of an electrical transmission tower is 15–50 m; we therefore used a particle size of 18 µm for the test.

4.4 Results and discussion

4.4.1 Surface characterization

The WCA and CAH of the pristine silicone rubber surface were 115° ± 1.8° and 43.4° ± 1.9°, respectively. A WCA of 166.6° ± 1.9° and 165.8° ± 1.3° and CAH of 0.6° ± 0.3° and 1.1° ± 0.6° for the µCM and APP-treated silicone rubber surfaces, respectively, testified to the superhydrophobic property of the produced samples. The presence of micro-nanostructures on the silicone surfaces satisfied the required condition of "low surface energy material and surface roughness" to achieve superhydrophobicity. The surface

profiles and SEM images of the surfaces at various magnifications are presented in Figure 4.2. Surface morphologies differed for each surface. Both 1D roughness (line roughness) and 2D roughness (area roughness) values were reported for comparative purposes (Table 4.1). Compared to a pristine surface, the micro compression molding process significantly increased surface roughness. The root-mean-square height (S_q) of the μCM surface increased ~5 times. Although the APP-treated surface possessed almost the same S_q as the pristine surface, the skewness and kurtosis values showed jagged surface structures with considerably higher peaks and lower valleys than those on the pristine surface.

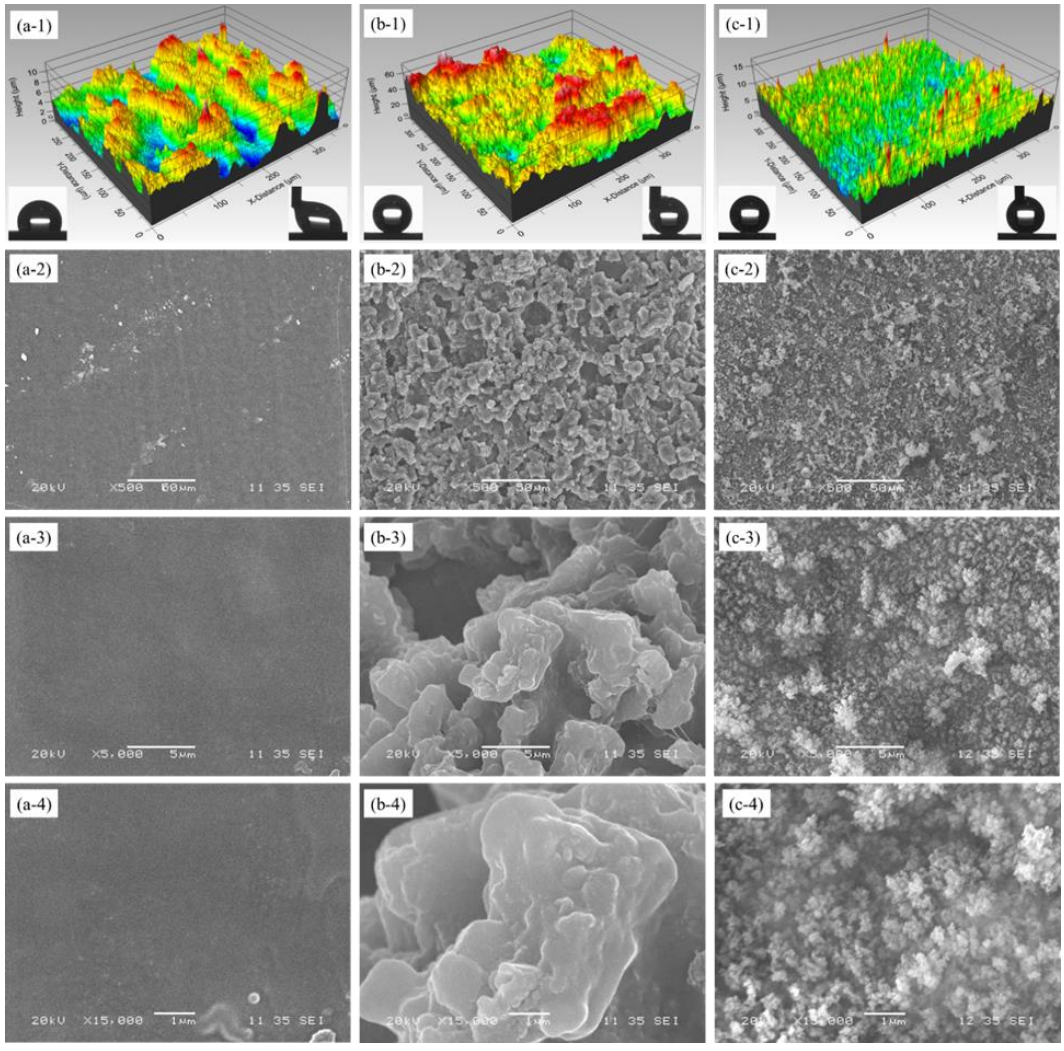

Figure 4.2. The 3D surface profiles of the (a-1) pristine, (b-1) μCM, and (c-1) APP-treated silicone rubber surfaces. SEM images of the (a-2, a-3, and a-4) pristine, (b-2, b-3, and b-4) μCM, and (c-2, c-3, and c-4) APP-treated silicone rubber surfaces. Inset images represent the water contact angle and contact angle hysteresis of the corresponding surfaces.

Table 4.1. Area and line roughness values obtained from profilometry analysis

	Pristine	**µCM**	**APP**
Area roughness (µm)			
Maximum peak to valley height (S_t)	11.68	71.54	16.38
Arithmetic mean height (S_a)	1.46	7.43	1.19
Root mean square height (S_q)	1.76	9.40	1.53
Skewness (S_{sk})	0.07	0.09	0.33
Kurtosis (S_{ku})	2.38	3.008	3.99
Line roughness (µm)			
Maximum peak to valley height (R_t)	5.196	15.16	5.79
Arithmetic mean deviation (R_a)	0.70	2.54	0.70
Root mean square deviation (R_q)	0.89	3.17	0.91

FTIR analysis assessed the presence of chemical bonds on the produced silicone rubber surfaces (Figure 4.3). The pristine and µCM surfaces showed identical absorption spectra of Si–$(CH_3)_2$, Si–O–Si, Si(CH_3), and –OH at the approximate positions of 805–855 cm^{-1}, 1000–1110 cm^{-1}, 1245–1275 cm^{-1}, and 3200–3550 cm^{-1}, respectively. For the APP-treated surface, the Si-containing bonds, in particular for Si–$(CH_3)_2$, were modified. Under plasma treatment, the Si–CH_3 bonds are prone to breakage due to their relatively low binding energy [315]. Moreover, the –OH spectrum almost vanished. The disappearance of hydroxyl groups (–OH) is attributed to the endothermic decomposition of alumina trihydrate (ATH) particles at high temperatures during the plasma treatment [312].

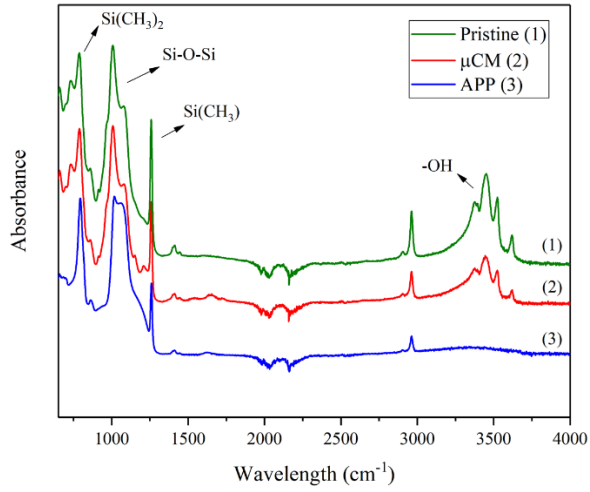

Figure 4.3. FTIR spectra for (1) pristine, (2) µCM and (3) APP-treated silicone rubber surfaces.

The CAH values of the produced superhydrophobic surfaces demonstrated that the created roughness led the surfaces to fall into a Cassie-Baxter state. However, we then carried out the droplet evaporation test to obtain more information about the kinetics of the interfacial interactions. Evaporation occurs due to the diffusion and/or convection of water molecules into the environment. Three modes of evaporation explain the changes in the WCA and contact line (CL) of a water droplet on a solid surface in calm air. Depending on the WCA or CL being constant or decreased, the modes are the constant contact line (CCL), the constant contact angle (CCA), and mixed modes. The emergence of each mode depends highly on surface geometry and chemistry, which directly influences the wetting regimes [316].

Figure 4.4 presents the evolution of WCA and CL due to the evaporation of small water droplets placed on hydrophobic and superhydrophobic surfaces. On the superhydrophobic surfaces, the water droplets underwent a linear decrease in CL and a gradual reduction of CA. These observations showed the mobility of the CL due to the low CAH of the superhydrophobic surfaces. Over time, the water droplet preserved its initial marble-like shape by which a consistent Cassie-Baxter regime could be confirmed [317]. On the pristine surface, however, the steep slope of WCA reduction, with the increase in CL during the first stages of evaporation, and followed by a sharp drop at later stages, indicated the high adhesion of the water droplet to the solid surface. The greater adhesion of the droplet to the pristine surface relative to its adhesion to the superhydrophobic surfaces caused greater evaporation from the upper portion of the droplet on the pristine surface rather than along the triple liquid/solid/air line. This causes the droplet to be flattened on the surface, thereby leading to a decreased WCA for the pristine surface. Moreover, the pinned CL of the pristine surface

over the mobile behavior of the CL on the superhydrophobic surfaces led to a different water droplet duration. The longer duration of a water droplet on a superhydrophobic surface, relative to that on a pristine surface, resulted from the high aspect ratio of the droplet, which led to a longer thermal resistance path, and the low effective thermal conductivity of the surface due to the presence of air pockets [318]. Moreover, three possibilities exist for water droplet evaporation on superhydrophobic surfaces. Evaporation can occur from the upper portion of the droplet, from the triple line, and from the contact line. The latter causes the presence of a water gas phase within the structures of the superhydrophobic surfaces. Comparing the behavior of the water droplet on the µCM and APP-treated superhydrophobic surfaces over time revealed that the presence of larger structures on the µCM surface facilitated a greater contact between the water liquid phase and water gas phase trapped within the surface structures. Consequently, the WCA of the µCM surface experienced a greater reduction than that of the APP-treated surface over time.

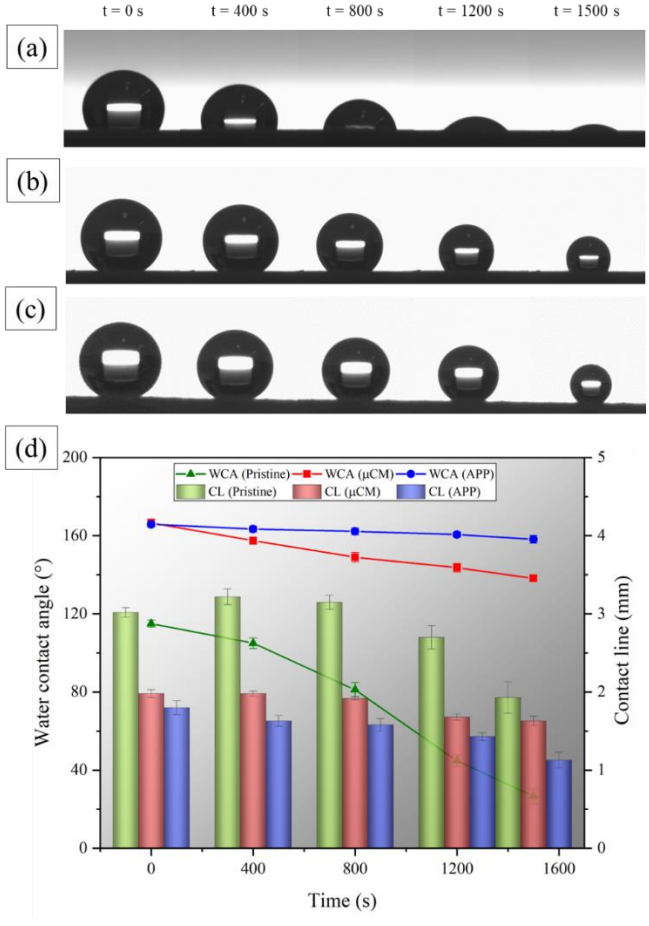

Figure 4.4. Images of droplet evaporation on (a) pristine, (b) µCM, and (c) APP-treated silicone rubber surfaces. (d) Changes to the water contact angle and contact line over time for each surface.

4.4.2 Icephobic properties

In the development of icephobic surfaces, two main properties are usually considered: anti-icing and de-icing. Anti-icing refers to a property of surface to delay or reduce ice accretion, whereas the de-icing approach is attributed to the removal of formed ice on the surface [319]. The anti-icing property of the produced surfaces was examined through the measurement of the WCA at below-zero temperatures and the freezing delay. The de-icing property, however, was examined using measurements of the ice adhesion strength based on the centrifuge and push-off tests.

4.4.2.1 Anti-icing property

To assess the behavior of the produced surfaces at supercooled temperatures, we measured the variation of WCA at various temperatures (Figure 4.5(a)). The WCA decreased for all surfaces at below-zero temperatures. This decrease was expected and can be attributed to water surface tension at low temperatures [235]. At low temperatures, the surface tension of the water droplets strengthens, thus leading to an increase in the internal pressure of a droplet and may provoke a transition from a Cassie-Baxter to a Wenzel regime [320]. The APP-treated surface displayed a relatively higher WCA than that of the µCM surface at freezing temperatures. This difference can be attributed to the better functionality of the lower surface roughness on the APP-treated surface compared to µCM surface roughness in the Cassie-to-Wenzel transition at freezing temperatures. A close inspection of the curve slope of each surface revealed that the WCA of the APP-treated surface decreased slower than that of the WCA for the µCM surface at temperatures between 15 and -10 °C. However, below -10 °C, the WCA of both surfaces decreased monotonically due to the increased internal pressure of the droplet and a possible wetting regime transition.

We also determined the delay in freezing onset, i.e., the initiation of water droplet freezing on the surface, for the produced surfaces. We present the results of freezing delay for three temperatures: -15 °C, -20 °C, and -25 °C (Figure 4.5(b)). We did not consider the freezing delays at -5 °C and -10 °C given that they were too long for this experiment. We observed a marked delay in freezing on the superhydrophobic surfaces due to the presence of micro-nanostructures when compared to the pristine surfaces, which lack these structures. As an initial explanation of such behavior is the reduced contact area between the water droplet and the surfaces when WCA is high. As such, the thermal conductivity decreased dramatically for

superhydrophobic surfaces compared to the pristine surface. In addition, the delay in freezing time stemmed from the micro air pockets trapped between the surface asperities to therefore act as a thermal barrier. Consequently, the formation of micro-nanostructures on the superhydrophobic surfaces led to less heat dissipation than observed from the smooth pristine surface [270]. Therefore, the greater the volume of a trapped air pocket, the longer the freezing delay. Using the profilometry technique, we determined that, compared to the pristine surface, the µCM and APP-treated surfaces entrapped 14.2× and 4.7× more air, respectively, within their surface structures. At -15 °C, the µCM surface showed a ~40% greater delay in freezing time compared to the APP-treated surface that had a relatively greater abundance of nanostructures. This difference was most significant at -25 °C. As for the µCM surface, the freezing delay time was ~2.5× greater than that of the APP-treated surface. This illustrates that surface roughness has a more considerable contribution to the freezing process at lower temperatures.

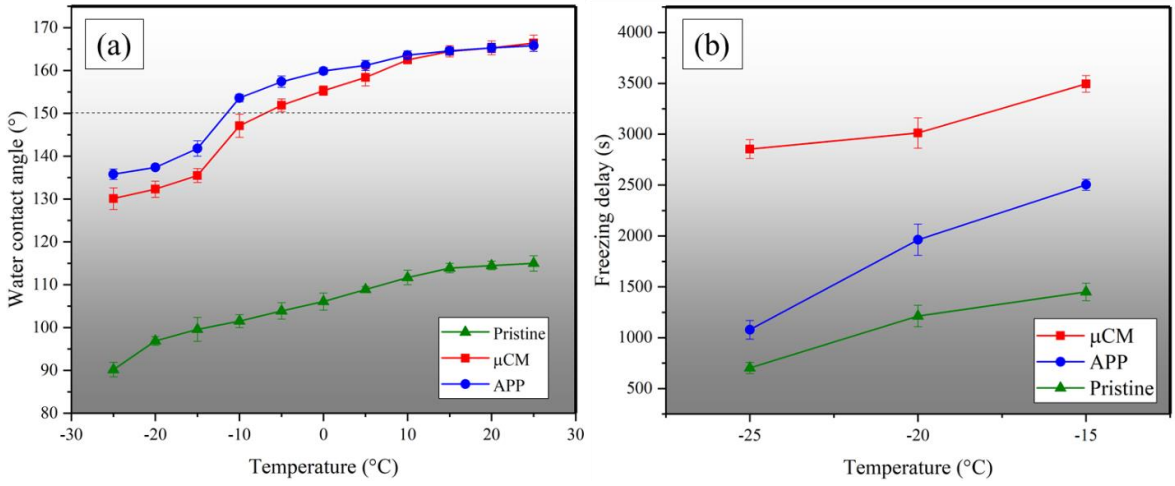

Figure 4.5. (a) Variation in water contact angle and (b) freezing delay at various temperatures for the pristine, µCM, and APP-treated surfaces (the dashed line in (a) shows the threshold of superhydrophobicity).

4.4.2.2 De-icing property

Through the push-off test, it was observed that both superhydrophobic surfaces reduced ice adhesion strength. While de-icing of the pristine surface required a pressure of 132.8 kPa, the µCM and APP-treated surfaces required only 90.1 kPa and 32.9 kPa, respectively, to become de-iced during the first icing/de-icing cycle (Figure 4.6(a)). The energy required for de-icing the pristine surface was ~30 mJ, whereas the µCM and APP-treated surfaces required only 8.75 mJ and 0.51 mJ, respectively (Figure 4.6(b)). Regarding the shape of the produced curves (Figure 4.6(b)), it can be concluded that the pristine and µCM surfaces showed the same

behavior when de-icing, the plastic deformation of ice [190]. In this case, the applied force to the ice pillar increases gradually until the force overcomes the adhesion force between the ice and top of the surface structures and detaches the interlocked ice from the surface asperities. The lower force required for the μCM surface, relative to the pristine surface, relates to the lower ice-surface contact area due to the higher WCA of the μCM surface and less interlocked ice between the surface asperities. However, the APP-treated curve showed a very different behavior, i.e., elastic deformation. A sudden jump in the curve was observed at the de-icing point showing that the amount of interlocked ice was negligible, and the applied force was only required to overcome the adhesion of ice to the top of the features [190]. Moreover, the creation of nano-cracks (initiated from nanostructures acting as points of stress concentration) during ice detachment was more probable on the APP-treated surface to facilitate ice removal. Thus, there is a similarity between the de-icing behavior of the pristine and μCM surfaces, a behavior that is in sharp contrast with that of the APP-treated surface.

The push-off test was repeated seven times on each surface to assess the durability of the surfaces under repetitive icing/de-icing cycles. The ice adhesion strength of the μCM surface did not necessarily increase (Figure 4.6(c)), and in some cases, ice adhesion strength was even lower after the first cycle of the test, e.g., cycles 2 and 5. This testifies to the durability of the μCM surface micro-nanostructures during the de-icing process. The ice adhesion strength of the APP-treated surface, on the other hand, increased gradually after the 4^{th} cycle, related to the removal of nanostructures during ice detachment (discussed in detail below).

We observed almost identical trends when the centrifuge tests assessed ice-covered surfaces under conditions of freezing drizzle (Figure 4.6(d)). The pristine silicone rubber surface showed an ice adhesion strength of about 120 ± 3.6 kPa; both superhydrophobic surfaces reduced the ice adhesion strength. The adhesion strength of the μCM surface did not significantly increase (even at the 6^{th} cycle, the ice adhesion strength remained low), while that of the APP-treated surface increased significantly through the seven icing/de-icing cycles. Thus, ice adhesion to the μCM surface depended highly on the probability that ice interlocked into the surface structures, while the increased ice adhesion strength of the APP-treated surface stemmed from the gradual deterioration of nanostructures. The SEM images of the surfaces after the 7^{th} icing/de-icing cycle are shown in Figure AII. 1.

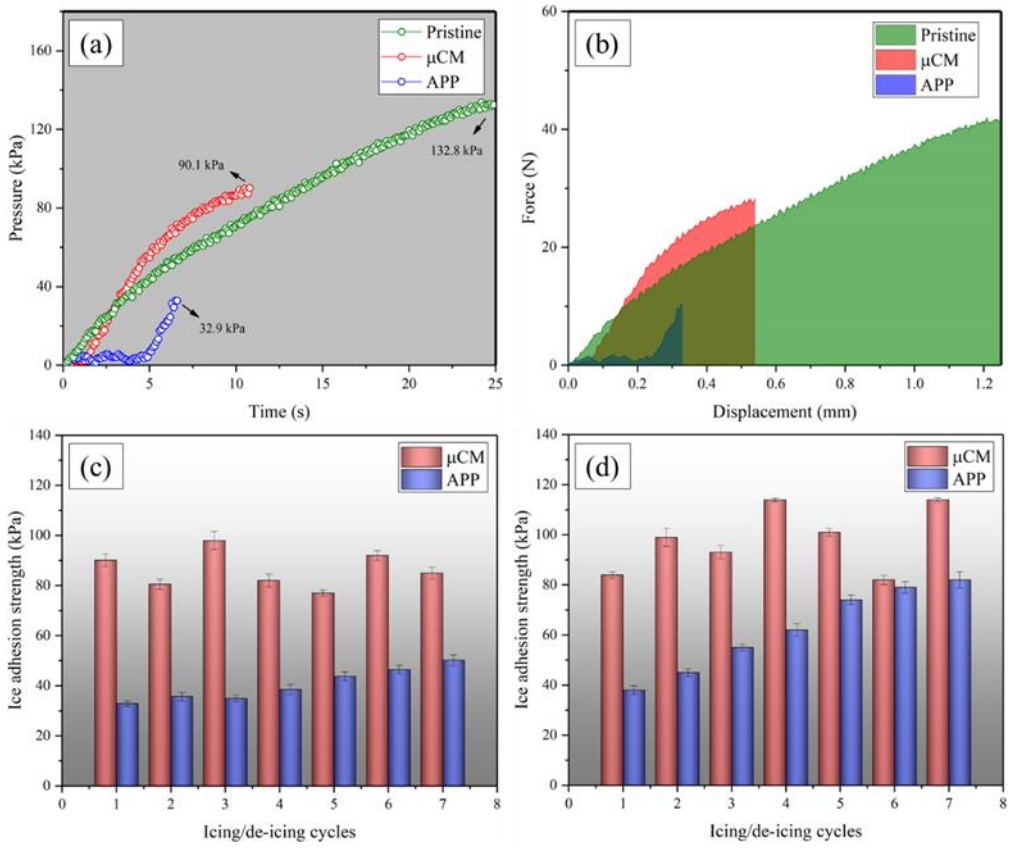

Figure 4.6. (a) De-icing pressure required for surfaces in the push-off test and (b) the corresponding de-icing energy of each surface. Ice adhesion strength for repetitive icing/de-icing cycles for the (c) push-off and (d) centrifuge tests.

Compared to the untreated silicone rubber surface, ice adhesion reduction varied between ~26% and ~42% for the µCM surface and decreased ~75% to ~62% for the APP-treated surface over seven icing/de-icing cycles in the push-off test (Table 4.2). In the centrifuge test, the ice adhesion strength decreased ~30% for the µCM surface and ~68% for the APP-treated surface after the first cycle (Table 4.2). The APP-treated surface showed a better de-icing property at each cycle although also showed a significant loss of its de-icing properties, whereas the µCM surface exhibited a lower reduction in ice adhesion but showed a greater durability against repetitive icing/de-icing cycles. The ice adhesion reduction factor (ARF) values—usually reported according to the ice adhesion strength of bare aluminum—offer a better understanding of the de-icing properties of the produced surfaces (Table AII. 1)

In terms of the de-icing properties of surfaces having hierarchical micro-nanostructures, surfaces having a lower surface roughness produced a lower ice adhesion. This relates to the interlocking of ice into the surface structures, which can result in enhanced adhesion strength. Davis et al. [321] observed that among three

surfaces having arithmetic mean surface roughness values of 8.7 µm, 2.7 µm, and 1.6 µm, the lowest ice adhesion strength was obtained for the surface having the lowest surface roughness. A comparison of the root mean square height (S_q) of the µCM and APP-treated surfaces (9.40 and 1.53, respectively) confirms this observation. However, higher surface roughness can improve surface durability against repetitive icing/de-icing cycles.

Table 4.2. The ice adhesion reduction values for the µCM and APP-treated surfaces during the push-off and centrifuge tests.

Ice adhesion reduction (%)	**Icing/de-icing cycles**		**1**	**2**	**3**	**4**	**5**	**6**	**7**
	push-off	µCM	32.3 ± 1.9	39.5 ± 2.3	26.3 ± 2.9	38.3 ± 1.9	42.1 ± 2.3	30.8 ± 1.9	36.1 ± 1.7
		APP	75.3 ± 1.7	73.2 ± 1.9	73.8 ± 2.6	71.0 ± 1.9	67.1 ± 1.3	65.0 ± 2.3	62.2 ± 1.7
	centrifuge	µCM	30.0 ± 1.3	17.5 ± 3.6	22.5 ± 2.7	15.0 ± 0.7	15.8 ± 1.6	31.7 ± 1.9	15.0 ± 0.7
		APP	68.3 ± 1.7	62.5 ± 1.7	54.2 ± 1.3	48.3 ± 2.6	38.3 ± 1.9	34.2 ± 2.3	30.8 ± 3.3

The differing results of the two measurement methods for ice adhesion (push-off test and centrifuge test) may stem from a difference between the type of ice formed in each test. In the push-off test, a non-impact bulk ice forms on the surface by placing a water pillar on the surface, and the icephobic behavior of the surfaces depends highly on the Cassie-Baxter consistency during the icing process. If the micro-nanostructures resist the penetration of water into the surface asperities before icing, a non-interlocked ice (Cassie ice) can form on the surface and produce a low ice adhesion strength. However, in the centrifuge test, the surfaces were covered with glaze ice produced by freezing drizzle; freezing drizzle represents one of the most severe icing conditions where the supercooled microdroplets can penetrate the surface structures. Therefore, the ice adhesion strength in the centrifuge test depended highly on the icing condition parameters, particularly the MVD [45]. The APP-treated surface, with reduced surface roughness, resisted the penetration of water microdroplets (size of 324 µm), whereas the water microdroplets could penetrate partially into the µCM surface structures producing a higher ice adhesion strength. The WCA and CAH of the produced surfaces were measured after the 7th cycle of icing/de-icing in both the push-off and centrifuge tests (Table AII. 2). Both surfaces presented a high WCA and low CAH to demonstrate the stability of water repellency after multiple icing/de-icing cycles. The

photographs of each surface at the 1st and 7th icing/de-icing cycles after ice accumulation and ice removal in the centrifuge test are presented in Figure AII. 2. In the 1st cycle, the spherical shape of supercooled water droplets freezing on the superhydrophobic surfaces highlighted the water-repellent property at a freezing temperature. This was not observed for the pristine surface. The rounded shape of the formed ice on the APP-treated surface at the 7th cycle illustrated its most favorable water-repellent property.

4.4.3 Durability properties

We investigated the durability of the produced superhydrophobic surfaces through various mechanical and chemical tests that represent the real-life applications, including abrasion using sandpaper, a finger-press test, a tape-peeling test, sandstorm simulation, ultrasonication treatment, continuous water droplet impacts, immersion in chemical solutions, and exposure to UV-light radiation. We closely monitored and recorded the WCA and CAH of the samples to study the capacity of a surface to recover its superhydrophobicity, where applicable.

4.4.3.1 Mechanical durability

The sandpaper abrasion test of superhydrophobic surfaces is effective for evaluating mechanical durability; however, studies often stop abrasion cycles before any deterioration of superhydrophobicity [215, 322, 323]. Here, we maintained the cycles once the superhydrophobic properties began to deteriorate to provide a thorough understanding of mechanical stability. The superhydrophobic properties of the µCM surface were not lost (WCA >150°) even after 300 abrasion cycles for abrasion pressures of 1.6 kPa and 3.2 kPa (Figure 4.7). However, the CAH increased to >10° after 250 cycles. Under these same conditions, i.e., abrasion pressures of 1.6 kPa and 3.2 kPa, the WCA of the APP-treated surfaces fell below 150° after 200 and 150 cycles, respectively. The CAH became >10° after 100 cycles. Increasing the abrasion pressure to 6.4 kPa, which is a relatively high pressure for any abrasion test, the µCM surface maintained its WCA >150° after 200 cycles, whereas the APP-treated surface showed a WCA <150° after 100 cycles. The CAH of the µCM surface increased to >10° after 100 cycles, whereas that of the APP-treated surface showed a CAH of ca. 20° after 50 cycles. This observation relates to the fast deterioration of surface micro-nanostructures under such high abrasion pressure.

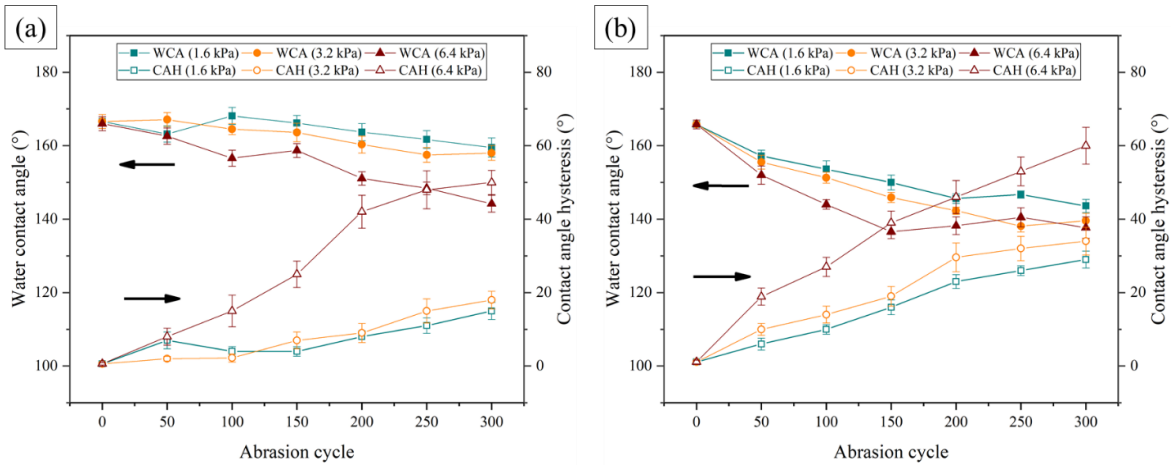

Figure 4.7. Water contact angle and contact angle hysteresis as a function of abrasion cycles using various abrasion pressures for (a) μCM and (b) APP-treated surfaces.

SEM images of the surfaces after being abraded for 300 cycles using sandpaper (Figure 4.8) illustrate the decreased micro-nanostructures on the surface after the abrasion process. When comparing surfaces abraded using pressures of 3.2 kPa and 6.4 kPa, we observed that the greater the abrasion pressure, the more the surface asperities wore out. Higher abrasion pressures produced flatter surfaces and removed the microstructures. The red outlines in Figure 4.8 illustrate areas where structures were lost due to abrasion, while the yellow outlines denote areas where the structures remained intact or less severely damaged. A greater number of yellow areas are present in samples subjected to 3.2 kPa abrasion pressures, explaining the relatively high WCA, whereas the greater number of red shapes in the sample abraded at 6.4 kPa indicates the flattened structures and, therefore, explains the reduced WCA and increased CAH.

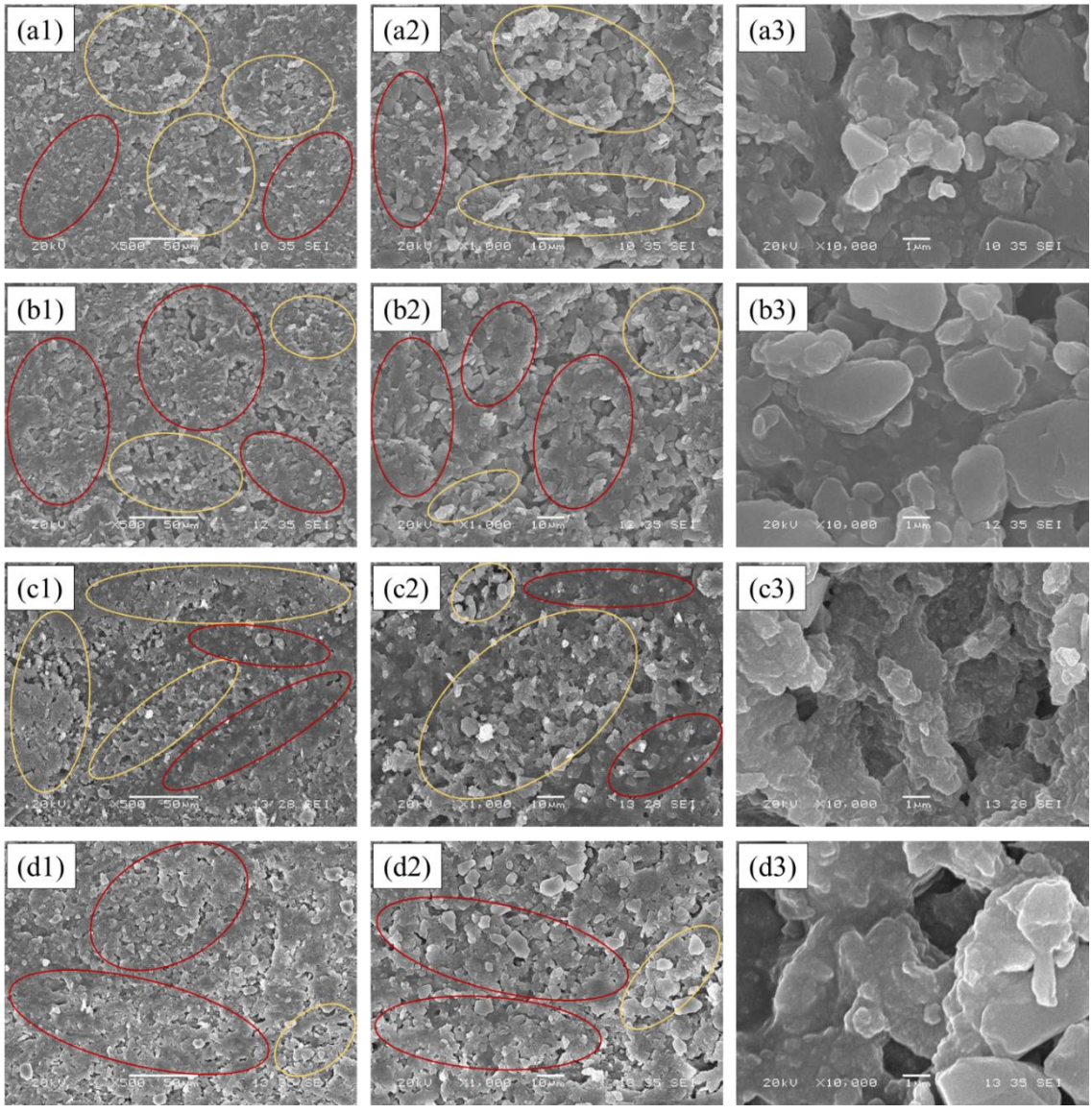

Figure 4.8. SEM images at various magnifications of (a1-a3) µCM surfaces abraded at 3.2 kPa pressure, (b1-b3) µCM surface abraded at 6.4 kPa pressure, (c1-c3) APP-treated surface abraded at 3.2 kPa pressure, and (d1-d3) APP-treated surface abraded at 6.4 kPa pressure.

We measured the WCA of both surfaces abraded at 6.4 kPa at regular intervals to determine the recovery of surface superhydrophobicity (Figure AII. 3(a)). The WCA of the µCM surface increased constantly up to 20 days after the tests, and it thereafter remained unchanged at the value of ~157°. For the µCM surface (an initial WCA of 166.6°), the recovery capability of the silicone surface was significant. The WCA of the APP-treated surface (an initial WCA of 165.8°), however, showed a slight increase after the first 10 days post-test and then remained at an almost constant value of ~143°, showing non-superhydrophobic behavior. During the abrasion test, the asperities may undergo two changes. First, the microstructures and nanostructures are worn

out as they are vulnerable to abrasion. This type of deformation is not reversible, which explains the permanent deterioration of CAH—CAH did not change considerably after the tests and remained >10° even after 50 days of rest for both prepared surfaces. Second, as the complete wearing of microstructures is less possible than the full loss of nanostructures, the microstructures are bent and stretched under pressure and drag forces. Therefore, there is a possibility of recovery due to the elastic properties of silicone rubber asperities, where microstructures can return upright and recover their initial position with time.

We also examined the durability of the produced silicone rubber surfaces via a finger-press test where we applied a pressure of 80 ± 8.8 kPa to the surfaces using a bare thumb (Figure 4.9(a)). This test can mimic human handling of a material to test whether a superhydrophobic surface can be suitable for commercial use. In addition to mechanical damage, a bare finger-press also adds salt and oil contaminants to the surface. Therefore, the finger-press test can both physically and chemically affect a superhydrophobic surface [200]. In our finger-press tests, the μCM surfaces degraded more than the APP-treated surfaces. Although the WCA of both surfaces decreased almost similarly and remained at >150° after 50 cycles (APP-treated showed a slightly more durable behavior), the CAH of the μCM surfaces increased markedly after 10 cycles, whereas the CAH of the APP-treated surface remained <10° even after 50 finger-press cycles.

The increase in WCA after a single day of recovery following the finger-press test was an important result (Figure AII. 3(b)). The WCA of the finger-pressed μCM surface increased from 148.5° to 164.2°, while the WCA of the APP-treated surface increased from 152.8° to 155.9°. The micro-nanostructured silicone asperities could therefore return to their initial position after the finger force was released due to the rubber elasticity. These post-pressure behaviors are explained by the different micro-nanostructures on the surfaces. A portion of the WCA loss can also be attributed to the added salt and oil contaminant from thumb to the surface. As such, some of the observed WCA recovery can be related to the migration of LMWS to the surface and covering the contamination molecules transferred to the surface by the thumb. Finally, after 10 days of recovery, the CAH of the μCM surface attained 9° (while the graph plateaued after Day 8). The CAH of the APP-treated surface did not show any significant change.

The tape-peeling test involved applying and removing a pressure-sensitive Scotch-600 tape with approximately 30 kPa pressure to the surface. According to Wang et al. [198], this pressure is much larger than

the pressure described in the standard test method for measuring adhesion by the tape test. In terms of the pressure placed onto the surface, this test combines the effects of the finger-press test and the adhesion test, as though the sample underwent 50 cycles of the finger-press test and tape-peeling test simultaneously. After 50 attach-detach cycles, both surfaces remained superhydrophobic with a WCA >160° and a CAH < 6° (Figure 4.9(b)).

In ultrasonication, the energy is applied by waves at an ultrasonic frequency (>20 kHz) within a liquid media. This energy can damage a surface lacking a strong physical morphology or a strong chemical bonding with the substrate [200]. The μCM surface was durable against long-term ultrasonication. After 4 h of continuous ultrasonication, the WCA of the μCM surface remained at ~160° and the CAH was at ~10° (Figure 4.9(c)), confirming the strong physical micro-nanostructured morphology of the prepared superhydrophobic surface. The APP-treated surface, however, was significantly vulnerable to ultrasonication. The WCA of the APP surface dropped below 150° after 60 min and was ~124° after 4 h. The CAH increased to >20° after 60 min and to ~60° after 4 h. This marked change occurs as nanostructures are removed from the APP-treated surface by the high levels of applied ultrasonic energy (Figure AII. 4).

We investigated the dynamic impact durability of the superhydrophobic surfaces under a liquid phase. This evaluation is very important in terms of the application of produced superhydrophobic surfaces under rain precipitation. We conducted this test using the parameters of ~1 $mL \cdot min^{-1}$ and we ran the test for 7000 seconds, i.e., ~120 mL water impacting a single point of the surface at a speed of 1.4 m/s, a speed equivalent to that of 3.0-mm diameter raindrops [324]. The WCA and CAH remained >150° and <10° after being exposed to a water jet impact, i.e., ~6000 droplet impact events, after 7000 s (Figure 4.9(d)). A reduction of the surficial anti-wetting properties can be attributed to the partial penetration of water into the surficial hierarchical structures due to the instantaneous pressure exerted on the surface [200].

The dynamic impact durability of the produced superhydrophobic surfaces under a solid phase was also examined. We simulated sandstorm conditions (average particle size of 18 μm) in a sandblasting machine. Each individual surface was exposed to the sand stream at a pressure of 20 psi for 20 min, and we recorded the WCA and CAH every 5 min (Figure 4.9(e)). Both surfaces showed a WCA >150° and a CAH <10° after 20

min of sandblasting (corresponding to a full year of real-life sandstorm events). The SEM images of the sandblasted surfaces are shown in Figure AII. 5.

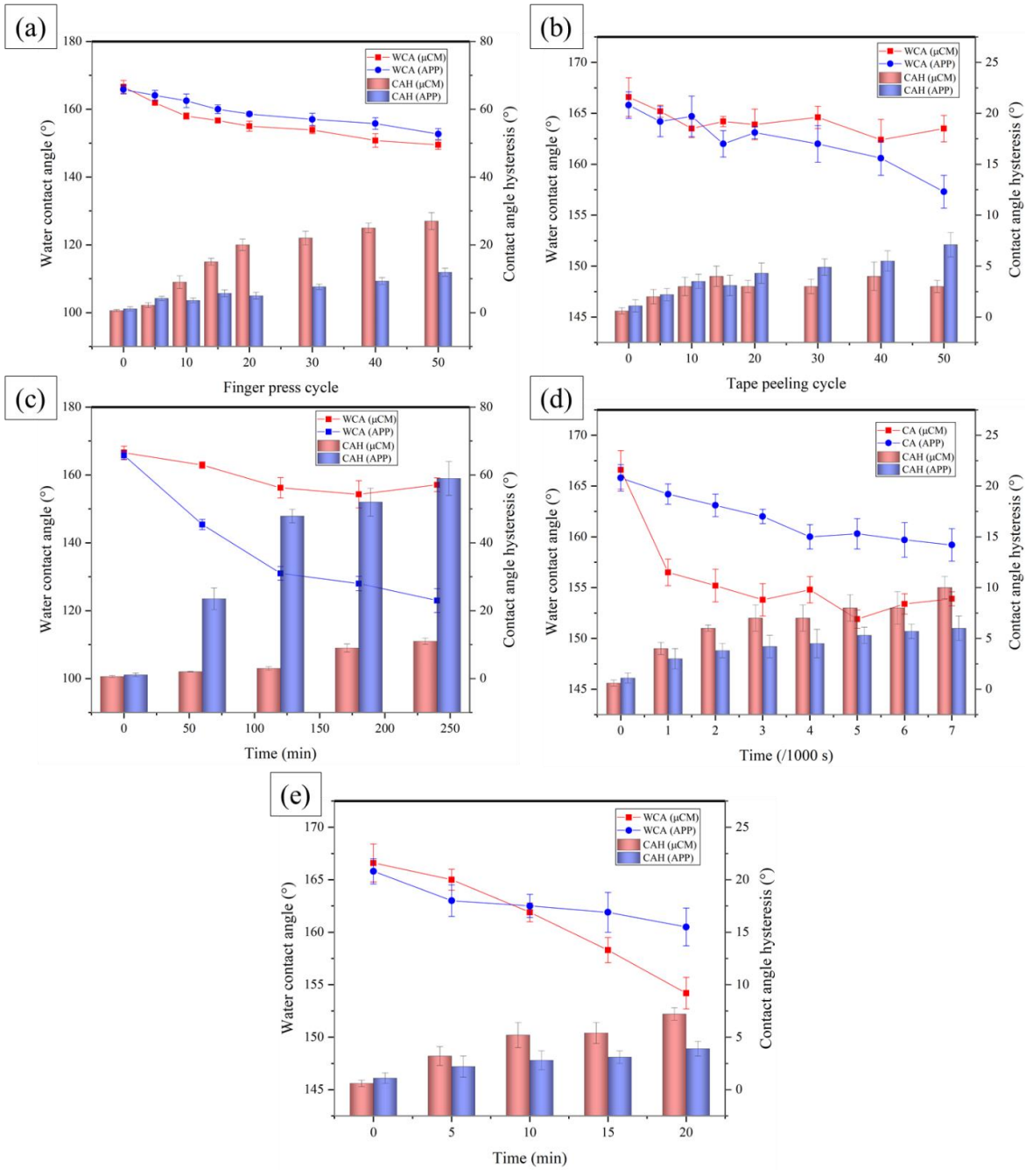

Figure 4.9. Water contact angle and contact angle hysteresis as a function of (a) finger-press cycle, (b) attach-detach cycle, (c) ultrasonication time, (d) continuous water droplet impact time, and (e) sandblasting time for μCM and App-treated surfaces.

4.4.3.2 Chemical durability

We then tested the durability of the produced superhydrophobic surfaces against buffer solutions of pH 2, pH 12, and deionized water of pH 7. After 15 days of immersion in the acidic solution, the WCA of the µCM surface remained >155°, while the CAH increased to 12°; thus, the surface was superhydrophobic with a weak roll-off property (Figure 4.10(a)). The µCM surface in the alkaline solution had a WCA remaining at >160° and a CAH remaining at <5°. The WCA of the µCM surface was >150° and the CAH increased to 30° after 15 days of water immersion. These observations can be attributed to the presence of oxide/hydroxide groups in the vicinity of the solutions for an extended period of time. On the µCM surface, the silicone rubber chains, as well as the ATH particles, react with the acid, base, and water to produce these oxide/hydroxide groups.

The APP-treated surface demonstrated extraordinary durability against the three aqueous media. A WCA >160° and CAH <5° testified to a desirable chemical durability of the APP-treated surface (Figure 4.10(b)). The APP process at elevated temperatures breaks the chemical bonds of the silicone rubber chains, and therefore the surface is mainly covered by silicon oxide [325]. These SiO_2 do not react with the acidic, alkaline, and neutral water media. As such, the SiO_2 acts as a shield to prevent chemical reactions on the APP-treated surface.

Due to the migration of LMWS molecules from the bulk material to the surface and the reorientation of methyl and hydroxyl groups by conformational changes, the optimal WCA and CAH conditions were recovered (Figure AII. 3(c)). This restoration was due to the rotation and movement of the LMWS chains that are thermodynamically driven to the surface to minimize free energy at the surface.

Finally, sunlight radiation is a major cause of damage to materials used outdoors. Hence, the durability of silicone surfaces used for outdoor applications, e.g., electrical insulation, is of great importance. The sun emits ultraviolet, visible light, and infrared waves, ultraviolet waves being the most destructive. The WCA and CAH of the superhydrophobic surface remained >150° and <10° respectively after being exposed to 1200 h of UV light, representing about six years under natural conditions (Figure 4.10(c)). The produced surfaces thus demonstrated resistance against accelerated UV-light exposure. The better performance of the APP-treated surface over that of the µCM surface is due to the silicon oxide layer formed on the surface acting as a shield against UV-light exposure.

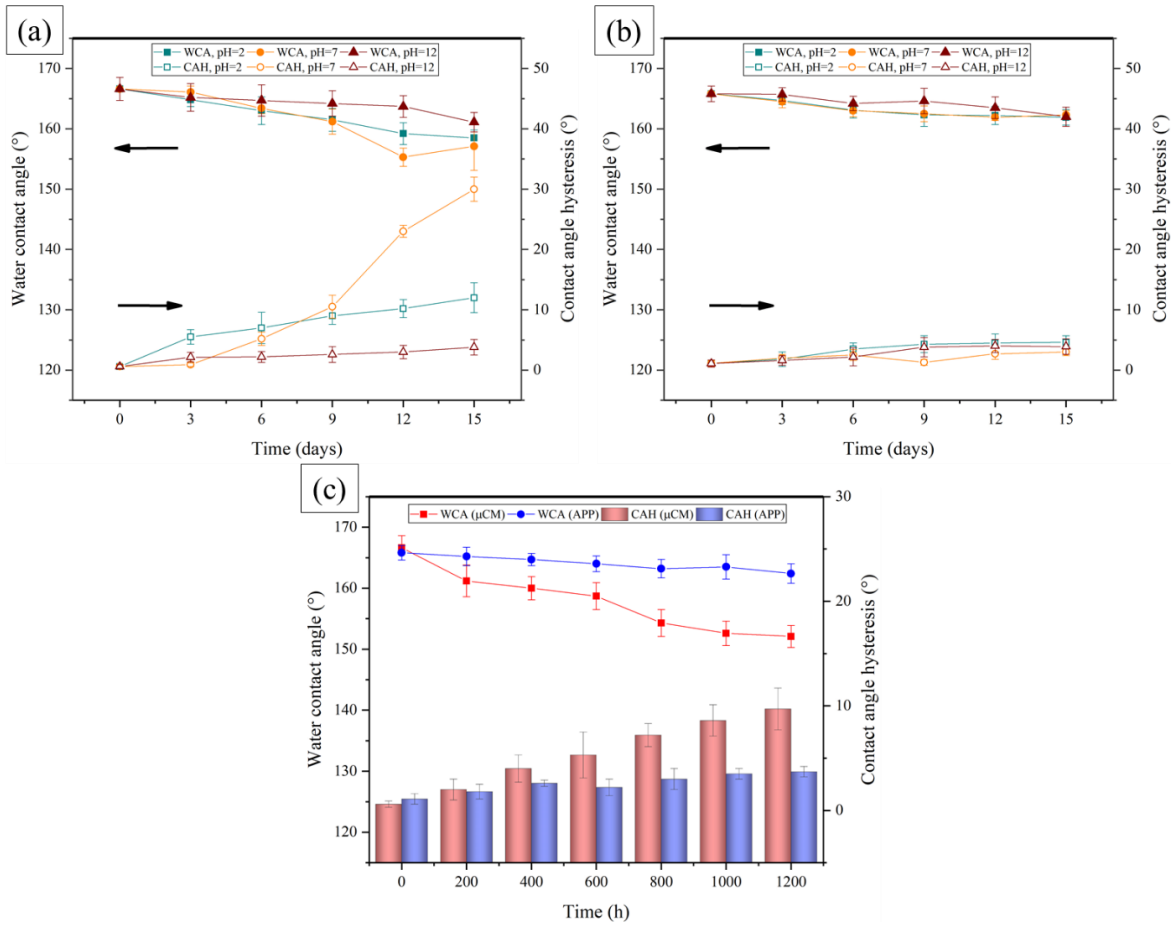

Figure 4.10. Water contact angle and contact angle hysteresis as a function of immersion time (days) in acidic, alkaline, and neutral solutions for (a) μCM and (b) APP-treated surfaces. (c) Water contact angle and contact angle hysteresis as a function of UV-light exposure time for μCM and APP-treated surfaces.

4.5 Conclusions

We produced superhydrophobic silicone rubber surfaces having a WCA >150° and a CAH <10° via straightforward direct replication method using a micro compression molding (μCM) system and a simple treatment by atmospheric pressure plasma (APP). The observed delay in the freezing time of droplets on the produced superhydrophobic surfaces stemmed from the creation of air pockets on their surfaces. The larger micro-nanostructures showed better anti-icing properties as they could trap more air within their micro air pockets. As for the μCM surface, the freezing delay time was ~2.5× more than that of APP-treated surface at –25 °C. Using centrifuge and push-off tests—with corresponding icing conditions of hard rime and bulk ice, respectively—we demonstrated that the produced superhydrophobic surfaces also decreased ice adhesion strength. The mechanism of ice removal for the μCM and the pristine surface was the plastic deformation of ice, while elastic deformation controlled ice removal from the APP-treated surface. Compared to a pristine

silicone rubber, the APP-treated surface (S_q = 1.53 µm) decreased the ice adhesion strength up to 75% in a push-off test and 68% in a centrifuge test, whereas the µCM surface (S_q = 9.40 µm) reduced ice adhesion strength up to 42% in a push-off test and 32% in a centrifuge test. Therefore, for surfaces having hierarchical micro-nanostructures, those surfaces with a lower surface roughness are characterized by a lower ice adhesion strength. The stronger physical bonding between the micro-nanostructures and the bulk material in the µCM surface, however, led to a relatively constant ice adhesion strength throughout repetitive icing/de-icing cycles. The durability of the produced silicone rubber superhydrophobic surfaces were tested through mechanical and chemical experiments. The samples showed desirable durability properties maintaining a WCA of >150° and a CAH of <10° in several tests. Silicone rubber materials also showed a self-repair capacity stemming from the elasticity of the rubber and migration of LMWS to the surface. This recovery compensated for the loss of anti-wetting properties in some destructive tests, and the WCA recovered after a couple of days.

Acknowledgement

The authors acknowledge the financial support from the Natural Sciences and Engineering Research Council of Canada (NSERC) and K-Line Insulators Limited, Toronto, Canada. We also thank the Anti-icing Materials International Laboratory (LIMA) for carrying out the centrifuge adhesion tests.

CHAPTER 5

ARTICLE 4: EVALUATING THE EFFECT OF PROCESSING PARAMETERS ON THE REPLICATION QUALITY IN THE MICRO COMPRESSION MOLDING OF SILICONE RUBBER

K. Maghsoudi, E. Vazirinasab, R. Jafari, G. Momen

Department of Applied Sciences, University of Quebec in Chicoutimi (UQAC)

555, boul. de l'Université, Chicoutimi, Québec, G7H 2B1, Canada

This article has been published in:

Materials and Manufacturing Processes

https://doi.org/10.1080/10426914.2020.1779942

5.1 Abstract

Given the role of micro-nanostructures in producing superhydrophobic and icephobic surfaces and the importance of high-quality replication of these micro-nanostructures in direct replication processes, we evaluated the effect of processing parameters on the superhydrophobicity, icephobicity, and replication quality of silicone rubber surfaces created via micro-compression molding. Molding pressure, mold temperature, curing time, and part thickness were selected as the processing parameters to be assessed. We used a response surface methodology to illustrate the optimal values of the selected processing parameters. Molding pressure and part thickness were the main influencing parameters to attain the superhydrophobicity, while curing time and mold temperature affected the crosslink density of the fabricated silicone rubber samples. In a second set of experiments, we assessed the replication quality of silicone rubber surfaces of variable thickness subjected to different molding pressures. Each part thickness had an optimal molding pressure for obtaining the best replication quality. Lower pressures did not provide adequate force to ensure that the silicone rubber filled the micro-nanostructures, whereas higher molding pressures had a destructive effect on the micro-nanostructures of the template surface. Surfaces having the highest replication quality also demonstrated the longest freezing delay and confirmed their potential use as anti-icing surfaces. Although all developed superhydrophobic surfaces showed icephobicity, the influence of processing parameters affecting ice adhesion was complex.

Keywords: Processing parameters; Superhydrophobicity; Icephobicity; Replication quality; Design of experiment; Micro-nanostructures

5.2 Introduction

Various processing techniques exist for fabricating polymer materials that have a specifically desired size and shape at the micro- or nanoscale. These techniques include micro-injection molding, micro-compression molding, hot embossing, casting, and 3D printing [28, 70]. Among these, micro-injection molding, micro-compression molding, and hot embossing are considered to be the most suitable mass-production processes for microfabrication because they offer high repeatability, lower fabrication costs, faster cycle times, the ability to produce multiple shapes, the simultaneous shaping of bulk and surface structures, and comparatively simple automation [28, 326].

The most critical aspect of the microfabrication process is achieving the required high precision. The level of precision is affected by several parameters, including the geometry and the thickness of the product, surface structure size, the aspect ratio of the structures, the shape and orientation of the structures relative to the material flow direction, and the processing parameters. The processing parameters have the most influence on precision and include mold temperature, melt temperature, packing pressure, flow velocity, and holding time.

The role of each parameter may differ depending on the selected material and applied microfabrication technique; for example, the role of melt temperature differs greatly between the microfabrication of thermoplastics and that of rubber materials. An increase in melt temperature decreases the viscosity of the thermoplastic, which is advantageous for obtaining a high-quality replication [327]. In contrast, the melt temperature in rubber processing must be kept as low as possible as an elevated temperature increases the rate of crosslinking. Any crosslinking before the filling of the cavity reduces the filling quality [28, 33]. The maximum height for micro-nanostructures is obtained at lower melt temperatures in the micro-injection molding of liquid silicone rubber (LSR) [33]. As another example, the holding time in the micro-injection molding of thermoplastics defines the cooling time of the material. However for rubber micro-compression molding, holding time determines the curing time of the rubber, and both have critical effects on the quality of the final parts. In terms of the role of substrate thickness, there remains considerable debate in the literature.

Filling capability has been shown to improve by decreasing substrate thickness [108], whereas other studies have shown that a reduction in substrate thickness leads to a deterioration of replication quality [328]. In the microfabrication of parts having micro-nanostructured surfaces, the thickness of the substrate is markedly greater than that of the micro-nanostructures. Hence, substrate thickness affects the in-cavity pressure profile and therefore affects filling quality. A thicker substrate hinders the increase of the in-cavity pressure; this results in a poorer replication quality, whereas a thinner substrate—by allowing the in-cavity pressure to increase—leads to a higher quality of filling [108].

As the combination of different processing parameters can lead to contradictory effects on the final product, the manipulation of microfabrication processing parameters is complicated. Consequently, the processing parameters must be carefully selected/manipulated in a certain manner to acquire the most desirable results.

At present, investigations of the effects of processing parameters on microfabrication processes have been limited mainly to the micro-injection molding of thermoplastics, such as polymethyl methacrylate (PMMA), polystyrene (PS), cyclic olefin copolymers (COC TOPAS), polypropylene (PP), liquid crystal polymer (LCP), and high-density polyethylene (HDPE) [108, 115, 248, 329-337]. Although some studies have investigated the micro-injection molding of rubber materials, e.g., liquid silicone rubber (LSR) [33], or rubber-containing polymers, such as thermoplastic elastomers (TPE) [338], high-impact modified polystyrene (HIPS) [339] and thermoplastic vulcanizates (TPVs) [339], or the micro-compression of thermoplastics [326], there remains a lack of comprehensive research on the microfabrication of rubber materials using micro-compression molding. As such, to the best of our knowledge, this study examines, for the first time, the influence of molding processing parameters on the superhydrophobic and icephobic properties of micro-nanostructured surfaces via a statistical assessment.

For a material to show superhydrophobic properties, i.e., a water contact angle (WCA) of >150° and a sliding angle (SA) of <10°, it should possess hydrophobic characteristics, and the surface should also include micro-nanostructures that roughen the surface [30]. These micro-nanostructures should be arranged so that a water droplet cannot penetrate the surface features due to the presence of entrapped air in the cavities, a state called the Cassie-Baxter regime. Otherwise, the water droplet penetrates into the surface features and the

Wenzel regime dominates [340]. The abovementioned microfabrication techniques are appealing for mass producing superhydrophobic surfaces. Multiple studies evaluated the fabrication of superhydrophobic polymer materials using micro-injection molding [88, 91, 93, 101], hot embossing [29, 132, 134, 259], and micro-compression molding [35, 107, 127, 304]. The produced superhydrophobic surfaces have potential uses for delaying ice formation (anti-icing) and reducing the energy needed for shedding formed ice (de-icing). Freezing delay time and ice adhesion strength measurements are commonly used as indices to evaluate the de-icing and anti-icing properties of superhydrophobic surfaces [184].

The increased probability of a coupling reaction between two macromolecules—produced from radical-radical recombination and macroradical addition—can create a "crosslinked" network structure [341, 342]. The crosslink density (CD) is defined as the number of crosslinked points per unit volume, expressed in $mol \cdot cm^{-3}$ [343]. The vulcanization reaction (crosslinking) respects the classical law of chemical reaction kinetics, and hence it is dominated by the process temperature [344]. By increasing curing temperature or curing time, the physical and mechanical properties may deteriorate due to the overcuring [344]. Therefore, the CD can affect the demolding quality, physical properties, and mechanical properties of the cured rubber.

Design of experiment (DoE) is a mathematical and structured method to investigate the effect of several controllable and uncontrollable factors simultaneously [112]. The DoE method helps to determine whether the independent and controlled variables/factors and their interactions significantly influence the dependent measurable quantity of interest/responses [223, 345]. It aims to predict outcomes by introducing various preconditions. DoE dissociates a signal from background noise. As such, the inherent error of the system can be estimated [53, 346].

The main objective of this study is to evaluate the effect of processing parameters on the superhydrophobic and icephobic properties and the replication quality of silicone rubber materials produced using micro-compression molding. We selected molding pressure, mold temperature, curing time, and part thickness as the processing parameters to evaluate the optimal combination of parameters. A DoE method was then carried out to identify the influence of four parameters on the superhydrophobic properties and crosslink density. Using the optimal values, the replication quality and its influence on the icephobicity of the

manufactured surface were assessed. The produced output response surface maps allow the results to be used in decision-making for fabricating superhydrophobic/icephobic silicone rubber surfaces.

5.3 Experimental

5.3.1 Materials and equipment

High-temperature vulcanized (HTV) silicone rubber (SR) was used as the process material. Micro-nanostructured aluminum (A6061) templates were produced via a chemical-etching method using a 15 wt.% hydrochloric acid solution and immersion of the aluminum templates in this solution for 2 h [125]. We used a micro-compression molding machine (Carver Inc. USA) having two temperature-adjustable platens. The hydraulic press system is capable of controlling precisely an applied force of 3 to 194 kN. Three-piece flat molds, all having a right rectangular prism cavity of 25×25 mm^2 with three thicknesses (3 mm, 6 mm, 9 mm), cast the rubber materials. The template was placed on the lower part of the mold into the cavity, and the rubber material was placed onto the template. The top of the mold was then closed. The mold was set in the press machine to begin the process. To determine an appropriate process window, we undertook an initial familiarization set of experiments. For this, we determined the most extreme levels at which an acceptable result could be attained. DoE then selected those processing parameters to be assessed for the experimental runs. After the process, the mold was opened, and the cured SR was detached from the aluminum template.

As a flawless demolding is essential for acquiring a high-quality micro-nanostructured surface [31, 347], we examined two groups of industrial release agents that differed in their base chemical component: a polydimethylsiloxane (PDMS)-based and a fluorochemical-based release agent. Although some studies have used silicone-based oil to improve the release of the polymer [107], our results with the PDMS-based release agent were not satisfactory; the release agent left a trace of oily contamination on the molded surface. The fluorochemical water-based release agent, however, produced the desired demolding results. The release agent should be cured on the micro-nanostructured template surface at the elevated temperature before conducting the molding process.

5.3.2 Surface characterization

The WCA was determined using a Kruss^{TM} DSA100 goniometer at 25 °C ± 0.5 °C with a 4-µL deionized water droplet, based on the Young-Laplace approximation. The SA was measured using a tilting plate with a

tunable angle from 0° to 90°. First, a 4-μL water droplet was placed carefully on the surface using a micropipette (AccuPet Pipettes). Then, the tilt angle was increased continuously, and the angle was recorded as the SA when the droplet began to slide or roll off the surface. To ensure the accuracy and reproducibility of our results, all wettability measurements were conducted at five different points on each sample; we report the average and standard deviation for each sample. We observed the micro-nanostructure morphology of the fabricated SR surfaces using a scanning electron microscope (JSM-6480 LV SEM manufactured by JEOL Japan). The replication quality (RQ) of the molded SR samples was assessed by the surface roughness values provided by a confocal laser microscopy profiler (Profil3D, Filmetrics, USA). The profiler also provided 2D and 3D profiles of the surfaces as well as the skewness (S_{sk}) and kurtosis (S_{ku}) coefficients.

The CD of the cured SR samples was measured via a swelling experiment, during which the swelling ratio and the average mass between the crosslink points (M_c) were also calculated. A ~200-mg slice of each sample was immersed in 50 mL of toluene for 72 h at room temperature. The sample arrived at an equilibrium swollen state. The sample was removed from the toluene and weighed immediately (m_1). The sample was then dried at 60 °C for 24 h and was weighed again (m_2). Given the density of rubber (ρ_r = 1.15 g/cm^3) and the density of toluene (ρ_s = 0.866 g/cm^3), the volume fraction of the SR in the swollen sample can be calculated as follows [348]:

$$\varphi = \frac{(\frac{m2}{\rho_r})}{(\frac{m2}{\rho_r})+(\frac{m1-m2}{\rho_s})} \qquad \textit{Eq. 5.1}$$

Therefore, the CD (ν) and M_c were calculated according to the Flory-Rehner theory [349].

$$\nu = \frac{-(ln(1-\varphi)+\varphi+\chi\varphi^2)}{V(\varphi^{\frac{1}{3}}-\frac{\varphi}{2})} \qquad \textit{Eq. 5.2}$$

$$M_C = \frac{\rho_r}{\nu} \qquad \textit{Eq. 5.3}$$

where χ is the Flory-Hoggins polymer-solvent interaction coefficient calculated, calculated as $\chi = 0.459 + 0.134\varphi + 0.59\varphi^2$, and V is the molar volume of toluene (106.7 mL/mol).

Using the same equipment as for the WCA measurements, the WCA at freezing temperatures and the freezing delay time were measured in a cold chamber where the sample stage (Peltier cooling controller) is

capable of reaching –30 °C with a control precision of 0.1 °C. The 4-µL water droplet, being filmed by the goniometer camera, was transparent upon its placement on the surface. With time, the droplet became non-transparent, representing the frozen state. The delay time of this state change was recorded as the freezing delay. Ice adhesion strength was determined using a push-off instrument. A thin cylindrical, 1-cm diameter plastic mold was placed on the sample and filled with deionized water. The ice formed after the mold was placed in a cold chamber at –10 °C for 24 h prior to testing. The de-icing process was conducted where the sample holder was pushed toward the force gauge at a rate of 0.05 $mm \cdot s^{-1}$ until the ice detached from the surface. The force was recorded at the moment of ice detachment.

5.3.3 Design of experiment

The multi-level parameters can not only have a direct effect on the responses, but their interactions can also affect the responses, complicating any interpretation of multiple factors. Nonetheless, determining the (non-)significant parameters is essential for developing superhydrophobic surfaces. We used a D-optimal method to optimize the combination of the multi-level factors. D-optimal designs are direct optimizations based on a chosen optimality criterion where a model is fit. This method is recommended when multiple quantitative factors are involved [346]. The curing time (t_c) and molding pressure (P) are 4-level factors, and the mold temperature (T_w) and part thickness (d) are 3-level factors (Table 5.1). In running the design, the number of experimental runs decreased from 144 (4 × 4 × 3 × 3) to 53 runs. The processing parameters of each of the 53 experimental runs are provided in Table AIII. 1.

Table 5.1. Processing parameters of 53 different experiment runs.

Factor	**Level**			
t_c **(min)**	1.5	3	6	9
P **(MPa)**	5	20	35	50
T_w **(°C)**	120	150	180	-
d **(mm)**	3	6	9	-

5.4 Results and discussion

To evaluate the effect of processing parameters on the superhydrophobic and physical properties of the produced surface, we used WCA, SA, and CD as the measured responses. To assess the RQ during the micro-compression molding, we assessed the roughness parameters, i.e., root mean square area roughness, skewness, and kurtosis of the surfaces. The results of WCA, SA, and CD for the produced surfaces are presented in Table 5.2.

Table 5.2. The results of water contact angle (WCA), sliding angle (SA), and crosslink density (CD) of the produced surfaces.

Responses				Responses			
Run no.	**WCA (°)**	**SA (°)**	**CD*10^{-4} (mol/cm^3)**	**Run no.**	**WCA (°)**	**SA (°)**	**CD*10^{-4} (mol/cm^3)**
1	160.2	5.3	3.94	**28**	166.0	3.3	3.73
2	161.9	3.7	4.39	**29**	160.3	4.7	3.05
3	160.2	4.7	4.41	**30**	161.9	3.7	4.28
4	155.7	6.7	3.63	**31**	161.3	3.7	4.63
5	163.5	3.3	4.18	**32**	164.0	2.0	4.52
6	162.9	3.7	4.54	**33**	159.6	5.7	3.07
7	163.1	3.7	3.42	**34**	148.7	21.7	4.02
8	155.0	7.7	2.89	**35**	154.4	17.3	4.17
9	158.4	7.3	4.09	**36**	150.1	18.7	4.42
10	156.6	8.0	4.31	**37**	152.8	19.7	3.69
11	159.6	4.0	4.71	**38**	151.1	15.0	2.94
12	158.0	6.3	4.68	**39**	154.6	9.3	4.28
13	161.9	3.0	3.77	**40**	155.3	7.7	4.29
14	158.4	5.7	4.23	**41**	155.7	7.7	4.48
15	162.8	4.7	4.29	**42**	156.6	7.0	4.56
16	157.5	5.3	4.34	**43**	155.7	4.3	3.41
17	155.0	7.7	3.18	**44**	154.9	12.7	3.35
18	155.6	8.3	4.16	**45**	158.7	5.7	4.4

19	159.5	15.3	4.49	**46**	156.6	2.3	4.49
20	156.3	6.7	4.5	**47**	160.3	3.0	4.61
21	157.7	11.0	3.25	**48**	159.8	3.3	3.47
22	159.1	7.0	4.15	**49**	162.7	2.7	4.47
23	159.5	7.3	4.16	**50**	161.2	2.0	4.53
24	158.6	4.7	4.51	**51**	162.6	2.7	4.5
25	157.2	3.0	3.96	**52**	160.3	3.7	4.16
26	165.6	1.3	4.13	**53**	162.0	6.7	3.98
27	169.6	1.0	4.26				

5.4.1 Response surface analysis

5.4.1.1 Analysis of variance (ANOVA)

Based on DoE design, quadratic models were developed to characterize the effects of different processing parameters and their interactions on WCA, SA, and CD. The resulting regression equations, in terms of actual factors, were as follows (only coefficients having a value >0.001 are included):

$$WCA = +129.405 + 1.061 \times A + 0.393 \times B - 0.002 \times C + 0.927 \times D - 0.001 \times A \times B + 0.113 \times A \times D + 0.003 \times B \times D + 0.004 \times C \times D - 0.142 \times A^2 - 0.001 \times B^2 - 0.287 \times D^2$$

$$SA = +48.262 - 0.611 \times A - 0.551 \times B - 0.026 \times C + 0.375 \times D + 0.003 \times A \times B + 0.001 \times A \times C - 0.098 \times A \times D + 0.002 \times B \times D - 0.006 \times C \times D + 0.045 \times A^2 + 0.002 \times B^2 + 0.155 \times D^2$$

$$CD = 10^{-4} \times (-10.944 + 0.261 \times A + 0.211 \times B + 0.001 \times C - 0.079 \times D - 0.002 \times A \times B + 0.003 \times A^2 - 0.001 \times B^2 + 0.002 \times D^2$$

where A, B, C, and D represent curing time, mold temperature, molding pressure, and part thickness, respectively. Analysis of variance (ANOVA) evaluated the significance of the effect of each variable (and their interactions with each other) on the responses and the adequacy of the developed models. ANOVA results for WCA, SA, and CD are presented in Table AIII. 2, Table AIII. 3, and Table AIII. 4, respectively. All regression

models were significant (p <0.0001). Adjusted R^2 values for WCA, SA, and CD (0.6921, 0.7896, and 0.9243, respectively) agreed reasonably well with the predicted R^2 values (0.5920, 0.7070, and 0.8974 for WCA, SA, and CD, respectively). The reliability of the predictive model was confirmed by the <0.2 difference between the adjusted R^2 and predicted R^2 of the developed models. Adequate model discrimination occurs with a signal-to-noise ratio of >4. Adequate precision values for WCA, SA, and CD were 12.8266, 15.6808, and 24.0876, respectively; therefore, the regression models were statistically significant and adequate for predicting and optimizing the micro-compression molding process.

5.4.1.2 Effect of processing parameters on the WCA

To better illustrate our results, we present the predicted models as 3D response surface plots. For the WCA, molding pressure (hereinafter pressure), part thickness (hereinafter thickness), their interaction, and the interaction between thickness and curing time (hereinafter time) were significant model terms. The 3D response surface relationship between thickness and pressure for WCA at the center level of time and mold temperature (hereinafter temperature), i.e., 5.3 min and 150 °C, respectively, is presented in Figure 5.1. Maximum WCA was achieved in the upper half of the pressure range and at the center level of thickness. By increasing thickness, the required pressure for achieving a higher WCA increased.

At higher thickness values, the WCA monotonically increased with pressure. At lower thickness values, however, a maximum WCA was produced at an optimal pressure. Therefore, increasing pressure does not necessarily lead to a higher WCA for all thicknesses. This pattern can be ascribed to the destructive effect of high pressure on the template micro-nanostructures at the lower thickness. At the lowest pressure value, i.e., 5 MPa, WCA increases with decreased thickness. This pattern is logical as at the lowest pressure, the thickness should be at a minimum for materials to properly fill the micro-nanostructures on the template surface.

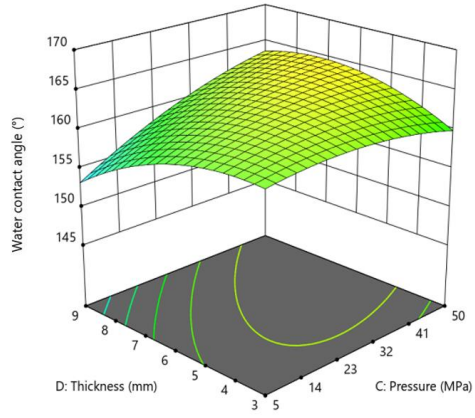

Figure 5.1. The 3D response surface relationship between part thickness and molding pressure on the WCA at the center level of curing time and mold temperature.

The interaction between thickness and time at the center level of temperature and pressure, i.e., 150 °C and 27.5 MPa, respectively, is presented in Figure 5.2. The highest WCA values were attained at a thickness of ≤6 mm and a time of ≤6 min. To obtain a high WCA, therefore, both thickness and time should be selected from the lower values. We observed the same results for the interaction between thickness and time when pressure was altered. Changing the pressure confirmed that thicker substrates require higher pressures (and vice versa) to replicate the micro-nanostructures properly. To obtain the best results, however, the lower half of values of time should be selected. The 3D response surface relationships between thickness and time for WCA at the lowest and highest pressure levels are presented in Figure AIII. 1 and Figure AIII. 2, respectively.

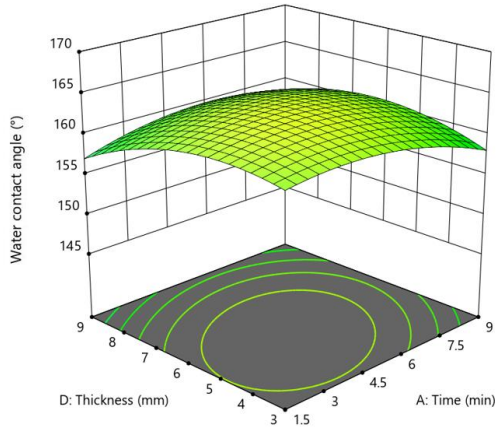

Figure 5.2. The 3D response surface relationship between part thickness and curing time on the WCA at the center level of molding pressure and mold temperature.

The interaction between pressure and temperature at the center level of part thickness and curing time, i.e., 6 mm and 5.3 min, respectively, is presented in Figure 5.3(a). We obtained a maximum WCA at pressures ≥32 MPa and temperatures around the center value (150 °C). This pattern reconfirms the positive effect of high pressure on WCA. The pressure-temperature graphs for the lowest and highest thickness values are presented in Figure AIII. 3 and Figure AIII. 4, respectively. In both cases, the optimal results in terms of WCA were achieved at the center level of temperature. This result stems from the effect of temperature on the constituted CD and subsequent effect on WCA (see Section 5-4-1-4 for discussion of this effect). The mid-range pressures were ideal for obtaining a high WCA at the lowest thickness values, whereas higher pressures were required to obtain a high WCA for the highest thickness values.

The study of the interaction between pressure and time revealed a curved effect of time on WCA. In other words, by increasing time up to its center level, WCA increased; beyond this threshold, however, WCA decreased. On the 3D response surface relation between pressure and time on WCA at center level of temperature and thickness, the highest WCAs were obtained at elevated pressures when the time was selected from the lower half of its range (Figure 5.3(b)). The time-pressure graphs at the lowest and highest thicknesses are presented in the supplementary (Figure AIII. 5 and Figure AIII. 6). A thinner substrate requires central-value pressures to attain a maximal WCA, while the thicker substrate requires higher pressures.

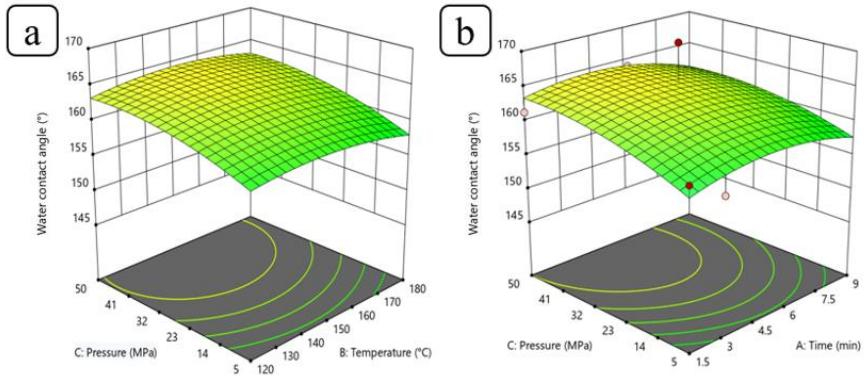

Figure 5.3. The 3D response surface relationship between (a) molding pressure and mold temperature and (b) molding pressure and curing time on the WCA at the center level of the absent parameters.

All observations regarding the effect of temperature and time involve understanding the effects of higher temperatures and longer times on formed crosslinks and rubber thermal expansion. A higher CD results in greater viscoelastic loss and a higher elastic modulus of the SR [350]. A higher elastic modulus makes

demolding more difficult, i.e., the silicone surface asperities interlocked with the template micro-nanostructures, make the prepared surfaces more difficult to detach from the template given their higher elastic modulus. Higher demolding forces can damage the micro-nanostructures on the rubber surface. Moreover, higher temperatures produce a greater thermal expansion of SR [351]. Therefore, higher temperatures or a longer duration of the process leads to the rubber compound receiving more heat and therefore resulting in greater thermal expansion of the SR. Demolding thus becomes more complicated as the adhesion or the friction forces increase between the rubber and template surface [352]. These conditions also reduce the RQ (see discussion below).

As such, we can conclude that pressure has the greatest effect on the achievable CA; however, higher pressure does not necessarily lead to a higher WCA. The optimal pressure level depends on part thickness. Although temperature appears to have no marked effect on WCA, elevated temperatures are not recommended due to the produced CD and undesired thermal expansion of SR. There is also an optimal curing time for achieving the desired WCA. It is therefore recommended to select as low of a processing duration as possible from within the optimal range.

5.4.1.3 Effect of processing parameters on the SA

The same parameters, i.e., thickness and pressure, their interactions, and the interaction between time and thickness are significant model factors for the SA. Our aim was to achieve as low a SA as possible. Figure 5.4 illustrates that at the center level of temperature and time the lowest SAs were achieved at pressure values between ~14 MPa and ~41 MPa for a thickness of 3 mm. By increasing the thickness, however, a higher pressure was required to maintain a low SA; at a thickness of 9 mm, for example, a pressure of 5 MPa resulted in a SA as high as ~18°, whereas a pressure of 50 MPa produced a SA as low as 2°. In terms of the ANOVA results (Table AIII. 2) for SA, the *p*-value obtained for thickness was 0.0012. Compared to *p*-value of thickness in the ANOVA results for WCA which was 0.0075, it can be concluded that the thickness is a more significant factor concerning the SA than the WCA. It should be noted that as identical samples are used, this is a valid comparison.

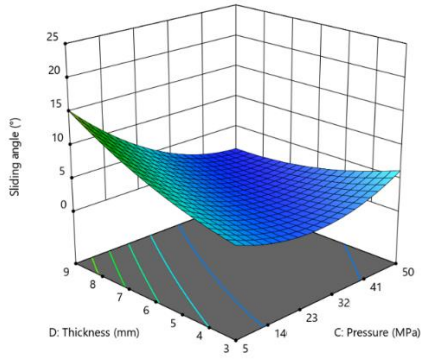

Figure 5.4. The 3D response surface relationship between part thickness and molding pressure on the SA at the center level of mold temperature and curing time.

In terms of the interaction between thickness and time (Figure 5.5), at the center level of pressure and temperature, the interaction of all values of thickness and time produced a SA <10°, a value that is desired for ultra–water repellency. However, we obtained the lowest SA when both thickness and time tended toward their minimal values, as observed for WCA. The thickness-time graphs at the lowest and highest pressures are presented in Figure AIII. 7 and Figure AIII. 8, respectively. We observed high SAs at the lowest pressure level even for the thinnest samples; however, the highest level of pressure led to ultra-low SAs, especially for the thicker samples.

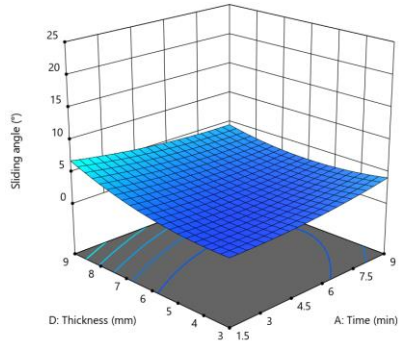

Figure 5.5. The 3D response surface relationship between part thickness and curing time on the SA at the center level of molding pressure and mold temperature.

To study further the effect of pressure on SA, we assessed the pressure-temperature and the pressure-time 3D response surface graphs. All favorable results occurred at pressure values greater than ~32 MPa (Figure 5.6). Changing the temperature and time has no significant effect on the SA when other parameters were set at their center level. This was confirmed by ANOVA as the *p*-values for time and temperature were 0.8772 and 0.8553, respectively.

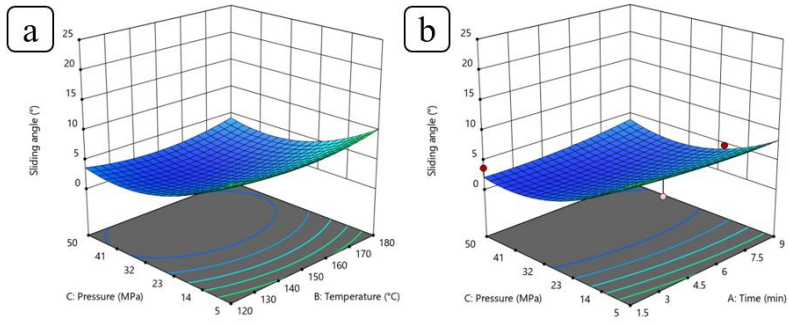

Figure 5.6. The 3D response surface relationship between (a) molding pressure and mold temperature and (b) molding pressure and curing time on the SA at the center level of the absent parameters.

5.4.1.4 Effect of processing parameters on the CD

The modulus of rubber at small elongations is essentially proportional to rubber CD. At higher elongations, it is related to filler-rubber interactions [343]. The relationship between Young's modulus (E) and the average molecular mass of the crosslink points (M_c) at small strains is stated as [353]:

$$E = 3\nu kT = 3\rho RT/M_c \qquad \textit{Eq. 5.4}$$

where ν is the number of chains per unit volume, i.e., CD, k is Boltzmann's constant, T is the absolute temperature, ρ is the density of rubber, and R is gas constant. As such, a lower M_c, which corresponds to a higher CD, leads to a greater Young's modulus. Hence, CD is a good representative of the mechanical properties of cured SR.

We found that all processing parameters, i.e., pressure, temperature, thickness, time, and the interaction between time and temperature, were all significant terms for modeling the CD. However of these terms, time, temperature, and their interaction were most significant.

The 3D response surface relationship between temperature and time on the CD at the center level of pressure and thickness (27.5 MPa and 6 mm, respectively) demonstrates an optimal value for temperature for achieving the highest CD at a given time (Figure 5.7). Thus, by increasing temperature, the CD increased due to the increased crosslinking (vulcanization) reaction rate. A high curing temperature enhanced the decomposition rate of the vulcanizing agent to produce more free radicals [354]; this led in general to a higher CD. However, increasing the curing temperature beyond the optimal value caused the CD to be reduced. At higher temperatures, crosslinking and chain scission occurred at the same time. As such, curing temperatures

that are set too high could reduce CD due to the dominance of chain scission at higher temperatures. Under such conditions, cross-bonds and large molecules degrade to widen the contracted network and increase the distance between the networks [354]. When assessing temperature with other parameters, e.g., time, pressure, and thickness, the optimal temperature varied, although it was generally around 140–150 °C.

The effect of time on the CD varied at low and high temperatures (Figure 5.7). At low temperatures, longer curing times increased the CD. Thus, a longer curing time compensated for the low temperature. At high temperatures, however, the reverse effect was observed; longer curing times at a high temperature reduced the CD due to a higher decomposition rate and chain scissoring.

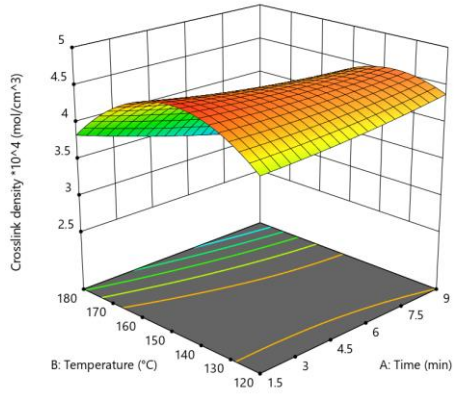

Figure 5.7. The 3D response surface relationship between mold temperature and curing time on the CD at the center level of molding pressure and part thickness.

A saddle-like relation, i.e., monotonic at both limits, was observed for both the pressure-temperature and thickness-temperature response surfaces (Figure 5.8). The CD increased up to an optimal curing temperature at a given pressure (or thickness); beyond this temperature, the CD was reduced. The changes in pressure (or thickness) at a given temperature value had no significant effect on the CD. Thus, interactions between pressure and temperature, as well as between thickness and temperature, were not significant. The ANOVA results for CD are provided in Table AIII. 4.

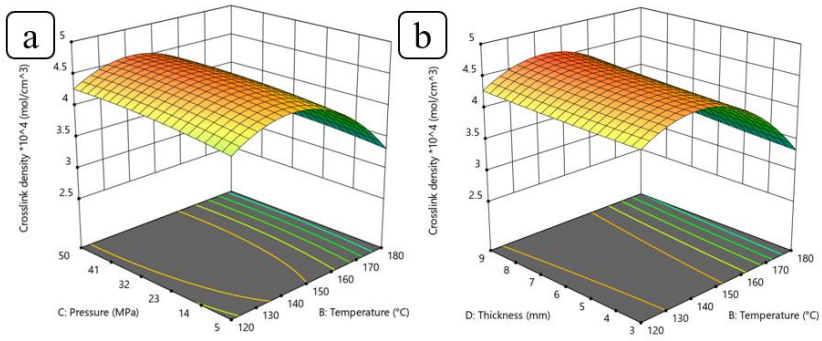

Figure 5.8. The 3D response surface relationship between (a) molding pressure and mold temperature and (b) part thickness and mold temperature on the CD at the center level of the absent parameters.

5.4.1.5 Effect of pressure and thickness on the RQ

From the set of designed experiments, thickness and pressure were recognized as the significant model factors of surface wettability. To evaluate RQ, we require the profiles of the produced samples subjected to various conditions. However, it was not feasible to run profilometry tests on 53 different samples. Therefore, we investigated only the effect of two significant factors controlling wettability, i.e., thickness and pressure, on RQ. Three levels were considered for each factor: pressures of 20, 35, and 50 MPa and thicknesses of 3, 6, and 9 mm. The 5-MPa pressure was eliminated due to its undesirable effect on surface wettability.

Table 5.3 shows the effect of pressure and thickness on the RQ and WCA at a fixed time and temperature (4.7 min and 149.0 °C, respectively). We selected these fixed values based on the optimal model obtained in Section 3.1. RQ is expressed as the root mean square area roughness value (S_q) for each sample compared to that of an aluminum template. The skewness and kurtosis values were also reported; these two values assess the effect of the processing parameters on surface roughness. The skewness coefficient indicates the degree of symmetry of the surface height about the mean plane [306, 355]. Therefore, zero skewness represents a fully symmetrical height distribution, positive skewness represents more peaks than valleys, and negative skewness reflects more valleys than peaks [356, 357]. The kurtosis coefficient describes the sharpness of the probability density of the profile. When S_{ku} >3, a jagged surface having a relatively high number of high peaks and low valleys is expected. S_{ku} <3 represents a flatter surface having a limited number of high peaks and low valleys [356]. As the produced surfaces have a WCA >150° and a SA <10°, the dominant wetting regime is Cassie-Baxter. Therefore, the WCA and SA of the produced samples were measured, and the solid-liquid area fraction of the Cassie-Baxter equation (*f*) was calculated according to the following equation [90]:

$$cos\theta_C = f_{SL}(1 + cos\theta_Y) - 1 \qquad \textit{Eq. 5.5}$$

where θ_C is the Cassie-Baxter apparent WCA, f_{SL} is the area fraction of solid-liquid interface, and θ_Y is the intrinsic WCA (for pristine silicone rubber θ_Y is 116° ± 2.0°).

RQs ranging from ~70% to ~96% were obtained by altering pressure and thickness. In terms of RQ and the associated wettability values, the higher the RQ, the greater the superhydrophobicity. A high-quality replication therefore led to higher WCA and lower SA values due to the most appropriate roughness being created on the SR surface. For example, the highest WCA (169.3°) and the lowest SA (1.7°) were obtained when RQ was 95.89% (S5). The results of RQ agreed well with the predicted models. The predicted model for the effect of thickness and pressure on WCA illustrated that each value of thickness behaved differently as pressure increased. Figure 5.9 presents the 3D surface profiles of all produced samples having different RQs. The 3D surface profiles of the aluminum template can be found in the supplementary materials (Figure AIII. 9).

Table 5.3. The effect of molding pressure and part thickness on the replication quality (RQ) and surface wettability of the produced surfaces.

	Processing parameter		Surface roughness parameter				Surface wettability		
Sample	**Molding pressure (MPa)**	**Part thickness (mm)**	**S_q (µm)**	**Skewness**	**Kurtosis**	**RQ (%)**	**WCA (°)**	**SA (°)**	***f* (%)**
Al template	**-**	**-**	**10.450**	**0.235**	**2.997**	**-**	**-**	**-**	**-**
S1	20	3	9.749	0.067	3.743	93.29	168.8 ± 0.7	3.0 ± 0.6	3.39
S2	35	3	8.747	–0.137	2.510	83.70	167.8 ± 0.8	3.0 ± 0.6	4.02
S3	50	3	7.444	–0.232	2.615	71.23	167.3 ± 1.1	5.3 ± 1.3	4.36
S4	20	6	7.406	–0.428	3.008	70.87	163.8 ± 1.2	4.3 ± 1.6	7.07
S5	35	6	10.020	0.067	3.795	95.89	169.3 ± 0.9	1.7 ± 0.3	3.10
S6	50	6	8.317	0.097	3.743	79.59	166.3 ± 1.6	3.7 ± 0.6	5.07
S7	20	9	7.150	–0.317	2.295	68.42	158.3 ± 0.5	9.3 ± 0.9	12.62
S8	35	9	7.551	–0.267	3.134	72.26	159.6 ± 0.6	5.7 ± 0.6	11.17
S9	50	9	9.403	–0.245	3.408	89.98	161.5 ± 0.7	3.3 ± 0.3	9.20

3-mm thickness

For 3-mm thickness, RQ decreased as pressure increased; therefore, the highest RQ was obtained at 20 MPa (S1). This reduction in RQ stemmed from the destructive effect of the pressure on the template micro-nanostructures as the higher pressures caused the micro-nanostructures on the template surface to be compressed and result in a relatively flatter SR surface. For example, Sample S3 had a kurtosis value of <3, whereas Sample S1 had near-zero skewness and a kurtosis >3.

6-mm thickness

Optimal RQ for the 6-mm thick samples was attained at the moderate pressure values, i.e., 35 MPa. The 20-MPa pressure was not sufficient for the rubber material to fill the structures, while the 50-MPa pressure (Sample S6) had a slight destructive effect on the micro-nanostructures, although this destructive effect was less than for the samples of 3-mm thickness. Sample S5 had the highest WCA and the lowest SA values among all samples due to its highest RQ (95.89%) and the most near-zero skewness values (0.067). In comparison, RQ was ~80% for Sample S6 and was ~71% for Sample S3.

9-mm thickness

For the 9-mm thick samples, WCA increased as pressure increased, and higher pressures produced a higher RQ. The 20-MPa pressure for Sample S7 was insufficient for the rubber material to fill the micro-nanostructures. The kurtosis of Sample S7 was <3 reflecting a rather flat surface with a limited number of high peaks and low valleys. Moreover, Sample S7 also had the highest skewness, indicating a non-symmetrical surface. Thus, a proper pressure profile was not established in the cavity, resulting in a non-symmetrical surface at the silicone-template interface that increased the probability of pinning a water droplet rolling across the surface. Hence, Sample S7 recorded the lowest WCA (158.3°) and the highest SA (9.3°). As pressure increased for the 9-mm thick samples (Samples S8 and S9), the RQ was enhanced, which resulted in surfaces having a kurtosis >3, more near-zero skewness, a greater WCA, and a lower SA.

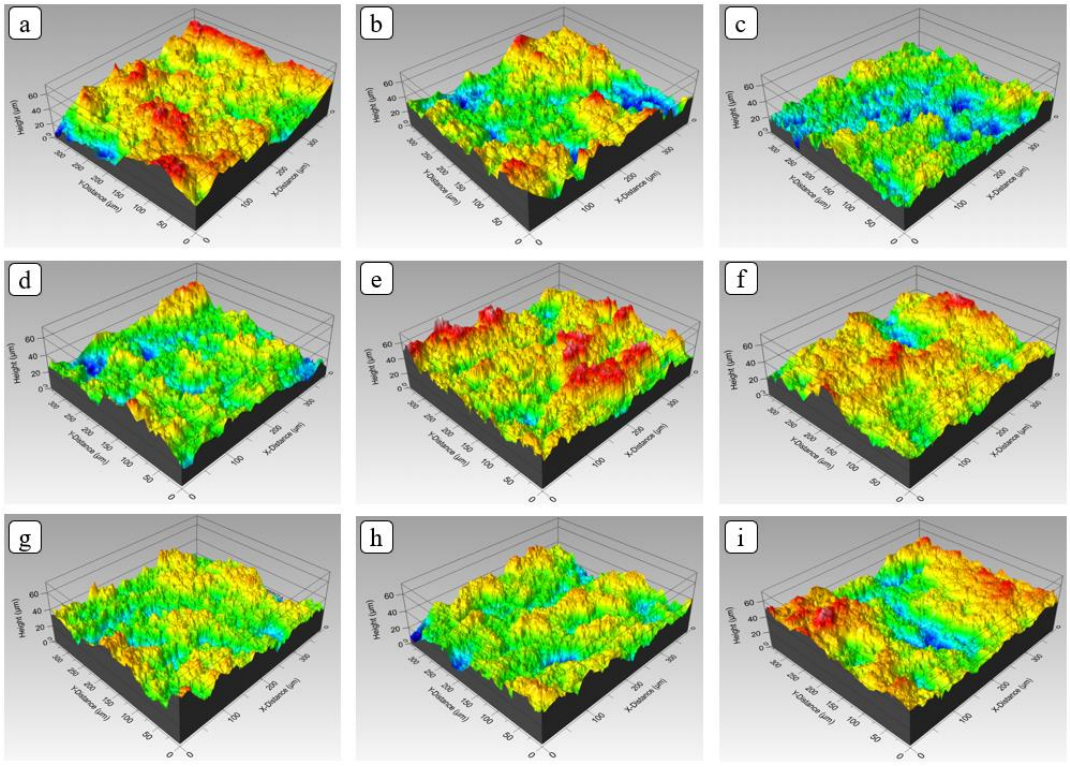

Figure 5.9. The 3D surface profiles of samples (a) S1, (b) S2, (c) S3, (d) S4, (e) S5, (f) S6, (g) S7, (h) S8, and (i) S9 representing various replication qualities. See Table 5.3 for details of the molding pressure and part thickness of each sample.

5.4.2 Icephobicity

The fabrication of icephobic materials targets two main objectives: (i) preventing or decreasing the accumulation of ice on a surface and (ii) reducing the ice adhesion strength [306, 358]. To evaluate the first property, the freezing delay time can be used as a criterion [359, 360], while the assessment of the second property relies on the common ice adhesion strength test. We measured the WCA of the samples at a freezing temperature (-25 °C), the freezing delay time, and the ice adhesion strength via a push-off test.

5.4.2.1 Contact angle at freezing temperature

The behavior of produced surfaces at a supercooled temperature of -25 °C, reflecting harsh icing conditions, was evaluated using the WCA. Due to the reduced surface tension of a water droplet at low temperatures, the WCA was lower than those measured at ambient temperature [125]. Among the nine samples, the highest and the lowest WCAs were achieved for the samples S5 and S7, respectively (Figure 5.10), in close agreement with WCAs at ambient temperature (Table 5.3). Thus, the WCA at freezing temperatures also

depends on the quality of the surface structures: high-quality replication that produces a surface having relatively symmetrical and jagged surface structures can ensure a high WCA at freezing temperatures.

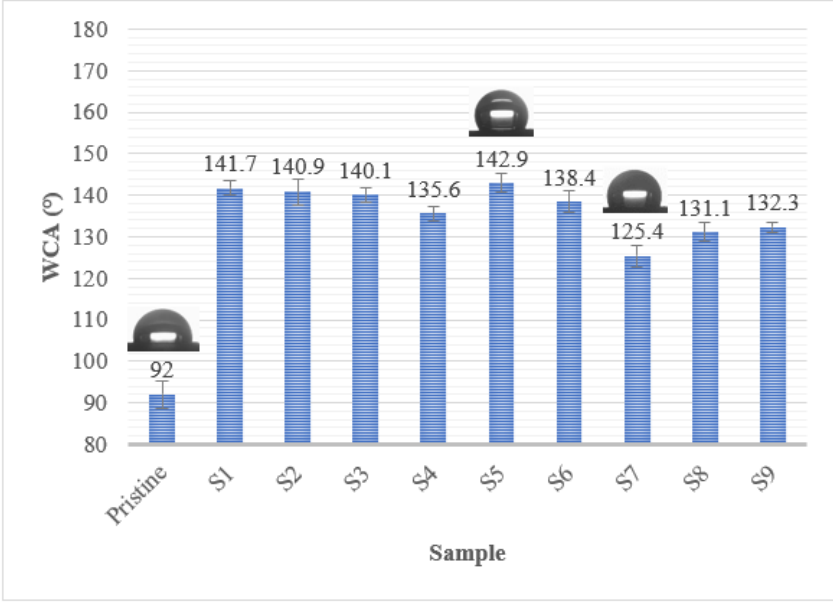

Figure 5.10. Water contact angle (WCA) results of the samples at -25 °C. Inset images represent the WCA of a water droplet on a pristine surface, Sample S5, and Sample S7.

5.4.2.2 Freezing delay

Nucleation at the water-surface interface is influenced by both the contact area between the water and surface and the energy barrier to heterogeneous nucleation [183, 361]. For samples at -25 °C, freezing delay times were affected by the surface roughness parameters, i.e., skewness and kurtosis, and by the solid-liquid area fraction of the Cassie-Baxter equation (*f*) obtained from the WCA (Figure 5.11). Surfaces having a lower solid-liquid interface, i.e., higher liquid-gas interface, showed longer freezing delays due to the lower heat dissipation along the surface derived from a higher WCA.

As there is a direct relationship between the volume of micro-air cavities that act as thermal insulation and the delay in droplet freezing [306, 362], the volume of the entrapped air in the micro-cavities was calculated using the profilometry technique. Figure 5.11 shows the $\nu_{superhydrophobic}$ / $\nu_{pristine}$ value, which is defined as the ratio between the volume of the entrapped air in the produced superhydrophobic surface to that of the pristine surface. A higher $\nu_{superhydrophobic}$ / $\nu_{pristine}$ resulted in the longer freezing delay due to less heat loss through the surface asperities.

All superhydrophobic surfaces demonstrated an enhanced anti-icing behavior compared to that of the pristine surface. A 2.24×–3.91× enhancement was observed for the various superhydrophobic surfaces. The high volume of entrapped air (representing the liquid-gas interface) acts in concert with the low solid-liquid area fraction (*f*) to delay ice formation. Samples S5, S6, S1, and S2, having the lowest *f* values, highest kurtosis, and highest $\nu_{superhydrophobic} / \nu_{pristine}$ values, demonstrated the best anti-icing capabilities. Sample S7, characterized by a high *f* and a low $\nu_{superhydrophobic} / \nu_{pristine}$ value, produced the slowest freezing time among the superhydrophobic surfaces. This result demonstrated the importance of replication quality when comparing the 74% increase in the freezing delay of the Sample S5 (RQ = ~96%) with Sample S7 (RQ = 68%).

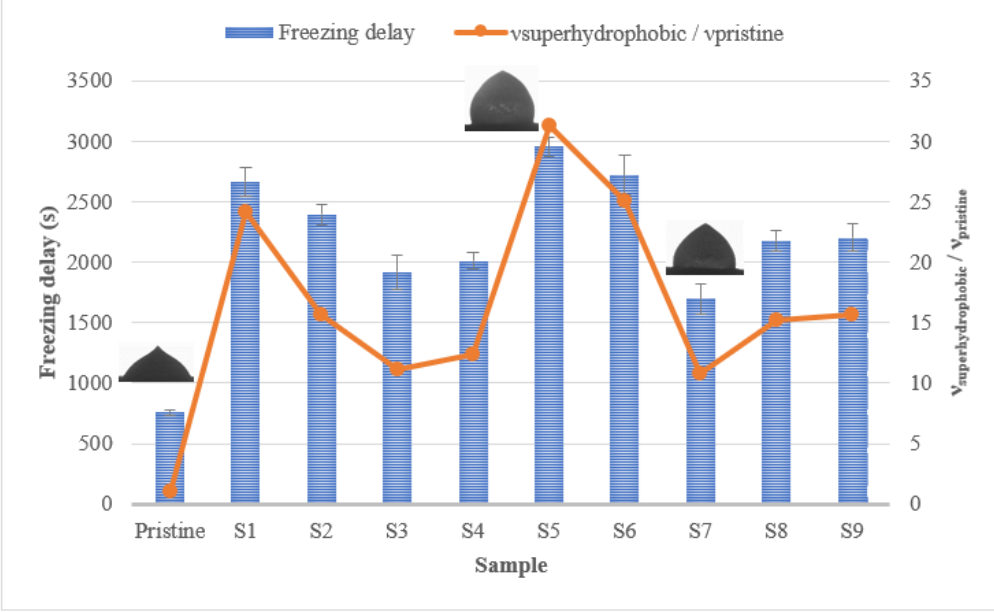

Figure 5.11. Freezing delay and the increased entrapped air pockets ratios for the samples at -25 °C. Inset images represent the droplets at the moment of complete freezing for the pristine surface, Sample S5, and Sample S7.

5.4.2.3 Ice adhesion strength

The icephobic enhancement percentage was defined as the reduced ice adhesion strength compared to the ice adhesion of the pristine surface. The ice adhesion of superhydrophobic surfaces decreased markedly (35% to 62%) compared to the pristine surface (Figure 5.12). However, among the superhydrophobic samples, Sample S2 showed the lowest ice adhesion strength (69.3 kPa) and the highest de-icing enhancement percentage (62%). Sample S8 showed the highest ice adhesion strength (118.5 kPa) and the lowest enhancement percentage (35%).

Ice adhesion strength was influenced by the kurtosis and the solid-liquid area fraction (*f*), but not in a straight-forward manner. The mechanical interlocking of ice with the surface asperities plays a vital role in ice adhesion [306, 363]. Therefore, for surfaces having relatively higher peaks and lower valleys, i.e., higher kurtosis, the probability of this mechanical interlocking is greater. On the other hand, a lower solid-liquid area fraction leads to less surface area in contact with the water, thereby reducing the interlocked area. Sample S2, having relatively low kurtosis and *f* values, produced the highest de-icing enhancement percentage. Although a surface having lower kurtosis is normally more favorable for producing de-icing properties, this is contingent on a high WCA, thus a low *f* value. For example, Sample S7 that had a low kurtosis value (2.295) also showed a relatively high ice adhesion strength, which was attributed to its high *f* value. In such a case, although the surface is relatively flatter and the probability of mechanical interlocking is less due to the lower kurtosis, the lower WCA and higher *f* values led to a higher contact area and thus a higher ice adhesion strength.

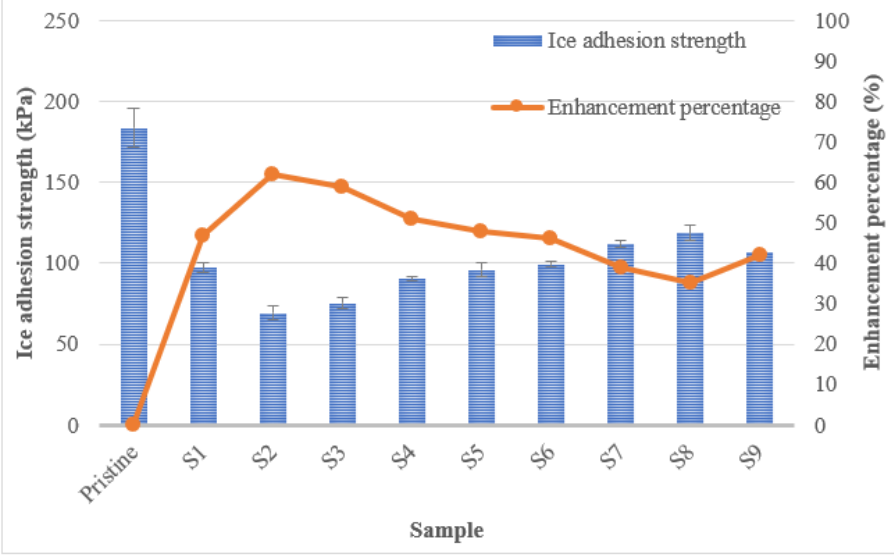

Figure 5.12. Ice adhesion strength and de-icing enhancement percentage of the various samples.

5.5 Conclusions

The fabrication of micro-nanostructured SR to achieve superhydrophobic and icephobic properties via a micro-compression molding technique is highly susceptible to the processing parameters. Various combinations of processing parameters had a decisive effect on the created superhydrophobicity, i.e., water contact angle (WCA), sliding angle (SA), crosslink density (CD), replication quality (RQ), and the icephobic properties of the produced surfaces. Therefore, to study the effect of processing parameters on these properties

of the micro compression–molded SR surfaces, we used response surface methodology and obtained the following conclusions:

(I) Part thickness, molding pressure, their interaction, as well as the interaction between curing time and part thickness were the significant processing parameters affecting the WCA. However, for different part thicknesses, increasing the pressure produced divergent effects. For the 3-mm and 6-mm thicknesses, an optimal pressure was observed to achieve the highest WCA, whereas at 9-mm thickness, the greater the pressure, the higher the CA.

(II) The center level of curing time and mold temperature were recommended to attain the highest WCA. A low process temperature and a short process time led to undesirable rubber curing. An elevated temperature and a longer process time, on the other hand, caused an increase in the rubber elastic modulus and undesired thermal expansion. All these resulted in damage during demolding due to the increased adhesion and friction forces.

(III) Part thickness and molding pressure were determined as the significant factors affecting SA. Although there was an optimal pressure for parts being 3-mm thick to achieve the lowest SA, a greater thickness required a higher pressure to attain a low SA. Interestingly, the thickness was found to be more significant in the results of SA than WCA. The time and temperature were insignificant factors in the SA prediction model.

(IV) All parameters for CD were significant; however, curing time, mold temperature, and their interaction were the most significant factors. An optimal temperature achieved the highest CD as increasing the temperature also increased in decomposition rate. The effect of time on CD affected the optimal temperature range. At lower temperatures, increasing the time increased the CD, while at higher temperatures, increased time decreased the CD.

(V) A second set of experiments studied the influence of processing parameters on RQ using different molding pressures and part thicknesses as the significant factors. The highest RQs were obtained at lower, middle, and higher pressures for 3-mm, 6-mm, and 9-mm thicknesses, respectively.

(VI) Surfaces having relatively higher peaks and lower valleys, i.e., a higher kurtosis, as well as a lower solid-liquid area fraction (*f*) showed a longer freezing delay due to the air pockets acting as thermal barriers and a lower contact area between a water droplet and the surface asperities.

(VII) Ice adhesion strength results were more complicated. A surface having a lower kurtosis was most favorable for icephobic properties; however, this icephobicity is contingent on a high WCA, and thus a low *f* value.

Acknowledgement

The authors acknowledge the financial support from the Natural Sciences and Engineering Research Council of Canada (NSERC) and K-Line Insulators Limited, Toronto, Canada.

CHAPTER 6

TOWARD IMPLEMENTATION IN INDUSTRY: DEVELOPMENT OF SUPERHYDROPHOBIC SILICONE RUBBER INSULATOR USING INJECTION MOLDING SYSTEM

6.1 Abstract

Compression molding, due to its relatively simple and much more economical process in comparison to injection molding, was selected as the system to produce superhydrophobic samples at the lab scale for the framework of this PhD project. Benefitting from the obtained results and given the specific mold geometry of the injection molding system, the appropriate mold inserts having micro-nanostructured surface were produced to run the tests using the injection molding system at K-Line Insulators Ltd. The same aluminum alloy was used to produce inserts with the same conditions by which the aluminum inserts were produced for compression molding. However, much efforts were needed to produce inserts with minimum dimensional change compatible with the complex mold geometry of the injection molding system. Then, a series of whole silicone rubber insulators having superhydrophobic properties on the sheath area were produced using injection molding system at K-Line Insulators Ltd. Moreover, regarding the interest of K-Line Insulators Ltd., the special alloy of their mold (stainless steel) was considered as the material for production of inserts. A special wet-chemical treatment was carried out to create micro-nanostructured insert surfaces. Therefore, the whole inert-making part of the project was repeated using the new insert material. The optimum conditions for making micro-nanostructured stainless-steel inserts were determined and silicone rubber surfaces were produced using compression molding accordingly. Then, the obtained results were used to produce inserts compatible with the injection mold geometry. Finally, using the inserts with the same material as the injection mold material, a series of whole silicone rubber insulators having superhydrophobic properties on the sheath area were produced via injection molding. However, the results of stainless-steel inserts were not presented in this thesis because of confidential agreements.

6.2 Introduction

Compression molding is one of the most common methods for producing high volume polymer parts and components. These parts and components are manufactured for use in various industries and different applications including transportation, construction, and electrical. While both thermosets and thermoplastics may be compression molded, the thermosetting polymers are the primary type of materials. Typically, the

compression molding process involves placing a precut, pre-weighed charge of material into the lower half of a heated mold. The heated upper half of the mold is then lowered compressing the material to the defined shape of the mold cavity. After material being cured due to the pressure and heat, the press opens, and the molded part is demolded (Figure 6.1). If there is any flash, it can be removed manually. However, compression molding is highly limited to the simple mold designs.

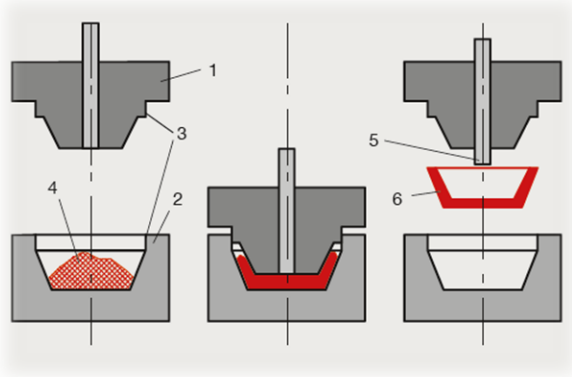

Figure 6.1. Schematic of a compression molding system [364].

Injection Molding is a manufacturing process for producing parts in large volume and complex geometries. It is most typically used in mass-production processes where the same part is being created thousands or even millions of times in succession. In general, injection molding machine consists of two main parts, an injection unit and a clamping unit. Based on how these parts are configured along with the machine, there would be vertical or horizontal injection molding machines [365].

Horizontal injection molding presses are the most common machines used today. The mold opens and closes on a horizontal path as well as the injection unit. Once the molten plastic has been injected into the mold and is ready for ejection, the horizontal press helps. Since the mold is on a horizontal path, once open, gravity assists with ejecting the part causing it to fall from the mold (Figure 6.2(a)). The vertical injection molding machine has a vertical clamping unit as well as a vertical injection unit. Therefore, the molding opening is on a vertical path (Figure 6.2(b)). Vertical injection molding machines are primarily used for softer or malleable products than rigid plastics. With the mold opening on a vertical path, the machine operator has easier access to the finished parts. Instead of having the pieces fall to the floor, they are handled with more care, which is beneficial especially if there are fragile or vulnerable components.

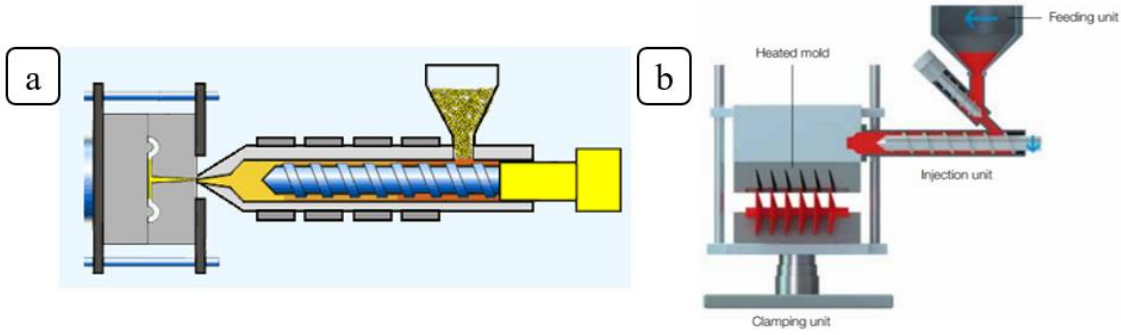

Figure 6.2. Schematic of (a) a horizontal, and (b) a vertical injection molding system [366].

The injection molding system may use a cold runner or a hot runner to carry the plastic from the injection unit to the cavities. A cold runner is a simple channel carved into the mold. The plastic that fills the cold runner cools as the part cools and is then ejected with the part as a sprue. A hot runner system is more complicated, often using cartridge heaters to keep the plastic in the runners hot as the part cools. After the part is ejected, the plastic remaining in a hot runner is injected into the next part. However, in the injection molding of rubber materials, in order to avoid undesirable crosslinking, cold runner is preferred. A vertical injection molding system for production of HTV silicone rubber insulator as shown in Figure 6.3 provided by K-Line Insulators Ltd. was used for the trials in the industry.

Figure 6.3. The injection molding system available at K-Line Insulators Ltd.

6.3 Insert making for injection molding

As the mold for producing high-voltage insulators has a complex geometry, the insert could not be produced simply on flat aluminum sheets. A movable part of the lower half of the mold in the sheath area was

considered. The inserts then were machined according to the inner cavity dimension. The total diameter of the movable part of the mold was ~114.3 mm and the diameter of the inner cavity was ~70 mm. Therefore, the insert can be inserted precisely in that part of the mold.

The aluminum alloy was A6061 with a chemical composition of Al 97.9 wt.%, Mg 1.0 wt.%, Si 0.60 wt.%, Cu 0.28 wt.%, Cr 0.20 wt.% (same as those inserts used for the compression molding process). The insert was precisely designed and machined to be inserted into the movable part of the mold in a way that no gap exists after insertion. Any dimensional change could make a flawless insertion impossible. Besides, any gap between the insert and mold wall could let rubber materials penetrate and the final part would be demolished. As the chemical etching is a corrosive method, to protect the insert surface against undesired etching and subsequent size reduction, the inserts were coated carefully prior to the chemical etching process.

Then, the coated inserts were chemically etched using three different hydrochloric acid (Laboratoire MAT, QC, Canada) concentrations of 10, 15, and 20 wt.% for 1, 2, 3, and 4 h. All etched inserts were ultrasonically cleaned with distilled water to remove any residual dust particles from their surfaces. The etched clean samples were dried in an oven at 70 °C for 1 h.

Throughout demolding step, rubber materials stick completely into the insert surface and make the final part demolished. Using a proper release agent could solve the problem; however, it does not guarantee a proper demolding due to the micro-nanostructures. Working with micro-nanostructures demands more specific strategies. Furthermore, due to the high molding pressure, the rubber materials entangle in the surface roughness and as they are cured in situ, a proper demolding is a serious challenge. Therefore, an antistiction coating was used to make the micro-nanostructured insert surface impermeable against rubber materials. The use of antistiction coatings can improve the quality of the molded surface and the uniformity of the structures while preserving surfaces without any polymer residues. An insert with antistiction coating could guarantee a non-damaging demolding in which the replicated rubber surface has the favorable roughness. Using an insert without antistiction coating not only led to a surface with undesired roughness, but also caused the insert structures to be filled with the rubber residues following the first molding cycle. These residues made it impossible to reuse the same insert. Therefore, a solution of diluted TPFS (Trichloro(1H,1H,2H,2H-

perfluorooctyl)silane) was used to make an antistiction coating on the curved aluminum insert surfaces (for the details see Chapter 2).

The replication processing steps in an injection molding system is the same as those in a compression molding system. There are only some minor differences. In the injection molding process, the insert was inserted into the mold (Figure 6.4(a)), then the fiberglass rod was placed into the mold (Figure 6.4(b)). The platens closed under the pressure, then the rubber materials were injected into the hot mold using the pressure applied by the reciprocating screw (Figure 6.4(c)). When the mold was full, regarding the adjusted volume known as *shot*, the screw shifted back and prepared for the next cycle. The mold opened and the cured part was demolded (Figure 6.4(d)).

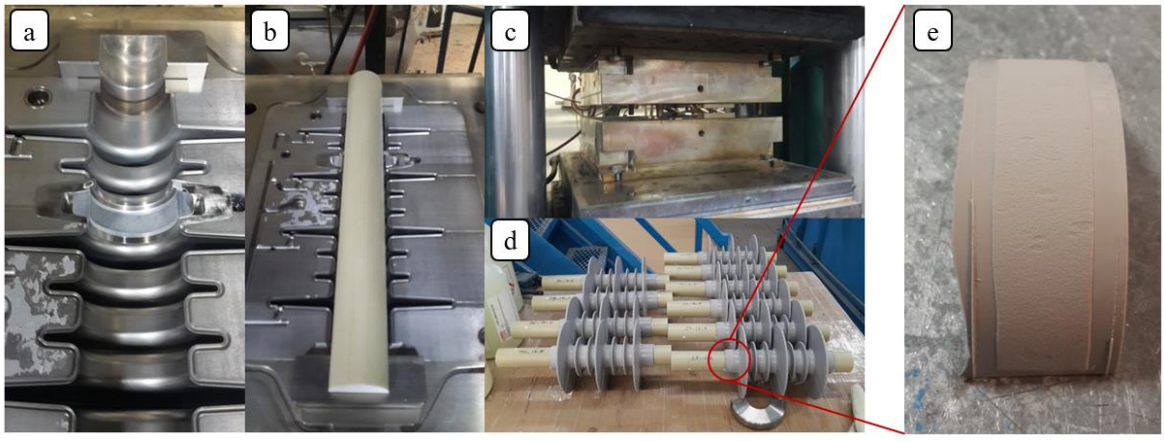

Figure 6.4. The processing steps for the injection molding of silicone rubber at K-Line Insulators Ltd. (a) The insertion of the produced insert into the mold, (b) the placement of the fiberglass rod, (c) closing the mold platens and injecting rubber into the mold cavity, (d) demolding the produced insulators having a superhydrophobic part in their sheath area, and (e) the cut superhydrophobic part from the insulator.

6.4 Results and discussion

Using the produced inserts, 40 various runs were designed and carried out to study the different aspects of the process including insert making conditions, the performance of the antistiction coatings and release agents, and the durability of the produced inserts during repetitive molding cycles. Like the results obtained from the compression molding, all samples showed WCA >160° and CAH and SA <5°. For the confidentiality reasons, only the results of one processing condition are provided here.

Figure 6.5 shows the images of water WCA and CAH for the pristine and superhydrophobic silicone rubber surfaces produced using injection molding system. The pristine silicone rubber showed the WCA and

CAH of 116.3° ± 1.7° and 43.2° ± 1.6°, respectively. The produced silicone rubber using the micro-nanostructured insert showed the WCA, CAH, and SA of 169.0° ± 1.7°, 0.9° ± 0.1°, and ~0°, respectively.

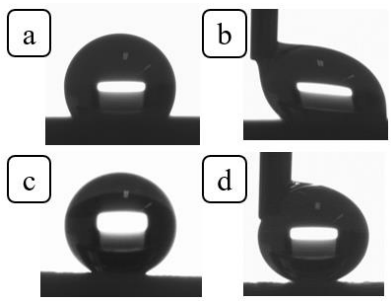

Figure 6.5. The images of water contact angle of the (a) pristine and (c) superhydrophobic silicone rubber surfaces, and the contact angle hysteresis of the (b) pristine and (d) superhydrophobic silicone rubber surfaces.

The creation of the micro-nanostructures responsible for the superhydrophobic behavior of the produced silicone rubber surface was observed using SEM images (Figure 6.6). It was confirmed that the micro-nanostructures on the aluminum insert surface were faithfully replicated on the silicone rubber surface during the injection molding process. The created micro-nanostructures on the silicone rubber surface in the injection molding system were similar to those produced via compression molding system.

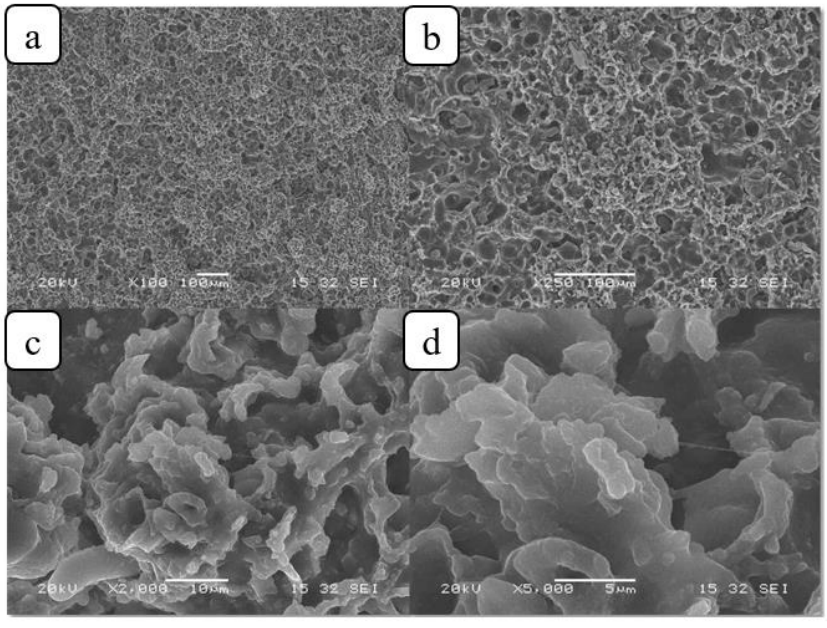

Figure 6.6. SEM images of the produced superhydrophobic silicone rubber surface using the injection molding system at different magnifications of (a) ×100, (b) ×250, (c) ×2000, and (d) ×5000.

6.5 Stainless steel as a new material to produce inserts for compression molding and injection molding systems

Following the successful results of the fabrication of superhydrophobic surfaces using aluminum inserts (both flat and curved via compression and injection molding systems, respectively) and regarding the interest of K-Line Insulators Ltd. to use stainless-steel material for insert making, we worked on the production of stainless-steel inserts having micro-nanostructures using wet-chemical etching method. The selected stainless steel was the same alloy as the injection mold alloy. It is a martensitic stainless steel that provides good corrosion resistance plus increased strength and hardness. Therefore, the etching process of this multi-component stainless steel was more complicated than that of aluminum etching process. Five different etching solutions were examined and three of them were selected to produce inserts. Using compression molding to produce superhydrophobic silicone rubber surfaces with the produced stainless-steel inserts, the etching conditions such as acid concentration, etching time, and the temperature of the etching media were optimized. Then, a series of curved stainless-steel inserts were machined. Using the optimal conditions, the micro-nanostructured stainless-steel curved inserts were produced for running the tests in the injection molding system. We successfully produced silicone rubber insulators having a superhydrophobic part in the sheath area via the injection molding of K-Line Insulators Ltd. using the stainless-steel inserts. For the confidentiality reasons, we do not present the results obtained from the stainless-steel inserts in the thesis. The obtained results made the company interested to modify their mold to produce superhydrophobic insulators in an industrial scale.

6.6 Conclusions

The results obtained from the laboratory experiments were successfully implemented in the industry. The aluminum curved inserts having micro-nanostructured surface and compatible with the injection mold geometry were produced. A series of whole silicone rubber insulators having the superhydrophobic properties in the sheath area were fabricated using the injection molding system at K-Line Insulators Ltd. Moreover, given the interest of the industry, the same stainless-steel alloy as the injection mold was considered as a new material for insert making. The optimal conditions were determined through the laboratory experiments using the compression molding. Then, the results were used to produce curved stainless-steel inserts for running tests in

the industry. Silicone rubber insulators having superhydrophobic properties in the sheath area were successfully fabricated using injection molding system at K-Line Insulators Ltd.

CONCLUSIONS

In this section, a summary of the main findings of this project is provided. First, partial conclusions corresponding to each chapter of the project are presented according to the order of their presentation in the thesis. Then, a general conclusion is provided.

Direct replication of micro-nanostructures in the fabrication of superhydrophobic silicone rubber surfaces by compression molding

In the first part of this project, a direct replication method was developed for the manufacturing of micro-nanostructured superhydrophobic silicone surfaces. The following results were found:

- All samples produced under the various etching conditions displayed water contact angles >160° and contact angle hysteresis <3°.
- The highest water repellency was achieved for the samples replicated from inserts produced with an acid concentration of 15 wt.%. This higher water repellency was due to the relatively higher surface roughness of the 15 wt.% acid samples compared to those produced from lower and higher acid concentration inserts. For example, sample C15H2 (insert was produced with an acid concentration of 15 wt.% for 2 h) showed a root mean square (R_q) roughness value of 7.90 µm, while R_q values for samples C10H2 and C20H2 were 5.80 µm and 5.81 µm, respectively. The higher R_q led to the higher WCA and lower CAH.
- Among the C15 samples, the best results were obtained for the etching time of 2 h. So, the acid concentration of 15 wt.% and etching time of 2 h were revealed as the optimal condition for producing insert.
- An antistiction coating containing fluorinated bonds was applied to the insert surfaces prior to molding. This guaranteed a flawless demolding where the micro-nanostructures on the insert and silicone rubber surface remained undamaged.
- To ensure that the fluorinated bonds of the insert surfaces did not transfer to the silicone rubber surfaces during the replication process, the FTIR analysis was conducted.
- The superhydrophobic samples remarkably delayed freezing onset (>3× compared to the pristine surface). It confirmed the icephobic capacity of the produced surfaces.

Rigorous testing to assess the self-cleaning properties of an ultra-water-repellent silicone rubber surface

In the second part of this project, the self-cleaning properties were thoroughly investigated. The following conclusions were drawn:

- The dominance and robustness of the Cassie-Baxter regime was necessary for emergence of self-cleaning properties. It was observed that the transition from the Cassie-Baxter regime to the Wenzel regime did not take place because of the desirable structures created on the silicone rubber surface. Hence, the surfaces were capable to display the self-cleaning ability during various conditions.
- A comprehensive set of experiments using various contaminants (i.e. kaolin, SiO_2, carbon black, salt) and several methods for applying the contaminants and cleaning the surface (i.e. sweeping, dropwise, immersion, spraying), under both wet and dry scenarios was undertaken. The test conditions were inspired by actual outdoor conditions to which electrical insulators are exposed.
- The maintained ultra-low CAH of the surfaces ensured that the self-cleaning properties remained robust for all tests.
- The "spraying of the contaminant suspension" was marked as the most severe condition. After five test cycles, it was observed that the hydrophobic property of the pristine surface deteriorated and produced a WCA of $77° \pm 3°$ and a CAH of $54° \pm 2°$. However, the superhydrophobic surface retained a WCA of $150.1° \pm 1.9°$ and a CAH of $16° \pm 2°$. Benefitting from the hydrophobic-recovery property (stemmed from the diffusion of the low molecular weight silicone from the bulk to the surface), and thanks to the self-cleaning property of the superhydrophobic silicone rubber surface, its WCA increased to $158.2° \pm 1.6°$ and its CAH decreased to $8° \pm 1°$ after two weeks.

Durability assessment of icephobic surfaces: the role of surface roughness and the ice adhesion measurement technique

In the third part of this project, the icephobic properties as well as the durability of the produced surfaces were studied. The following conclusions were drawn:

- The anti-icing properties of the produced superhydrophobic surfaces were observed by the delay in freezing time which was due to the creation of air pockets on their surfaces. The larger micro-nanostructures showed better anti-icing properties because of more entrapped micro air pockets i.e. ~2.5 times more delay in ice formation at –25 °C.
- Compared to the pristine silicone rubber, the superhydrophobic silicone rubber surface reduced ice adhesion strength up to 42% in push-off test and 32% in centrifuge test.
- The strong physical bonding between micro-nanostructures and the bulk material in the compression molded surface led to a relatively constant ice adhesion strength during repetitive icing/de-icing cycles.
- The produced silicone rubber samples showed desirable durability properties where the WCA was >150° and CAH was <10° against several tests. It was observed that the recovery properties of the silicone rubber materials can compensate for the anti-wetting loss in some destructive tests resulted in WCA retrieval after some days.

Evaluating the effect of processing parameters on the superhydrophobicity, icephobicity, and replication quality of silicone rubber surfaces using a response surface methodology

The fabrication of micro-nanostructured silicone rubbers to realize the superhydrophobic and icephobic properties via micro compression molding technique is highly susceptible to the processing parameters. Various set of processing parameters had decisive effect on the superhydrophobicity i.e. contact angle (WCA) and sliding angle (SA), crosslink density (CD) as a representative of the physical properties of the produced rubber, the replication quality (RQ), and the icephobic properties. Therefore, to study the effect of processing parameters on those properties of the micro-compression molded silicone rubber surfaces, the response surface methodology was used, and the following conclusions were drawn:

- In the study of the effect of processing parameters on the WCA, the part thickness, molding pressure and their interaction as well as the interaction between curing time and part thickness were the significant processing parameters. However, for different part thicknesses, increasing the molding pressure produced divergent effects. For the 3-mm and 6-mm thicknesses, an optimal pressure was observed to achieve the highest WCA. Whereas the more the pressure, the higher the WCA at 9-mm thickness was achieved.

- The center level of curing time and mold temperature were recommended to attain the highest WCA. A low process temperature and a short process time led to undesirable rubber curing. An elevated temperature and a longer process time, on the other hand, caused an increase in the rubber elastic modulus and undesired thermal expansion. All these resulted in damage during demolding due to the increased adhesion and friction forces.
- Part thickness and molding pressure were determined as the significant factors affecting SA. There was an optimum pressure for each thickness to achieve the lowest SA. The higher thicknesses, however, demanded higher pressures to attain a low SA. Interestingly, the thickness was found to be more significant in the results of SA than WCA. The time and temperature were insignificant factors in the SA prediction model.
- Although all parameters were significant concerning the CD, curing time, mold temperature, and their interaction were the most significant factors. An optimal temperature achieved the highest CD as increasing the temperature also increased in decomposition rate. The effect of time on the CD affected the optimal temperature range. At lower temperatures, increasing the time increased the CD, while at higher temperatures, increased time decreased the CD.
- A second set of experiments studied the influence of processing parameters on the RQ using different molding pressures and part thickness as the significant factors. The highest RQs were obtained at lower, middle, and higher pressures for 3-mm, 6-mm, and 9-mm thicknesses, respectively.
- Surfaces having relatively higher peaks and lower valleys, i.e. higher kurtosis, as well as a lower solid-liquid area fraction (f) showed a longer freezing delay due to the air pockets acting as thermal barriers and a lower contact area between a water droplet and the surface asperities.
- Ice adhesion strength results were more complicated. A surface having a lower kurtosis was most favorable for icephobic properties; however, this icephobicity is contingent on a high WCA, and thus a low f value.

Toward implementation in industry: Development of superhydrophobic silicone rubber insulator using injection molding system

- The results obtained from the laboratory experiments were successfully implemented in the industrial injection system. Aluminum curved inserts having micro-nanostructured surface and compatible with the injection mold geometry were produced. A series of whole silicone rubber insulators having superhydrophobic properties in their sheath area were fabricated using the injection molding system at K-Line Insulators Ltd.
- Given the interest of the industry, the same stainless-steel alloy as the injection mold material was considered as a new material for insert making. The optimal conditions were determined during the laboratory experiments using the compression molding. Then, the results were used to produce stainless-steel curved inserts for running tests in the industry. Silicone rubber insulators having superhydrophobic properties in the sheath area were fabricated using the injection molding system at K-Line Insulators Ltd.

General conclusions

In the present project, to overcome the issues associated with the ice and pollution accumulation on the surface of high-voltage outdoor insulators, and to circumvent the problems attributed to the use of coatings, superhydrophobic high-temperature vulcanized (HTV) silicone rubber was produced as the high-voltage insulator housing materials. The polymer processing systems namely injection molding and compression molding were employed to fabricate the superhydrophobic silicone rubber surfaces using the direct replication approach out of bulk material. Regarding the metals used for mold making, aluminum alloy was selected as insert or template materials. The wet-chemical etching was used to create desirable micro-nanostructures on the insert surfaces. It was revealed that there was an optimum acid concentration and etching time where the best superhydrophobicity was achieved following the replication process. Moreover, it was confirmed that applying an antistiction coating on the insert surface was crucial to obtain a flawless demolding where a high-quality replication was sought after. Due to the dominance and consistency of the Cassie-Baxter regime on the water repellent surfaces, they illustrated self-cleaning properties. The self-cleaning behavior of the produced

surfaces was examined through various real outdoor imitated conditions. The icephobic properties of the superhydrophobic surfaces were determined via two aspects: anti-icing and de-icing capabilities of the surface. The remarkable delayed ice formation on the surfaces displayed their anti-icing properties, while the reduced ice adhesion strength testified for the de-icing capability of the produced superhydrophobic surfaces. It was revealed that processing parameters significantly affected the wettability properties and the replication quality in various means. Among the different processing parameters, the molding pressure and the mold thickness were recognized as the most influential parameters to achieve water repellency and high-quality replication. Finally, the results obtained in the laboratory experiments were applied in an industrial injection system. Using injection molding system available at K-Line Insulators Ltd., silicone rubber insulators were successfully produced having superhydrophobic properties in the sheath area.

RECOMMENDATIONS

In this project, superhydrophobic silicone rubber surfaces were fabricated using polymer processing systems via the direct replication concept. The produced surfaces exhibited ultra-water-repellent, self-cleaning, and icephobic properties. There yet remains many additional issues that are worth investigating. Herein, some suggestions for future work are proposed.

- Concerning the insert fabrication, other facile methods to create micro-nanostructured inserts such as sandblasting, anodization, and boiling water can be studied. The conditions leading to the best superhydrophobicity after replication should be determined and the reproducibility should be studied.
- As far as insert fabrication is concerned, one the alternative materials is stainless steel. However, it demands more investigation in order to obtain the appropriate micro-nanostructures. Compared to aluminum, the chemical etching process of stainless steel is elaborated and highly affected by the type of the chemical materials used, concentration, etching time, and etching temperature. (In the near future, we will publish a paper on the fabrication of superhydrophobic surfaces replicated on stainless-steel inserts having various surface structures.)
- Regarding the wettability properties, the regular surface structures having certain dimensions are of great interest. The chemical etching process produces irregular or non-ordered surface roughness where the distribution of surface structures is random. To produce ordered structures, employing micromachining or laser drilling is recommended.
- The presence of ordered surface structures provides with myriad opportunities for studying the wettability properties via different phenomena. These studies highly dependant on the roughness-property relationship include Cassie to Wenzel transition, water evaporation, droplet freezing, dynamic droplet impact, etc. (In the near future, we will publish a paper on the fabrication of hierarchical regular microstructured surfaces with superhydrophobicity.)
- During the experiment of water droplet impacting, we have observed several different behaviors of the surfaces with different surface wettability. These behaviors can be divided into bouncing (fully or partial), splashing, or deposition. There are also some transition states where more than one phenomenon was observed. A comprehensive study to find a correlation between the surface characteristics and the water droplet impacting behavior is suggested. (In the near future, we will publish

a paper on the evaluating the capability of surfaces having various structures and wettability properties to repel incoming water droplets.)

- As the main application of the HTV silicone rubber is for high-voltage insulators, the electrical properties of the produced superhydrophobic surfaces including inclined-plane tracking and erosion test (IPT) according to ASTM D2303 or IEC 60587 standards can also be investigated.
- It was observed in this project that the low molecular weight silicone (LMWS) play a decisive role in the regeneration of the lost water repellency. This is very important in terms of self-cleaning and durability properties of the superhydrophobic silicone rubber surfaces. The nature, significance, and magnitude of this contribution can be studied rigorously.
- It was confirmed that the quality of replication defined by the degree of material filling in the micro-nanostructures is of great importance in the direct replication method. To this end, the effect of processing parameters particularly the molding pressure in the fabrication of structured surfaces via numerical simulation can provide a good understanding of the direct replication in the fabrication of microstructured surfaces.
- As observed throughout this project, the durability properties of both superhydrophobic surface under various stresses and inserts having micro-nanostructures through multiple molding cycles is of great importance. Providing a model predicting the lifetime of the surface properties as a function of the operation stresses would be practical to the end-users.

APPENDIX I

SUPPORTING INFORMATION FOR ARTICLE 2

RIGOROUS TESTING TO ASSESS THE SELF-CLEANING PROPERTIES OF AN ULTRA-WATER-REPELLENT SILICONE RUBBER SURFACE

K. Maghsoudi, G. Momen, R. Jafari, M. Farzaneh

Department of Applied Sciences, University of Quebec in Chicoutimi (UQAC)

555, boul. de l'Université, Chicoutimi, Québec, G7H 2B1, Canada

This article has been published in:

Surface and Coatings Technology, Volume 374, 25 September 2019, Pages 557-568

https://doi.org/10.1016/j.surfcoat.2019.05.073

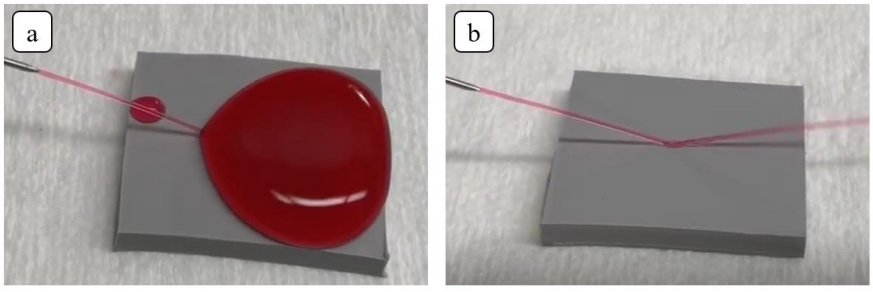

Figure AI. 1. Water-jet impact test on (a) pristine silicone rubber and (b) superhydrophobic silicone rubber surfaces. (The water is colored by aqueous red ink to aid observation).

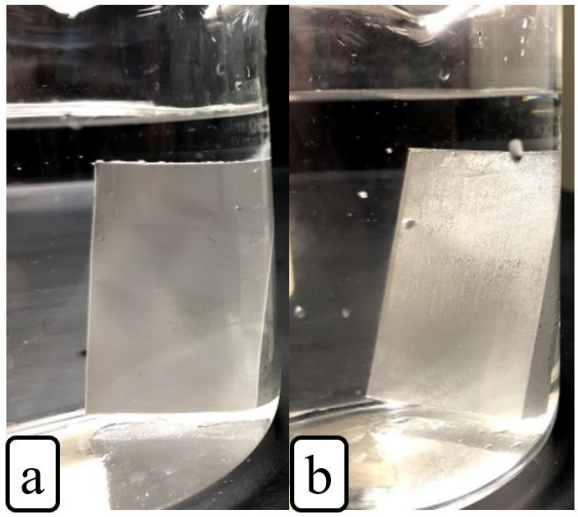

Figure AI. 2. (a) Pristine silicone rubber and (b) superhydrophobic silicone rubber surfaces underwater.

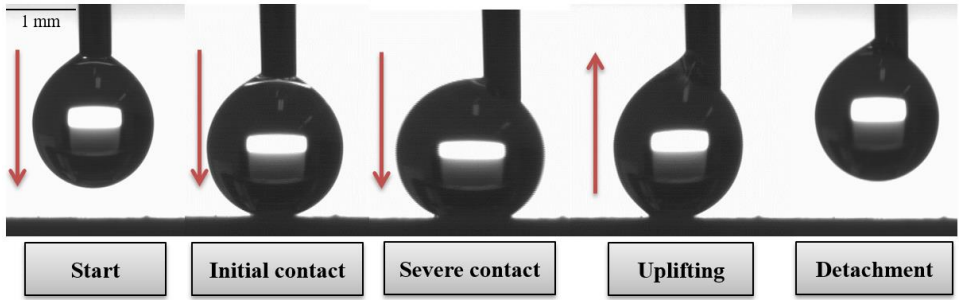

Figure AI. 3. Sequential images showing the severe droplet contact with the superhydrophobic silicone rubber surface.

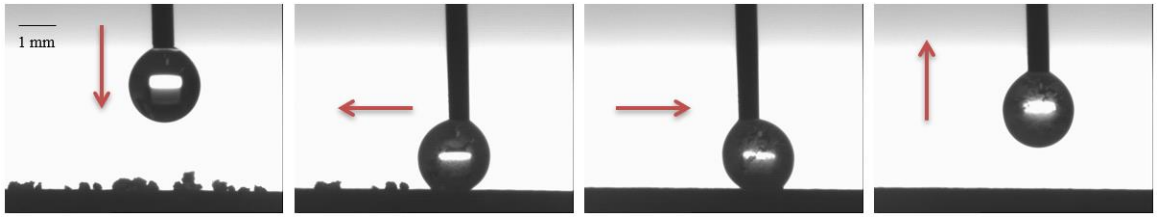

Figure AI. 4. Sequential images of the collecting process of the contaminant by a rolling water droplet along the surface (left to right).

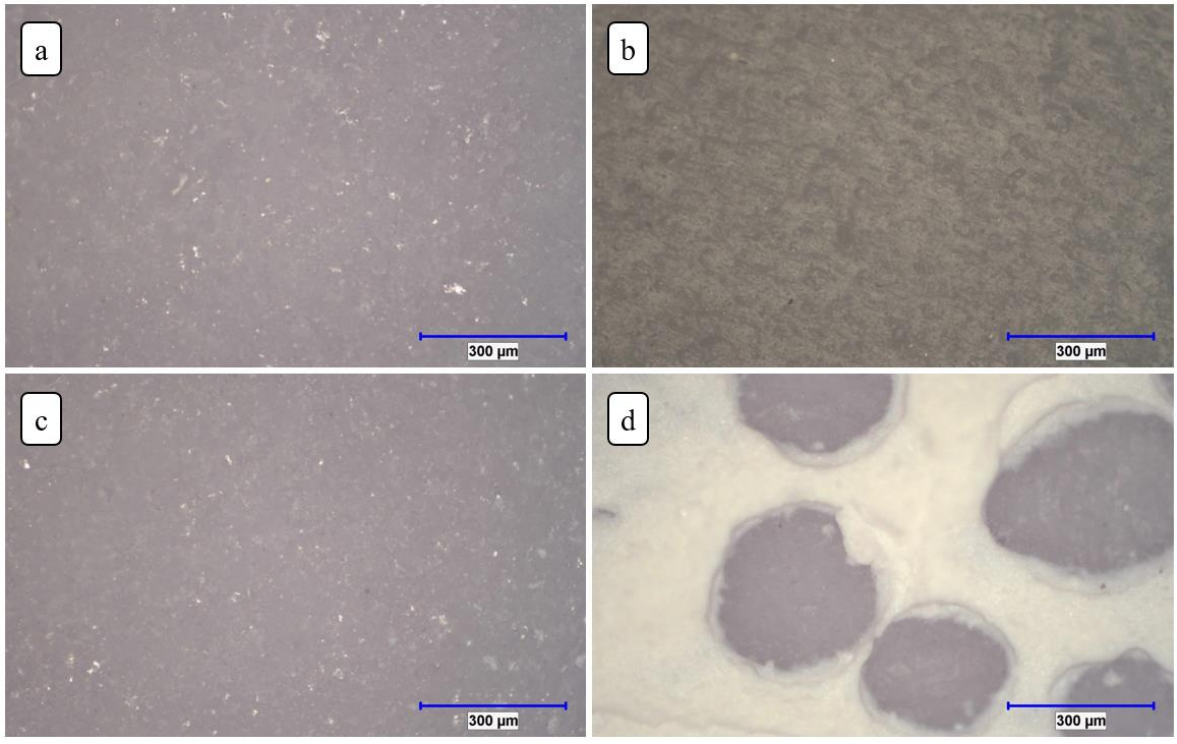

Figure AI. 5. Optical microscope images of the (a) superhydrophobic silicone rubber (SHSR) and (b) pristine silicone rubber (PSR) surfaces before applying droplets of kaolin suspension and images of the (c) SHSR and (d) PSR surfaces after rinsing of the surfaces.

APPENDIX II

SUPPORTING INFORMATION FOR ARTICLE 3

ICEPHOBIC AND DURABILITY ASSESSMENT OF SUPERHYDROPHOBIC SURFACES: THE ROLE OF SURFACE ROUGHNESS AND THE ICE ADHESION MEASUREMENT TECHNIQUE

K. Maghsoudi, E. Vazirinasab, G. Momen, R. Jafari

Department of Applied Sciences, University of Quebec in Chicoutimi (UQAC)

555, boul. de l'Université, Chicoutimi, Québec, G7H 2B1, Canada

This article is under review at:

Materials Processing Technology

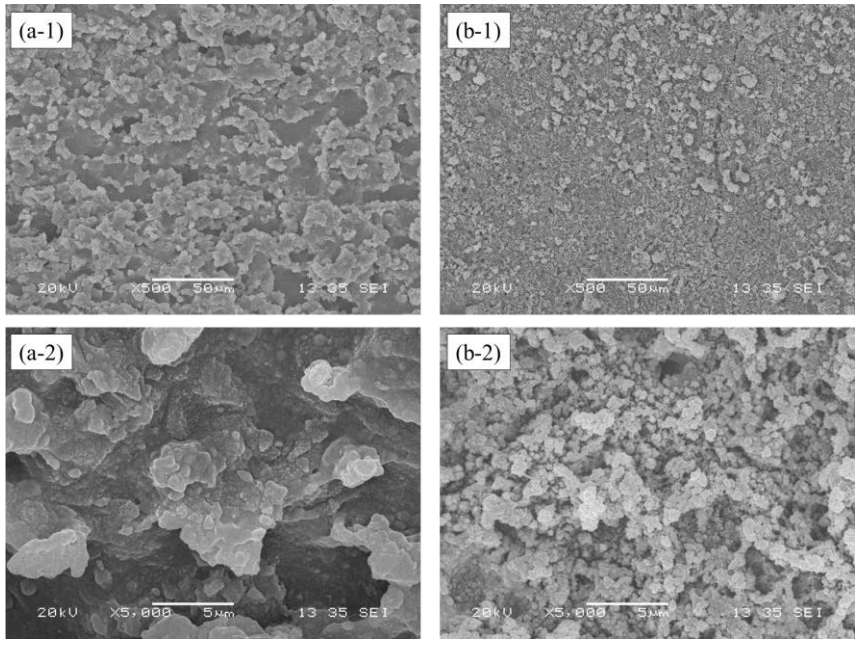

Figure AII. 1. SEM images after 7th icing/de-icing cycle in the centrifuge test at two magnifications for (a-1 & a-2) µCM and (b-1 & b-2) APP-treated surfaces.

Table AII. 1. Ice adhesion reduction factor (ARF) of the µCM and APP-treated surfaces relative to the ice adhesion strength of an aluminum surface (A6061) for push-off and centrifuge tests.

Adhesion reduction Factor (ARF)	**Icing/de-icing cycles**		**1**	**2**	**3**	**4**	**5**	**6**	**7**
	push-off	µCM	9.0 ± 1.3	10.1 ± 0.9	8.2 ± 1.1	9.9 ± 1.1	10.6 ± 2.2	8.7 ± 2.1	9.5 ± 0.9
		APP	25.2 ± 2.6	23.7 ± 2.1	23.2 ± 1.0	20.4 ± 2.0	18.6 ± 1.9	18.3 ± 1.8	18.0 ± 1.8
	centrifuge	µCM	8.7 ± 1.2	7.4 ± 0.8	7.8 ± 0.6	6.4 ± 0.9	7.2 ± 1.3	8.9 ± 1.4	6.4 ± 1.1
		APP	19.2 ± 2.2	16.2 ± 2.1	13.3 ± 2.6	11.8 ± 1.0	9.9 ± 0.6	9.2 ± 0.9	8.9 ± 0.9

The ice adhesion reduction factor (ARF) is defined as:

τ (bare aluminum)/τ (superhydrophobic silicone rubber).

It should be noted that the τ (bare aluminum) was measured as 810 ± 125 kPa.

Table AII. 2. Water contact angle and contact angle hysteresis of the µCM and APP-treated surfaces before and after push-off and centrifuge tests.

	Before icing/de-icing cycles		**After 7 icing/de-icing cycles**	
	WCA (°)	CAH (°)	WCA (°)	CAH (°)
µCM	166.6 ± 1.9	0.6 ± 0.3	163.6 ± 1.0	4.7 ± 0.1
APP	165.8 ± 1.3	1.1 ± 0.6	164.0 ± 0.1	3.9 ± 0.7

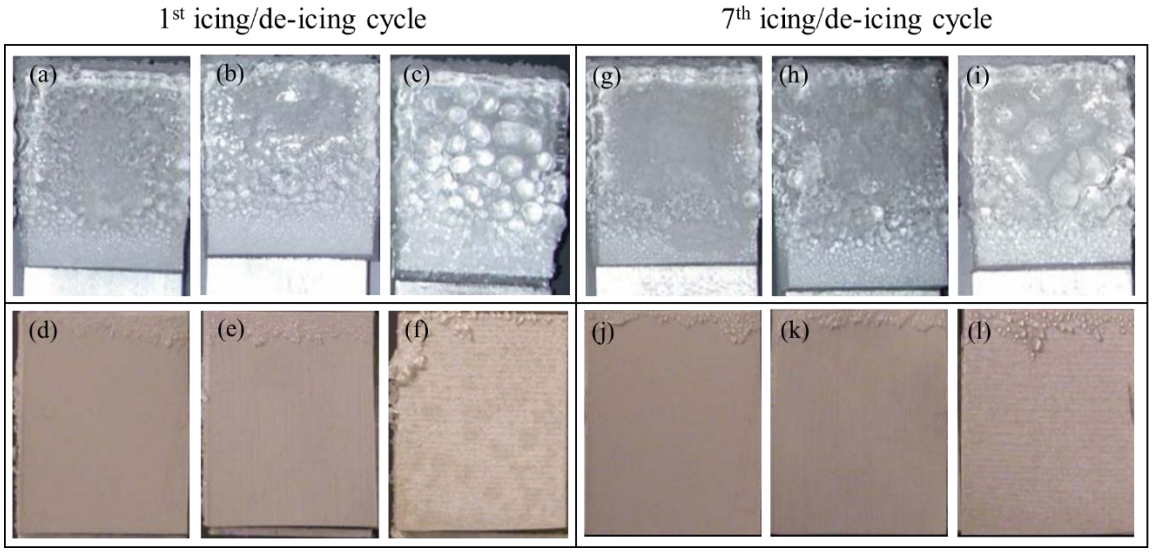

Figure AII. 2. Photographs of the 1st icing/de-icing cycle of the (a, d) pristine, (b, e) µCM, and (c, f) APP-treated surfaces after ice accumulation and after ice removal in the centrifuge test. Photographs of the 7st icing/de-icing cycle of the (g, j) pristine, (h, k) µCM, and (i, l) APP-treated surfaces after ice accumulation and after ice removal in the centrifuge test.

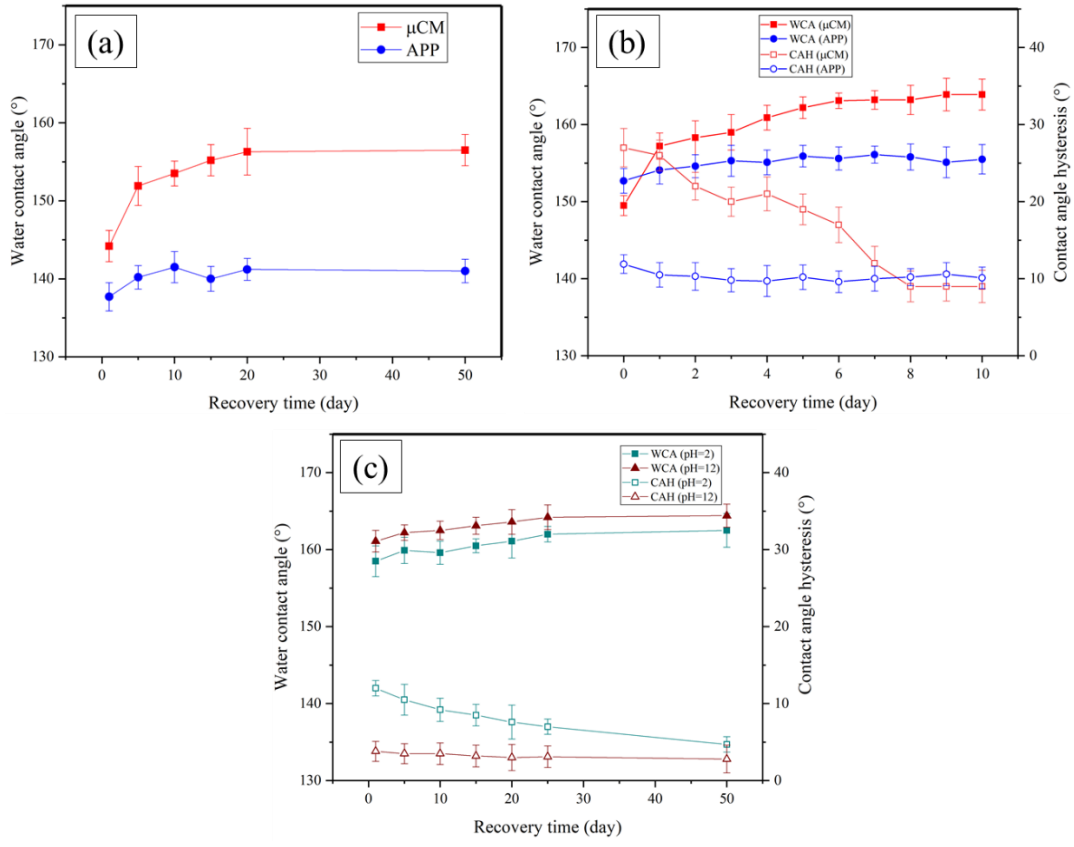

Figure AII. 3. (a) Recovered WCA as a function of time for the sandpaper-abrasion test for the µCM and APP-treated surfaces abraded at 6.4 kPa; (b) recovered WCA and CAH as a function of time for the finger-press tests for the µCM and APP-treated surfaces; and (c) recovered WCA and CAH as a function of time for the µCM sample immersed in acidic and alkaline solutions.

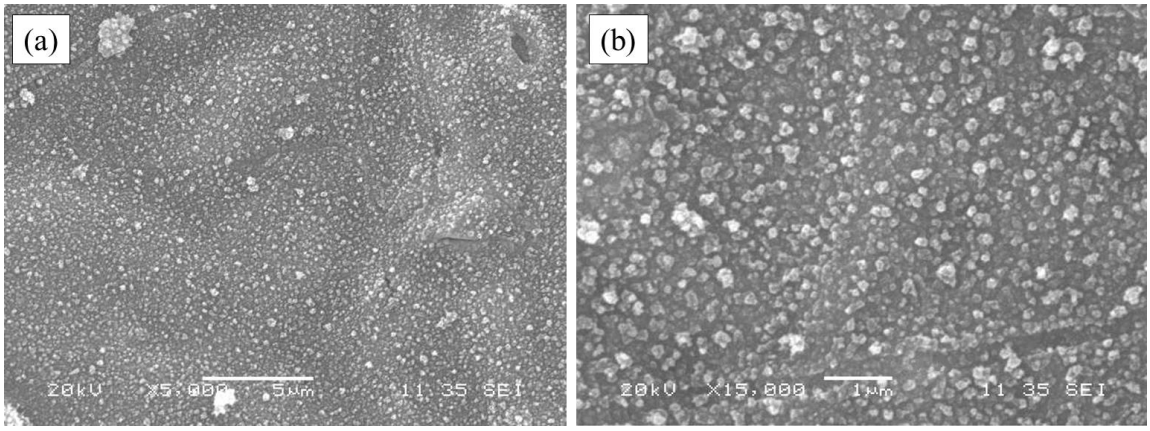

Figure AII. 4. SEM images of the APP-treated surface after ultrasonication test at a magnifications of (a) ×5000 and (b) ×15000.

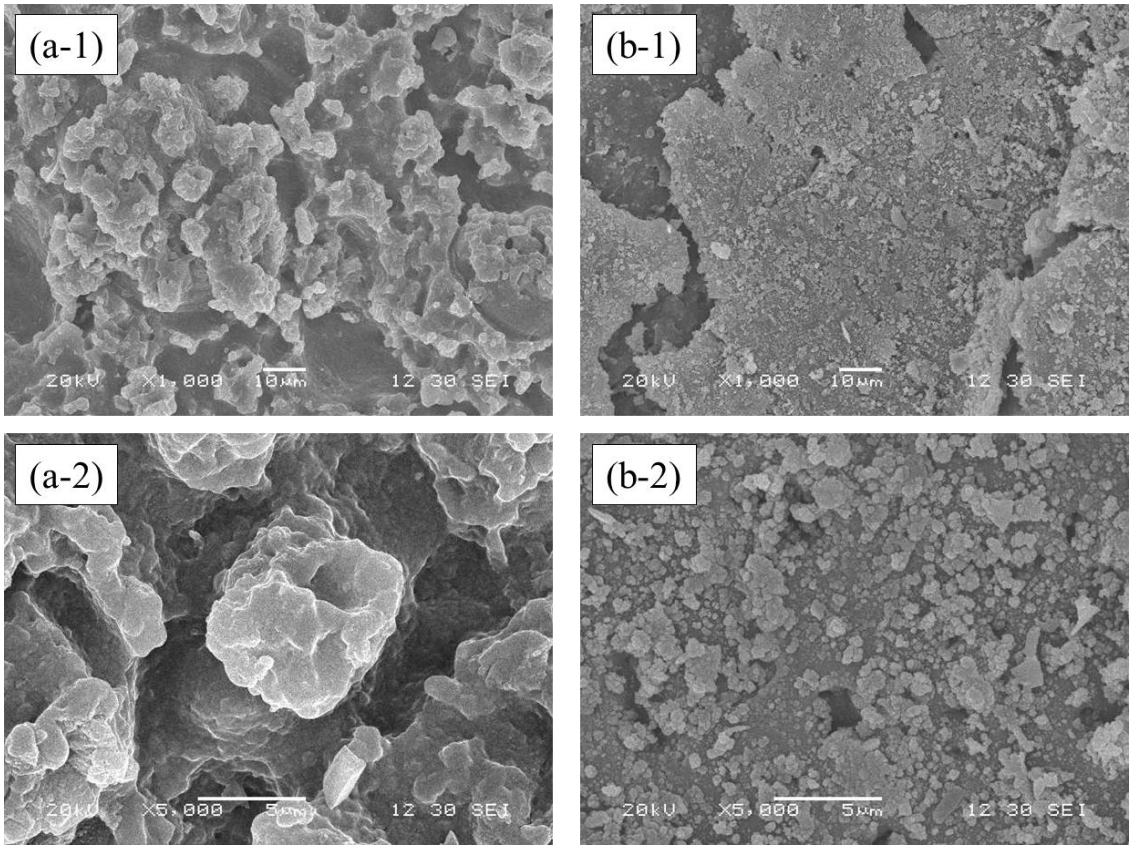

Figure AII. 5. SEM images of a sandblasted (a-1 & a-2) µCM surface and (b-1 & b-2) APP-treated surface at two magnifications.

To study the durability of the produced surfaces against UV-light radiation, the average annual sunlight energy in normal direction at a site located in Ontario, Toronto reported as 8.1-13.4 $MJ.m^{-2}$ [367] was considered. Given that only 3-6 percent of natural sunlight is in the UV region reached to the earth, the annual mean of UV radiant exposure was calculated as follows:

$0.05 \times 13.4\ MJ.m^{-2} = 670{,}000\ J.m^{-2}$

Therefore, to simulate the same amount of energy reached to the surfaces by the UVA-340 fluorescent lamps in the QUV accelerated weathering tester, almost 209 h is needed:

$\text{Time} = 670{,}000\ J.m^{-2} / 0.89\ W.m^{-2} = 209\ h$

APPENDIX III

SUPPORTING INFORMATION FOR ARTICLE 4

EVALUATING THE EFFECT OF PROCESSING PARAMETERS ON THE REPLICATION QUALITY IN THE MICRO COMPRESSION MOLDING OF SILICONE RUBBER

K. Maghsoudi, E. Vazirinasab, G. Momen, R. Jafari

Department of Applied Sciences, University of Quebec in Chicoutimi (UQAC)

555, boul. de l'Université, Chicoutimi, Québec, G7H 2B1, Canada

This article has been published in:

Materials and Manufacturing Processes

https://doi.org/10.1080/10426914.2020.1779942

Table AIII. 1. Processing parameters of the 53 different experiment runs.

Factors					**Factors**				
Run No.	**Curing time (t_c)**	**Mold temperature (T_w)**	**Molding pressure (P)**	**Part thickness (d)**	**Run No.**	**Curing time (t_c)**	**Mold temperature (T_w)**	**Molding pressure (P)**	**Part thickness (d)**
Unit	**min**	**°C**	**MPa**	**mm**	**Unit**	**min**	**°C**	**MPa**	**mm**
1	3	120	5	3	**28**	3	180	35	6
2	6	150	5	3	**29**	9	180	35	6
3	9	150	5	3	**30**	3	120	50	6
4	1.5	180	5	3	**31**	1.5	150	50	6
5	6	120	20	3	**32**	6	150	50	6
6	1.5	150	20	3	**33**	9	180	50	6
7	3	180	20	3	**34**	1.5	120	5	9
8	9	180	20	3	**35**	6	120	5	9
9	6	120	35	3	**36**	1.5	150	5	9

10	9	120	35	3	**37**	3	180	5	9
11	3	150	35	3	**38**	9	180	5	9
12	6	150	35	3	**39**	1.5	120	20	9
13	1.5	180	35	3	**40**	9	120	20	9
14	1.5	120	50	3	**41**	3	150	20	9
15	3	150	50	3	**42**	6	150	20	9
16	9	150	50	3	**43**	6	180	20	9
17	6	180	50	3	**44**	9	180	20	9
18	9	120	5	6	**45**	3	120	35	9
19	1.5	150	5	6	**46**	1.5	150	35	9
20	3	150	5	6	**47**	9	150	35	9
21	6	180	5	6	**48**	6	180	35	9
22	3	120	20	6	**49**	6	120	50	9
23	6	120	20	6	**50**	9	120	50	9
24	9	150	20	6	**51**	3	150	50	9
25	1.5	180	20	6	**52**	1.5	180	50	9
26	1.5	120	35	6	**53**	3	180	50	9
27	6	150	35	6					

Based on their significant *p*-values ($p < 0.05$), molding pressure (C), part thickness (D), the interaction of the curing time and thickness (AD), the interaction between molding pressure and part thickness (CD), the second-order effect of the curing time (A^2) and part thickness (D^2) were identified as the significant factors affecting CA.

For SA, molding pressure (C), part thickness (D), the interaction of the curing time and part thickness (AD), the interaction between molding pressure and part thickness (CD) as well as the second-order effect of mold temperature (B^2), molding pressure (C^2), and part thickness (D^2) had a significant effect ($p < 0.05$).

Curing time (A), mold temperature (B), molding pressure (C), part thickness (D), the interaction of curing time and mold temperature (AB) and the second-order effect of mold temperature (B^2) significantly influenced (p <0.05) crosslink density (CD).

Table AIII. 2. ANOVA results for water contact angle (WCA).

Source	**Sum of squares**	**df**	**Mean square**	**F-value**	**p-value**
Model	652.95	14	46.64	9.35	< 0.0001
A-Curing time	8.73	1	8.73	1.75	0.1938
B-Mold temperature	2.40	1	2.40	0.4814	0.4920
C-Molding pressure	146.66	1	146.66	29.40	< 0.0001
D-Part thickness	39.86	1	39.86	7.99	0.0075
AB	0.5906	1	0.5906	0.1184	0.7327
AC	3.30	1	3.30	0.6611	0.4212
AD	30.75	1	30.75	6.16	0.0176
BC	0.6848	1	0.6848	0.1373	0.7131
BD	1.22	1	1.22	0.2448	0.6236
CD	155.32	1	155.32	31.13	< 0.0001
A^2	36.21	1	36.21	7.26	0.0105
B^2	18.49	1	18.49	3.71	0.0617
C^2	19.20	1	19.20	3.85	0.0572
D^2	73.43	1	73.43	14.72	0.0005
Residual	189.59	38	4.99		
Cor. total	842.54	52			

Table AIII. 3. ANOVA results for sliding angle (SA).

Source	Sum of squares	df	Mean square	F-value	p-value
Model	1004.11	14	71.72	14.94	< 0.0001
A-Curing time	0.1163	1	0.1163	0.0242	0.8772
B-Mold temperature	0.1618	1	0.1618	0.0337	0.8553
C-Molding pressure	289.16	1	289.16	60.22	< 0.0001
D-Part thickness	59.34	1	59.34	12.36	0.0012
AB	1.63	1	1.63	0.3386	0.5641
AC	14.41	1	14.41	3.00	0.0913
AD	23.22	1	23.22	4.84	0.0340
BC	0.5604	1	0.5604	0.1167	0.7345
BD	0.5215	1	0.5215	0.1086	0.7435
CD	268.12	1	268.12	55.84	< 0.0001
A^2	3.64	1	3.64	0.7583	0.3893
B^2	28.80	1	28.80	6.00	0.0190
C^2	108.93	1	108.93	22.69	< 0.0001
D^2	21.35	1	21.35	4.45	0.0416
Residual	182.46	38	4.80		
Cor. total	1186.57	52			

Table AIII. 4. ANOVA results for crosslink density (CD).

Source	Sum of squares	df	Mean square	F-value	p-value
Model	12.18	14	0.8702	46.34	< 0.0001
A-Curing time	0.4530	1	0.4530	24.13	< 0.0001
B-Mold temperature	5.14	1	5.14	273.66	< 0.0001
C-Molding pressure	0.1726	1	0.1726	9.19	0.0044
D-Part thickness	0.1993	1	0.1993	10.61	0.0024
AB	1.06	1	1.06	56.70	< 0.0001
AC	0.0025	1	0.0025	0.1307	0.7197
AD	0.0001	1	0.0001	0.0040	0.9502
BC	0.0060	1	0.0060	0.3199	0.5750
BD	0.0266	1	0.0266	1.42	0.2411
CD	0.0567	1	0.0567	3.02	0.0903
A^2	0.0156	1	0.0156	0.8295	0.3682
B^2	4.85	1	4.85	258.36	< 0.0001
C^2	0.0286	1	0.0286	1.52	0.2251
D^2	0.0030	1	0.0030	0.1584	0.6928
Residual	0.7135	38	0.0188		
Cor. total	12.90	52			

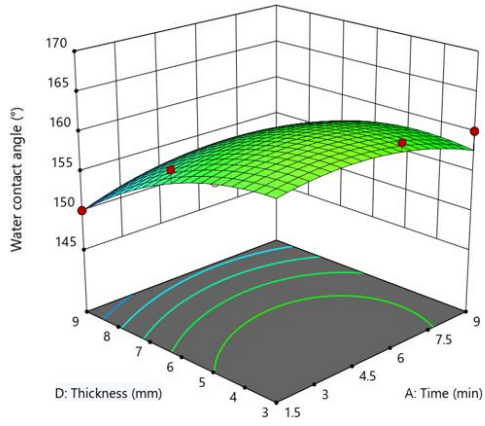

Figure AIII. 1. The 3D response surface relationship between part thickness and curing time on the WCA at the lowest level of molding pressure and at center level of mold temperature.

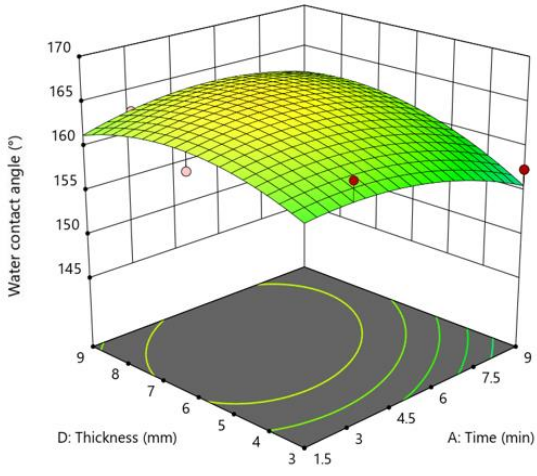

Figure AIII. 2. The 3D response surface relationship between part thickness and curing time on the WCA at the highest level of molding pressure and at center level of mold temperature.

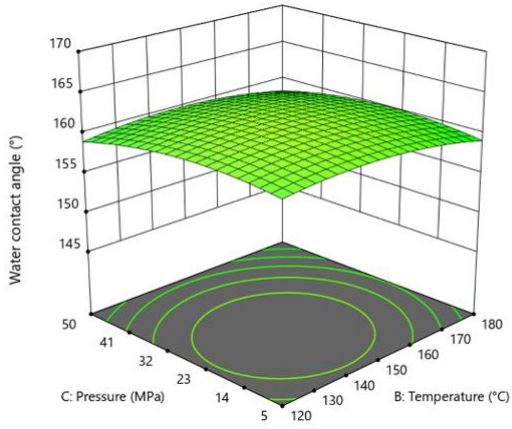

Figure AIII. 3. The 3D response surface relationship between molding pressure and mold temperature on the WCA at the lowest level of part thickness and at the center level of curing time.

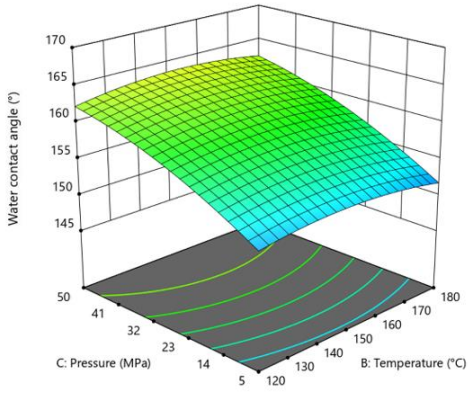

Figure AIII. 4. The 3D response surface relationship between molding pressure and mold temperature on the WCA at the highest level of part thickness and at the center level of curing time.

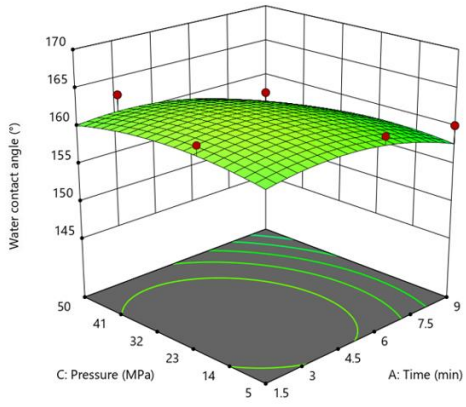

Figure AIII. 5. The 3D response surface relationship between molding pressure and curing time on the WCA at lowest level of part thickness and at center level mold temperature.

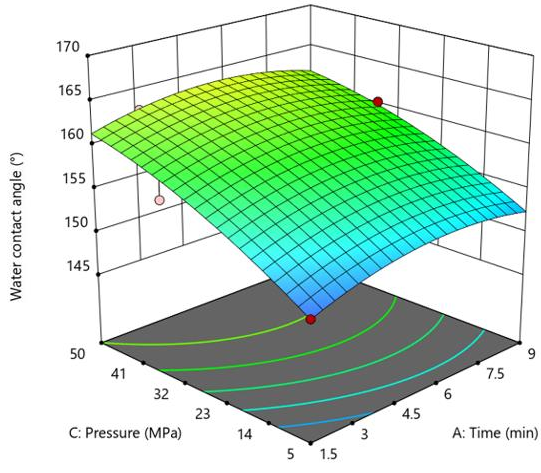

Figure AIII. 6. The 3D response surface relationship between molding pressure and curing time on the WCA at highest level of part thickness and at center level mold temperature.

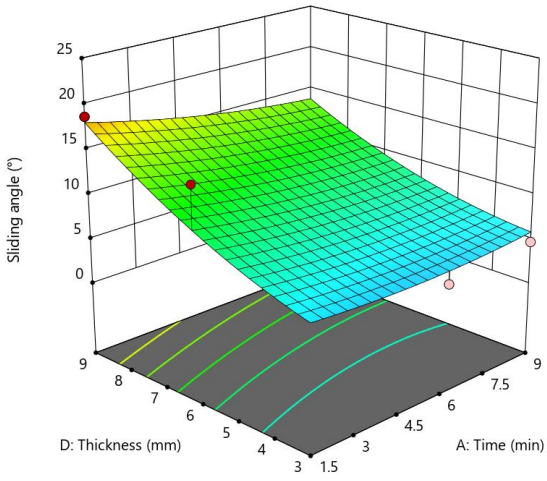

Figure AIII. 7. The 3D response surface relationship between part thickness and curing time on the SA at the lowest level of molding pressure and at the center level of mold temperature.

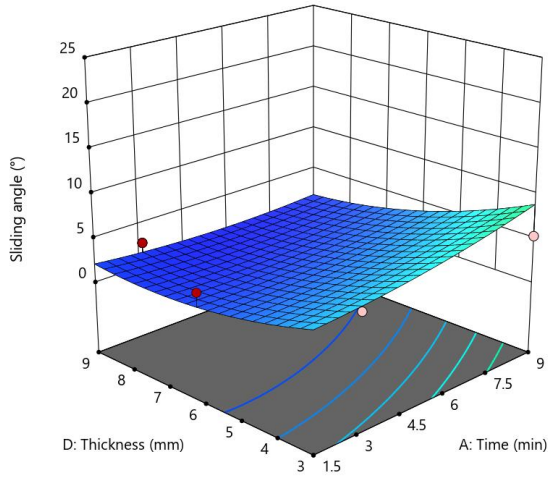

Figure AIII. 8. The 3D response surface relationship between part thickness and curing time on the SA at the highest level of molding pressure and at the center level of mold temperature.

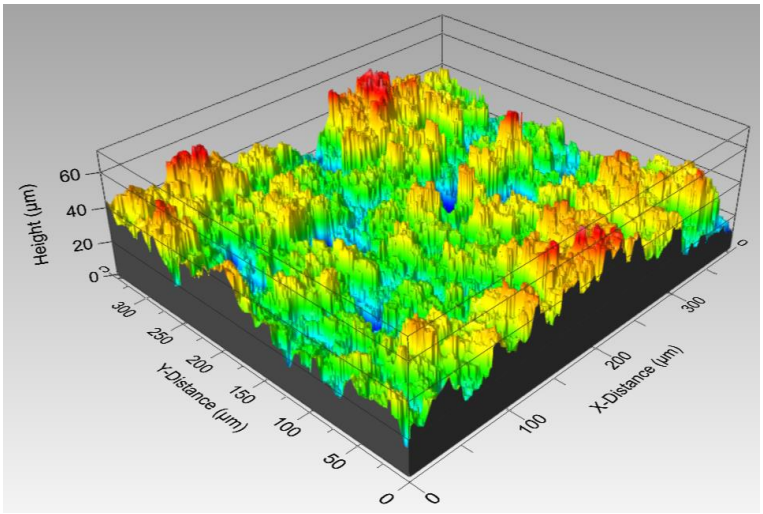

Figure AIII. 9. The 3D surface profile of the aluminum template.

REFERENCES

[1] S. Khatoon, A. A. Khan, and S. Singh, "A review of the flashover performance of high voltage insulators constructed with modern insulating materials," *Transactions on Electrical Electronic Materials,* vol. 18, no. 5, pp. 246-249, 2017.

[2] M. Farzaneh, "Insulator flashover under icing conditions," *IEEE Transactions on Dielectrics Electrical Insulation,* vol. 21, no. 5, pp. 1997-2011, 2014.

[3] http://www.inmr.com/pollution-flashover-insulators/, "Pollution flashover of insulators," 2019.

[4] https://volcanoes.usgs.gov/volcanic_ash/insulator_flashover.html, "Insulator Flashover," 2015.

[5] M. Farzaneh, C. Volat, and J. Zhang, "Role of air gaps on AC withstand voltage of an ice-covered insulator string," *IEEE transactions on dielectrics electrical insulation,* vol. 13, no. 6, pp. 1350-1357, 2006.

[6] M. Ehsani, H. Borsi, E. Gockenbach, J. Morshedian, and G. Bakhshandeh, "An investigation of dynamic mechanical, thermal, and electrical properties of housing materials for outdoor polymeric insulators," *European polymer journal,* vol. 40, no. 11, pp. 2495-2503, 2004.

[7] G. Momen and M. Farzaneh, "Survey of micro/nano filler use to improve silicone rubber for outdoor insulators," *Rev. Adv. Mater. Sci,* vol. 27, no. 1, pp. 1-13, 2011.

[8] http://www.ferrabyrne.co.uk/product/insulators/, "EPDM Insulators," 2019.

[9] K.-L. I. Limited, "Distribution Silicone Insulators," 2013.

[10] K. L. Chrzan, W. L. Vosloo, and J. P. Holtzhausen, "Leakage current on porcelain and silicone insulators under sea or light industrial pollution," *IEEE Transactions on Power Delivery,* vol. 26, no. 3, pp. 2051-2052, 2011.

[11] B. Dong, X. Jiang, J. Hu, L. Shu, and C. Sun, "Effects of artificial polluting methods on AC flashover voltage of composite insulators," *IEEE Transactions on Dielectrics Electrical Insulation,* vol. 19, no. 2, pp. 714-722, 2012.

[12] A. Nekahi, S. McMeekin, and M. Farzaneh, "Effect of pollution severity and dry band location on the flashover characteristics of silicone rubber surfaces," *Electrical Engineering,* vol. 99, no. 3, pp. 1053-1063, 2017.

[13] H. Su, Z. Jia, Z. Sun, Z. Guan, and L. Li, "Field and laboratory tests of insulator flashovers under conditions of light ice accumulation and contamination," *IEEE Transactions on Dielectrics Electrical insulation,* vol. 19, no. 5, pp. 1681-1689, 2012.

[14] M. Farzaneh and W. A. Chisholm, "Effects of ice and snow on the electrical performance of power network insulators," in *Atmospheric Icing of Power Networks*: Springer, 2008, pp. 269-325.

[15] F. Arianpour, M. Farzaneh, and S. Kulinich, "Hydrophobic and ice-retarding properties of doped silicone rubber coatings," *Applied Surface Science,* vol. 265, pp. 546-552, 2013.

[16] Y. Yang, J. Li, J. Hu, Y. Zhao, X. Jiang, and C. Sun, "Experimental study on icing properties of superhydrophobic coatings on insulators," *Gaodianya Jishu/ High Voltage Engineering,* vol. 36, no. 3, pp. 621-626, 2010.

[17] G. Momen and M. Farzaneh, "Study of ice accumulation on nanocomposite semiconducting coatings," in *2010 Annual Report Conference on Electrical Insulation and Dielectic Phenomena,* 2010, pp. 1-4: IEEE.

[18] Z. Xu *et al.*, "Anti-icing performance of RTV coating with different resistivity on insulators," in *2010 Annual Report Conference on Electrical Insulation and Dielectic Phenomena*, 2010, pp. 1-4: IEEE.
[19] M. Dimitropoulou, D. Pylarinos, K. Siderakis, E. Thalassinakis, and M. Danikas, "Comparative investigation of pollution accumulation and natural cleaning for different HV insulators," *Engineering, Technology Applied Science Research*, vol. 5, no. 2, pp. 764-774, 2015.
[20] R. H. Ras and A. Marmur, *Non-wettable surfaces: theory, preparation and applications*. Royal Society of Chemistry, 2016.
[21] J. Jeevahan, M. Chandrasekaran, G. B. Joseph, R. Durairaj, and G. Mageshwaran, "Superhydrophobic surfaces: a review on fundamentals, applications, and challenges," *Journal of Coatings Technology Research*, vol. 15, no. 2, pp. 231-250, 2018.
[22] J. He, *Self-cleaning Coatings: Structure, Fabrication and Application*. Royal Society of Chemistry, 2016.
[23] Q. Yang *et al.*, "Air cushion convection inhibiting icing of self-cleaning surfaces," *ACS applied materials & interfaces*, vol. 8(42), pp. 29169-29178, 2016.
[24] A. Work and Y. Lian, "A critical review of the measurement of ice adhesion to solid substrates," *Progress in Aerospace Sciences*, vol. 98, pp. 1-26, 2018.
[25] S. Kulinich and M. Farzaneh, "Ice adhesion on super-hydrophobic surfaces," *Applied Surface Science*, vol. 255, no. 18, pp. 8153-8157, 2009.
[26] G. Momen, M. Farzaneh, and R. Jafari, "Wettability behaviour of RTV silicone rubber coated on nanostructured aluminium surface," *Applied Surface Science*, vol. 257, no. 15, pp. 6489-6493, 2011.
[27] J. Chen *et al.*, "Superhydrophobic surfaces cannot reduce ice adhesion," *Applied Physics Letters*, vol. 101, no. 11, p. 111603, 2012.
[28] K. Maghsoudi, R. Jafari, G. Momen, and M. Farzaneh, "Micro-nanostructured polymer surfaces using injection molding: A review," *Materials Today Communications*, vol. 13, pp. 126-143, 2017.
[29] S. D. Bhagat and M. C. Gupta, "Superhydrophobic microtextured polycarbonate surfaces," *Surface Coatings Technology*, vol. 270, pp. 117-122, 2015.
[30] E. Vazirinasab, R. Jafari, and G. Momen, "Application of superhydrophobic coatings as a corrosion barrier: A review," *Surface and Coatings Technology*, vol. 341, pp. 40-56, 2018.
[31] M. Zhou, X. Xiong, B. Jiang, and C. Weng, "Fabrication of high aspect ratio nanopillars and micro/nano combined structures with hydrophobic surface characteristics by injection molding," *Applied Surface Science*, vol. 427, pp. 854-860, 2018.
[32] J. Noh, J.-H. Lee, S. Na, H. Lim, and D.-H. Jung, "Fabrication of hierarchically micro-and nano-structured mold surfaces using laser ablation for mass production of superhydrophobic surfaces," *Japanese Journal of Applied Physics*, vol. 49, no. 10R, p. 106502, 2010.
[33] C. Hopmann, C. Behmenburg, U. Recht, and K. Zeuner, "Injection molding of superhydrophobic liquid silicone rubber surfaces," *Silicon*, vol. 6, no. 1, pp. 35-43, 2014.
[34] A. Ahuja *et al.*, "Nanonails: A simple geometrical approach to electrically tunable superlyophobic surfaces," *Langmuir*, vol. 24, no. 1, pp. 9-14, 2008.

[35] K.-M. Lee, C.-V. Ngo, J.-Y. Jeong, E.-c. Jeon, T.-J. Je, and D.-M. Chun, "Fabrication of an anisotropic superhydrophobic polymer surface using compression molding and dip coating," *Coatings*, vol. 7, no. 11, p. 194, 2017.
[36] K. Maghsoudi, G. Momen, R. Jafari, M. Farzaneh, and T. Carreira, "Micro-Nanostructured Silicone Surfaces for Highvoltage Application," in *2018 IEEE Conference on Electrical Insulation and Dielectric Phenomena (CEIDP)*, 2018, pp. 179-182: IEEE.
[37] K. Maghsoudi, G. Momen, R. Jafari, M. Farzaneh, and T. Carreira, "Micro-nanostructured silicone rubber surfaces using compression molding," in *Materials Science Forum*, 2018, vol. 941, pp. 1802-1807: Trans Tech Publ.
[38] G. Momen and M. Farzaneh, "Simple process to fabricate a superhydrophobic coating," *Micro Nano Letters*, vol. 6, no. 6, pp. 405-407, 2011.
[39] R. Chakradhar, V. D. Kumar, J. Rao, and B. J. Basu, "Fabrication of superhydrophobic surfaces based on ZnO–PDMS nanocomposite coatings and study of its wetting behaviour," *Applied Surface Science*, vol. 257, no. 20, pp. 8569-8575, 2011.
[40] K. Golovin, M. Boban, J. M. Mabry, and A. Tuteja, "Designing self-healing superhydrophobic surfaces with exceptional mechanical durability," *ACS applied materials interfaces*, vol. 9, no. 12, pp. 11212-11223, 2017.
[41] S. Das, S. Kumar, S. K. Samal, S. Mohanty, and S. K. Nayak, "A review on superhydrophobic polymer nanocoatings: recent development and applications," *Industrial Engineering Chemistry Research*, vol. 57, no. 8, pp. 2727-2745, 2018.
[42] R. Jafari and M. Farzaneh, "A simple method to create superhydrophobic aluminium surfaces," in *materials science forum*, 2012, vol. 706, pp. 2874-2879: Trans Tech Publ.
[43] I. Yilgor, S. Bilgin, M. Isik, and E. Yilgor, "Facile preparation of superhydrophobic polymer surfaces," *Polymer*, vol. 53, no. 6, pp. 1180-1188, 2012.
[44] G. Momen and M. Farzaneh, "Facile approach in the development of icephobic hierarchically textured coatings as corrosion barrier," *Applied Surface Science*, vol. 299, pp. 41-46, 2014.
[45] G. Momen, R. Jafari, and M. Farzaneh, "Ice repellency behaviour of superhydrophobic surfaces: Effects of atmospheric icing conditions and surface roughness," *Applied Surface Science*, vol. 349, pp. 211-218, 2015.
[46] H. C. Barshilia, A. Ananth, N. Gupta, and C. Anandan, "Superhydrophobic nanostructured Kapton® surfaces fabricated through Ar+ O2 plasma treatment: Effects of different environments on wetting behaviour," *Applied Surface Science*, vol. 268, pp. 464-471, 2013.
[47] H. S. Salapare III, F. Guittard, X. Noblin, E. T. de Givenchy, F. Celestini, and H. Ramos, "Stability of the hydrophilic and superhydrophobic properties of oxygen plasma-treated poly (tetrafluoroethylene) surfaces," *Journal of colloid interface science*, vol. 396, pp. 287-292, 2013.
[48] L. F. Mobarakeh, R. Jafari, and M. Farzaneh, "Robust icephobic, and anticorrosive plasma polymer coating," *Cold Regions Science Technology*, vol. 151, pp. 89-93, 2018.
[49] E. Vazirinasab, R. Jafari, and G. Momen, "Wetting and Self-Cleaning Properties of Silicone Rubber Surfaces Treated by Atmospheric Plasma Jet," in *2018 IEEE*

Conference on Electrical Insulation and Dielectric Phenomena (CEIDP), 2018, pp. 239-242: IEEE.

[50] R. Jafari, G. Momen, and E. Eslami, "Fabrication of icephobic aluminium surfaces by atmospheric plasma jet polymerisation," *Surface Engineering,* vol. 35, no. 5, pp. 450-455, 2019.

[51] E. Vazirinasab, R. Jafari, G. Momen, and T. Carreira, "Simple Fabrication of Superhydrophobic Surfaces Using Atmospheric-Pressure Plasma," in *Materials Science Forum*, 2018, vol. 941, pp. 1808-1814: Trans Tech Publ.

[52] R. Jafari, L. F. Mobarakeh, and M. Farzaneh, "Water-repellency enhancement of nanostructured plasma-polymerized HMDSO coatings using grey-based taguchi method," *Nanoscience Nanotechnology Letters,* vol. 4, no. 3, pp. 369-374, 2012.

[53] E. Vazirinasab, R. Jafari, and G. Momen, "Evaluation of atmospheric-pressure plasma parameters to achieve superhydrophobic and self-cleaning HTV silicone rubber surfaces via a single-step, eco-friendly approach," *Surface and Coating Technology,* vol. 375, pp. 100-111, 2019.

[54] F. Arianpour, M. Farzaneh, and R. Jafari, "Hydrophobic and ice-phobic properties of self-assembled monolayers (SAMs) coatings on AA6061," *Progress in Organic Coatings,* vol. 93, pp. 41-45, 2016.

[55] Y. Wang, J. Xue, Q. Wang, Q. Chen, and J. Ding, "Verification of icephobic/anti-icing properties of a superhydrophobic surface," *ACS applied materials interfaces,* vol. 5, no. 8, pp. 3370-3381, 2013.

[56] L. Wu, J. Zhang, B. Li, L. Fan, L. Li, and A. Wang, "Facile preparation of super durable superhydrophobic materials," *Journal of Colloid and Interface Science,* vol. 432, pp. 31-42, 2014.

[57] I. Sas, R. E. Gorga, J. A. Joines, and K. A. Thoney, "Literature review on superhydrophobic self-cleaning surfaces produced by electrospinning," *Journal of Polymer Science Part B: Polymer Physics,* vol. 50, no. 12, pp. 824-845, 2012.

[58] A. Milionis *et al.*, "Superhydrophobic/superoleophilic magnetic elastomers by laser ablation," *Applied Surface Science,* vol. 351, pp. 74-82, 2015.

[59] J. Zhang, J. Li, and Y. Han, "Superhydrophobic PTFE surfaces by extension," *Macromolecular Rapid Communications,* vol. 25, no. 11, pp. 1105-1108, 2004.

[60] M. A. Nilsson, R. J. Daniello, and J. P. Rothstein, "A novel and inexpensive technique for creating superhydrophobic surfaces using Teflon and sandpaper," *Journal of Physics D: Applied Physics,* vol. 43, no. 4, p. 045301, 2010.

[61] S. E. Lee, K. W. Lee, J.-H. Kim, K.-C. Lee, S. S. Lee, and S. U. Hong, "Mass-producible superhydrophobic surfaces," *Chemical Communications,* vol. 47, no. 43, pp. 12005-12007, 2011.

[62] W.-S. Guan, H.-X. Huang, and B. Wang, "Topographic design and application of hierarchical polymer surfaces replicated by microinjection compression molding," *Journal of Micromechanics Microengineering,* vol. 23, no. 10, p. 105010, 2013.

[63] Y. H. Yeong and M. C. Gupta, "Hot embossed micro-textured thin superhydrophobic Teflon FEP sheets for low ice adhesion," *Surface Coatings Technology,* vol. 313, pp. 17-23, 2017.

[64] M. Nosonovsky and B. Bhushan, "Roughness-induced superhydrophobicity: a way to design non-adhesive surfaces," *Journal of Physics: Condensed Matter,* vol. 20, no. 22, p. 225009, 2008.

[65] N. K. Andersen and R. Taboryski, "Multi-height structures in injection molded polymer," *Microelectronic Engineering,* vol. 141, pp. 211-214, 2015.
[66] A. Pruna, J. Ramiro, and L. Belforte, "Preliminary study on different technological tools and polymeric materials towards superhydrophobic surfaces for automotive applications," *Journal of Physics Chemistry of Solids,* vol. 74, no. 11, pp. 1640-1645, 2013.
[67] P.-C. Lin and S. Yang, "Mechanically switchable wetting on wrinkled elastomers with dual-scale roughness," *Soft Matter,* vol. 5, no. 5, pp. 1011-1018, 2009.
[68] M. Wang *et al.*, "Microstructured superhydrophobic anti-reflection films for performance improvement of photovoltaic devices," *Materials Research Bulletin,* vol. 91, pp. 208-213, 2017.
[69] J. Giboz, T. Copponnex, and P. Mélé, "Microinjection molding of thermoplastic polymers: a review," *Journal of micromechanics microengineering,* vol. 17, no. 6, p. R96, 2007.
[70] R. Jafari, C. Cloutier, A. Allahdini, and G. Momen, "Recent progress and challenges with 3D printing of patterned hydrophobic and superhydrophobic surfaces," *The International Journal of Advanced Manufacturing Technology,* pp. 1-14, 2019.
[71] S. Liparoti, R. Pantani, A. Sorrentino, V. Speranza, and G. Titomanlio, "Hydrophobicity tuning by the fast evolution of mold temperature during injection molding," *Polymers,* vol. 10, no. 3, p. 322, 2018.
[72] J. Vera, A.-C. Brulez, E. Contraires, M. Larochette, S. Valette, and S. Benayoun, "Influence of the polypropylene structure on the replication of nanostructures by injection molding," *Journal of Micromechanics Microengineering,* vol. 25, no. 11, p. 115027, 2015.
[73] H.-K. Koponen *et al.*, "Modification of cycloolefin copolymer and poly (vinyl chloride) surfaces by superimposition of nano-and microstructures," *Applied Surface Science,* vol. 253, no. 12, pp. 5208-5213, 2007.
[74] I. Saarikoski, M. Suvanto, and T. A. Pakkanen, "Modification of polycarbonate surface properties by nano-, micro-, and hierarchical micro–nanostructuring," *Applied Surface Science,* vol. 255, no. 22, pp. 9000-9005, 2009.
[75] E. Puukilainen, H.-K. Koponen, Z. Xiao, S. Suvanto, and T. A. Pakkanen, "Nanostructured and chemically modified hydrophobic polyolefin surfaces," *Colloids Surfaces A: Physicochemical Engineering Aspects,* vol. 287, no. 1-3, pp. 175-181, 2006.
[76] Y. Yoo *et al.*, "Injection molding of a nanostructured plate and measurement of its surface properties," *Current Applied Physics,* vol. 9, no. 2, pp. e12-e18, 2009.
[77] P. Wu, C. Cheng, C. Chang, T. Wu, and J. Wang, "Fabrication of large-area hydrophobic surfaces with femtosecond-laser-structured molds," *Journal of Micromechanics Microengineering,* vol. 21, no. 11, p. 115032, 2011.
[78] D. Jucius, A. Guobienė, and V. Grigaliūnas, "Surface texturing of polytetrafluoroethylene by hot embossing," *Applied Surface Science,* vol. 256, no. 7, pp. 2164-2169, 2010.
[79] Y.-H. Huang, J.-T. Wu, and S.-Y. Yang, "Direct fabricating patterns using stamping transfer process with PDMS mold of hydrophobic nanostructures on surface of micro-cavity," *Microelectronic Engineering,* vol. 88, no. 6, pp. 849-854, 2011.
[80] N. A. Nordin and P. Styring, "Superhydrophobic ski bases for reduced water adhesion," *Procedia Engineering,* vol. 72, pp. 605-610, 2014.

[81] D. Jucius *et al.*, "Hot embossing of PTFE: Towards superhydrophobic surfaces," *Applied Surface Science,* vol. 257, no. 6, pp. 2353-2360, 2011.
[82] J. Kwon, H. Shin, Y. Seo, B. Kim, H. Lee, and J. Lee, "Simple fabrication method of hierarchical nano-pillars using aluminum anodizing processes," *Current Applied Physics,* vol. 9, no. 2, pp. e81-e85, 2009.
[83] H. Tokuhisa, S. Tsukamoto, S. Morita, S. Ise, M. Tomita, and N. Shirakawa, "Fabrication of micro-textured surfaces for a high hydrophobicity by evaporative patterning using screen mesh templates," *Applied Surface Science,* vol. 400, pp. 64-70, 2017.
[84] T. Senn, J. Esquivel, M. Lörgen, N. Sabaté, and B. Löchel, "Replica molding for multilevel micro-/nanostructure replication," *Journal of micromechanics microengineering,* vol. 20, no. 11, p. 115012, 2010.
[85] M. Psarski, J. Marczak, J. Grobelny, and G. Celichowski, "Superhydrophobic surface by replication of laser micromachined pattern in epoxy/alumina nanoparticle composite," *Journal of Nanomaterials,* vol. 2014, p. 41, 2014.
[86] B. K. Lee *et al.*, "Fabrication of a Large-Area Hierarchical Structure Array by Combining Replica Molding and Atmospheric Pressure Plasma Etching," *Advanced Materials Interfaces,* vol. 2, no. 11, p. 1500141, 2015.
[87] T. Young, "III. An essay on the cohesion of fluids," *Philosophical transactions of the royal society of London,* no. 95, pp. 65-87, 1805.
[88] C. Weng, F. Wang, M. Zhou, D. Yang, and B. Jiang, "Fabrication of hierarchical polymer surfaces with superhydrophobicity by injection molding from nature and function-oriented design," *Applied Surface Science,* vol. 436, pp. 224-233, 2018.
[89] R. N. Wenzel, "Resistance of solid surfaces to wetting by water," *Industrial & Engineering Chemistry,* vol. 28, no. 8, pp. 988-994, 1936.
[90] A. Cassie and S. Baxter, "Wettability of porous surfaces," *Transactions of the Faraday society,* vol. 40, pp. 546-551, 1944.
[91] E. Huovinen, J. Hirvi, M. Suvanto, and T. A. Pakkanen, "Micro–micro hierarchy replacing micro–nano hierarchy: a precisely controlled way to produce wear-resistant superhydrophobic polymer surfaces," *Langmuir,* vol. 28, no. 41, pp. 14747-14755, 2012.
[92] B. K. Nayak, P. O. Caffrey, C. R. Speck, and M. C. Gupta, "Superhydrophobic surfaces by replication of micro/nano-structures fabricated by ultrafast-laser-microtexturing," *Applied Surface Science,* vol. 266, pp. 27-32, 2013.
[93] E. Puukilainen, T. Rasilainen, M. Suvanto, and T. A. Pakkanen, "Superhydrophobic polyolefin surfaces: controlled micro-and nanostructures," *Langmuir,* vol. 23, no. 13, pp. 7263-7268, 2007.
[94] J. Feng, M. Huang, and X. Qian, "Fabrication of Polyethylene Superhydrophobic Surfaces by Stretching-Controlled Micromolding," *Macromolecular Materials Engineering,* vol. 294, no. 5, pp. 295-300, 2009.
[95] Y. H. Cho, Y. S. Seo, I. Y. Moon, B. H. Kim, and K. Park, "Facile fabrication of superhydrophobic poly (methyl methacrylate) substrates using ultrasonic imprinting," *Journal of Micromechanics Microengineering,* vol. 23, no. 5, p. 055019, 2013.
[96] D. Hong, I. Ryu, H. Kwon, J.-J. Lee, and S. Yim, "Preparation of superhydrophobic, long-neck vase-like polymer surfaces," *Physical Chemistry Chemical Physics,* vol. 15, no. 28, pp. 11862-11867, 2013.

[97] M. Nosonovsky and B. Bhushan, "Roughness optimization for biomimetic superhydrophobic surfaces," *Microsystem Technologies,* vol. 11, no. 7, pp. 535-549, 2005.
[98] J. M. Stormonth-Darling and N. Gadegaard, "Injection moulding difficult nanopatterns with hybrid polymer inlays," *Macromolecular Materials Engineering,* vol. 297, no. 11, pp. 1075-1080, 2012.
[99] K. Mielonen and T. A. Pakkanen, "Superhydrophobic hierarchical three-level structures on 3D polypropylene surfaces," *Journal of Micromechanics Microengineering,* vol. 29, no. 2, p. 025006, 2019.
[100] E. Bormashenko, R. Grynyov, G. Chaniel, H. Taitelbaum, and Y. Bormashenko, "Robust technique allowing manufacturing superoleophobic surfaces," *Applied Surface Science,* vol. 270, pp. 98-103, 2013.
[101] I. Saarikoski, F. Joki-Korpela, M. Suvanto, T. T. Pakkanen, and T. A. Pakkanen, "Superhydrophobic elastomer surfaces with nanostructured micronails," *Surface Science,* vol. 606, no. 1-2, pp. 91-98, 2012.
[102] M. Despa, K. Kelly, and J. Collier, "Injection molding of polymeric LIGA HARMs," *Microsystem Technologies,* vol. 6, no. 2, pp. 60-66, 1999.
[103] O. Rötting, W. Röpke, H. Becker, and C. Gärtner, "Polymer microfabrication technologies," *Microsystem Technologies,* vol. 8, no. 1, pp. 32-36, 2002.
[104] R. H. Pedersen, Q. Xu, J. M. Stormonth-Darling, and N. Gadegaard, "Strategies for high quality injection moulding of polymer nanopillars," *Macromolecular Materials Engineering,* vol. 300, no. 2, pp. 172-180, 2015.
[105] W. Michaeli and T. Kamps, "Micro assembly injection moulding with plasma treated inserts," *Microsystem Technologies,* vol. 14, no. 12, pp. 1903-1907, 2008.
[106] T. Jiang *et al.*, "Ultrashort picosecond laser processing of micro-molds for fabricating plastic parts with superhydrophobic surfaces," *Applied Physics A,* vol. 108, no. 4, pp. 863-869, 2012.
[107] D.-M. Chun, G. Davaasuren, C.-V. Ngo, C.-S. Kim, G.-Y. Lee, and S.-H. Ahn, "Fabrication of transparent superhydrophobic surface on thermoplastic polymer using laser beam machining and compression molding for mass production," *CIRP Annals,* vol. 63, no. 1, pp. 525-528, 2014.
[108] D. Masato, M. Sorgato, and G. Lucchetta, "Analysis of the influence of part thickness on the replication of micro-structured surfaces by injection molding," *Materials & Design,* vol. 95, pp. 219-224, 2016.
[109] W. Michaeli, F. Klaiber, and S. Scholz, "Investigations in variothermal injection moulding of microstructures and microstructured surfaces," *Multi-Material Micro Manufacture,* 2008.
[110] G. Lucchetta, M. Sorgato, S. Carmignato, and E. Savio, "Investigating the technological limits of micro-injection molding in replicating high aspect ratio micro-structured surfaces," *CIRP Annals-Manufacturing Technology,* vol. 63, no. 1, pp. 521-524, 2014.
[111] G. Lucchetta, E. Ferraris, G. Tristo, and D. Reynaerts, "Influence of mould thermal properties on the replication of micro parts via injection moulding," *Procedia CIRP,* vol. 2, pp. 113-117, 2012.
[112] M. Packianather, C. Griffiths, and W. Kadir, "Micro injection moulding process parameter tuning," *Procedia CIRP,* vol. 33, pp. 400-405, 2015.

[113] C. Griffiths, G. Tosello, S. Dimov, S. Scholz, A. Rees, and B. Whiteside, "Characterisation of demoulding parameters in micro-injection moulding," *Microsystem Technologies,* vol. 21, no. 8, pp. 1677-1690, 2015.
[114] C. Griffiths, S. Dimov, S. Scholz, G. Tosello, and A. Rees, "Influence of injection and cavity pressure on the Demoulding force in micro-injection moulding," *Journal of Manufacturing Science and Engineering,* vol. 136, no. 3, p. 031014, 2014.
[115] A.-C. Liou and R.-H. Chen, "Injection molding of polymer micro-and sub-micron structures with high-aspect ratios," *The International Journal of Advanced Manufacturing Technology,* vol. 28, no. 11-12, pp. 1097-1103, 2006.
[116] M. Matschuk and N. B. Larsen, "Injection molding of high aspect ratio sub-100 nm nanostructures," *Journal of Micromechanics and Microengineering,* vol. 23, no. 2, p. 025003, 2012.
[117] Q. Su and M. D. Gilchrist, "Demolding forces for micron-sized features during micro-injection molding," *Polymer Engineering & Science,* vol. 56, no. 7, pp. 810-816, 2016.
[118] K. Delaney, G. Bissacco, and D. Kennedy, "A structured review and classification of demolding issues and proven solutions," *International Polymer Processing,* vol. 27, no. 1, pp. 77-90, 2012.
[119] G. R. Berger, C. Steffel, and W. Friesenbichler, "A study on the role of wetting parameters on friction in injection moulding," *International Journal of Materials and Product Technology,* vol. 52, no. 1-2, pp. 193-211, 2016.
[120] C. H. Wu and W. J. Liang, "Effects of geometry and injection-molding parameters on weld-line strength," *Polymer Engineering & Science,* vol. 45, no. 7, pp. 1021-1030, 2005.
[121] J. Giboz, T. Copponnex, and P. Mélé, "Microinjection molding of thermoplastic polymers: a review," *Journal of Micromechanics and Microengineering,* vol. 17, no. 6, p. R96, 2007.
[122] Z. Peng, L. Gang, T. Yangchao, and T. Xuehong, "The properties of demoulding of Ni and Ni-PTFE moulding inserts," *Sensors and Actuators A: Physical,* vol. 118, no. 2, pp. 338-341, 2005.
[123] B. Liu *et al.*, "Study on hierarchical structured PDMS for surface super-hydrophobicity using imprinting with ultrafast laser structured models," *Applied Surface Science,* vol. 364, pp. 528-538, 2016.
[124] T. Lv *et al.*, "Superhydrophobic surface with shape memory micro/nanostructure and its application in rewritable chip for droplet storage," *ACS nano,* vol. 10, no. 10, pp. 9379-9386, 2016.
[125] K. Maghsoudi, G. Momen, R. Jafari, and M. Farzaneh, "Direct replication of micro-nanostructures in the fabrication of superhydrophobic silicone rubber surfaces by compression molding," *Applied Surface Science,* vol. 458, pp. 619-628, 2018.
[126] C.-V. Ngo, G. Davaasuren, H.-S. Oh, and D.-M. Chun, "Transparency and superhydrophobicity of cone-shaped micropillar array textured polydimethylsiloxane," *International Journal of Precision Engineering Manufacturing,* vol. 16, no. 7, pp. 1347-1353, 2015.
[127] Z. Zhan *et al.*, "Creating Superhydrophobic Polymer Surfaces with Superstrong Resistance to Harsh Cleaning and Mechanical Abrasion Fabricated by Scalable One-Step Thermal-Imprinting," *Advanced Materials Interfaces,* p. 1900240, 2019.

[128] M. Heckele and W. Schomburg, "Review on micro molding of thermoplastic polymers," *Journal of Micromechanics Microengineering,* vol. 14, no. 3, p. R1, 2003.
[129] K. Mielonen, M. Suvanto, and T. Pakkanen, "Curved hierarchically micro-micro structured polypropylene surfaces by injection molding," *Journal of Micromechanics Microengineering,* vol. 27, no. 1, 2017.
[130] Y. Jiang, M. Suvanto, and T. A. Pakkanen, "Durable and mass producible polymer surface structures with different combinations of micro–micro hierarchy," *Journal of Micromechanics Microengineering,* vol. 26, no. 1, p. 015009, 2015.
[131] B.-Y. Cao, J. Kong, Y. Xu, K.-L. Yung, and A. Cai, "Polymer nanowire arrays with high thermal conductivity and superhydrophobicity fabricated by a nano-molding technique," *Heat Transfer Engineering,* vol. 34, no. 2-3, pp. 131-139, 2013.
[132] C. W. Berendsen, M. Škereň, D. Najdek, and F. Černý, "Superhydrophobic surface structures in thermoplastic polymers by interference lithography and thermal imprinting," *Applied Surface Science,* vol. 255, no. 23, pp. 9305-9310, 2009.
[133] E. Celia, T. Darmanin, E. T. de Givenchy, S. Amigoni, and F. Guittard, "Recent advances in designing superhydrophobic surfaces," *Journal of colloid interface science,* vol. 402, pp. 1-18, 2013.
[134] S. F. Toosi, S. Moradi, M. Ebrahimi, and S. G. Hatzikiriakos, "Microfabrication of polymeric surfaces with extreme wettability using hot embossing," *Applied Surface Science,* vol. 378, pp. 426-434, 2016.
[135] D. Gong, J. Long, P. Fan, D. Jiang, H. Zhang, and M. Zhong, "Thermal stability of micro–nano structures and superhydrophobicity of polytetrafluoroethylene films formed by hot embossing via a picosecond laser ablated template," *Applied Surface Science,* vol. 331, pp. 437-443, 2015.
[136] C.-H. Lim, S.-Y. Han, J.-D. Eo, K. Kim, and W.-B. Kim, "Superhydrophobic hierarchical structures produced through novel low-cost stamp fabrication and hot embossing of thermoplastic film," *Journal of Mechanical Science Technology,* vol. 29, no. 12, pp. 5107-5111, 2015.
[137] Z. Yan, X. Liang, Y. Gao, and Y. Liu, "Aging and self-healing properties of superhydrophobic silicone rubber," *IEEE Transactions on Dielectrics Electrical Insulation,* vol. 23, no. 6, pp. 3531-3538, 2016.
[138] M. Röhrig *et al.*, "Nanofur for biomimetic applications," *Advanced Materials Interfaces,* vol. 1, no. 4, p. 1300083, 2014.
[139] A. Y. Y. Ho *et al.*, "Lotus bioinspired superhydrophobic, self-cleaning surfaces from hierarchically assembled templates," *Journal of Polymer Science Part B: Polymer Physics,* vol. 52, no. 8, pp. 603-609, 2014.
[140] M. Röhrig *et al.*, "Hot pulling and embossing of hierarchical nano-and micro-structures," *Journal of Micromechanics Microengineering,* vol. 23, no. 10, p. 105014, 2013.
[141] F. Vüllers *et al.*, "Bioinspired superhydrophobic highly transmissive films for optical applications," *Small,* vol. 12, no. 44, pp. 6144-6152, 2016.
[142] W. Sun, Y. Zhou, and Z. Chen, "Fabrication of honeycomb-structured porous film from polystyrene via polymeric particle-assisted breath figures method," *Macromolecular Research,* vol. 21, no. 4, pp. 414-418, 2013.

[143] J. Huang *et al.*, "Research on Hydrophobic and Superhydrophobic Properties of Patterned Structure with Controllable Nano to Microstructural Hierarchy," *Macromolecular Chemistry Physics*, vol. 216, no. 23, pp. 2279-2286, 2015.
[144] A. T. Mulroney and M. C. Gupta, "Optically transparent superhydrophobic polydimethylsiloxane by periodic surface microtexture," *Surface Coatings Technology*, vol. 325, pp. 308-317, 2017.
[145] S.-H. Park, S. Lee, D. Moreira, P. R. Bandaru, I. Han, and D.-J. Yun, "Bioinspired superhydrophobic surfaces, fabricated through simple and scalable roll-to-roll processing," *Scientific reports*, vol. 5, p. 15430, 2015.
[146] M. Sun *et al.*, "Artificial lotus leaf by nanocasting," *Langmuir*, vol. 21, no. 19, pp. 8978-8981, 2005.
[147] S. Verbanic, O. Brady, A. Sanda, C. Gustafson, and Z. J. Donhauser, "A novel general chemistry laboratory: Creation of biomimetic superhydrophobic surfaces through replica molding," *Journal of Chemical Education*, vol. 91, no. 9, pp. 1477-1480, 2014.
[148] P. Guo, Y. Zheng, C. Liu, J. Ju, and L. Jiang, "Directional shedding-off of water on natural/bio-mimetic taper-ratchet array surfaces," *Soft Matter*, vol. 8, no. 6, pp. 1770-1775, 2012.
[149] Z. Ortega, N. Díaz, M. Alemán-Domínguez, A. Romero, M. Monzón, and J. Gómez-Tejedor, "Fabrication of Superhydrophobic Polyethylene Parts by Rotomolding," *International Polymer Processing*, vol. 31, no. 1, pp. 104-107, 2016.
[150] W.-S. Guan, H.-X. Huang, and A.-F. Chen, "Tuning 3D topography on biomimetic surface for efficient self-cleaning and microfluidic manipulation," *Journal of Micromechanics Microengineering*, vol. 25, no. 3, p. 035001, 2015.
[151] W. Barthlott and C. Neinhuis, "Purity of the sacred lotus, or escape from contamination in biological surfaces," *Planta*, vol. 202, no. 1, pp. 1-8, 1997.
[152] I. P. Parkin and R. G. Palgrave, "Self-cleaning coatings," *Journal of Materials Chemistry*, vol. 15, no. 17, pp. 1689-1695, 2005.
[153] M. Zhang, S. Feng, L. Wang, and Y. Zheng, "Lotus effect in wetting and self-cleaning," *Biotribology*, vol. 5, pp. 31-43, 2016.
[154] Y. C. Jung and B. Bhushan, "Mechanically durable carbon nanotube− composite hierarchical structures with superhydrophobicity, self-cleaning, and low-drag," *ACS Nano*, vol. 3, no. 12, pp. 4155-4163, 2009.
[155] B. Bhushan, Y. C. Jung, and K. Koch, "Self-cleaning efficiency of artificial superhydrophobic surfaces," *Langmuir*, vol. 25, no. 5, pp. 3240-3248, 2009.
[156] B. Bhushan and Y. C. Jung, "Natural and biomimetic artificial surfaces for superhydrophobicity, self-cleaning, low adhesion, and drag reduction," *Progress in Materials Science*, vol. 56, no. 1, pp. 1-108, 2011.
[157] M. Nosonovsky and B. Bhushan, "Multiscale friction mechanisms and hierarchical surfaces in nano-and bio-tribology," *Materials Science Engineering: R: Reports*, vol. 58, no. 3-5, pp. 162-193, 2007.
[158] M. Nosonovsky and B. Bhushan, "Do hierarchical mechanisms of superhydrophobicity lead to self-organized criticality?," *Scripta Materialia*, vol. 59, no. 9, pp. 941-944, 2008.
[159] H. Bagheri, M. Aliofkhazraei, H. M. Forooshani, and A. S. Rouhaghdam, "Facile fabrication of uniform hierarchical structured (UHS) nanocomposite surface with

high water repellency and self-cleaning properties," *Applied Surface Science,* vol. 436, pp. 1134-1146, 2018.
[160] A. Nakajima, K. Hashimoto, T. Watanabe, K. Takai, G. Yamauchi, and A. Fujishima, "Transparent superhydrophobic thin films with self-cleaning properties," *Langmuir,* vol. 16, no. 17, pp. 7044-7047, 2000.
[161] Q. Shang and Y. Zhou, "Fabrication of transparent superhydrophobic porous silica coating for self-cleaning and anti-fogging," *Ceramics International,* vol. 42, no. 7, pp. 8706-8712, 2016.
[162] S. Nishimoto and B. Bhushan, "Bioinspired self-cleaning surfaces with superhydrophobicity, superoleophobicity, and superhydrophilicity," *Rsc Advances,* vol. 3, no. 3, pp. 671-690, 2013.
[163] H. Hanaei, M. K. Assadi, and R. Saidur, "Highly efficient antireflective and self-cleaning coatings that incorporate carbon nanotubes (CNTs) into solar cells: A review," *Renewable Sustainable Energy Reviews,* vol. 59, pp. 620-635, 2016.
[164] Z. Liu, W. Wang, R. Xie, X.-J. Ju, and L.-Y. Chu, "Stimuli-responsive smart gating membranes," *Chemical Society Reviews,* vol. 45, no. 3, pp. 460-475, 2016.
[165] G. Momen, M. Farzaneh, and A. Nekahi, "Properties and applications of superhydrophobic coatings in high voltage outdoor insulation: A review," *IEEE Transactions on Dielectrics and Electrical Insulation,* vol. 24, no. 6, pp. 3630-3646, 2017.
[166] P. Charalampidis, M. Albano, H. Griffiths, A. Haddad, and R. T. Waters, "Silicone rubber insulators for polluted environments part 1: enhanced artificial pollution tests," *IEEE Transactions on Dielectrics and Electrical Insulation,* vol. 21, no. 2, pp. 740-748, 2014.
[167] I. E. Commission, "Artificial pollution tests on high-voltage insulators to be used on AC systems," *International Standard IEC,* vol. 507, 1991.
[168] B. Dong, X. Jiang, J. Hu, L. Shu, and C. Sun, "Effects of artificial polluting methods on AC flashover voltage of composite insulators," *IEEE Transactions on Dielectrics and Electrical Insulation,* vol. 19, no. 2, 2012.
[169] D. Swift, C. Spellman, and A. Haddad, "Hydrophobicity transfer from silicone rubber to adhering pollutants and its effect on insulator performance," *IEEE Transactions on Dielectrics and Electrical Insulation,* vol. 13, no. 4, pp. 820-829, 2006.
[170] I. Gutman and A. Dernfalk, "Pollution tests for polymeric insulators made of hydrophobicity transfer materials," *IEEE Transactions on Dielectrics and Electrical Insulation,* vol. 17, no. 2, 2010.
[171] N. Yu, X. Xiao, Z. Ye, G. J. S. Pan, and C. Technology, "Facile preparation of durable superhydrophobic coating with self-cleaning property," vol. 347, pp. 199-208, 2018.
[172] D. Eisenberg, S. Laustsen, and J. Stege, "Wind turbine blade coating leading edge rain erosion model: Development and validation," *Wind Energy,* 2018.
[173] R. Jafari, G. Momen, and E. Eslami, "Fabrication of icephobic aluminium surfaces by atmospheric plasma jet polymerisation," *Surface Engineering,* pp. 1-6, 2018.
[174] M. Susoff, K. Siegmann, C. Pfaffenroth, and M. Hirayama, "Evaluation of icephobic coatings—Screening of different coatings and influence of roughness," *Applied Surface Science,* vol. 282, pp. 870-879, 2013.

[175] R. Menini, Z. Ghalmi, and M. Farzaneh, "Highly resistant icephobic coatings on aluminum alloys," *Cold Regions Science Technology*, vol. 65, no. 1, pp. 65-69, 2011.
[176] R. Jafari, G. Momen, and M. Farzaneh, "Durability enhancement of icephobic fluoropolymer film," *Journal of Coatings Technology Research*, vol. 13, no. 3, pp. 405-412, 2016.
[177] F. Wang, W. Ding, J. He, and Z. Zhang, "Phase transition enabled durable anti-icing surfaces and its DIY design," *Chemical Engineering Journal*, vol. 360, pp. 243-249, 2019.
[178] D. Chen, M. D. Gelenter, M. Hong, R. E. Cohen, and G. H. McKinley, "Icephobic surfaces induced by interfacial nonfrozen water," *ACS applied materials interfaces*, vol. 9, no. 4, pp. 4202-4214, 2017.
[179] Z. A. Janjua *et al.*, "Performance and durability tests of smart icephobic coatings to reduce ice adhesion," *Applied Surface Science*, vol. 407, pp. 555-564, 2017.
[180] R. Menini and M. Farzaneh, "Advanced icephobic coatings," *Journal of adhesion science technology*, vol. 25, no. 9, pp. 971-992, 2011.
[181] Q. Li and Z. Guo, "Fundamentals of icing and common strategies for designing biomimetic anti-icing surfaces," *Journal of Materials Chemistry A*, vol. 6, no. 28, pp. 13549-13581, 2018.
[182] M. I. Jamil, A. Ali, F. Haq, Q. Zhang, X. Zhan, and F. Chen, "Icephobic strategies and materials with superwettability: design principles and mechanism," *Langmuir*, vol. 34, no. 50, pp. 15425-15444, 2018.
[183] A. Alizadeh *et al.*, "Dynamics of ice nucleation on water repellent surfaces," *Langmuir*, vol. 28, no. 6, pp. 3180-3186, 2012.
[184] P. Guo, Y. Zheng, M. Wen, C. Song, Y. Lin, and L. Jiang, "Icephobic/anti-icing properties of micro/nanostructured surfaces," *Advanced Materials*, vol. 24, no. 19, pp. 2642-2648, 2012.
[185] Y. Shen, H. Tao, S. Chen, L. Zhu, T. Wang, and J. Tao, "Icephobic/anti-icing potential of superhydrophobic Ti6Al4V surfaces with hierarchical textures," *Rsc Advances*, vol. 5, no. 3, pp. 1666-1672, 2015.
[186] C. Wei, B. Jin, Q. Zhang, X. Zhan, and F. Chen, "Anti-icing performance of super-wetting surfaces from icing-resistance to ice-phobic aspects: Robust hydrophobic or slippery surfaces," *Journal of Alloys Compounds*, vol. 765, pp. 721-730, 2018.
[187] E. J. Y. Ling, V. Uong, J.-S. b. Renault-Crispo, A.-M. Kietzig, and P. Servio, "Reducing ice adhesion on nonsmooth metallic surfaces: wettability and topography effects," *ACS applied materials interfaces*, vol. 8, no. 13, pp. 8789-8800, 2016.
[188] P. Hao, C. Lv, and X. Zhang, "Freezing of sessile water droplets on surfaces with various roughness and wettability," *Applied physics letters*, vol. 104, no. 16, p. 161609, 2014.
[189] P. Eberle, M. K. Tiwari, T. Maitra, and D. Poulikakos, "Rational nanostructuring of surfaces for extraordinary icephobicity," *Nanoscale*, vol. 6, no. 9, pp. 4874-4881, 2014.
[190] M. Zou, S. Beckford, R. Wei, C. Ellis, G. Hatton, and M. Miller, "Effects of surface roughness and energy on ice adhesion strength," *Applied Surface Science*, vol. 257, no. 8, pp. 3786-3792, 2011.
[191] Y. He, C. Jiang, X. Cao, J. Chen, W. Tian, and W. Yuan, "Reducing ice adhesion by hierarchical micro-nano-pillars," *Applied Surface Science*, vol. 305, pp. 589-595, 2014.

[192] L. Mishchenko, B. Hatton, V. Bahadur, J. A. Taylor, T. Krupenkin, and J. Aizenberg, "Design of ice-free nanostructured surfaces based on repulsion of impacting water droplets," *ACS nano,* vol. 4, no. 12, pp. 7699-7707, 2010.
[193] E. J. Y. Ling, V. Uong, J.-S. b. Renault-Crispo, A.-M. Kietzig, and P. Servio, "Reducing ice adhesion on nonsmooth metallic surfaces: wettability and topography effects," *ACS Applied Materials & Interfaces,* vol. 8, no. 13, pp. 8789-8800, 2016.
[194] C. E. Cansoy, H. Y. Erbil, O. Akar, and T. Akin, "Effect of pattern size and geometry on the use of Cassie–Baxter equation for superhydrophobic surfaces," *Colloids Surfaces A: Physicochemical Engineering Aspects,* vol. 386, no. 1-3, pp. 116-124, 2011.
[195] E. Jenner, C. Barbier, and B. D'Urso, "Durability of hydrophobic coatings for superhydrophobic aluminum oxide," *Applied Surface Science,* vol. 282, pp. 73-76, 2013.
[196] H. Zhou, H. Wang, H. Niu, A. Gestos, X. Wang, and T. Lin, "Fluoroalkyl silane modified silicone rubber/nanoparticle composite: a super durable, robust superhydrophobic fabric coating," *Advanced Materials,* vol. 24, no. 18, pp. 2409-2412, 2012.
[197] K. Golovin, M. Boban, J. M. Mabry, and A. Tuteja, "Designing Self-Healing Superhydrophobic Surfaces with Exceptional Mechanical Durability," *ACS Applied Materials & Interfaces,* vol. 9, no. 12, pp. 11212-11223, 2017.
[198] N. Wang, D. Xiong, Y. Deng, Y. Shi, and K. Wang, "Mechanically robust superhydrophobic steel surface with anti-icing, UV-durability, and corrosion resistance properties," *ACS Applied Materials & Interfaces,* vol. 7, no. 11, pp. 6260-6272, 2015.
[199] E. Huovinen, L. Takkunen, T. Korpela, M. Suvanto, T. T. Pakkanen, and T. A. Pakkanen, "Mechanically robust superhydrophobic polymer surfaces based on protective micropillars," *Langmuir,* vol. 30, no. 5, pp. 1435-1443, 2014.
[200] A. Milionis, E. Loth, and I. S. Bayer, "Recent advances in the mechanical durability of superhydrophobic materials," *Advances in Colloid and Interface Science,* vol. 229, pp. 57-79, 2016.
[201] L. Boinovich, A. M. Emelyanenko, and A. S. Pashinin, "Analysis of long-term durability of superhydrophobic properties under continuous contact with water," *ACS Applied Materials & Interfaces,* vol. 2, no. 6, pp. 1754-1758, 2010.
[202] C.-H. Xue and J.-Z. Ma, "Long-lived superhydrophobic surfaces," *Journal of Materials Chemistry A,* vol. 1, no. 13, pp. 4146-4161, 2013.
[203] T. Verho, C. Bower, P. Andrew, S. Franssila, O. Ikkala, and R. H. Ras, "Mechanically durable superhydrophobic surfaces," *Advanced Materials,* vol. 23, no. 5, pp. 673-678, 2011.
[204] C. Su, Y. Xu, F. Gong, F. Wang, and C. Li, "The abrasion resistance of a superhydrophobic surface comprised of polyurethane elastomer," *Soft Matter,* vol. 6, no. 24, pp. 6068-6071, 2010.
[205] M. Li, Y. Li, F. Xue, and X. Jing, "Water-based acrylate copolymer/silica hybrids for facile preparation of robust and durable superhydrophobic coatings," *Applied Surface Science,* vol. 447, pp. 489-499, 2018.
[206] F. Wang, S. Yu, J. Ou, M. Xue, and W. Li, "Mechanically durable superhydrophobic surfaces prepared by abrading," *Journal of Applied Physics,* vol. 114, no. 12, p. 124902, 2013.

[207] J. Zhang, B. Li, L. Wu, and A. Wang, "Facile preparation of durable and robust superhydrophobic textiles by dip coating in nanocomposite solution of organosilanes," *Chemical Communications,* vol. 49, no. 98, pp. 11509-11511, 2013.
[208] Q. L. Wang, D. D. Zhu, Y. Chen, and X. D. Guo, "A fabrication method of microneedle molds with controlled microstructures," *Materials Science and Engineering: C,* vol. 65, pp. 135-142, 2016.
[209] X. Deng *et al.*, "Transparent, thermally stable and mechanically robust superhydrophobic surfaces made from porous silica capsules," *Advanced Materials,* vol. 23, no. 26, pp. 2962-2965, 2011.
[210] S. S. Latthe *et al.*, "A mechanically bendable superhydrophobic steel surface with self-cleaning and corrosion-resistant properties," *Journal of Materials Chemistry A,* vol. 3, no. 27, pp. 14263-14271, 2015.
[211] W.-H. Huang and C.-S. Lin, "Robust superhydrophobic transparent coatings fabricated by a low-temperature sol–gel process," *Applied Surface Science,* vol. 305, pp. 702-709, 2014.
[212] Z. He *et al.*, "Fabrication of a transparent superamphiphobic coating with improved stability," *Soft Matter,* vol. 7, no. 14, pp. 6435-6443, 2011.
[213] Y. Yoo, J. B. You, W. Choi, and S. G. Im, "A stacked polymer film for robust superhydrophobic fabrics," *Polymer Chemistry,* vol. 4, no. 5, pp. 1664-1671, 2013.
[214] Z. She, Q. Li, Z. Wang, L. Li, F. Chen, and J. Zhou, "Researching the fabrication of anticorrosion superhydrophobic surface on magnesium alloy and its mechanical stability and durability," *Chemical Engineering Journal,* vol. 228, pp. 415-424, 2013.
[215] J. Guo, H. Qian, P. Liu, and J. Ma, "Fabrication of durability superhydrophobic LDH coating on zinc sheet surface via NH4F-assisted in-situ growth and post-modification for enhancing anti-corrosion and anti-icing," *Applied Clay Science,* vol. 180, p. 105182, 2019.
[216] Y. Gao, J. Wang, X. Liang, Z. Yan, Y. Liu, and Y. Cai, "Investigation on permeation properties of liquids into HTV silicone rubber materials," *IEEE Transactions on Dielectrics and Electrical Insulation,* vol. 21, no. 6, pp. 2428-2437, 2014.
[217] M. Amin, M. Akbar, and M. Salman, "Composite insulators and their aging: An overview," *Science in China Series E: Technological Sciences,* vol. 50, no. 6, pp. 697-713, 2007.
[218] Z. Yan, X. Liang, C. Wu, W. Bao, S. Li, and Y. Liu, "Aging and recovery of superhydrophobic silicone rubber under electrical and non-electrical stresses," in *Electrical Insulation and Dielectric Phenomena (CEIDP), 2015 IEEE Conference on*, 2015, pp. 189-192: IEEE.
[219] M. Bhagyashree, K. Shivabasappa, S. Raavichandran, and S. Kumar, "Study of HTV Silicone Rubber with Different Concentrations of Filler ATH," *International Journal on Emerging Technologies,* vol. 6, no. 2, p. 72, 2015.
[220] D. Bodas and C. Khan-Malek, "Formation of more stable hydrophilic surfaces of PDMS by plasma and chemical treatments," *Microelectronic engineering,* vol. 83, no. 4-9, pp. 1277-1279, 2006.
[221] N. J. Shirtcliffe, G. McHale, M. I. Newton, G. Chabrol, and C. C. Perry, "Dual-Scale Roughness Produces Unusually Water-Repellent Surfaces," *Advanced Materials,* vol. 16, no. 21, pp. 1929-1932, 2004.

[222] H. Liao, A.-S. Andersson, D. Sutherland, S. Petronis, B. Kasemo, and P. Thomsen, "Response of rat osteoblast-like cells to microstructured model surfaces in vitro," *Biomaterials,* vol. 24, no. 4, pp. 649-654, 2003.
[223] R. Jafari and M. Farzaneh, "Development a simple method to create the superhydrophobic composite coatings," *Journal of Composite Materials,* vol. 47, no. 25, pp. 3125-3129, 2013.
[224] R. Jafari, S. Asadollahi, and M. Farzaneh, "Applications of plasma technology in development of superhydrophobic surfaces," *Plasma Chemistry and Plasma Processing,* vol. 33, no. 1, pp. 177-200, 2013.
[225] X. Liu, W. Wu, X. Wang, Z. Luo, Y. Liang, and F. Zhou, "A replication strategy for complex micro/nanostructures with superhydrophobicity and superoleophobicity and high contrast adhesion," *Soft matter,* vol. 5, no. 16, pp. 3097-3105, 2009.
[226] P. Zylka, "On the surface performance of superhydrophobic silicone rubber specimens fabricated by direct replica method," *IEEE Transactions on Dielectrics and Electrical Insulation,* vol. 21, no. 3, pp. 1183-1188, 2014.
[227] R. Liao, Z. Zuo, C. Guo, Y. Yuan, and A. Zhuang, "Fabrication of superhydrophobic surface on aluminum by continuous chemical etching and its anti-icing property," *Applied Surface Science,* vol. 317, pp. 701-709, 2014.
[228] D. K. Sarkar, M. Farzaneh, and R. W. Paynter, "Superhydrophobic properties of ultrathin rf-sputtered Teflon films coated etched aluminum surfaces," *Materials letters,* vol. 62, no. 8, pp. 1226-1229, 2008.
[229] R. Menini and M. Farzaneh, "Elaboration of Al 2 O 3/PTFE icephobic coatings for protecting aluminum surfaces," *Surface and Coatings Technology,* vol. 203, no. 14, pp. 1941-1946, 2009.
[230] Y. Liu, J. Liu, S. Li, Y. Wang, Z. Han, and L. Ren, "One-step method for fabrication of biomimetic superhydrophobic surface on aluminum alloy," *Colloids and Surfaces A: Physicochemical and Engineering Aspects,* vol. 466, pp. 125-131, 2015.
[231] S. Zheng *et al.*, "Development of stable superhydrophobic coatings on aluminum surface for corrosion-resistant, self-cleaning, and anti-icing applications," *Materials & Design,* vol. 93, pp. 261-270, 2016.
[232] Y. Zhang, X. Yu, H. Wu, and J. Wu, "Facile fabrication of superhydrophobic nanostructures on aluminum foils with controlled-condensation and delayed-icing effects," *Applied Surface Science,* vol. 258, no. 20, pp. 8253-8257, 2012.
[233] R. Jafari and M. Farzaneh, "Fabrication of superhydrophobic nanostructured surface on aluminum alloy," *Applied Physics A: Materials Science & Processing,* vol. 102, no. 1, pp. 195-199, 2011.
[234] M. Vlaskin, E. Shkolnikov, and A. Bersh, "Oxidation kinetics of micron-sized aluminum powder in high-temperature boiling water," *international journal of hydrogen energy,* vol. 36, no. 11, pp. 6484-6495, 2011.
[235] M. Rahimi, A. Afshari, and E. Thormann, "Effect of aluminum substrate surface modification on wettability and freezing delay of water droplet at subzero temperatures," *ACS Applied Materials & Interfaces,* vol. 8, no. 17, pp. 11147-11153, 2016.
[236] R. Jafari, R. Menini, and M. Farzaneh, "Superhydrophobic and icephobic surfaces prepared by RF-sputtered polytetrafluoroethylene coatings," *Applied Surface Science,* vol. 257, no. 5, pp. 1540-1543, 2010.

[237] P. Hernández, A. Murawko, J. Martínez, G. Peláez, and E. Ares, "Replication of micro laser textures by injection molding," *Procedia Engineering*, vol. 63, pp. 885-894, 2013.
[238] B. K. Nayak and M. C. Gupta, "Self-organized micro/nano structures in metal surfaces by ultrafast laser irradiation," *Optics and Lasers in Engineering*, vol. 48, no. 10, pp. 940-949, 2010.
[239] R. Jagdheesh, J. García-Ballesteros, and J. Ocaña, "One-step fabrication of near superhydrophobic aluminum surface by nanosecond laser ablation," *Applied Surface Science*, vol. 374, pp. 2-11, 2016.
[240] Z. J. Davis *et al.*, "AFM lithography of aluminum for fabrication of nanomechanical systems," *Ultramicroscopy*, vol. 97, no. 1, pp. 467-472, 2003.
[241] C. Zhang, P. Yi, L. Peng, X. Lai, and J. Ni, "Fabrication of Moth-Eye Nanostructure Arrays Using Roll-to-Roll UV-Nanoimprint Lithography With an Anodic Aluminum Oxide Mold," *IEEE Transactions on Nanotechnology*, vol. 14, no. 6, pp. 1127-1137, 2015.
[242] X. Wang, S. Xu, M. Cong, H. Li, Y. Gu, and W. Xu, "Hierarchical Structural Nanopore Arrays Fabricated by Pre-patterning Aluminum using Nanosphere Lithography," *Small*, vol. 8, no. 7, pp. 972-976, 2012.
[243] F. Wang, F. Lv, Y. Liu, C. Li, and Y. Lv, "Ice adhesion on different microstructure superhydrophobic aluminum surfaces," *Journal of Adhesion Science and Technology*, vol. 27, no. 1, pp. 58-67, 2013.
[244] Y. Zhang, D. Ge, and S. Yang, "Spray-coating of superhydrophobic aluminum alloys with enhanced mechanical robustness," *Journal of colloid and interface science*, vol. 423, pp. 101-107, 2014.
[245] A. M. Escobar and N. Llorca-Isern, "Superhydrophobic coating deposited directly on aluminum," *Applied Surface Science*, vol. 305, pp. 774-782, 2014.
[246] A. B. Christiansen, J. S. Clausen, N. A. Mortensen, and A. Kristensen, "Injection moulding antireflective nanostructures," *Microelectronic Engineering*, vol. 121, pp. 47-50, 2014.
[247] A.-K. Holthusen, O. Riemer, J. Schmütz, and A. Meier, "Mold machining and injection molding of diffractive microstructures," *Journal of Manufacturing Processes*, vol. 26, pp. 290-294, 2017.
[248] M. Zhou, B. Jiang, C. Weng, and L. Zhang, "Experimental study on the replication quality of micro–nano cross-shaped structure arrays in injection molding," *Microsystem Technologies*, vol. 23, no. 4, pp. 983-989, 2017.
[249] K. Nagato, T. Hamaguchi, and M. Nakao, "Injection compression molding of high-aspect-ratio nanostructures," *Journal of Vacuum Science & Technology B, Nanotechnology and Microelectronics: Materials, Processing, Measurement, and Phenomena*, vol. 29, no. 6, p. 06FG10, 2011.
[250] D. Masato, M. Sorgato, and G. Lucchetta, "Characterization of the micro injection-compression molding process for the replication of high aspect ratio micro-structured surfaces," *Microsystem Technologies*, vol. 23, no. 8, pp. 3661-3670, 2017.
[251] M. Rohde, A. Derdouri, and M. R. Kamal, "Micro replication by injection-compression molding," *International Polymer Processing*, vol. 24, no. 3, pp. 288-297, 2009.

[252] Y. Chen, Y. Y. Allen, D. Yao, F. Klocke, and G. Pongs, "A reflow process for glass microlens array fabrication by use of precision compression molding," *Journal of micromechanics and microengineering,* vol. 18, no. 5, p. 055022, 2008.
[253] S.-d. Moon, N. Lee, and S. Kang, "Fabrication of a microlens array using micro-compression molding with an electroformed mold insert," *Journal of Micromechanics and Microengineering,* vol. 13, no. 1, p. 98, 2002.
[254] D.-M. Chun, G. Davaasuren, C.-V. Ngo, C.-S. Kim, G.-Y. Lee, and S.-H. Ahn, "Fabrication of transparent superhydrophobic surface on thermoplastic polymer using laser beam machining and compression molding for mass production," *CIRP Annals-Manufacturing Technology,* vol. 63, no. 1, pp. 525-528, 2014.
[255] P. He *et al.*, "Bulk metallic glass mold for high volume fabrication of micro optics," *Microsystem Technologies,* vol. 22, no. 3, pp. 617-623, 2016.
[256] H. Becker and U. Heim, "Hot embossing as a method for the fabrication of polymer high aspect ratio structures," *Sensors and Actuators A: Physical,* vol. 83, no. 1, pp. 130-135, 2000.
[257] C.-J. Ting, M.-C. Huang, H.-Y. Tsai, C.-P. Chou, and C.-C. Fu, "Low cost fabrication of the large-area anti-reflection films from polymer by nanoimprint/hot-embossing technology," *Nanotechnology,* vol. 19, no. 20, p. 205301, 2008.
[258] L. Peng, Y. Deng, P. Yi, and X. Lai, "Micro hot embossing of thermoplastic polymers: a review," *Journal of Micromechanics and Microengineering,* vol. 24, no. 1, p. 013001, 2013.
[259] J. Wang, P. Yi, Y. Deng, L. Peng, X. Lai, and J. Ni, "Recovery behavior of thermoplastic polymers in micro hot embossing process," *Journal of Materials Processing Technology,* vol. 243, pp. 205-216, 2017.
[260] C.-J. Weng *et al.*, "Advanced anticorrosive coatings prepared from the mimicked xanthosoma sagittifolium-leaf-like electroactive epoxy with synergistic effects of superhydrophobicity and redox catalytic capability," *Chemistry of Materials,* vol. 23, no. 8, pp. 2075-2083, 2011.
[261] S. D. Bhagat and M. C. Gupta, "Superhydrophobic microtextured polycarbonate surfaces," *Surface and Coatings Technology,* vol. 270, pp. 117-122, 2015.
[262] B.-Y. Cao *et al.*, "Superhydrophobicity of self-organized surfaces of polymer nanowire arrays fabricated by a nano-injection moulding technique," *Journal of Thermal Science and Technology,* vol. 6, no. 2, pp. 204-209, 2011.
[263] T. Rasilainen, M. Suvanto, and T. A. Pakkanen, "Anisotropically microstructured and micro/nanostructured polypropylene surfaces," *Surface Science,* vol. 603, no. 14, pp. 2240-2247, 2009.
[264] S. Sarbada and Y. C. Shin, "Superhydrophobic contoured surfaces created on metal and polymer using a femtosecond laser," *Applied Surface Science,* vol. 405, pp. 465-475, 2017.
[265] F. Madidi, G. Momen, and M. Farzaneh, "Development of a Stable TiO2 Nanocomposite Self-Cleaning Coating for Outdoor Applications," *Advances in Materials Science and Engineering,* vol. 2016, 2016.
[266] G. Momen and M. Farzaneh, "Simple process to fabricate a superhydrophobic coating," *Micro & Nano Letters,* vol. 6, no. 6, pp. 405-407, 2011.
[267] S. A. Seyedmehdi, H. Zhang, and J. Zhu, "Superhydrophobic RTV silicone rubber insulator coatings," *Applied Surface Science,* vol. 258, no. 7, pp. 2972-2976, 2012.

[268] S. H. Yoon *et al.*, "Effect of processing parameters, antistiction coatings, and polymer type when injection molding microfeatures," *Polymer Engineering & Science*, vol. 50, no. 2, pp. 411-419, 2010.
[269] M. Matschuk, H. Bruus, and N. B. Larsen, "Nanostructures for all-polymer microfluidic systems," *Microelectronic Engineering*, vol. 87, no. 5, pp. 1379-1382, 2010.
[270] G. Heydari, E. Thormann, M. Järn, E. Tyrode, and P. M. Claesson, "Hydrophobic surfaces: topography effects on wetting by supercooled water and freezing delay," *The Journal of Physical Chemistry C*, vol. 117, no. 42, pp. 21752-21762, 2013.
[271] G. Heydari, "Toward Anti-icing and De-icing Surfaces: Effects of Surface Topography and Temperature," KTH Royal Institute of Technology, 2016.
[272] D. Wu *et al.*, "Facile creation of hierarchical PDMS microstructures with extreme underwater superoleophobicity for anti-oil application in microfluidic channels," *Lab on a Chip*, vol. 11, no. 22, pp. 3873-3879, 2011.
[273] S. Liu *et al.*, "Self-cleaning transparent superhydrophobic coatings through simple sol–gel processing of fluoroalkylsilane," *Applied Surface Science*, vol. 351, pp. 897-903, 2015.
[274] B. Bhushan, "Biomimetics: lessons from nature–an overview," ed: The Royal Society, 2009.
[275] Z. Guo, W. Liu, and B.-L. Su, "Superhydrophobic surfaces: from natural to biomimetic to functional," *Journal of Colloid and Interface Science*, vol. 353, no. 2, pp. 335-355, 2011.
[276] K. Ellinas, A. Tserepi, and E. Gogolides, "Durable superhydrophobic and superamphiphobic polymeric surfaces and their applications: A review," *Advances in Colloid Interface Science*, vol. 250, pp. 132-157, 2017.
[277] U. Mehmood, F. A. Al-Sulaiman, B. Yilbas, B. Salhi, S. Ahmed, and M. K. Hossain, "Superhydrophobic surfaces with antireflection properties for solar applications: A critical review," *Solar Energy Materials Solar Cells*, vol. 157, pp. 604-623, 2016.
[278] Y. Shen, X. Wu, J. Tao, C. Zhu, Y. Lai, and Z. Chen, "Icephobic materials: fundamentals, performance evaluation, and applications," *Progress in Materials Science*, 2019.
[279] M. Padaki *et al.*, "Membrane technology enhancement in oil–water separation. A review," *Desalination*, vol. 357, pp. 197-207, 2015.
[280] R. K. Gupta, G. J. Dunderdale, M. W. England, and A. Hozumi, "Oil/water separation techniques: a review of recent progresses and future directions," *Journal of Materials Chemistry A*, vol. 5, no. 31, pp. 16025-16058, 2017.
[281] X. Wang, J. Yu, G. Sun, and B. Ding, "Electrospun nanofibrous materials: a versatile medium for effective oil/water separation," *Materials Today*, vol. 19, no. 7, pp. 403-414, 2016.
[282] J. T. Simpson, S. R. Hunter, and T. Aytug, "Superhydrophobic materials and coatings: a review," *Reports on Progress in Physics*, vol. 78, no. 8, p. 086501, 2015.
[283] Y. T. Cheng, D. Rodak, C. Wong, and C. Hayden, "Effects of micro-and nano-structures on the self-cleaning behaviour of lotus leaves," *Nanotechnology*, vol. 17, no. 5, p. 1359, 2006.
[284] Y. C. Jung and B. Bhushan, "Dynamic effects induced transition of droplets on biomimetic superhydrophobic surfaces," *Langmuir*, vol. 25, no. 16, pp. 9208-9218, 2009.

[285] S. LeClear, J. LeClear, K.-C. Park, and W. Choi, "Drop impact on inclined superhydrophobic surfaces," *Journal of Colloid and Interface Science*, vol. 461, pp. 114-121, 2016.
[286] X. Li, L. Zhang, X. Ma, and H. Zhang, "Dynamic characteristics of droplet impacting on prepared hydrophobic/superhydrophobic silicon surfaces," *Surface and Coatings Technology*, vol. 307, pp. 243-253, 2016.
[287] R. Ramachandran, "Effects of surface topography and vibrations on wetting: Superhydrophobicity, icephobicity and corrosion resistance," 2016.
[288] S. S. Latthe *et al.*, "Self-cleaning and superhydrophobic CuO coating by jet-nebulizer spray pyrolysis technique," *CrystEngComm*, vol. 17, no. 13, pp. 2624-2628, 2015.
[289] A. B. Gurav *et al.*, "Superhydrophobic coatings prepared from methyl-modified silica particles using simple dip-coating method," *Ceramics International*, vol. 41, no. 2, pp. 3017-3023, 2015.
[290] H. Yoon, H. Kim, S. S. Latthe, M.-w. Kim, S. Al-Deyab, and S. S. Yoon, "A highly transparent self-cleaning superhydrophobic surface by organosilane-coated alumina particles deposited via electrospraying," *Journal of Materials Chemistry A*, vol. 3, no. 21, pp. 11403-11410, 2015.
[291] Z. He *et al.*, "Fabrication of superhydrophobic coating via a facile and versatile method based on nanoparticle aggregates," *Applied Surface Science*, vol. 258, no. 7, pp. 2544-2550, 2012.
[292] S. Qiang, K. Chen, Y. Yin, and C. Wang, "Robust UV-cured superhydrophobic cotton fabric surfaces with self-healing ability," *Materials & Design*, vol. 116, pp. 395-402, 2017.
[293] X. Sheng and J. Zhang, "Air layer on superhydrophobic surface underwater," *Colloids and Surfaces A: Physicochemical and Engineering Aspects*, vol. 377, no. 1-3, pp. 374-378, 2011.
[294] Y.-L. Zhang, H. Xia, E. Kim, and H.-B. Sun, "Recent developments in superhydrophobic surfaces with unique structural and functional properties," *Soft Matter*, vol. 8, no. 44, pp. 11217-11231, 2012.
[295] P. Varshney, S. S. Mohapatra, and A. Kumar, "Fabrication of mechanically stable superhydrophobic aluminium surface with excellent self-cleaning and anti-fogging properties," *Biomimetics*, vol. 2, no. 1, p. 2, 2017.
[296] M. Toma, G. Loget, and R. M. Corn, "Flexible teflon nanocone array surfaces with tunable superhydrophobicity for self-cleaning and aqueous droplet patterning," *ACS Applied Materials & Interfaces*, vol. 6, no. 14, pp. 11110-11117, 2014.
[297] M. Satapathy *et al.*, "Fabrication of durable porous and non-porous superhydrophobic LLDPE/SiO2 nanoparticles coatings with excellent self-cleaning property," vol. 341, pp. 31-39, 2018.
[298] W. Tong, D. Xiong, N. Wang, C. Yan, T. J. S. Tian, and C. Technology, "Green and timesaving fabrication of a superhydrophobic surface and its application to anti-icing, self-cleaning and oil-water separation," vol. 352, pp. 609-618, 2018.
[299] S.-P. Fu *et al.*, "Dynamic study of liquid drop impact on supercooled cerium dioxide: anti-icing behavior," *Langmuir*, vol. 32, no. 24, pp. 6148-6162, 2016.
[300] K. Inoue and A. Yamaguchi, "Synthesis of Al4SiC4," *Journal of the American Ceramic Society*, vol. 86, no. 6, pp. 1028-1030, 2003.
[301] C. O. Mgbemena, N. O. Ibekwe, R. Sukumar, and A. R. Menon, "Characterization of kaolin intercalates of oleochemicals derived from rubber seed (Hevea brasiliensis)

and tea seed (Camelia sinensis) oils," *Journal of King Saud University-Science,* vol. 25, no. 2, pp. 149-155, 2013.
[302] H. Hillborg and U. Gedde, "Hydrophobicity recovery of polydimethylsiloxane after exposure to corona discharges," *Polymer,* vol. 39, no. 10, pp. 1991-1998, 1998.
[303] E. Vazirinasab, R. Jafari, and G. Momen, "Application of superhydrophobic coatings as a corrosion barrier: A review," *Surface and Coatings Technology,* 2017.
[304] K. Maghsoudi, G. Momen, R. Jafari, and M. Farzaneh, "Rigorous testing to assess the self-cleaning properties of an ultra-water-repellent silicone rubber surface," *Surface and Coatings Technology,* vol. 374, pp. 557-568, 2019.
[305] R. Jafari, G. Momen, and M. Farzaneh, "Durability enhancement of icephobic fluoropolymer film," *Journal of Coatings Technology and Research,* vol. 13, no. 3, pp. 405-412, 2016.
[306] E. Vazirinasab, K. Maghsoudi, R. Jafari, and G. Momen, "A comparative study of the icephobic and self-cleaning properties of Teflon materials having different surface morphologies," *Journal of Materials Processing Technology,* vol. 276, p. 116415, 2020.
[307] Z. Ghalmi and M. Farzaneh, "Experimental investigation to evaluate the effect of PTFE nanostructured roughness on ice adhesion strength," *Cold Regions Science Technology,* vol. 115, pp. 42-47, 2015.
[308] A. Lazauskas *et al.*, "Water droplet behavior on superhydrophobic SiO2 nanocomposite films during icing/deicing cycles," *Materials Characterization,* vol. 82, pp. 9-16, 2013.
[309] H. Hillborg, M. Sandelin, and U. W. Gedde, "Hydrophobic recovery of polydimethylsiloxane after exposure to partial discharges as a function of crosslink density," *Polymer,* vol. 42, no. 17, pp. 7349-7362, 2001.
[310] Z. Yan, X. Liang, C. Wu, W. Bao, S. Li, and Y. Liu, "Aging and recovery of superhydrophobic silicone rubber under electrical and non-electrical stresses," in *2015 IEEE Conference on Electrical Insulation and Dielectric Phenomena (CEIDP)*, 2015, pp. 189-192: IEEE.
[311] H. Liu, G. A. Cash, R. D. Sovar, G. A. George, and D. Birtwhistle, "Studies of the diffusion of low molecular weight silicone fluids on polluted hv silicone insulators. I. use of diffuse reflectance FTIR," *IEEE Transactions on Dielectrics Electrical Insulation,* vol. 13, no. 4, pp. 877-884, 2006.
[312] E. Vazirinasab, R. Jafari, and G. Momen, "Evaluation of atmospheric-pressure plasma parameters to achieve superhydrophobic and self-cleaning HTV silicone rubber surfaces via a single-step, eco-friendly approach," *Surface and Coatings Technology,* vol. 375, pp. 100-111, 2019.
[313] C. Sansom, P. Comley, P. King, H. Almond, C. Atkinson, and E. Endaya, "Predicting the effects of sand erosion on collector surfaces in CSP plants," *Energy Procedia,* vol. 69, pp. 198-207, 2015.
[314] M. Qiang, F. Chen, A. Zhou, S. Xiao, J. Zhang, and Z. Wang, "Impacts of wind velocity on sand and dust deposition during dust storm as inferred from a series of observations in the northeastern Qinghai–Tibetan Plateau, China," *Powder Technology,* vol. 175, no. 2, pp. 82-89, 2007.
[315] H. Zhang, Y. Tu, Y. Lu, Z. Xu, C. Chen, and L. Xie, "Study on aging characteristics of silicone rubber insulator sheds using FTIR," in *2012 IEEE International Symposium on Electrical Insulation*, 2012, pp. 83-86: IEEE.

[316] K. R. Khedir *et al.*, "Advanced studies of water evaporation kinetics over teflon-coated tungsten nanorod surfaces with variable hydrophobicity and morphology," *The Journal of Physical Chemistry C,* vol. 115, no. 28, pp. 13804-13812, 2011.
[317] D. Chu, A. Nemoto, and H. Ito, "Enhancement of dynamic wetting properties by direct fabrication on robust micro–micro hierarchical polymer surfaces," *Applied Surface Science,* vol. 300, pp. 117-123, 2014.
[318] S. Dash and S. V. Garimella, "Droplet evaporation dynamics on a superhydrophobic surface with negligible hysteresis," *Langmuir,* vol. 29, no. 34, pp. 10785-10795, 2013.
[319] X. Huang *et al.*, "A survey of icephobic coatings and their potential use in a hybrid coating/active ice protection system for aerospace applications," *Progress in Aerospace Sciences,* 2019.
[320] F. Behroozi and P. Behroozi, "Determination of surface tension from the measurement of internal pressure of mini soap bubbles," *American Journal of Physics,* vol. 79, no. 11, pp. 1089-1093, 2011.
[321] A. Davis, Y. H. Yeong, A. Steele, I. S. Bayer, and E. Loth, "Superhydrophobic nanocomposite surface topography and ice adhesion," *ACS Applied Materials & Interfaces,* vol. 6, no. 12, pp. 9272-9279, 2014.
[322] J.-H. Zhi, L.-Z. Zhang, Y. Yan, and J. Zhu, "Mechanical durability of superhydrophobic surfaces: The role of surface modification technologies," *Applied Surface Science,* vol. 392, pp. 286-296, 2017.
[323] G. Ren *et al.*, "A simple way to an ultra-robust superhydrophobic fabric with mechanical stability, UV durability, and UV shielding property," *Journal of Colloid and Interface Science,* vol. 522, pp. 57-62, 2018.
[324] J. H. Van Boxel, "Numerical model for the fall speed of rain drops in a rain fall simulator," in *Workshop on Wind and Water Erosion,* 1997, pp. 77-85.
[325] Z. Wang *et al.*, "Effect of aluminum hydroxide on low-molecular-weight siloxane distribution and microstructure of high-temperature vulcanized silicone rubber," *Journal of Applied Polymer Science,* vol. 135, no. 6, p. 45803, 2018.
[326] S.-d. Moon, N. Lee, and S. Kang, "Fabrication of a microlens array using micro-compression molding with an electroformed mold insert," *Journal of Micromechanics Microengineering,* vol. 13, no. 1, p. 98, 2002.
[327] B. Sha, S. Dimov, C. Griffiths, and M. Packianather, "Investigation of micro-injection moulding: Factors affecting the replication quality," *Journal of Materials Processing Technology,* vol. 183, no. 2-3, pp. 284-296, 2007.
[328] M. Song, Z. Liu, M. Wang, T. Yu, and D. Zhao, "Research on effects of injection process parameters on the molding process for ultra-thin wall plastic parts," *Journal of Materials Processing Technology,* vol. 187, pp. 668-671, 2007.
[329] M. Song, H. Zhao, J. Liu, C. Liu, and J. Li, "Replication of large scale micro pillar array with different diameters by micro injection molding," *Microsystem Technologies,* vol. 23, no. 6, pp. 2087-2096, 2017.
[330] Q. Nguyen, X. Chen, Y. Lam, and C. Yue, "Effects of polymer melt compressibility on mold filling in micro-injection molding," *Journal of Micromechanics Microengineering,* vol. 21, no. 9, p. 095019, 2011.
[331] F. De Santis and R. Pantani, "Development of a rapid surface temperature variation system and application to micro-injection molding," *Journal of Materials Processing Technology,* vol. 237, pp. 1-11, 2016.

[332] N. Zhang, J. Chu, C. J. Byrne, D. Browne, and M. Gilchrist, "Replication of micro/nano-scale features by micro injection molding with a bulk metallic glass mold insert," *Journal of Micromechanics Microengineering*, vol. 22, no. 6, p. 065019, 2012.
[333] G. Lucchetta, M. Sorgato, S. Carmignato, and E. Savio, "Investigating the technological limits of micro-injection molding in replicating high aspect ratio micro-structured surfaces," *CIRP Annals*, vol. 63, no. 1, pp. 521-524, 2014.
[334] P. Wlodarski and J. Pittman, "Replication of surface micro-features using variothermal injection molding: Application to micro-fluidics," *Polymer Engineering Science*, vol. 58, no. 10, pp. 1726-1738, 2018.
[335] V. Speranza, S. Liparoti, M. Calaon, G. Tosello, R. Pantani, and G. Titomanlio, "Replication of micro and nano-features on iPP by injection molding with fast cavity surface temperature evolution," *Materials and Design*, vol. 133, pp. 559-569, 2017.
[336] S. H. Yoon *et al.*, "Effect of processing parameters, antistiction coatings, and polymer type when injection molding microfeatures," *Polymer Engineering Science*, vol. 50, no. 2, pp. 411-419, 2010.
[337] V. Bellantone, R. Surace, G. Trotta, and I. Fassi, "Replication capability of micro injection moulding process for polymeric parts manufacturing," *The International Journal of Advanced Manufacturing Technology*, vol. 67, no. 5-8, pp. 1407-1421, 2013.
[338] F. Baruffi, M. Calaon, and G. Tosello, "Effects of micro-injection moulding process parameters on accuracy and precision of thermoplastic elastomer micro rings," *Precision Engineering*, vol. 51, pp. 353-361, 2018.
[339] M. D. J. Vega, J. Mead, and C. Barry, "Injection molding microstructured substrates from rubber-containing polymers," in *AIP Conference Proceedings*, 2016, vol. 1779, no. 1, p. 020012: AIP Publishing.
[340] C. Lee *et al.*, "Two types of Cassie-to-Wenzel wetting transitions on superhydrophobic surfaces during drop impact," *Soft Matter*, vol. 11, no. 23, pp. 4592-4599, 2015.
[341] Q. Wang, F. Wang, and K. Cheng, "Effect of crosslink density on some properties of electron beam-irradiated styrene–butadiene rubber," *Radiation Physics Chemistry*, vol. 78, no. 11, pp. 1001-1005, 2009.
[342] J. Bibiao, Y. Yang, J. Xiang, Z. Rongqi, H. Jianjun, and W. Wenyun, "Preparation of hyperbranched polymers by self-condensing vinyl radical polymerization," *European Polymer Journal*, vol. 37, no. 10, pp. 1975-1983, 2001.
[343] Y. L. Lu *et al.*, "Impact of curing temperature on microstructures and properties of isobutylene–isoprene rubber/clay nanocomposites," *Applied Polymer Science*, vol. 110, no. 2, pp. 1034-1042, 2008.
[344] R. L. Fan, Y. Zhang, F. Li, Y. X. Zhang, K. Sun, and Y. Z. Fan, "Effect of high-temperature curing on the crosslink structures and dynamic mechanical properties of gum and N330-filled natural rubber vulcanizates," *Polymer Testing*, vol. 20, no. 8, pp. 925-936, 2001.
[345] R. Mathieu, I. Baghdadi, O. Briat, P. Gyan, and J.-M. Vinassa, "D-optimal design of experiments applied to lithium battery for ageing model calibration," *Energy*, vol. 141, pp. 2108-2119, 2017.
[346] H. Tye, "Application of statistical 'design of experiments' methods in drug discovery," *Drug Discovery Today*, vol. 9, no. 11, pp. 485-491, 2004.

[347] C.-C. Kuo and Y.-J. Wang, "Development of a micro-hot-embossing mold with high replication fidelity using surface modification," *Materials Manufacturing Processes,* vol. 29, no. 9, pp. 1101-1110, 2014.
[348] H. Zhang, H. Yang, B. Shentu, S. Chen, and M. Chen, "Effect of titanium dioxide on the UV-C ageing behavior of silicone rubber," *Journal of Applied Polymer Science,* vol. 135, no. 14, p. 46099, 2018.
[349] P. J. Flory and J. Rehner Jr, "Statistical mechanics of cross-linked polymer networks I. Rubberlike elasticity," *The Journal of Chemical Physics,* vol. 11, no. 11, pp. 512-520, 1943.
[350] D. Yang, L. Zhang, H. Liu, Y. Dong, Y. Yu, and M. Tian, "Lead magnesium niobate-filled silicone dielectric elastomer with large actuated strain," *Journal of Applied Polymer Science,* vol. 125, no. 3, pp. 2196-2201, 2012.
[351] L. C. Sim, S. Ramanan, H. Ismail, K. Seetharamu, and T. Goh, "Thermal characterization of Al2O3 and ZnO reinforced silicone rubber as thermal pads for heat dissipation purposes," *Thermochimica Acta,* vol. 430, no. 1-2, pp. 155-165, 2005.
[352] V. Trabadelo, H. Schift, S. Merino, S. Bellini, and J. Gobrecht, "Measurement of demolding forces in full wafer thermal nanoimprint," *Microelectronic Engineering,* vol. 85, no. 5-6, pp. 907-909, 2008.
[353] I. M. Ward and D. W. Hadley, *An introduction to the mechanical properties of solid polymers*. 1993.
[354] X. Wang, Z. Xia, B. Yuan, H. Zhou, Z. Li, and N. Chen, "Effect of curing temperature on the properties of conductive silicone rubber filled with carbonyl permalloy powder," *Materials & Design,* vol. 51, pp. 287-292, 2013.
[355] M. Merola, A. Ruggiero, J. S. De Mattia, and S. Affatato, "On the tribological behavior of retrieved hip femoral heads affected by metallic debris. A comparative investigation by stylus and optical profilometer for a new roughness measurement protocol," *Measurement,* vol. 90, pp. 365-371, 2016.
[356] E. Gadelmawla, M. Koura, T. Maksoud, I. Elewa, and H. Soliman, "Roughness parameters," *Journal of Materials Processing Technology,* vol. 123, no. 1, pp. 133-145, 2002.
[357] M. Sedlaček, B. Podgornik, and J. Vižintin, "Correlation between standard roughness parameters skewness and kurtosis and tribological behaviour of contact surfaces," *Tribology International,* vol. 48, pp. 102-112, 2012.
[358] X. Yin *et al.*, "Integration of self-lubrication and near-infrared photothermogenesis for excellent anti-icing/deicing performance," *Advanced Functional Materials,* vol. 25, no. 27, pp. 4237-4245, 2015.
[359] M.-H. Kim, D. R. Kim, and K.-S. Lee, "Stochastic approach to the anti-freezing behaviors of superhydrophobic surfaces," *International Journal of Heat Mass Transfer,* vol. 106, pp. 841-846, 2017.
[360] A. M. Emelyanenko, L. B. Boinovich, A. A. Bezdomnikov, E. V. Chulkova, and K. A. Emelyanenko, "Reinforced superhydrophobic coating on silicone rubber for longstanding anti-icing performance in severe conditions," *ACS Applied Materials Interfaces,* vol. 9, no. 28, pp. 24210-24219, 2017.
[361] L. Boinovich, A. M. Emelyanenko, V. V. Korolev, and A. S. Pashinin, "Effect of wettability on sessile drop freezing: when superhydrophobicity stimulates an extreme freezing delay," *Langmuir,* vol. 30, no. 6, pp. 1659-1668, 2014.

[362] Q. Yang *et al.*, "Air cushion convection inhibiting icing of self-cleaning surfaces," *ACS Applied Materials Interfaces,* vol. 8, no. 42, pp. 29169-29178, 2016.
[363] K. K. Varanasi, T. Deng, J. D. Smith, M. Hsu, and N. Bhate, "Frost formation and ice adhesion on superhydrophobic surfaces," *Applied Physics Letters,* vol. 97, no. 23, p. 234102, 2010.
[364] https://www.kunststoff-deutschland.com/html/aareplast_ag.html, "Kunststoff-Deutschland," 2015.
[365] D. M. Bryce, *Plastic injection molding: Manufacturing startup and management*. Society of Manufacturing Engineers, 1999.
[366] https://www.toolcraft.co.uk/plastic-injection-moulding/advice/help-injection-moulding-process.htm, "ToolcraftPlastics," 2018.
[367] N. R. Canada. (2017). *Photovoltaic and solar resource maps*. Available: https://www.nrcan.gc.ca/18366

Publications

Book Chapter

"Fabrication of polymer micro-nanostructured surfaces: mold inserts, processing parameters and demolding", K. Maghsoudi, R. Jafari, G. Momen, M. Farzaneh, NOVA Science Publishers, Chapter 1 in book entitled "Polymer Surfaces: Fabrication, Modification and Applications", 2018.

Journal Articles

1- **"Evaluating the effect of processing parameters on the replication quality in the micro compression molding of silicone rubber"**, K. Maghsoudi, E. Vazirinasab, R. Jafari, G. Momen, *Materials and Manufacturing Processes*, 2020. DOI: 10.1080/10426914.2020.1779942.

2- **"Icephobicity and durability assessment of superhydrophobic surfaces: the role of surface roughness and the ice adhesion measurement technique"**, K. Maghsoudi, E. Vazirinasab, G. Momen, R. Jafari, *Materials Processing Technology*, Under review.

3- **"Advances in the fabrication of superhydrophobic polymeric surfaces by polymer molding processes"**, K. Maghsoudi, E. Vazirinasab, G. Momen, R. Jafari, *ACS I&EC Research*, 59, 20, 9343-9363, 2020. DOI: 10.1021/acs.iecr.0c00508.

4- **"Potential anti-icing application of encapsulated phase change material-embedded coatings"**, A. Azimi, A. Allahdini, K. Maghsoudi, R. Jafari, G. Momen, *Journal of Energy Storage*, Under revision.

5- **"Rigorous testing to assess the self-cleaning properties of an ultra-water-repellent silicone rubber surface"**, K. Maghsoudi, G. Momen, R. Jafari, M. Farzaneh, *Surface and Coating Technology*, 374, 557-568, 2019. DOI: 10.1016/j.surfcoat.2019.05.073.

6- **"A comparative study of the icephobic and self-Cleaning properties of Teflon materials having different surface morphologies"**, E. Vazirinasab, K. Maghsoudi, R. Jafari, G. Momen, *Materials Processing Technology*, 276, 116415, 2020. DOI: 10.1016/j.jmatprotec.2019.116415.

7- **"Direct replication of micro-nanostructures in the fabrication of superhydrophobic silicone rubber surfaces by compression molding"**, K. Maghsoudi, G. Momen, R. Jafari, M. Farzaneh, *Applied Surface Science*, 458, 619-628, 2018. DOI: 10.1016/j.apsusc.2018.07.099.

8- **"Micro-nanostructured polymer surfaces using injection molding-A review"**, K. Maghsoudi, R. Jafari, G. Momen, M. Farzaneh, *Materials Today Communications*, 13, 126-143, 2017. DOI: 10.1016/j.mtcomm.2017.09.013.

9- **"Micro-Nanostructured Silicone Rubber Surfaces Using Compression Molding**", K. Maghsoudi, G. Momen, R. Jafari, M. Farzaneh, & T. Carreira, *Materials Science Forum*, 941, 1802-1807, 2018. DOI: 10.4028/www.scientific.net/MSF.941.1802.

Under Preparation Articles

10- **"Drop dynamic behavior on superhydrophobic surfaces; theoretical analysis and machine learning predictive approach"**.

11- **"Fabrication of exceptional hierarchical micro-micro-nanostructured surface with superhydrophobicity"**.

Conferences

1- **"Development of icephobic PDMS coatings by a hybrid approach",** K. Maghsoudi, G. Momen, R. Jafari, *Smart Coatings*, Orlando, Florida, USA, Feb. 2020.

2- **"A new methodology to assess the self-cleaning properties",** K. Maghsoudi, G. Momen, R. Jafari, *QCAM Symposium,* University of Montreal, Montreal, Quebec, Canada, Nov. 2019.

3- **"Self-cleaning properties of injection molded superhydrophobic silicone rubber for high-voltage insulators",** K. Maghsoudi, G. Momen, R. Jafari, M. Farzaneh, T. Carreira, *INMR World Congress,* Tucson, Arizona, USA, Oct. 2019.

4- **"Micro-nanostructured silicone surfaces for high-voltage application",** K. Maghsoudi, G. Momen, R. Jafari, M. Farzaneh, T. Carriera, *IEEE Conference on Electrical Insulation and Dielectric Phenomena (CEIDP),* Cancun, Mexico, Oct. 2018.

5- **"Micro-Nanostructured Silicone Rubber Surfaces Using Compression Molding**", K. Maghsoudi, G. Momen, R. Jafari, M. Farzaneh, & T. Carreira, Thermec'2018, *International Conference on Processing & Manufacturing of Advanced Materials,* Paris, France, July 2018.

6- **"Fabrication de caoutchouc de silicone superhydrophobe par réplication directe",** K. Maghsoudi, G. Momen, R. Jafari, M. Farzaneh, *86^{e} congrès de l'ACFAS*, UQAC, Chicoutimi, Quebec, Canada, May 2018.

7- **"Micro-nanostructured silicone rubber using direct replication",** K. Maghsoudi, R. Jafari, G. Momen, M. Farzaneh, *1st Annual QCAM Symposium,* University of Sherbrooke, Canada, Oct. 2017.